



University of Crete
School of Sciences
Department of Physics



IESL - FORTH

Doctor of Philosophy Thesis

Sensing Resonating Devices Fabricated on Optical Fibers Using Multi-photon Polymerization Technique

Vasileia N. Melissinaki

Supervisor: Prof. C. Fotakis
Advisors: Dr. S. Pissadakis & Dr. M. Farsari

Heraklion, Crete
December 2017

Πανεπιστήμιο Κρήτης
Σχολή Θετικών Επιστημών
Τμήμα Φυσικής

Διδακτορική Διατριβή

Αισθητήριες διατάξεις αντιχείων
συντονισμού εγγεγραμμένες σε
οπτικές ίνες με χρήση μη
γραμμικού φωτοπολυμερισμού

Βασιλεία Ν. Μελισσινάκη

Υπεύθυνος Καθηγητής: Καθ. Κ. Φωτάκης
Επιβλέποντες: Δρ. Μ. Φαρσάρη & Δρ. Σ. Πισσαδάκης

Ηράκλειο Κρήτης
Δεκέμβριος 2017

Table of Contents

Acknowledgments – Ευχαριστίες	11
Περίληψη	13
Abstract	15
Chapter 1	17
Introduction	17
1.1 Fiber-optic sensors; operational characteristics and applications	17
1.1.1 Optical fiber sensors for gaseous and vapor species detection	18
1.1.2 Fiber-optic gas and liquid sensors based on Fabry-Perot interferometers ..	21
1.1.3 Fiber-optic gas or vapors sensors based on whispering-gallery mode (WGM) resonators	24
1.2 Multi-photon Lithography and its applications	25
1.2.1 Whispering-gallery mode micro-resonators fabricated by multi-photon lithography	25
1.2.2 Multi-photon lithography onto optical fibers	26
1.3 Project outline, motivation and applications	26
1.3.1 Project outline	26
1.3.2 Motivation	27
1.3.3 Applications of the devices presented in this thesis	28
1.4 Thesis outline	29
References	30
Chapter 2	41
Theoretical background	41
2.1 Optical Fibers	41
2.1.1 Classifications of optical fibers and fiber parameters	42
2.1.2 Mechanism of Light Propagation in Optical Fibers; Total Internal Reflection	43
2.1.3 Numerical Aperture of optical fiber	45
2.1.4 Material and doping	46
2.1.5 Fiber Losses	46
2.1.5a Attenuation losses in optical fibers	47
2.1.5b Fiber loss mechanisms	48
2.2 Electromagnetic Wave Theory for Optical Fibers	50
2.2.1 Wave theory for TE modes of step-index fibers	54
2.2.2 Wave theory for TM modes of step-index fibers	55

2.2.3 Wave theory for hybrid modes of step-index fibers.....	56
2.2.4 Linearly polarized modes (LP) for weakly guiding approximation.....	59
2.3 Tapered optical fibers.....	63
2.3.1 Fabrication and characteristics of tapered optical fibers.....	63
2.3.2 The shape of tapered optical fibers	65
2.3.2a Determining the taper shape by the specified elongation conditions....	68
2.3.2b Determining the conditions in order to produce a specific taper shape	69
2.3.3 Penetration depth of evanescent field at tapered fibers	70
2.4 Fabry-Perot interferometers	70
2.4.1 Principle of Fabry-Perot interferometers	71
2.5 Whispering-gallery modes resonators.....	73
2.5.1 Light propagation in single ring WGM resonator.....	73
2.5.2 Light propagation in parallel coupled double ring WGM resonators	76
2.6 Multi-photon Polymerization Technique	78
2.6.1 Sequential and simultaneous two-photon absorption (TPA).....	78
2.6.2 Cross-section in the focused spot for single and multi-photon absorption	79
2.6.3 Description of polymerization based on radical initiators	80
2.7 Summary.....	82
References.....	82

Chapter 3 89

Materials and Methods..... 89

3.1 Hybrid materials.....	89
3.1.1 Synthesis of hybrid materials.....	90
3.1.1a Synthesis of the hybrid material for the fabrication of the endface Fabry-Perot microresonators.....	91
3.1.1b Synthesis of the hybrid material for the fabrication of Whispering Gallery Mode (WGM) microring resonators onto tapered fibers	91
3.2 Optical fiber preparation and DLW process	92
3.2.1 Preparation of optical fiber samples for the fabrication of the endface Fabry-Perot microresonators.....	92
3.2.2 Preparation of optical fiber tapered samples for the fabrication of the WGM microring resonators onto them.	94
3.2.3 Direct Laser Writing (DLW) set-up and processes	96
3.2.3a DLW set-up and process for the fabrication of the endface Fabry-Perot microresonators.....	96
3.2.3b DLW set-up and process for the fabrication of WGM microring resonators onto tapered fibers	97
3.3 Summary - Conclusions.....	98

References.....	101
Chapter 4	103
Fabry-Perot optical fiber endface microresonators	103
4.1 Micro-drum FP optical fiber endface resonator; design and principle of operation	103
4.1.1 Spectral characterization of the optical fiber endface FP micro-drum resonator.....	104
4.1.2 Simulating the reflection spectrum of the multiple FP optical fiber microdrum resonator using two-beam optical interference approximation.....	105
4.1.3 Simulating the reflection spectrum of the multiple FP optical fiber microdrum resonator using the Finite - Difference Time - Domain (FDTD) method.....	109
4.2 Microfunnel FP optical fiber endface resonator; design and principle of operation	110
4.2.1 Spectral characterization of the endface FP microfunnel resonator	111
4.2.2 Simulating the reflection spectrum of the multiple FP optical fiber endface microfunnel resonator using two-beam optical interference approximation	112
4.2.3 Simulating the reflection spectrum of the multiple FP microfunnel resonator using the Finite - Difference Time - Domain (FDTD) method.....	114
4.3 Microprism FP endface resonator; design, principle of operation and spectral characterization	115
4.3.1 Spectral characterization of the endface FP microprism resonator.....	116
4.3.2 Simulating the reflection spectrum of the multiple FP microprism resonator using two-beam optical interference approximation.....	116
4.3.3 Simulating the reflection spectrum of the multiple FP microprism resonator using the Finite - Difference Time - Domain (FDTD) method.....	119
4.4 Summary.....	121
References.....	122
Chapter 5	125
Fabry-Perot optical fiber endface micro-resonators; devices and processing	125
5.1 Experimental apparatus used for the characterization of the FP optical fiber endface sensing probes.	126
5.1.1 Experimental apparatus used for the characterization of the FP microresonators for the detection of vapor species.....	126
5.1.1a Characterization of the first FP sensing device for the detection of organic solvent vapors	127
5.1.1b Characterization of the FP microresonator for the detection of chlorinated organic solvent vapors (Cl-VOCs).....	128

5.1.2 Experimental apparatus used for the characterization of the FP microresonators for the detection of liquid species.	129
5.2 Fiber-endface FP microresonator tested for the detection of organic solvent vapors.....	130
5.2.1 Sensing of ethanol vapors using the endface FP resonator as-fabricated .	131
5.2.1a Simulating the results of the micro-prism endface FP optical fiber resonator as-fabricated	133
5.2.1b Confirming the sensing mechanism using the micro-funnel endface FP optical fiber resonator as-fabricated.....	136
5.2.1c Testing the as-fabricated micro-prism endface FP optical fiber resonator at slightly higher temperature	136
5.2.1d Recovery of the endface FP optical fiber resonator after ethanol measurements by flushing the chamber with nitrogen	137
5.2.2 Annealing process of the micro-prism endface FP resonator	138
5.2.3 Sensing of chloroform vapors using the endface FP resonator.....	144
5.2.4 Operation of the sensing probe under ambient air conditions	147
5.3 Fiber-endface FP microresonator with distinct response to different chlorinated organic solvents vapors.....	148
5.3.1 Spectral response of the FP sensing device to Cl-VOCs	149
5.3.1a Recovery of the endface FP optical fiber resonator after Cl-VOCs measurements, by flushing the chamber nitrogen.....	151
5.3.1b Testing the FP optical fiber resonator at slightly higher temperature .	152
5.3.2 Simulating the sensing performance of the endface FP optical fiber sensor to the presence of dichloromethane vapors.....	153
5.4 Fiber-endface FP microresonator for probing of oily samples	156
5.4.1 Spectral response of the FP sensing device to oily samples	156
5.5 Conclusions.....	162
References.....	163

Chapter 6 169

Ring resonators imprinted on tapered fibers..... 169

6.1 Experimental configurations used for the spectral characterization of the microring resonators	169
6.2 Single ring microresonators fabricated onto tapered optical fiber.....	171
6.2.1 First demonstration of single ring on tapered fiber.....	171
6.2.2 Parameterization of the photopolymerization process	176
6.2.3 Fabrication of microrings with different thickness	177
6.3 Coupled and defected ring resonators structures	179
6.3.1 Parallel coupled microring resonators	179
6.3.2 Defected microring resonator	187

6.4 Summary and Conclusions	188
References.....	189
Chapter 7	193
Ring resonators on tapered fibers; devices and processing	193
7.1 Experimental apparatus for the characterization of the ring resonating optical fiber structures	193
7.2 First device: Single ring WGM microsensor for ethanol vapors detection	195
7.2.1 Characterization of the sensing probe.....	195
7.2.2 Sensing of ethanol vapors using single ring WGM microresonator device	197
7.3 Second device: WGM Coupled microresonators device for gas sensing	201
7.3.1 Characterization of sensing probe using diatomic Nitrogen and Krypton	201
7.3.2 Comparison between Nitrogen and Krypton sensing	206
7.4 Third device: WGM Coupled microsensor for ethanol vapors detection	207
7.4.1 Sensing of ethanol vapors using a coupled WGM microresonator device	207
7.4.2 Comparison of single and coupled WGM microring ethanol sensing devices.....	210
7.5 Summary and Conclusions	210
References.....	211
Chapter 8	215
Conclusions	215
8.1 Summary and conclusions for the endface FP optical fiber devices.....	215
8.2 Summary and conclusions for the WGM microring resonating devices fabricated directly onto tapered fibers	217
8.3 Applications of the devices presented in this thesis.....	219
References.....	220
Publications.....	223
Conferences.....	224
Funding	225

Acknowledgments – Ευχαριστίες

Για εκπόνηση αυτής της διδακτορικής διατριβής συνέβαλαν αρκετοί άνθρωποι, τους οποίους θα ήθελα να ευχαριστήσω.

Κατ'αρχήν, θα ήθελα να ευχαριστήσω τον επιβλέποντα αυτής της διατριβής, Ομότιμο Καθηγητή του τμήματος Φυσικής του Πανεπιστημίου Κρήτης, Κωνσταντίνο Φωτάκη, ο οποίος μου έδωσε την ευκαιρία να εργαστώ στο Ι.Η.Δ.Λ. κατά την διάρκεια διεξαγωγής των πειραμάτων.

Στη συνέχεια, να ευχαριστήσω εξίσου θερμά τους δύο επιβλέποντες, ερευνητές Α' του Ι.Η.Δ.Λ., Δρ. Μαρία Φαρσάρη και Δρ. Σταύρο Πισσαδάκη, για την πολύτιμη υποστήριξη τους τόσο υλικοτεχνικά όσο και επιστημονικά. Την Δρ. Μαρία Φαρσάρη για την φιλοξενία στο εργαστήριο μη γραμμικής λιθογραφίας όπου κατασκευάστηκαν οι δομές που χρησιμοποιήθηκαν σε αυτή την διατριβή και τον Δρ. Σταύρο Πισσαδάκη για την καθοδήγηση κατά την διάρκεια του χαρακτηρισμού των οπτικών αισθητήρων στο εργαστήριο φωτονικών υλικών και διατάξεων.

Επιπλέον, να ευχαριστήσω θερμά τους Καθηγητές του τμήματος Φυσικής του Πανεπιστημίου Κρήτης, Θ. Π. Ρακιτζή και Δ. Χαραλαμπίδη, τον αναπληρωτή Καθηγητή του τμήματος Επιστήμης και Τεχνολογίας Υλικών του Πανεπιστημίου Κρήτης Δρ. Ν. Χρόνη, και τέλος τον Δρ. Χ. Ριζιώτη, ερευνητή Γ' του Εθνικού Ιδρύματος Ερευνών για την συμμετοχή τους στην επταμελή εξεταστική επιτροπή της παρούσας διατριβής.

Να ευχαριστήσω ακόμα, την Δρ. Μαρία Κωνσταντάκη για την βοήθεια της στο εργαστήριο των φωτονικών υλικών και διατάξεων και ειδικότερα για την παροχή των θερμικά εφελκυσμένων οπτικών ινών. Την κα Α. Μανουσάκη για την βοήθεια της στην μελέτη των δειγμάτων με την χρήση του Ηλεκτρονικού Μικροσκοπίου Σάρωσης.

Θα ήθελα επίσης να ευχαριστήσω θερμά, τον Δρ. Ι. Κονιδάκη για την συνεργασία μας στην κατανόηση των μηχανισμών της αλληλεπίδρασης των διαλυτών με τους αισθητήρες που δημιουργήθηκαν και την Δρ. Κ. Κοσμά για την βοήθεια της και τις γνώσεις που μου μετέδωσε στην προσομοίωση των αισθητήρων με υπολογιστικά προγράμματα, αλλά και στην ψυχολογική υποστήριξη καθόλη την διάρκεια της διδακτορικής διατριβής. Επιπλέον να ευχαριστήσω την Ε.-Α. Καμπουράκη για την βοήθεια της στη σύνθεση των υβριδικών υλικών και για τις συζητήσεις μας όσον αφορά τα πειράματα, αλλά και την συμπαράσταση όλα αυτά τα χρόνια.

Να ευχαριστήσω ακόμα όλα τα παιδιά από τα δύο εργαστήρια για την αρμονική συνύπαρξη στον ίδιο χώρο και τις συμβουλές που ανταλλάσσαμε. Επίσης να ευχαριστήσω την Δρ. Μ. Συγγέτου και όλα τα υπόλοιπα κορίτσια που μοιραζόμασταν όλα αυτά τα χρόνια το ίδιο γραφείο και ήταν εκεί για ότι και αν χρειαζόμουν.

Τέλος το μεγαλύτερο και θερμότερο ευχαριστώ θα ήθελα να το πω στην οικογένεια μου και τον σύζυγό μου Δρ. Γ. Μπαρμπαρή, οι οποίοι με στήριζαν και με στηρίζουν με υπομονή και κατανόηση σε κάθε μου βήμα.

Σας ευχαριστώ πολύ όλους!

Περίληψη

Στόχος της παρούσας διδακτορικής διατριβής είναι ο συνδιασμός της τεχνικής της πολυφωτονικής λιθογραφίας και τον οπτικών ινών με σκοπό την κατασκευή εύρωστων και λειτουργικών διατάξεων οπτικών ινών, οι οποίες θα χρησιμοποιηθούν ως αισθητήριες διατάξεις για την ανίχνευση αέριων ή υγρών μέσων. Επιπλέον η παρούσα διατριβή μελετά και παρουσιάζει τα πλεονεκτήματα και τα μειονεκτήματα της απευθείας εγγραφής με Laser, μικρο-οπτικών αντιχείων εγκλωβισμού του φωτός επάνω σε οπτικές ίνες.

Δυο διαφορετικά είδη αντιχείων εγκλωβισμού του φωτός κατασκευάστηκαν απευθείας επάνω σε οπτικές ίνες, με την τεχνική του πολυφωτονικού πολυμερισμού. Συγκεκριμένα θα παρουσιαστούν (i) διατάξεις οπτικών ινών βασισμένες σε Fabry-Perot συμβολόμετρα, κατασκευασμένα στην διατομή οπτικών ινών καθώς επίσης και (ii) αντιχεία τρόπων ψιθυρισμού σε σχήμα δαχτυλιδιού κατασκευασμένα απευθείας επάνω σε θερμικά εφελκυσμένες οπτικές ίνες. Και οι δύο διατάξεις αντιχείων λειτουργούν στην περιοχή των 1550 nm μηκών κύματος. Για την κατασκευή των μικρο-οπτικών αντιχείων χρησιμοποιήθηκαν υβριδικά οργανικά-ανόργανα φωτοευαίσθητα υλικά. Επιπλέον, νέες μέθοδοι αναπτύχθηκαν και χρησιμοποιήθηκαν για την προετοιμασία των δειγμάτων.

Αρχικά θα παρουσιαστούν τρεις διαφορετικές διατάξεις οπτικών ινών βασισμένες σε Fabry-Perot συμβολόμετρα, κατασκευασμένες στην διατομή οπτικών ινών, καθώς επίσης και τα αποτελέσματα από την χρήση τους ως αισθητήριες διατάξεις για τον εντοπισμό ατμών οργανικών διαλυτών όπως η αιθανόλη και χλωριωμένων οργανικών διαλυτών. Επιπλέον, οι διατάξεις αυτές χρησιμοποιήθηκαν και για την ανίχνευση ελαιωδών υγρών μέσων. Λόγω της διέγερσης των οπτικών αντιχείων μέσω της διάδοσης του φωτός, μέσω του πυρήνα των οπτικών ινών, μπορούν να καταγραφούν οι διαφορές στον δείκτη διάθλασης που δημιουργούνται λόγω της παρουσίας των ατμών ή των υγρών μέσα στην οπτική κοιλότητα των αντιχείων, μέσω των φασμάτων ανάκλασης.

Στην συνέχεια θα παρουσιαστούν διάφορα αντιχεία τρόπων ψιθυρισμού σε σχήμα δαχτυλιδιού κατασκευασμένα απευθείας επάνω σε θερμικά εφελκυσμένες οπτικές ίνες, καθώς επίσης και συζευγμένα αντιχεία τρόπων ψιθυρισμού. Οι διατάξεις αυτές χρησιμοποιήθηκαν ως αισθητήρες για τον εντοπισμό ατμών αιθανόλης, καθώς επίσης και για την ανίχνευση αδρανών αερίων όπως το διατομικό Άζωτο (N_2) και το Κρυπτό (Kr), μέσω της καταγραφής των φασμάτων διέλευσης.

Abstract

The aim of this thesis is to combine standard single mode optical fibers and multi-photon lithography in order to produce robust and functional fiber-optic devices that will be exploited as fiber-optic gas or liquid sensors in the time being; also constituting basic platforms for other sensing and switching devices. Further, this study investigates in depth the advantages and disadvantages of the direct laser fabrication of micro-optical light resonating cavities onto the optical fibers.

For these reasons two different kinds of light resonating structures were fabricated by multi-photon polymerization technique directly onto single mode, telecom optical fibers. In particular, (i) fiber-optic devices based on Fabry-Perot interferometers fabricated on the endface of optical fibers and (ii) whispering-gallery mode micro-ring resonators fabricated directly onto tapered optical fibers will be demonstrated. In both cases hybrid organic-inorganic photosensitive materials were used for the fabrication of the light resonating components. For the fabrication of these fiber-optic interferometric devices new processes for the sample preparation had to be explored and developed. Furthermore, the designs of the interferometric components and their fabrication parameters had to be studied in order to produce functional structures. The spectral performance of both resonating devices was tested in the wavelength region of 1550 nm.

Initially, three different designs of fiber-optic devices based on Fabry-Perot interferometers were fabricated on the endface of optical fibers, namely, microdrum, microfunnel and microprism. Their fringe visibilities that were recorded were up to ~ 22 dB, while the free spectral range (FSR) was differ according to the length cavity, for example for a length cavity of ~ 18 μm the corresponding FSR was ~ 68 nm. The microprism endface FP devices were tested as vapor sensors for the detection of ethanol and chlorinated organic solvents vapors with sensitivities down to 4 ppm. Their sensitivities with respect to the surface porosity of the fabricated micro-prism sensing head were studied by reducing the pores size of the photopolymerized reflection surface using annealing treatment processes. Results show the dependence of the sensitivity and selectivity/specificity upon the porosity of the fabricated FP cavity. Moreover, the studies revealed that the operation mechanism of the fabricated sensing device did not depended only on the optical and vapor pressure characteristics of the solvents but also on their molecular structure and affinity to the sensing surfaces, thus revealing distinct spectral response versus sensing time. In addition, sensing mechanism of the devices was based on physisorption phenomena, allowing the full recover of the sensing probes to their initial spectral response (after pumping with nitrogen) and their reuse for several times. Sensitivities of $\sim 1.5 \times 10^3$ nm/RIU were recorded in case of ethanol vapors. For the liquid sensor the device was used for the probing of substances of oily media. Experiments revealed that each of the oily liquids exhibited a distinct spectral response versus sensing time, depending on the diffusion process of the oily liquid into the photopolymerized porous reflection surface.

Regarding to the second part of this thesis, we proposed and realized for the first time the fabrication of micro-ring resonators directly onto tapered single mode telecommunication fibers by employing the multi-photon polymerization technique. Such an approach allowed the demonstration of integrated and robust tapered optical fiber WGM resonators of straightforward packaging capabilities. A fabricated ring of 20 μm diameter and thickness of ~ 900 nm onto a taper of 2.4 μm diameter, revealed fringe visibility of 20 dB and Q factor of 3.55×10^3 operating in TM polarization. Parallel coupled microresonators with different center to center distances were also fabricated resulting fringe visibility of 38.5 dB and Q factor of 3.82×10^3 operating in TE polarization. The single and coupled microring resonators were tested as vapor sensors for ethanol species. The sensing devices presented sensitivities down to 0.5 ppm. The parallel coupled ring sensor was also tested as a pressure sensor for the detection of inert gases (N_2 and Kr). Pressures down to 50 mbar were recorded.

Chapter 1

Introduction

Fiber-optic sensors have been shown for first time in 1970s, while their emergence was prompted by the realization of low-loss single-mode optical fibers [1, 2]. Since then, numerous fiber-optic sensors have been demonstrated in academic laboratories around the world, aiming either to replace the existing conventional sensors or to penetrate fiber-optic sensors into new application areas.

1.1 Fiber-optic sensors; operational characteristics and applications

A fiber-optic sensor system consists of an optical source (laser, LED, laser diode, *etc.*), an optical fiber, a sensing or modulator element transducing the measurand to an optical signal, and an optical detector (optical spectrum analyzer, *etc.*) [3, 4].

Fiber-optic sensors are often grouped into two basic classes according to the manner in which the optical fiber is used, namely to intrinsic or all-fiber and extrinsic or hybrid sensors. In case of the intrinsic fiber-optic sensors the modulation takes place directly in the fiber, while in extrinsic sensors, the modulation is performed by some external transducer [2, 4, 5].

More detailed, intrinsic fiber optic directly employs an optical fiber as the sensitive material, sensor head, and also as the medium to transport the optical signal with information of the perturbation environment to be measured. They operate through the direct modulation of the light guided into the optical fiber. The light does not leave the fiber, except at the detection end, the output, of the sensor. These sensors can use interferometric configurations, fiber Bragg grating, long period fiber grating, or special fibers (doped fibers) designed to be sensitive to specific perturbations.

On the other hand, in extrinsic fiber-optic sensors the optical fiber is simply used to guide the light to and from a location at which an optical sensor head is located. The sensor head is external to the optical fiber and is usually based on miniature optical components, which are designed to modulate the properties of light in response to changes in the environment with respect to physical perturbations of interest. Thus, in this configuration, one fiber transmits optical energy to the sensor head. Then, this light is suitably modulated and is coupled back to the optical detector.

Owing to their unique characteristics such as small size, high flexibility, low propagating loss, large bandwidth, high sensitivity and accuracy, simultaneous sensing ability, remote sensing and immunity to electromagnetic interference, fiber-optic sensors exploit a diverse range of phenomena and effects [3, 4]. To date, the most highlighted application fields of fiber-optic sensors are in large composite and concrete structures, electrical power industry monitoring, medicine, rehabilitation and biosensing, chemical sensing, and gas and oil industries [3, 5, 6]. A variety of studies have been made to utilize optical fibers as sensing indicators for temperature,

humidity, refractive index, viscosity, pressure, strain, displacement, vibration and several other environmental factors [3, 7, 8]. Furthermore, their sensing abilities have been considerably enhanced by utilizing innovative fiber optic technologies of fiber gratings, fiber interferometers such as Fabry-Perot (FP) or whispering-gallery mode (WGM) resonators, Brillouin or Raman scattering, surface plasmon resonance, micro-structured fibers etc. [5, 7, 8].

1.1.1 Optical fiber sensors for gaseous and vapor species detection

The detection of gas and volatile organic compounds (VOCs) has a significant impact in a wide range of everyday and more specialized applications [9-11]. Gas and VOCs sensors are widely used in industries to ensure safety (e.g. via detection of toxic or flammable gases), or measure key species in products (ie food and beverages) and processes. Moreover, high sensitivity gas detectors is widespread in atmospheric science, where they are used to measure and estimate the profile and pathways of different gas species circulating, including highly active greenhouse gases. Furthermore, various gases biomarker are also under study for use in breath diagnostics, including ethanol [12-14], ammonia (NH₃) [15-17] and few others [18].

Detection of gases is traditionally dominated by laboratory analytical equipment such as gas chromatographs, field effect gas sensors, semiconductor gas sensors, electrochemical devices or catalytic bead gas sensors and more [19, 20]. Catalytic bead gas sensors based on pellistors are robust devices that respond well in detecting flammable gases close to the lower explosive limit, however suffer from zero drift at parts per million (ppm) levels [10]. Semiconductor gas sensors can be highly sensitive at the low ppm level, however they suffer from drift and cross-respond to other gases and during changes at the humidity levels during measurements [20]. Electrochemical gas sensors can be relatively specific to individual gases and they are sensitive at ppm or ppb levels, however they have limited lifetimes and also suffer from cross-response issues and at the presence of humidity [20]. In contrast, gas sensors based on optical absorption offer fast temporal responses, minimal drift and high gas specificity, with zero cross-response to other gases, as long as their transducing material and optical design is suitably considered.

Fiber-optic gas and VOCs sensors had been developed over the last decays and they are good candidates for many applications due to their properties and the fact that they can be used for on-line monitoring [9, 10]. For example, they can be used in environments where the inflammability risk is high (e.g. at the presence of fuel or heating gases) since they do not need electric power to work. Moreover due their immunity to electromagnetic interferences they can be used at electric power industries to detect toxic gases [21]. Optical fiber sensors can be also used in non-invasive applications, from food control to the measurement of gases dissolved in liquids [22, 23]. Finally, they can also be used in health diagnoses systems such as breath diagnostic tools (e.g. spirometers) [24] or even for gases dissolved in bio-fluids (e.g. blood, urine etc.) [25]. Finally, the possibility of multiplexation of the optical fiber sensors permits deployment of several optical fiber sensors over a grid,

rendering possible the implementation of a multi-point sensor network. Different approaches, techniques and materials will be presented below indicatively, for the fabrication of fiber-optic gas sensors, exploited by different academic research groups.

Zinc oxide nanorods or nanoparticles incorporated with optical fibers are used by many different research groups in order to form gas sensors. Konstantaki, et al., had presented an ethanol vapor detection probe based on an optical fiber long period grating overlaid with a zinc oxide (ZnO) nanorods layer, developed onto the cladding of the fiber using aqueous chemical growth [26]. The growth of the ZnO nanorods overlayer onto the long period grating cladding was monitored in real time for investigating its effect on the spectral properties of the device and its subsequent role in the sensing mechanism. This probe had been used in order to correlate the growth time of the ZnO layer and the ethanol vapor detection performance. Reversible spectral changes of the notch extinction ratio of more than 4dB were recorded for ~50Torr (~67 mbar) of ethanol vapor concentration. Additionally, H. Fu et al. had coated a tapered microfiber with zinc oxide nanoparticle incorporated graphene oxide (GO-ZnO) [15]. GO-ZnO nanocomposites were serving as electron acceptors which trapping electrons after ammonia absorption and then changing the surface refractive index of the optical microfiber resulting wavelength shift of the transmission spectra. This sensor had been used to detect ammonia in different connections from 4 ppm to 140 ppm at room temperature resulting a ~5 nm spectral shift in case of 4 ppm ammonia detection.

Other groups are using metal coatings in order to fabricate the gas sensing/transducing area. For example, A. Gonzalez-Vila et al. had synthesized a conductive molecularly imprinted polymer around the cylindrical surface of a gold-coated optical fiber following an electro-polymerization process [27]. The metal film was used as a working electrode during the procedure in order to make the polymer grow on top of it. In addition, the fiber core was previously photo-inscribed with a tilted fiber Bragg grating to benefit from its surrounding refractive index sensitivity. Light was coupled to the fiber cladding by the grating planes excites a plasmon wave on the gold surface, enhancing its refractometric properties. The polymer-coated sensor was able to work into gaseous atmospheres and the performance of the sensor was tested by detecting ethanol, acetone and toluene vapors, resulting a sensitivity of 0.44pm/ppm in case of ethanol vapors.

Other researchers, as K. Yamini, et al., had used nanocrystalline nickel oxide embedded coatings to fabricate clad modified optical fiber gas sensor for sensing volatile organic compound vapours (VOCs) such as formaldehyde, ammonia, ethanol and methanol up to 500 ppm [28]. They had synthesized two different nickel oxide crystallite sizes such as 24 nm and 76 nm by calcination of reverse precipitated nickel hydroxide subsequently at 450 °C and 900 °C for 30 min. Their gas sensing measurement conclude that the lower crystallite size (24 nm) nickel oxide nanocrystals exhibited superior sensitivity to all the concentrations of test vapours as compared with higher crystallite size (76 nm) sample because of the higher surface area.

J. C. Echeverría et al. investigated the response of three fiber optic sensing elements prepared at pH 10 from phenyltriethoxysilane (PhTEOS) and tetraethylsilane (TEOS) mixtures with 30, 40, and 50% PhTEOS in the silicon precursor mixture [29]. The films were synthesized by the sol–gel method and affixed to the end of optical fibers by the dip-coating technique. Fourier transform infrared spectroscopy, N₂ adsorption–desorption at 77 K and X-ray diffraction analysis were used to characterize the xerogels. They had observed that, at a given pressure of *n*-hexane, the response of each sensing element decreased with temperature, indicating an exothermic process that confirmed the role of adsorption in the overall performance of the sensing elements. The isosteric adsorption enthalpies were obtained from the calibration curves at different temperatures.

In contrary, other researchers are using graphene layers in order to fabricate fiber-optic gas sensors. For example, J. Y Zhang et al. had used single-mode optical fibers and they had polished the fiber core via wheel side-polishing [30]. The exposed fiber core areas were coated with graphene-doped tin oxide in order to fabricate a graphene-based optical fiber methane sensor. The sensor exhibited a linear fitting for methane concentrations from 5% - 55%. S. Tabassum et al. had used a different approach in their work [31]. They had presented a method of patterning nanostructures on the cleaved endface of an optical fiber in order to fabricate a high-performance fiber-optic gas sensor. The fabrication method utilized an ultraviolet assisted nano-imprint lithography to transfer nanoscale patterns from a pre-formed stamp to the fiber tip. By this way a periodic array of polymer nanoposts were formed at the fiber tip and coated with titanium dioxide to serve as a guided mode resonant (GMR) device. A gas sensor was realized by coating the GMR structure with a thin layer of graphene oxide (GO) nanosheets. Volatile organic compounds, such as ethylene and methanol, were detected by the sensor. The sensor provided sensitivities of 0.92 and 1.37 pm/ppm for ethylene and methanol vapors, respectively. Z. H. Zhang et al. fabricated a probe to detect water and ethanol vapors, by coating the endface of a standard multimode optical fiber with fluorescent silicon quantum dots (Si-QDs) [32]. When the sensor was exposed to different vapors, the luminescence intensity of the Si-QDs varied over timescales of a few seconds to hours. The Si-quantum-dot-based fiber sensor show a fast response time and detection limits down to ~380 ppm of ethanol, but the true quantification was difficult due to variations from the one sample to other.

M. Yan et al. proposed a multicomponent gas sensor based on an etched optical fiber, for measuring H₂, CO₂, CH₄ and CO in humid high temperature environments [33]. A single sensor element comprised of a perovskite La_{0.3}Sr_{0.7}TiO₃ oxide thin film layer coated on silica optical fiber which cladding layer was etched by buffered hydrofluoric acid was used. The sensing responses consisted of two wavelength-specific near infrared (NIR) mechanisms, namely broadband absorption associated with the metal oxide layer, and wavelength localized thermal emission responses associated with the hydroxyl defects within the silica fiber. Successful discrimination of H₂ and CO₂ on a single fiber sensor was achieved, where the results are both stable and reversible for flow rates from 10 to 100 sccm.

Another approach for the fabrication of fiber-optic gas sensors is the use of tapered optical fibers in combination with a coating in order to have a sensitive system. For example, N. E Gonzalez-Sierra et al. used a tapered optical fiber functionalized with palladium nanoparticles for sensing of hydrogen and volatile organic compounds (VOCs) [34]. The tapered optical fiber sensor was fabricated using a single-mode optical fiber by the flame-brushing technique, while the functionalization of the optical fiber was performed using an aqueous solution of palladium chloride by drop-casting technique assisted for laser radiation. The detection principle of the sensor was based on the changes in the optical properties of palladium nanoparticles when they were exposed to reducing gases, which caused a variation in the absorption of evanescent waves. By this way, the fabricated sensor was able to sense ~240ppm of acetone, 60 ppm of 2-propanol and ~12 ppm of xylene. Another ammonia gas sensor that was used tapered fibers was proposed by L. Sun et al. [17]. At that study the sensor based on a silica gel coated microfiber coupler (MFC). The MFC structure was formed by two tapered fibers with 3 μm waist diameter each, which were fabricated by using a customized microheater brushing technique. Then a silica gel coating was prepared by a sol-gel technique and applied on the surface of the MFC as a thin layer. The experimental results show that the coating thickness strongly affected the sensitivity of the MFC-based sensor to ammonia gas concentration. For a sensor with a 90 nm silica gel coating thickness, the highest measurement sensitivity was 2.23 nm/ppm, while the measured response and recovery times were ~ 50 and 35 seconds, respectively.

On the other hand, C. Caucheteur et al. proposed an ultrasensitive plasmonic optical fiber platform operating in air [35]. They had used a highly tilted Bragg grating which was coated with a gold layer. By this way a spectral comb of narrowband-cladding modes were excited with effective indices near 1.0 and below. Using conventional spectral interrogation, they measured shifts of the SPP-matched resonances in response to static atmospheric pressure changes down to 1kPa (10 mbar) with 204nm/RIU.

As it was presented above, there are many different techniques and materials that one can use in order to fabricate a fiber-optic gas sensor. There are also fiber-optic gas sensors based on Fabry-Perot interferometers and whispering-gallery mode resonators that will be presented in details in the following sections, since both of these interferometric components were used for the fabrication of the fiber-optic sensing devices that will be presented in this thesis.

1.1.2 Fiber-optic gas and liquid sensors based on Fabry-Perot interferometers

Fabry-Perot (FP) interferometers are simple design, photonic elements that can provide decent light localization performance [36]. Several techniques have been developed for the fabrication of fiber-optic sensors based on Fabry-Perot (FP) interferometer [37, 38]. The most common techniques that have been extensively used are laser micromachining methods [39-41], chemical etching [42, 43], fusion splicing of single mode fibers (SMF) with photonic-crystal fibers (PCF) [44] or

microstructured optical fibers (MOF) [45] and dip-coating methods [46]. By this was FP cavities can be implemented in-line, on the cladding or on the endface of the optical fiber.

Fabry-Perot cavities can be used for detecting changes occurring either within the resonance optical path, or loss and phase changes occurring at the reflected surfaces. Fiber-optic FP resonators have been used for measuring temperature [44, 45, 47, 48], pressure [49-52], strain [42, 53-55], pH [56], displacement [57], surface analysis [58] etc. Moreover, fiber-optic FP sensors have been widely used for the measurements of refractive index changes due to the presence of gaseous or liquid species within their cavities, since they can offer a number of specific advantages over other optical fiber sensors, such as high sensitivity, high measurement range, ability for multi-parametric sensing, rapid response, etc. Below, some examples from fiber-optic sensors for gaseous or liquid species based on refractive index measurements will be presented.

Many different research groups are using the fusion splicing technique between single mode fibers and hollow silica tubes (HST), hollow core fibers (HCF), photonic crystal (PCF) or microstructured optical fibers (MOF) in order to fabricate the FP cavities. For example, P. Jia et al. had fabricated a temperature-compensated Fabry-Perot interferometric gas refractive-index sensor, by inserting a single-mode fiber (SMF) and a hollow silica tube (HST) with an inner diameter of 5 μm [59]. The light was reflected and refracted multiple times between the end facets of the SMF and HST, and the RI changes in the open-cavity FP interferometric sensor could be detected by determining the wavelength shift of the interference spectrum. Experimental results show that the gas RI sensor has a linear sensitivity of approximately 1546 nm/RIU from room temperature to 800°C. Ferreira et al. had also proposed a Fabry-Perot cavity based on a pure silica diaphragm-free hollow tube [60]. Its operation was based on a first reflection of light at the end of the single-mode fiber that illuminated the silica rod and in a second reflection that took place at the end of the rod. The FP cavity was characterized for high temperature, pressure and refractive index sensing, showing useful characteristics for the measurement of these three parameters. The diaphragm-free configuration simplifies the measurement of the refractive index of fluids.

In addition, Y. Z. Tan et al. had proposed a high finesse hollow-core photonic bandgap fiber (HC-PBF) resonating Fabry-Perot gas cells [61]. These gas cells were made with a piece of HC-PBF sandwiched by two single mode fibers with mirrored ends. Experiments with a 9.4 cm long Fabry-Perot gas cell with a finesse of 68 demonstrated a detection limit of 7 ppm acetylene. Moreover, J.J. Tian et al. had proposed a microfluidic fiber-optic refractive index (RI) sensor based on an in-line Fabry-Perot interferometer, which was formed by silica tube sandwiched by two microstructured optical fibers [62]. The micro-sized holes in the MOF naturally function as microfluidic channels through which liquid samples could be efficiently and conveniently delivered into and out of the Fabry-Perot cavity by a pressure/vacuum pump system for high-performance RI measurement. Due to the microfluidic capability enabled by the MFs, only sub microliter sample was required. Furthermore, Y. J. Rao et al. demonstrated a refractive-index sensor which was based

on an intrinsic Fabry-Perot interferometer (IFPI) formed by a section of endlessly single-mode photonic crystal fiber (EPCF) and conventional single-mode fiber [63]. This miniature fiber-optic sensor was demonstrated for the measurement of the refractive index change of glycerin solution by measuring its fringe visibility change solely. The refractive-index resolution that was achieved and the repeatability was $\sim 2 \times 10^{-5}$ and ± 0.5 % FS in the linear operating range. Additionally, T. Z. Ming Deng presented a miniaturized fiber-optic Fabry-Perot interferometer for highly sensitive refractive index measurement, which was consisting of fused spliced single-mode fiber (SMF) to a graded-index multimode fiber (MMF) and at the end a photonic crystal fiber (PCF) [64]. This device was tested for the refractive indices of various liquids including acetone and ethanol at room temperature. The sensitivity for measurement of refractive index change of ethanol was 1138 nm/RIU at the wavelength of 1550 nm. Finally, a fiber-optic sensor formed by multi-step splicing and etching of different kinds of optical fibers was presented by S. Pevec et al. [65]. The final Fabry-Perot cavity had been formed at the tip of an optical fiber that utilized a silica nanowire within a radius of between 225 nm and 600 nm. Sensitivity in excess of 800 nm/RIU was demonstrated within an aquatic medium, while the entire sensor structure was shorter than 1 mm with a diameter equal to the standard fiber diameter.

Another technique that is usually used for the fabrication of fiber-optic Fabry-Perot cavities is the micromachining. In this direction, Z. L. Ran et al. proposed a Fabry-Perot optical fiber tip sensor for high-resolution refractive-index measurement fabricated by using laser micromachining [39]. The sensor head consisted of a short air Fabry-Perot cavity near the tip of a single-mode fiber. The external refractive index was determined according to the maximum fringe contrast of the interference fringes in the reflective spectrum of the sensor. Such a sensor can provide a refractive-index resolution of $\sim 4 \times 10^{-5}$ in its linear operating range. Moreover, C. R. Liao et al. demonstrated a fiber in-line Fabry-Perot interferometer cavity sensor for refractive index measurement [66]. The interferometer cavity was formed by drilling a micro-hole at the cleaved fiber end facet, followed by fusion splicing. A micro-channel was inscribed by femtosecond laser micromachining to vertically cross the cavity to allow liquid to flow in. The refractive index sensitivity obtained was ~ 994 nm/RIU. Finally, T. Wei et al. proposed a miniaturized fiber in-line Fabry-Perot interferometer, with an open micro-notch cavity fabricated by one-step fs laser micromachining, for highly sensitive refractive index measurement [67]. The device was tested for measurement of the refractive indices of various liquids including isopropanol, acetone and methanol at room temperature, as well as the temperature-dependent refractive index of deionized water from 3 to 90°C. The sensitivity for measurement of refractive index change of water was 1163 nm/RIU at the wavelength of 1550 nm. The temperature cross-sensitivity was about 1.1×10^{-6} RIU/°C.

A different technique for the fabrication of the fiber-optic Fabry-Perot interferometer is the dip-coating method. W. W. Ma et al. had proposed an optical fiber Fabry-Perot interferometer based on poly (ethyleneimine) (PEI)/ poly (vinyl alcohol) (PVA) blend membrane, by coating a 15 μ m PEI/PVA blend film on the end-face of a cleaved single-mode fiber [21]. The functional material layer based on

PEI/PVA blend polymer exhibits reversible optical path difference change because of absorption and release of CO₂ gas molecules. Moreover, X. Y. Zhang et al. demonstrated an end-of-fiber poly-dimethylsiloxane (PDMS) cap based fiber Fabry-Perot interferometer, which could be used for simultaneous measurement of refractive index (RI) and temperature with extremely low cross sensitivity [46]. The RI and temperature sensitivities of the interferometer were -240.425 dB/RI unit based on extinction ratio measurement in the RI range of 1.3625–1.4150 and 385.46 pm/°C in the temperature range of 25 °C–60 °C, respectively.

1.1.3 Fiber-optic gas or vapors sensors based on whispering-gallery mode (WGM) resonators

Many different techniques such as laser micromachining, electron beam lithography, etching, multi-photon lithography, drop-casting, loop or knot of tapered optical fibers, adjusting microspheres on the endface of optical fibers or onto tapered fibers or even within the capillaries of microstructured optical fibers etc. [68-78] have been used in order to fabricate whispering gallery mode (WGM) microcavities of different designs, like microring [77], microdisk [79], microtoroid [80], microsphere [78, 81], microbottle [74], etc.

Fiber optic sensors based on whispering gallery modes (WGMs) have attracted increasing interest due to their wide range of potential application such as lasing [82-84], nonlinear optics [85], optomechanics [86], optofluidics [87], filters [88, 89], refractometric sensors [90], force sensors [91], pressure sensors [92], biosensors [93, 94], gas sensors [95], temperature sensors [71, 96] etc.

Recently, gas and chemical vapor sensors based on WGM micro-resonators have been proposed and investigated. N. M. Hanumegowda et al. had developed a highly sensitive refractometric sensor based on fused silica microsphere resonators [90]. The spectral position of the whispering gallery mode of the sphere shifted in response to the refractive index change in the surrounding medium. A sensitivity of approximately 30 nm/RIU was achieved. The detection limit of refractive index change was of the order of 10⁻⁷ RIU.

Moreover, G Zhang et al. had proposed a volatile organic compounds sensor, built on a silicon-on-insulator (SOI)-based photonic platform [97]. The sensor consisted of a high-Q factor ring-resonator and it was tested with acetone vapor, achieving a detection limit of 200 ppm. The sensor obtained relative high sensitivity (1.7 pm/1000 ppm), fast response time (~20 s) and the stability of < 1 pm drift.

Also, Y. Sun et al. had developed a rapid chemical-vapor sensor based on optofluidic ring resonators consisting of a glass capillary whose circular wall supports the circulating waveguide modes [98]. The inner surface of the ring resonator was coated with a vapor-sensitive polymer. The analyte and polymer interaction causes the polymer refractive index to change, which was detected as a WGM spectral shift. The sensor exhibited sub-second detection and recovery time with a flow rate of 1 mL/min. The detection limit was estimated to be 5.6x10⁻⁶ refractive index units. Ethanol and hexane vapors were used as a model system, and chemical differentiation

was demonstrated with different polymer coatings.

By using a different approach, A. Ksendozov et al. had proposed an integrated optics chemical sensor based on a ring resonator with an ethyl cellulose polymer coating has been demonstrated [99]. The resonator was fabricated using SiO₂ and Si_xN_y materials. The sensitivity to isopropanol in air was 50 ppm.

On the other hand, F. Pang et al. had fabricated a planar waveguide ring resonator by organic–inorganic hybrid sol–gel materials and investigated its sensitivity to ethanol vapors [100]. It was found that dips in the transmission spectrum of the device shifted to longer wavelengths when the ethanol concentration was increased. The sensor’s sensitivity showed a linear relation with the ethanol concentration, showing a coefficient of 1.13 pm/ppm. In addition, the transmission loss of the ring resonator decreased with increasing the ethanol concentration.

H. Wei et al. proposed a sensitive refractometric polymer micro-resonator sensor fabricated using direct laser writing [101]. The design consisted of two tapered waveguides that could be coupled by single mode fibers, two “Y” splitting waveguides that were combined in a Mach–Zehnder interferometer (MZI) configuration and a micro-cylinder that evanescently coupled with the arms of the MZI. The resonant wavelength shifted in response to the refractive index change in the surrounding medium of the micro-cylinder. The sensitivity of device when it was immersed in water was 154.84 nm/RIU.

1.2 Multi-photon Lithography and its applications

Multi-photon lithography (MPL) is a powerful 3D printing technique which enables the “direct writing” of computer-designed structures within the volume of a photosensitive material [102, 103]. This technique was first demonstrated in 1997 [104], and it was used by the photonics community for the fabrication of 3D photonic crystals and nano-photonic devices [105-108]. Today, it is used in many different fields such as microfluidics [109], biomedical implants [110, 111], complex 3D scaffolds for cell cultures and tissue engineering [112-117], micro-optical components [118, 119].

1.2.1 Whispering-gallery mode micro-resonators fabricated by multi-photon lithography

Multi-photon lithography has been also used for the fabrication of Whispering-gallery mode micro-disk and micro-ring resonators, onto glass substrates.

High-*Q* polymer whispering gallery micro-disks resonators have been fabricated and demonstrated by Z.P. Liu et al. [120]. They had used zirconium/silicon hybrid sol-gel photosensitive material. The quality factors of the fabricated whispering gallery microcavities were up to 1.48×10^5 limited by the material absorption, while the surface roughness was less than 12 nm. Moreover, A. Schell et al. fabricated combined micro-disk resonators with optical interconnects using a photoresist containing nanodiamonds including nitrogen vacancy-centers [75]. As an example for possible functionality, single-photon generation, collection, and transport were

accomplished. Finally, T. Grossman et al. fabricated high-Q polymeric micro-disks on silicon [79]. The quality factors of the passive cavities were above 10^6 in the 1300 nm wavelength region. Micro-disk lasers were realized by doping the resist with dye, resulting in laser emission at visible wavelengths.

On the other hand, G. M. Parsanasab, et al, had demonstrated an optically pumped polymer micro-ring laser fabricated by two photon polymerization of SU-8 [77]. Rhodamine B was used as the gain medium doped in SU-8. The laser cavity was a double coupled micro-ring structure. Single mode lasing was obtained from the two coupled rings each with 30 μm and 29 μm radii. Low laser threshold of 0.4 $\mu\text{J}/\text{mm}^2$ was achieved using 1 μm wide polymer waveguides and the quality factor was greater than 10^4 at 612.4 nm wavelength. Finally, H. Wei et al. had also fabricated a micro-ring resonator that had been also discussed in section 1.1.3 [101].

1.2.2 Multi-photon lithography onto optical fibers

Over the last decade, multi-photon lithography had been also used in order 3D micro-optical elements to be fabricated directly onto the end-face of optical fibers, while exploiting the specific optical interface.

More specifically, photonic elements including micro-prisms, woodpile and chiral photonic crystals [121-123], micro-lenses (spherical, cylindrical, conical, toric lenses) [121, 123-126], parabolic micro-reflectors [127], spherical surface-enhanced Raman scattering (SERS) radar configurations [128], phase masks [129], axicons [130-132], gradient index anti-reflective coatings [133] and polarization filtering [123], have been fabricated on the endface of optical fibers in recent years by several groups.

The fabricated elements are being used in a variety of applications such as beam shaping or focusing [123, 126], SERS sensors [128], or even in bio-imaging [124] and biomedical applications [132].

1.3 Project outline, motivation and applications

1.3.1 Project outline

This project focuses on the fabrication of two different kinds of light resonating structures fabricated by multi-photon polymerization technique directly onto single mode, telecom optical fibers. In particular, fiber-optic devices based on Fabry-Perot interferometers fabricated on the endface of optical fibers will be introduced in the first part, while in the second part whispering-gallery mode micro-ring resonators fabricated directly onto tapered optical fibers (produced from single mode telecom optical fibers) will be demonstrated. In both cases hybrid organic-inorganic photosensitive materials were used for the fabrication of the light resonating components.

The aim of this thesis is to combine standard single mode optical fibers and multi-photon lithography in order to produce robust and functional fiber-optic devices that will be exploited as fiber-optic gas or liquid sensors in the time being; also constituting basic platforms for other sensing and switching devices. Further, this

study investigates in depth the advantages and disadvantages of the direct laser fabrication of micro-optical light resonating cavities onto the optical fibers.

For the fabrication of these fiber-optic interferometric devices new processes for the sample preparation had to be explored and developed. Furthermore, the designs of the interferometric components and their fabrication parameters had to be studied in order to produce functional structures. In addition, for their characterization as gas sensors, specially designed gas chambers had to be designed and fabricated.

Basic theoretical models were introduced in order to explain the experimental results obtained, also supporting a first design of the optical structures planned.

1.3.2 Motivation

The project motivation may be divided into two parts. The first part is related to the materials and techniques that are being used for developing fiber-optic gas sensors of high selectivity and sensitivity. The second part is related to the general idea of developing WGM optical fiber devices of high robustness, Q-factor performance, capable in coupling light and operating far from the optical bench, thus being suitable for packaging.

Regarding to the first part, aiming to increase the sensitivity limits of optical fiber-optic gas sensors while improving their selectivity, different chemical fabrication procedures and techniques have been used. Over the last years, polymers [134, 135], metal coatings [27], inorganic oxides [26], graphene [30, 136], palladium nanoparticles [34], vapo-chromic materials [137], and fluorescent dyes [138] etc. have been used to form a layer or a cavity that acts as a sensing actuation element overlaid at a specific sensing area, i.e. fiber endface, cladding, or inside hollow capillaries. In most cases, the principal sensing operation relies on chemisorption processes on the surface of the actuating material and the formation of chemical bonds that consequently affect its optical signature (usually refractive index and/or absorption), that in turn are interrogated through suitable optical schemes. The reaction between the sensing element and the gas via the chemisorption process enhances significantly the selectivity of the sensor device, as it can be planned in accordance to the detection solvent and the desired sensing operation. However, the formation of chemical bonds and the binding of gas molecules on the surface of the actuation element is often hard to revert without causing damage and/or surface corrosion that reduce the sensing device performance and re-usability.

On the other hand, most of the times a multi-step procedure is necessary in order these materials to be fixated on the area of interest at the fiber-optic device. By this way, the time that is required for the preparation of the sample increases, and also increases the possibility of an error during the process or even the damage of the sample.

The same could also happen in case of multi-step procedures, like laser micromachining method for the fabrication of either Fabry-Perot based fiber-optic sensors [40] or for the fabrication of WGM resonators [69, 80] and moreover for splicing and etching methods that applied for the fabrication of Fabry-Perot based

fiber-optic sensors [65].

As it was already mentioned in section 1.2.2, multi-photon lithography had been already used in order to fabricate micro-optical components on the endface of optical fibers. However, this technique had not used yet in order to fabricate fiber-optic sensors.

In this thesis, we move a step forward and we propose for the first time in our knowledge, the use of multi-photon polymerization technique for the fabrication of endface Fabry-Perot fiber-optic devices that are explored as gas and liquid sensors. The material that is used for these experiments is a hybrid organic-inorganic photosensitive material that does not required any further fixation process in order to be used for the sensing experiments. By this way, robust and functional endface Fabry-Perot fiber-optic devices are fabricated in a single-step process.

Regarding the second part, the excitation of the WGM microresonators, in most of these cases, is achieved by the use of an external tapered fiber which has to be in close vicinity/contact with the WGM microresonator [74, 139]; while relying on coupling systems that are susceptible to environmental disturbance and they lack of robustness and packagability. Small external vibrations or misalignments could change the optimum coupling conditions and as a consequence the spectral response of the microresonator to be deteriorated. Moreover, the use of high-resolution 3D translation stages for the alignment of the tapered fiber to the WGM microresonators would make the system expensive and bulky, limiting the portability of the device. To overcome these problems, either specific bases were used to keep the tapered fibers in touch with the resonators [101], or the devices were being packaged after the achievement of the optimum coupling conditions [140-142].

In this thesis, we propose and realize for the first time the fabrication of micro-ring resonators directly onto tapered single mode telecommunication fibers by employing the multi-photon polymerization technique. Such an approach will allow the demonstration of integrated and robust tapered optical fiber WGM resonators of straightforward packaging capabilities, while preserving high quality light localization and spectral characteristics. Furthermore, a number of ring resonating devices are presented including photonic molecules, which are in turn used for the ultrasensitive detection of pressure variations in inert gasses, depicting the potential capabilities of the devices and processes demonstrated herein.

1.3.3 Applications of the devices presented in this thesis

The fabricated endface Fabry-Perot fiber-optic devices had been tested as gas sensors for the detection of ethanol [143] and chlorinated volatile organic compounds [144] and also as liquid sensors for oily samples [145]. On the other hand, the WGM micro-ring resonators had been tested as gas sensors for the detection of ethanol vapors, as well as for the measurement of pressure variation of inert Nitrogen and Krypton gases.

Ethanol vapor sensing can be found in beverage and food industry related with fermentation processes, as well as in the automotive fuel sector, wherein ethanol can

be mixed with gasoline for tuning octane performance and fuel price. Moreover, the detection of ethanol in ppm concentrations can be quite advantageous for specific breath analysis applications, related to the early diagnosis of lung cancer [12, 146, 147] and metabolic diseases [13, 148], while being implemented in a standard spirometric diagnostic process in off-line mode [24].

The detection of chlorinated volatile organic compounds (Cl-VOCs) can also have significant impact applications in environmental and industrial safety monitoring, since they are widely used substances for a large variety of everyday household and industrial products such as pharmaceuticals, pesticides, freon refrigerants liquids, paper, rubber and dyes [149]. On the other hand, the endface Fabry-Perot fiber-optic device tested with oily samples can be further tested in order to develop fiber-optic sensing probes for the identification of adulterants [150] and plasticizers [151] in oily media targeting the olive oil markets.

Finally, Nitrogen and Krypton are gases that are widely used in laboratory and industrial processes thus it is important to monitor their concentration levels in high accuracy [152] using the WGM devices onto optical fiber tapers. Also, the photonic molecules fabricated in this thesis can find direct applications in optomechanical resonators [153-155], slow light devices and add-drop multiplexers and switches [156-159].

1.4 Thesis outline

- Chapter 1 presents a general introduction on the fiber-optic gas sensors especially those based on Fabry-Perot interferometers and whispering-gallery mode resonators. Moreover, the work that has been done since today by multi-photon lithography on whispering-gallery mode resonators and on the fabrication of micro-optical elements on the endface of optical fibers has been also discussed in this chapter. Finally, the motivation and the outline of this thesis is presented.
- Chapter 2 presents the theoretical background of the optical fibers, their characteristics and the propagation of light as electromagnetic wave, through the optical fiber waveguide will be presented since they constitute the guiding platforms for the fabrication of the photopolymerized microresonators. Moreover the theory for tapered optical fibers which were used for exciting whispering-gallery mode microresonators will also be presented. Finally, the basic principles and characteristic parameters of the Fabry-Perot interferometers and the Whispering-gallery mode ring resonators as well as the physical mechanisms governing the multi-photon polymerization technique will be discussed.
- In Chapter 3, the experimental apparatuses used for the fabrication of the fiber-optic devices, the materials and the preparation processes of the optical fiber samples, as well as, the direct laser writing (DLW) protocol followed in this thesis will be presented.

- The principle of operation for three different designs of Fabry-Perot (FP) microresonators fabricated on the endface of commercially available single mode fibers by multi-photon polymerization technique will be presented in Chapter 4. Moreover, their spectral response as well as simulated spectra through two-beam optical interference approximation and finite difference time domain (FDTD) will be also appended.
- The fabricated FP micro-prism endface fiber-optic resonators were tested as gas sensors while exposed to ethanol and chlorinated volatile organic compounds (VOCs) and as liquid sensor by immersion into oily samples. The results obtained from these experiments as well as theoretical models that were developed for the explanation of these results will be presented in Chapter 5.
- In Chapter 6 the single and double parallel whispering-gallery mode micro-rings resonators that were fabricated by multi-photon polymerization technique directly on tapered optical fibers will be presented. The differences that were observed due to the different design characteristics (diameter, thickness, distance between the rings etc.) will be also discussed. Moreover, some first simulations through finite-difference time domain will be presented.
- The fabricated whispering-gallery mode micro-rings resonating devices were tested as gas sensors to ethanol vapors and to nitrogen and krypton gases. The experimental results will be presented and discussed in Chapter 7.
- Finally the conclusions and proposals for future research directions will be presented in Chapter 8.

References

- [1] J. Hecht, *City of Light: The Story of Fiber Optics*. New York: Oxford University Press, 1999.
- [2] E. Udd, "An overview of fiber-optic sensors," *Review of Scientific Instruments*, vol. 66, pp. 4015-4030, 1995.
- [3] S. Naseer, S. A. Aljunid, M. S. Salim, R. B. Ahmad, and R. Kamaruddin, "Toward Optical Sensors: Review and Applications," *Journal of Physics: Conference Series*, vol. 423, p. 012064, 2013.
- [4] X. Li, C. Yang, S. Yang, and G. Li, "Fiber-Optical Sensors: Basics and Applications in Multiphase Reactors," *Sensors*, vol. 12, p. 12519, 2012.
- [5] B. Gholamzadeh and H. Nabovati, *Fiber optic sensors* vol. 42, 2008.
- [6] B. Robert, "Fibre optic sensors: a review of today's applications," *Sensor Review*, vol. 31, pp. 304-309, 2011.
- [7] B. Lee, "Review of the present status of optical fiber sensors," *Optical Fiber Technology*, vol. 9, pp. 57-79, 2003/04/01/ 2003.
- [8] B. D. Gupta, *Fiber Optic Sensors: Principles and Applications*. Pitam Pura, New Delhi: New India Publicing Agency, 2006.
- [9] C. Elosua, I. Matias, C. Bariain, and F. Arregui, "Volatile Organic Compound Optical Fiber Sensors: A Review," *Sensors*, vol. 6, p. 1440, 2006.

- [10] J. Hodgkinson and R. P. Tatam, "Optical gas sensing: a review," *Measurement Science & Technology*, vol. 24, Jan 2013.
- [11] C. Elosua, F. J. Arregui, I. D. Villar, C. Ruiz-Zamarreño, J. M. Corres, C. Barriain, *et al.*, "Micro and Nanostructured Materials for the Development of Optical Fibre Sensors," *Sensors*, vol. 17, p. 2312, 2017.
- [12] K. Mitsubayashi, K. Yokoyama, T. Takeuchi, and I. Karube, "Gas-Phase Biosensor For Ethanol," *Analytical Chemistry*, vol. 66, pp. 3297-3302, Oct 15 1994.
- [13] S. Nair, K. Cope, R. H. Terence, and A. M. Diehl, "Obesity and female gender increase breath ethanol concentration: Potential implications for the pathogenesis of nonalcoholic steatohepatitis," *American Journal of Gastroenterology*, vol. 96, pp. 1200-1204, Apr 2001.
- [14] H. Kudo, M. Sawai, Y. Suzuki, X. Wang, T. Gessei, D. Takahashi, *et al.*, "Fiber-optic bio-sniffer (biochemical gas sensor) for high-selective monitoring of ethanol vapor using 335nm UV-LED," *Sensors and Actuators B: Chemical*, vol. 147, pp. 676-680, 2010/06/03/ 2010.
- [15] H. Fu, Y. Jiang, J. Ding, J. Zhang, M. Zhang, Y. Zhu, *et al.*, "Zinc oxide nanoparticle incorporated graphene oxide as sensing coating for interferometric optical microfiber for ammonia gas detection," *Sensors and Actuators B: Chemical*, vol. 254, pp. 239-247, 2018/01/01/ 2018.
- [16] A. L. Khalaf, F. S. Mohamad, N. A. Rahman, H. N. Lim, S. Paiman, N. A. Yusof, *et al.*, "Room temperature ammonia sensor using side-polished optical fiber coated with graphene/polyaniline nanocomposite," *Optical Materials Express*, vol. 7, pp. 1858-1870, Jun 2017.
- [17] L. Sun, Y. Semenova, Q. Wu, D. J. Liu, J. H. Yuan, T. Ma, *et al.*, "High Sensitivity Ammonia Gas Sensor Based on a Silica-Gel-Coated Microfiber Coupler," *Journal of Lightwave Technology*, vol. 35, pp. 2864-2870, Jul 2017.
- [18] B. Huang, C. Lei, C. Wei, and G. Zeng, "Chlorinated volatile organic compounds (Cl-VOCs) in environment - sources, potential human health impacts, and current remediation technologies," *Environment International*, vol. 71, pp. 118-138, Oct 2014.
- [19] S. Capone, A. Forleo, L. Francioso, R. Rella, P. Siciliano, J. Spadavecchia, *et al.*, "Solid state gas sensors: State of the art and future activities," *Journal of Optoelectronics and Advanced Materials*, vol. 5, pp. 1335-1348, 2003.
- [20] X. Liu, S. Cheng, H. Liu, S. Hu, D. Zhang, and H. Ning, "A Survey on Gas Sensing Technology," *Sensors*, vol. 12, p. 9635, 2012.
- [21] W. W. Ma, R. H. Wang, Q. Z. Rong, Z. H. Shao, W. L. Zhang, T. Guo, *et al.*, "CO₂ Gas Sensing Using Optical Fiber Fabry-Perot Interferometer Based on Polyethyleneimine/Poly (Vinyl Alcohol) Coating," *Ieee Photonics Journal*, vol. 9, p. 8, Jun 2017.
- [22] P. Biswas, N. Basumallick, K. Dasgupta, A. Ghosh, and S. Bandyopadhyay, "Application of strongly overcoupled resonant modes of long-period fiber gratings to measure the adulteration of olive oil," *Applied Optics*, vol. 55, pp. 5118-5126, Jul 2016.
- [23] L. Coelho, D. Viegas, J. L. Santos, and J. de Almeida, "Detection of Extra Virgin Olive Oil Thermal Deterioration Using a Long Period Fibre Grating Sensor Coated with Titanium Dioxide," *Food and Bioprocess Technology*, vol. 8, pp. 1211-1217, Jun 2015.

- [24] N. Queralto, A. N. Berliner, B. Goldsmith, R. Martino, P. Rhodes, and S. H. Lim, "Detecting cancer by breath volatile organic compound analysis: a review of array-based sensors," *Journal of Breath Research*, vol. 8, Jun 2014.
- [25] K. Farhadi, R. Maleki, and R. Tahmasebi, "Preparation of Al₂O₃/TiO₂ composite sol-gel fiber for headspace solid-phase microextraction of chlorinated organic solvents from urine," *Journal of Separation Science*, vol. 34, pp. 1669-1674, Jul 2011.
- [26] M. Konstantaki, A. Klini, D. Anglos, and S. Pissadakis, "An ethanol vapor detection probe based on a ZnO nanorod coated optical fiber long period grating," *Optics Express*, vol. 20, pp. 8472-8484, Apr 2012.
- [27] A. Gonzalez-Vila, M. Debliquy, D. Lahem, C. Zhang, P. Megret, and C. Caucheteur, "Molecularly imprinted electropolymerization on a metal-coated optical fiber for gas sensing applications," *Sensors and Actuators B-Chemical*, vol. 244, pp. 1145-1151, Jun 2017.
- [28] K. Yamini, B. Renganathan, A. R. Ganesan, and T. Prakash, "Clad modified optical fiber gas sensors based on nanocrystalline nickel oxide embedded coatings," *Optical Fiber Technology*, vol. 36, pp. 139-143, Jul 2017.
- [29] J. C. Echeverria, I. Calleja, P. Moriones, and J. J. Garrido, "Fiber optic sensors based on hybrid phenyl-silica xerogel films to detect n-hexane: determination of the isosteric enthalpy of adsorption," *Beilstein Journal of Nanotechnology*, vol. 8, pp. 475-484, Feb 2017.
- [30] J. Y. Zhang, E. J. Ding, S. C. Xu, Z. H. Li, X. X. Wang, and F. Song, "Sensitization of an optical fiber methane sensor with graphene," *Optical Fiber Technology*, vol. 37, pp. 26-29, 2017/09/01/ 2017.
- [31] S. Tabassum, R. Kumar, and L. Dong, "Nanopatterned Optical Fiber Tip for Guided Mode Resonance and Application to Gas Sensing," *Ieee Sensors Journal*, vol. 17, pp. 7262-7272, Nov 2017.
- [32] Z. H. Zhang, R. Lockwood, J. G. C. Veinot, and A. Meldrum, "Detection of ethanol and water vapor with silicon quantum dots coupled to an optical fiber," *Sensors and Actuators B-Chemical*, vol. 181, pp. 523-528, May 2013.
- [33] M. Yan, J. Tylczak, Y. Yu, G. Panagakos, and P. Ohodnicki, "Multi-component optical sensing of high temperature gas streams using functional oxide integrated silica based optical fiber sensors," *Sensors and Actuators B: Chemical*, vol. 255, pp. 357-365, 2018/02/01/ 2018.
- [34] N. E. Gonzalez-Sierra, L. D. Gomez-Pavon, G. F. Perez-Sanchez, A. Luis-Ramos, P. Zaca-Moran, J. M. Munoz-Pacheco, *et al.*, "Tapered Optical Fiber Functionalized with Palladium Nanoparticles by Drop Casting and Laser Radiation for H₂ and Volatile Organic Compounds Sensing Purposes," *Sensors*, vol. 17, p. 12, Sep 2017.
- [35] C. Caucheteur, T. Guo, F. Liu, B. O. Guan, and J. Albert, "Ultrasensitive plasmonic sensing in air using optical fibre spectral combs," *Nature Communications*, vol. 7, Nov 2016.
- [36] Z.-L. R. Yun-Jiang Rao, Yuan Gong, *Fiber-Optic Fabry-Perot Sensors: An Introduction*: CRC Press 2017.
- [37] M. R. Islam, M. M. Ali, M. H. Lai, K. S. Lim, and H. Ahmad, "Chronology of Fabry-Perot Interferometer Fiber-Optic Sensors and Their Applications: A Review," *Sensors*, vol. 14, pp. 7451-7488, Apr 2014.
- [38] B. H. Lee, Y. H. Kim, K. S. Park, J. B. Eom, M. J. Kim, B. S. Rho, *et al.*, "Interferometric Fiber Optic Sensors," *Sensors*, vol. 12, p. 2467, 2012.

- [39] Z. L. Ran, Y. J. Rao, W. J. Liu, X. Liao, and K. S. Chiang, "Laser-micromachined Fabry-Perot optical fiber tip sensor for high-resolution temperature-independent measurement of refractive index," *Optics Express*, vol. 16, pp. 2252-2263, Feb 2008.
- [40] G. Gruca, D. Chavan, J. Rector, K. Heeck, and D. Iannuzzi, "Demonstration of an optically actuated ferrule-top device for pressure and humidity sensing," *Sensors and Actuators a-Physical*, vol. 190, pp. 77-83, Feb 1 2013.
- [41] D. Helie, S. Gouin, and R. Vallee, "Assembling an endcap to optical fibers by femtosecond laser welding and milling," *Optical Materials Express*, vol. 3, pp. 1742-1754, Oct 1 2013.
- [42] V. R. Machavaram, R. A. Badcock, and G. F. Fernando, "Fabrication of intrinsic fibre Fabry-Perot sensors in silica fibres using hydrofluoric acid etching," *Sensors and Actuators A: Physical*, vol. 138, pp. 248-260, 2007/07/20/2007.
- [43] S. Pevec and D. Donlagic, "Miniature all-fiber Fabry-Perot sensor for simultaneous measurement of pressure and temperature," *Applied Optics*, vol. 51, pp. 4536-4541, Jul 2012.
- [44] T. Zhu, T. Ke, Y. Rao, and K. S. Chiang, "Fabry-Perot optical fiber tip sensor for high temperature measurement," *Optics Communications*, vol. 283, pp. 3683-3685, 2010/10/01/2010.
- [45] A. Lopez-Aldaba, A. Pinto, M. Lopez-Amo, O. Frazão, J. Santos, J. Baptista, *et al.*, "Experimental and Numerical Characterization of a Hybrid Fabry-Pérot Cavity for Temperature Sensing," *Sensors*, vol. 15, p. 8042, 2015.
- [46] X. Y. Zhang, Y. S. Yu, C. C. Zhu, C. Chen, R. Yang, Y. Xue, *et al.*, "Miniature End-Capped Fiber Sensor for Refractive Index and Temperature Measurement," *IEEE Photonics Technology Letters*, vol. 26, pp. 7-10, 2014.
- [47] S. Pevec and D. Donlagic, "High resolution, all-fiber, micro-machined sensor for simultaneous measurement of refractive index and temperature," *Optics Express*, vol. 22, pp. 16241-16253, Jun 30 2014.
- [48] Y. J. Lu and M. Han, "Fiber-optic temperature sensor using dual fabry-perot cavities filled with gas of different pressure," *Sensors and Actuators a-Physical*, vol. 261, pp. 229-234, Jul 2017.
- [49] J. Zhu, M. Wang, L. Chen, X. Ni, and H. Ni, "An optical fiber Fabry-Perot pressure sensor using corrugated diaphragm and angle polished fiber," *Optical Fiber Technology*, vol. 34, pp. 42-46, 3// 2017.
- [50] S. Pevec and D. Donlagic, "Miniature fiber-optic sensor for simultaneous measurement of pressure and refractive index," *Optics Letters*, vol. 39, pp. 6221-6224, Nov 2014.
- [51] W. P. Chen, D. N. Wang, B. Xu, C. L. Zhao, and H. F. Chen, "Multimode fiber tip Fabry-Perot cavity for highly sensitive pressure measurement," *Scientific Reports*, vol. 7, p. 6, Mar 2017.
- [52] X. Zou, N. Wu, Y. Tian, Y. Zhang, J. Fitek, M. Maffeo, *et al.*, "Ultrafast Fabry-Perot fiber-optic pressure sensors for multimedia blast event measurements," *Applied Optics*, vol. 52, pp. 1248-1254, 2013/02/20 2013.
- [53] Y. J. Rao and Z. L. Ran, "Fiber-optic Fabry-Perot sensors take the strain under high temperature," *Laser Focus World*, vol. 47, pp. 71-74, Nov 2011.
- [54] S. Pevec and D. Donlagic, "All-fiber, long-active-length Fabry-Perot strain sensor," *Optics Express*, vol. 19, pp. 15641-15651, 2011/08/01 2011.

- [55] X. Chen, F. Shen, Z. Wang, Z. Huang, and A. Wang, "Micro-air-gap based intrinsic Fabry-Perot interferometric fiber-optic sensor," *Applied Optics*, vol. 45, pp. 7760-7766, 2006/10/20 2006.
- [56] J. Li, F. Albri, R. R. J. Maier, W. Shu, J. Sun, D. P. Hand, *et al.*, "A Micro-Machined Optical Fiber Cantilever as a Miniaturized pH Sensor," *Ieee Sensors Journal*, vol. 15, pp. 7221-7228, Dec 2015.
- [57] J. H. Chen, X. G. Huang, J. R. Zhao, J. Tao, W. X. He, and S. H. Liu, "Fabry-Perot interference-based fiber-optic sensor for small displacement measurement," *Optics Communications*, vol. 283, pp. 3315-3319, Sep 2010.
- [58] C. H. van Hoorn, D. C. Chavan, B. Tiribilli, G. Margheri, A. J. G. Mank, F. Ariese, *et al.*, "Opto-mechanical probe for combining atomic force microscopy and optical near-field surface analysis," *Optics Letters*, vol. 39, pp. 4800-4803, 2014/08/15 2014.
- [59] P. Jia, G. Fang, T. Liang, Y. Hong, Q. Tan, X. Chen, *et al.*, "Temperature-compensated fiber-optic Fabry-Perot interferometric gas refractive-index sensor based on hollow silica tube for high-temperature application," *Sensors and Actuators B: Chemical*, vol. 244, pp. 226-232, 2017/06/01/ 2017.
- [60] M. S. Ferreira, L. Coelho, K. Schuster, J. Kobelke, J. L. Santos, and O. Frazao, "Fabry-Perot cavity based on a diaphragm-free hollow-core silica tube," *Optics Letters*, vol. 36, pp. 4029-4031, Oct 2011.
- [61] Y. Z. Tan, W. Jin, F. Yang, Y. Qi, C. Z. Zhang, Y. C. Lin, *et al.*, "Hollow-Core Fiber-Based High Finesse Resonating Cavity for High Sensitivity Gas Detection," *Journal of Lightwave Technology*, vol. 35, pp. 2887-2893, Jul 2017.
- [62] J. J. Tian, Y. J. Lu, Q. Zhang, and M. Han, "Microfluidic refractive index sensor based on an all-silica in-line Fabry-Perot interferometer fabricated with microstructured fibers," *Optics Express*, vol. 21, pp. 6633-6639, Mar 2013.
- [63] Y. J. Rao, M. Deng, D. W. Duan, and T. Zhu, "In-line fiber Fabry-Perot refractive-index tip sensor based on endlessly photonic crystal fiber," *Sensors and Actuators a-Physical*, vol. 148, pp. 33-38, Nov 2008.
- [64] T. Z. Ming Deng, Yun-Jiang Rao and Hong Li, "Miniaturized Fiber-Optic Fabry-Perot Interferometer for Highly Sensitive Refractive Index Measurement," *Journal of Electronic Science and Technology of China*, vol. 6, pp. 365-, 2008.
- [65] S. Pevec and D. Donlagic, "Nanowire-based refractive index sensor on the tip of an optical fiber," *Applied Physics Letters*, vol. 102, p. 213114, 2013.
- [66] C. R. Liao, T. Y. Hu, and D. N. Wang, "Optical fiber Fabry-Perot interferometer cavity fabricated by femtosecond laser micromachining and fusion splicing for refractive index sensing," *Optics Express*, vol. 20, pp. 22813-22818, 2012/09/24 2012.
- [67] T. Wei, Y. K. Han, Y. J. Li, H. L. Tsai, and H. Xiao, "Temperature-insensitive miniaturized fiber inline Fabry-Perot interferometer for highly sensitive refractive index measurement," *Optics Express*, vol. 16, pp. 5764-5769, Apr 2008.
- [68] Y. Ding, H. Fan, X. Zhang, X. Jiang, and M. Xiao, "Ultralow-threshold neodymium-doped microsphere lasers on a silicon chip," *Optics Communications*, vol. 395, pp. 51-54, Jul 15 2017.
- [69] J. Lin, Y. Xu, Z. Fang, M. Wang, J. Song, N. Wang, *et al.*, "Fabrication of high-Q lithium niobate microresonators using femtosecond laser micromachining," *Scientific Reports*, vol. 5, Jan 28 2015.

- [70] H. Xu and H. Sun, "Femtosecond laser 3D fabrication of whispering-gallery-mode microcavities," *Science China Physics, Mechanics & Astronomy*, vol. 58, p. 114202, 2015.
- [71] B. Ozel, R. Nett, T. Weigel, G. Schweiger, and A. Ostendorf, "Temperature sensing by using whispering gallery modes with hollow core fibers," *Measurement Science and Technology*, vol. 21, p. 5, Sep 2010.
- [72] G. A. Rodriguez, S. Hu, and S. M. Weiss, "Porous silicon ring resonator for compact, high sensitivity biosensing applications," *Optics Express*, vol. 23, pp. 7111-7119, Mar 23 2015.
- [73] M. W. Puckett, R. Sharma, F. Vallini, S. Shahin, F. Monifi, P. N. Barrina, *et al.*, "Silicon nanoridge array waveguides for nonlinear and sensing applications," *Optics Express*, vol. 23, pp. 28224-28233, Nov 2 2015.
- [74] J. M. Ward, Y. Yang, and S. N. Chormaic, "Glass-on-Glass Fabrication of Bottle-Shaped Tunable Microlasers and their Applications," *Scientific Reports*, vol. 6, p. 8, Apr 2016.
- [75] A. W. Schell, J. Kaschke, J. Fischer, R. Henze, J. Wolters, M. Wegener, *et al.*, "Three-dimensional quantum photonic elements based on single nitrogen vacancy-centres in laser-written microstructures," *Scientific Reports*, vol. 3, Apr 2 2013.
- [76] Y. Wang, H. Y. Li, L. Y. Zhao, B. Wu, S. Q. Liu, Y. J. Liu, *et al.*, "A review of droplet resonators: Operation method and application," *Optics and Laser Technology*, vol. 86, pp. 61-68, Dec 2016.
- [77] G. M. Parsanasab, M. Moshkani, and A. Gharavi, "Femtosecond laser direct writing of single mode polymer micro ring laser with high stability and low pumping threshold," *Optics Express*, vol. 23, pp. 8310-8316, Apr 2015.
- [78] K. Kosma, G. Zito, K. Schuster, and S. Pissadakis, "Whispering gallery mode microsphere resonator integrated inside a microstructured optical fiber," *Optics Letters*, vol. 38, pp. 1301-1303, 2013/04/15 2013.
- [79] T. Grossmann, S. Schleede, M. Hauser, T. Beck, M. Thiel, G. von Freymann, *et al.*, "Direct laser writing for active and passive high-Q polymer microdisks on silicon," *Optics Express*, vol. 19, pp. 11451-11456, Jun 2011.
- [80] J. T. Lin, S. J. Yu, Y. G. Ma, W. Fang, F. He, L. L. Qiao, *et al.*, "On-chip three-dimensional high-Q microcavities fabricated by femtosecond laser direct writing," *Optics Express*, vol. 20, p. 6, Apr 2012.
- [81] K. Milenko, I. Konidakis, and S. Pissadakis, "Silver iodide phosphate glass microsphere resonator integrated on an optical fiber taper," *Optics Letters*, vol. 41, pp. 2185-2188, 2016/05/15 2016.
- [82] S. M. Spillane, T. J. Kippenberg, and K. J. Vahala, "Ultralow-threshold Raman laser using a spherical dielectric microcavity," *Nature*, vol. 415, pp. 621-623, 02/07/print 2002.
- [83] D. Ristić, S. Berneschi, M. Camerini, D. Farnesi, S. Pelli, C. Trono, *et al.*, "Photoluminescence and lasing in whispering gallery mode glass microspherical resonators," *Journal of Luminescence*, vol. 170, pp. 755-760, 2016/02/01/ 2016.
- [84] M. Kuwata-Gonokami, S. Ozawa, R. H. Jordan, A. Dodabalapur, H. E. Katz, M. L. Schilling, *et al.*, "Polymer microdisk and microring lasers," *Optics Letters*, vol. 20, pp. 2093-2095, 1995/10/15 1995.
- [85] G. Kozyreff, J. Luis Dominguez-Juarez, and J. Martorell, "Nonlinear optics in spheres: from second harmonic scattering to quasi-phase matched generation in whispering gallery modes," *Laser & Photonics Reviews*, vol. 5, pp. 737-749, Nov 2011.

- [86] T. J. Kippenberg and K. J. Vahala, "Cavity Opto-Mechanics," *Optics Express*, vol. 15, pp. 17172-17205, 2007/12/10 2007.
- [87] J. D. Suter, Y. Sun, D. J. Howard, J. A. Viator, and X. Fan, "PDMS embedded opto-fluidic microring resonator lasers," *Optics Express*, vol. 16, pp. 10248-10253, 2008/07/07 2008.
- [88] P. Rabiei and W. H. Steier, "Tunable polymer double micro-ring filters," *Ieee Photonics Technology Letters*, vol. 15, pp. 1255-1257, Sep 2003.
- [89] P. Rabiei, W. H. Steier, C. Zhang, and L. R. Dalton, "Polymer micro-ring filters and modulators," *Journal of Lightwave Technology*, vol. 20, pp. 1968-1975, Nov 2002.
- [90] N. M. Hanumegowda, C. J. Stica, B. C. Patel, I. White, and X. D. Fan, "Refractometric sensors based on microsphere resonators," *Applied Physics Letters*, vol. 87, Nov 2005.
- [91] T. Ioppolo, M. Kozhevnikov, V. Stepaniuk, M. V. Ötügen, and V. Sheverev, "Micro-optical force sensor concept based on whispering gallery mode resonators," *Applied Optics*, vol. 47, pp. 3009-3014, 2008/06/01 2008.
- [92] T. Ioppolo and M. V. Ötügen, "Pressure tuning of whispering gallery mode resonators," *Journal of the Optical Society of America B*, vol. 24, pp. 2721-2726, 2007/10/01 2007.
- [93] F. Vollmer, D. Braun, A. Libchaber, M. Khoshima, I. Teraoka, and S. Arnold, "Protein detection by optical shift of a resonant microcavity," *Applied Physics Letters*, vol. 80, pp. 4057-4059, 2002.
- [94] H.-C. Ren, F. Vollmer, S. Arnold, and A. Libchaber, "High-Q microsphere biosensor - analysis for adsorption of rodlike bacteria," *Optics Express*, vol. 15, pp. 17410-17423, Dec 10 2007.
- [95] Q. Ma, L. Huang, Z. Guo, and T. Rossmann, *Whispering-Gallery Mode Silica Micro-Sensors for Temperature and Gas-Phase Concentration Measurements*, 2010.
- [96] G. Guan, S. Arnold, and V. Otugen, "Temperature Measurements Using a Microoptical Sensor Based on Whispering Gallery Modes," *AIAA Journal*, vol. 44, pp. 2385-2389, 2006/10/01 2006.
- [97] G. Zhang, X. L. Feng, B. Liedberg, and A. Q. Liu, "Gas Sensor for Volatile Organic Compounds Detection Using Silicon Photonic Ring Resonator," *Procedia Engineering*, vol. 168, pp. 1771-1774, 2016/01/01/ 2016.
- [98] Y. Sun, S. I. Shopova, G. Frye-Mason, and X. Fan, "Rapid chemical-vapor sensing using optofluidic ring resonators," *Optics Letters*, vol. 33, pp. 788-790, 2008/04/15 2008.
- [99] A. Ksendzov, M. L. Homer, and A. M. Manfreda, "Integrated optics ring-resonator chemical sensor with polymer transduction layer," *Electronics Letters*, vol. 40, pp. 63-65, Jan 2004.
- [100] F. Pang, X. Han, F. Chu, J. Geng, H. Cai, R. Qu, *et al.*, "Sensitivity to alcohols of a planar waveguide ring resonator fabricated by a sol-gel method," *Sensors and Actuators B: Chemical*, vol. 120, pp. 610-614, 2007/01/10/ 2007.
- [101] H. M. Wei and S. Krishnaswamy, "Direct Laser Writing Polymer Micro-Resonators for Refractive Index Sensors," *Ieee Photonics Technology Letters*, vol. 28, pp. 2819-2822, Dec 2016.
- [102] F. Maria, V. Maria, and N. C. Boris, "Multiphoton polymerization of hybrid materials," *Journal of Optics*, vol. 12, p. 124001, 2010.

- [103] K. S. Lee, D. Y. Yang, S. H. Park, and R. H. Kim, "Recent developments in the use of two-photon polymerization in precise 2D and 3D microfabrications," *Polymers for Advanced Technologies*, vol. 17, pp. 72-82, Feb 2006.
- [104] S. Maruo, O. Nakamura, and S. Kawata, "Three-dimensional microfabrication with two-photon-absorbed photopolymerization," *Optics Letters*, vol. 22, pp. 132-134, 1997/01/15 1997.
- [105] S. Juodkazis, V. Mizeikis, and H. Misawa, "Three-dimensional microfabrication of materials by femtosecond lasers for photonics applications," *Journal of Applied Physics*, vol. 106, p. 051101, 2009.
- [106] I. Sakellari, E. Kabouraki, D. Gray, V. Purlys, C. Fotakis, A. Pikulin, *et al.*, "Diffusion-Assisted High-Resolution Direct Femtosecond Laser Writing," *Acs Nano*, vol. 6, pp. 2302-2311, Mar 2012.
- [107] I. Sakellari, A. Gaidukeviciute, A. Giakoumaki, D. Gray, C. Fotakis, M. Farsari, *et al.*, "Two-photon polymerization of titanium-containing sol-gel composites for three-dimensional structure fabrication," *Applied Physics a-Materials Science & Processing*, vol. 100, pp. 359-364, Aug 2010.
- [108] E. Kabouraki, A. N. Giakoumaki, P. Danilevicius, D. Gray, M. Vamvakaki, and M. Farsari, "Redox Multiphoton Polymerization for 3D Nanofabrication," *Nano Letters*, vol. 13, pp. 3831-3835, 2013/08/14 2013.
- [109] L. Amato, Y. Gu, N. Bellini, S. M. Eaton, G. Cerullo, and R. Osellame, "Integrated three-dimensional filter separates nanoscale from microscale elements in a microfluidic chip," *Lab on a Chip*, vol. 12, pp. 1135-1142, 2012.
- [110] C. Schizas, V. Melissinaki, A. Gaidukeviciute, C. Reinhardt, C. Ohrt, V. Dedoussis, *et al.*, "On the design and fabrication by two-photon polymerization of a readily assembled micro-valve," *International Journal of Advanced Manufacturing Technology*, vol. 48, pp. 435-441, May 2010.
- [111] S. Galanopoulos, N. Chatzidai, V. Melissinaki, A. Selimis, C. Schizas, M. Farsari, *et al.*, "Design, Fabrication and Computational Characterization of a 3D Micro-Valve Built by Multi-Photon Polymerization," *Micromachines*, vol. 5, pp. 505-514, Sep 2014.
- [112] V. Melissinaki, A. A. Gill, I. Ortega, M. Vamvakaki, A. Ranella, J. W. Haycock, *et al.*, "Direct laser writing of 3D scaffolds for neural tissue engineering applications," *Biofabrication*, vol. 3, p. 045005, 2011.
- [113] M. T. Raimondi, S. M. Eaton, M. M. Nava, M. Lagana, G. Cerullo, and R. Osellame, "Two-photon laser polymerization: from fundamentals to biomedical application in tissue engineering and regenerative medicine," *Journal of Applied Biomaterials & Functional Materials*, vol. 10, pp. 56-66, 2012.
- [114] A. Ovsianikov, A. Deiwick, S. Van Vlierberghe, P. Dubruel, L. Moller, G. Drager, *et al.*, "Laser Fabrication of Three-Dimensional CAD Scaffolds from Photosensitive Gelatin for Applications in Tissue Engineering," *Biomacromolecules*, vol. 12, pp. 851-858, Apr 2011.
- [115] P. Danilevicius, L. Georgiadi, C. J. Pateman, F. Claeysens, M. Chatzinikolaidou, and M. Farsari, "The effect of porosity on cell ingrowth into accurately defined, laser-made, polylactide-based 3D scaffolds," *Applied Surface Science*, vol. 336, pp. 2-10, May 2015.
- [116] M. Malinauskas, P. Danilevicius, D. Baltriukiene, M. Rutkauskas, A. Zukauskas, Z. Kairyte, *et al.*, "3D ARTIFICIAL POLYMERIC SCAFFOLDS FOR STEM CELL GROWTH FABRICATED BY FEMTOSECOND LASER," *Lithuanian Journal of Physics*, vol. 50, pp. 75-82, 2010.

- [117] J. Torgersen, A. Ovsianikov, V. Mironov, N. Pucher, X. H. Qin, Z. Q. Li, *et al.*, "Photo-sensitive hydrogels for three-dimensional laser microfabrication in the presence of whole organisms," *Journal of Biomedical Optics*, vol. 17, p. 10, Oct 2012.
- [118] E. Harnisch, M. Russew, J. Klein, N. Konig, H. Crailsheim, and R. Schmitt, "Optimization of hybrid polymer materials for 2PP and fabrication of individually designed hybrid microoptical elements thereof," *Optical Materials Express*, vol. 5, pp. 456-461, Feb 2015.
- [119] C. Reinhardt, S. Passinger, B. N. Chichkov, C. Marquart, I. P. Radko, and S. I. Bozhevolnyi, "Laser-fabricated dielectric optical components for surface plasmon polaritons," *Optics Letters*, vol. 31, pp. 1307-1309, May 2006.
- [120] Z. P. Liu, Y. Li, Y. F. Xiao, B. B. Li, X. F. Jiang, Y. Qin, *et al.*, "Direct laser writing of whispering gallery microcavities by two-photon polymerization," *Applied Physics Letters*, vol. 97, p. 3, Nov 2010.
- [121] H. E. Williams, D. J. Freppon, S. M. Kuebler, R. C. Rumpf, and M. A. Melino, "Fabrication of three-dimensional micro-photon structures on the tip of optical fibers using SU-8," *Optics Express*, vol. 19, pp. 22910-22922, Nov 2011.
- [122] M. Malinauskas, A. Zukauskas, V. Purlys, A. Gaidukeviciute, Z. Balevicius, A. Piskarskas, *et al.*, "3D microoptical elements formed in a photostructurable germanium silicate by direct laser writing," *Optics and Lasers in Engineering*, vol. 50, pp. 1785-1788, Dec 2012.
- [123] T. Gissibl, S. Thiele, A. Herkommer, and H. Giessen, "Sub-micrometre accurate free-form optics by three-dimensional printing on single-mode fibres," *Nature Communications*, vol. 7, p. 9, Jun 2016.
- [124] T. Gissibl, S. Thiele, A. Herkommer, and H. Giessen, "Two-photon direct laser writing of ultracompact multi-lens objectives," *Nature Photonics*, vol. 10, pp. 554-+, Aug 2016.
- [125] M. Malinauskas, A. Zukauskas, V. Purlys, K. Belazaras, A. Momot, D. Paipulas, *et al.*, "Femtosecond laser polymerization of hybrid/integrated micro-optical elements and their characterization," *Journal of Optics*, vol. 12, Dec 2010.
- [126] A. Žukauskas, *Improvement of the Fabrication Accuracy of Fiber Tip Microoptical Components via Mode Field Expansion* vol. 9, 2014.
- [127] S. Bianchi, V. P. Rajamanickam, L. Ferrara, E. Di Fabrizio, C. Liberale, and R. Di Leonardo, "Focusing and imaging with increased numerical apertures through multimode fibers with micro-fabricated optics," *Optics Letters*, vol. 38, pp. 4935-4938, Dec 2013.
- [128] Z. W. Xie, S. F. Feng, P. J. Wang, L. S. Zhang, X. Ren, L. Cui, *et al.*, "Demonstration of a 3D Radar-Like SERS Sensor Micro- and Nanofabricated on an Optical Fiber," *Advanced Optical Materials*, vol. 3, pp. 1232-1239, Sep 2015.
- [129] T. Gissibl, M. Schmid, and H. Giessen, "Spatial beam intensity shaping using phase masks on single-mode optical fibers fabricated by femtosecond direct laser writing," *Optica*, vol. 3, pp. 448-451, Apr 2016.
- [130] G. Cojoc, C. Liberale, P. Candeloro, F. Gentile, G. Das, F. De Angelis, *et al.*, "Optical micro-structures fabricated on top of optical fibers by means of two-photon photopolymerization," *Microelectronic Engineering*, vol. 87, pp. 876-879, 2010/05/01/ 2010.

- [131] G. S. Sokolovskii, V. Melissinaki, V. V. Dudelev, S. N. Losev, K. K. Soboleva, E. D. Kolykhalova, *et al.*, "Superfocusing of high- M^2 semiconductor laser beams: experimental demonstration," in *SPIE Photonics Europe*, 2014, p. 7.
- [132] G. S. Sokolovskii, V. V. Dudelev, V. Melissinaki, S. N. Losev, K. K. Soboleva, A. G. Deryagin, *et al.*, "Optical trapping with superfocused high- M^2 laser diode beam," in *SPIE LASE*, 2015, p. 7.
- [133] M. Kowalczyk, J. Haberko, and P. Wasylczyk, "Microstructured gradient-index antireflective coating fabricated on a fiber tip with direct laser writing," *Optics Express*, vol. 22, pp. 12545-12550, May 2014.
- [134] L. Athanasekos, A. El Sachat, S. Pispas, and C. Riziotis, "Amphiphilic Diblock Copolymer-Based Multiagent Photonic Sensing Scheme," *Journal of Polymer Science Part B-Polymer Physics*, vol. 52, pp. 46-54, Jan 1 2014.
- [135] M. Giordano, A. Russo, A. Cusano, and G. Mensitieri, "An high sensitivity optical sensor for chloroform vapours detection based on nanometric film of delta-form syndiotactic polystyrene," *Sensors and Actuators B-Chemical*, vol. 107, pp. 140-147, May 27 2005.
- [136] S. Some, Y. Xu, Y. Kim, Y. Yoon, H. Qin, A. Kulkarni, *et al.*, "Highly Sensitive and Selective Gas Sensor Using Hydrophilic and Hydrophobic Graphenes," *Scientific Reports*, vol. 3, Jun 5 2013.
- [137] C. Barriain, I. R. Matias, I. Romeo, J. Garrido, and M. Laguna, "Detection of volatile organic compound vapors by using a vapochromic material on a tapered optical fiber," *Applied Physics Letters*, vol. 77, pp. 2274-2276, Oct 9 2000.
- [138] T. A. Dickinson, K. L. Michael, J. S. Kauer, and D. R. Walt, "Convergent, self-encoded bead sensor arrays in the design of an artificial nose," *Analytical Chemistry*, vol. 71, pp. 2192-2198, Jun 1 1999.
- [139] F. Monifi, Ş. K. Özdemir, and L. Yang, "Tunable add-drop filter using an active whispering gallery mode microcavity," *Applied Physics Letters*, vol. 103, p. 181103, 2013.
- [140] Y. Dong, K. Wang, and X. Jin, "Package of a dual-tapered-fiber coupled microsphere resonator with high Q factor," *Optics Communications*, vol. 350, pp. 230-234, 9/1/ 2015.
- [141] G. Zhao, Ş. K. Özdemir, T. Wang, L. Xu, E. King, G.-L. Long, *et al.*, "Raman lasing and Fano lineshapes in a packaged fiber-coupled whispering-gallery-mode microresonator," *Science Bulletin*, vol. 62, pp. 875-878, 2017/06/30/ 2017.
- [142] J. X. Song, J. T. Lin, J. L. Tang, Y. Liao, F. He, Z. H. Wang, *et al.*, "Fabrication of an integrated high-quality-factor (high-Q) optofluidic sensor by femtosecond laser micromachining," *Optics Express*, vol. 22, pp. 14792-14802, Jun 2014.
- [143] V. Melissinaki, M. Farsari, and S. Pissadakis, "A Fiber-Endface, Fabry-Perot Vapor Microsensor Fabricated by Multiphoton Polymerization," *Ieee Journal of Selected Topics in Quantum Electronics*, vol. 21, p. 10, Jul-Aug 2015.
- [144] V. Melissinaki, I. Konidakis, M. Farsari, and S. Pissadakis, "Fiber endface Fabry-Perot microsensor with distinct response to vapors of different chlorinated organic solvents," *IEEE Sensors Journal*, vol. PP, pp. 1-1, 2016.
- [145] V. Melissinaki, M. Farsari, and S. Pissadakis, "A Fiber Optic Fabry-Perot Cavity Sensor for the Probing of Oily Samples," *Fibers*, vol. 5, p. 1, 2017.
- [146] R. F. Machado, D. Laskowski, O. Deffenderfer, T. Burch, S. Zheng, P. J. Mazzone, *et al.*, "Detection of lung cancer by sensor array analyses of exhaled breath," *American Journal of Respiratory and Critical Care Medicine*, vol. 171, pp. 1286-1291, Jun 1 2005.

- [147] J. Rudnicka, M. Walczak, T. Kowalkowski, T. Jezierski, and B. Buszewski, "Determination of volatile organic compounds as potential markers of lung cancer by gas chromatography-mass spectrometry versus trained dogs," *Sensors and Actuators B-Chemical*, vol. 202, pp. 615-621, Oct 2014.
- [148] F. Baldini and A. G. Mignani, "Optical-fiber medical sensors," *Mrs Bulletin*, vol. 27, pp. 383-387, May 2002.
- [149] A. McCulloch, "Chloroform in the environment: occurrence, sources, sinks and effects," *Chemosphere*, vol. 50, pp. 1291-1308, 3// 2003.
- [150] G. Fragaki, A. Spyros, G. Siragakis, E. Salivaras, and P. Dais, "Detection of Extra Virgin Olive Oil Adulteration with Lampante Olive Oil and Refined Olive Oil Using Nuclear Magnetic Resonance Spectroscopy and Multivariate Statistical Analysis," *Journal of Agricultural and Food Chemistry*, vol. 53, pp. 2810-2816, 2005/04/01 2005.
- [151] X. Bi, X. Pan, S. Yuan, and Q. Wang, "Plasticizer Contamination in Edible Vegetable Oil in a U.S. Retail Market," *Journal of Agricultural and Food Chemistry*, vol. 61, pp. 9502-9509, 2013/10/02 2013.
- [152] <https://www.lenntech.com/periodic/elements/kr.htm>.
- [153] M. Tomes and T. Carmon, "Photonic Micro-Electromechanical Systems Vibrating at X-band (11-GHz) Rates," *Physical Review Letters*, vol. 102, Mar 2009.
- [154] G. Bahl, J. Zehnpfennig, M. Tomes, and T. Carmon, "Stimulated optomechanical excitation of surface acoustic waves in a microdevice," *Nature Communications*, vol. 2, p. 403, 07/26/online 2011.
- [155] T. Carmon, H. Rokhsari, L. Yang, T. J. Kippenberg, and K. J. Vahala, "Temporal behavior of radiation-pressure-induced vibrations of an optical microcavity phonon mode," *Physical Review Letters*, vol. 94, p. 4, Jun 2005.
- [156] A. K. Dunn, A. Devor, H. Bolay, M. L. Andermann, M. A. Moskowitz, A. M. Dale, *et al.*, "Simultaneous imaging of total cerebral hemoglobin concentration, oxygenation, and blood flow during functional activation," *Optics Letters*, vol. 28, pp. 28-30, 2003/01/01 2003.
- [157] H. Du, F. Chau, and G. Zhou, "Mechanically-Tunable Photonic Devices with On-Chip Integrated MEMS/NEMS Actuators," *Micromachines*, vol. 7, p. 69, 2016.
- [158] B. A. Dorin and W. N. Ye, "Two-mode division multiplexing in a silicon-on-insulator ring resonator," *Optics Express*, vol. 22, pp. 4547-4558, 2014/02/24 2014.
- [159] F. Monifi, S. K. Ozdemir, and L. Yang, "Tunable add-drop filter using an active whispering gallery mode microcavity," *Applied Physics Letters*, vol. 103, p. 4, Oct 2013.

Chapter 2

Theoretical background

It is of great importance for one to study the theoretical analysis of the means and techniques that will be used during the experimental processes. Therefore, a consistent theoretical approach could be used either to predict the results of the experimental process, or alternatively, may be used in order to prove and explain the experimental results. Moreover, many times the theoretical models and simulations proved to be useful for understanding the underlying physical mechanisms of the experimental results.

Within this thesis, fiber optics and multi-photon polymerization technique were combined in order to produce microsensors based on Fabry-Perot interferometry and whispering-gallery-mode (WGM) resonators. Thus, in the present chapter the basic principles of the materials and techniques that are required for these experiments will be presented and discussed.

Initially, the categories of the optical fibers and their characteristics will be presented, constituting the guiding platforms for the fabrication of the photopolymerized microresonators. Moreover, the propagation of light, as electromagnetic wave, through the optical fiber waveguide will be analytically presented, since the optical fibers that were used for spectrally interrogating the fabricated resonating devices. Then, the theory for tapered optical fibers will be presented; such a type of optical fibers were used for exciting whispering-gallery mode microresonators. The basic principles and characteristic parameters of the Fabry-Perot interferometers and the Whispering-gallery mode ring resonators (single and parallel coupled double rings) will be discussed. Finally, the physical mechanisms governing the multi-photon polymerization technique will be briefly presented.

2.1 Optical Fibers

Guiding of light by refraction, the principle that makes light propagation in optical fibers possible, was first demonstrated by J. D. Colladon and in Paris in the early 1840s [1]. Later, in 1888 Doctors Roth and Reuss used bent glass rods to illuminate body cavities [2]. On 1910 Hondros and Debye described the propagation of electromagnetic radiation in cylindrical dielectric wires [3].

In 1953, Dutch scientist B. van Heel first demonstrated image transmission through bundles of optical fibers with a transparent cladding. The same year, H. Hopkins and N. S. Kapany at Imperial College in London succeeded in making image-transmitting bundles with fibers, and their article titled "A flexible fibrescope, using static scanning" was published in the journal Nature in 1954 [4]. Kapany coined the term 'fiber optics' in an article in Scientific American in 1960, and wrote the first book about the new field.

In 1961, E. Snitzer of American Optical published a theoretical description of single mode fibers whose core would be so small and could carry light with only one

wave-guide mode. Snitzer was able to demonstrate a laser directed through a thin glass fiber which was sufficient for medical applications, but for communication applications the light loss became too great.

C. Kao and G. Hockham, of Standard Communications Laboratories in England, published a paper in 1964 demonstrating, theoretically, that light loss in existing glass fibers could be reduced below 20 dB/km by removing impurities.

The crucial attenuation limit of 20 dB/km was first achieved in 1970 by researchers, P. C. Schultz, and F. Zimar working for American glass maker Corning Glass Works. They demonstrated a fiber with 17 dB/km attenuation by doping silica glass with titanium. A few years later they produced a fiber with only 4 dB/km attenuation using germanium dioxide as the core dopant. Further on this Payne and Gambling demonstrated a phosphosilicate optical fiber of 2.7dB/Km loss on 1974 [5].

Initially high-quality optical fibers could only be manufactured at 2 meters per second. Chemical engineer T. Mensah joined Corning in 1983 and increased the speed of manufacture to over 50 meters per second, making optical fiber cables cheaper than traditional copper ones. The major breakthrough for both the optical fiber communications and sensing fields was the invention of the Erbium doped optical fiber amplifier (EDFA) working at the 1530nm window, by Mears, Reekie, Payne, et al, on 1987 [6]. These innovations ushered in the era of optical fiber telecommunication.

The emerging field of photonic crystals led to the development in 1991 of photonic-crystal fiber, which guides light by diffraction from a periodic structure, rather than by total internal reflection. The photonic crystal fibers first demonstrated by Russell consisted of a hexagonal lattice of air holes in a silica fiber, with a solid (1996) or hollow (1998) core at the center where light is guided. The first photonic crystal fibers became commercially available in 2000.

Nowadays, fiber optic technology find a variety of applications in medicine, military, telecommunication, industry, networking, broadcast industries etc. Bellow, the principle of light propagation in optical fibers, the classifications of optical fibers, and their characteristic parameters, as well as, their optical loss mechanisms will be presented.

2.1.1 Classifications of optical fibers and fiber parameters

In its simplest form, an optical fiber consists of a central glass core of a high refractive index, surrounded by a cladding layer, which refractive index is slightly lower than the core index; and an outer plastic polymeric jacket for adding mechanical durability [7-9].

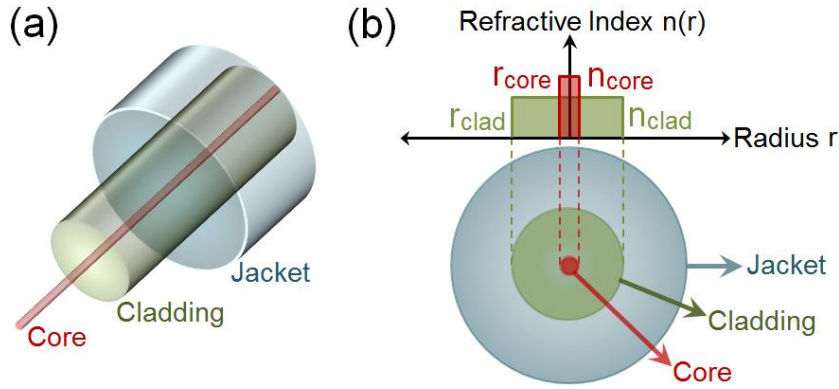


Fig. 2.1. (a) Schematic illustration of a step-index fiber, consisting of the core, the cladding and a polymeric plastic jacket. (b) Cross section of a step-index optical fiber and the refractive index profile.

Figure 2.1 shows schematically the cross section and refractive-index profile of such an optical fiber which is known as step-index fiber [9, 10].

Two fundamental parameters that characterize an optical fiber are presented below. The relative core-cladding index difference Δ , which is defined as [7, 8, 11]:

$$\Delta = \frac{n_{core} - n_{clad}}{n_{core}} \quad (2.1)$$

and the so called normalized frequency V , which is the parameter to determine the quality of guidance supported by the optical fiber [8, 12], defined as:

$$V = k_0 r \sqrt{(n_{core}^2 - n_{clad}^2)} \quad (2.2)$$

where $k_0 = 2\pi/\lambda$, r is the core radius, and λ is the wavelength of light. For a step-index fiber, only the lowest order mode (fundamental mode) propagates in the fiber, if V is smaller than 2.405. Optical fibers designed to satisfy this condition are called single-mode fibers.

The optical fibers are classified into two types: the single-mode fibers (SMF) and the multimode fiber (MMF). In our experiments only single-mode optical fibers operating at 1550 nm wavelength, were used and more specifically SMF-28e (Corning) with a core diameter of 8.2 μm and a cladding diameter of 125 μm . [13]

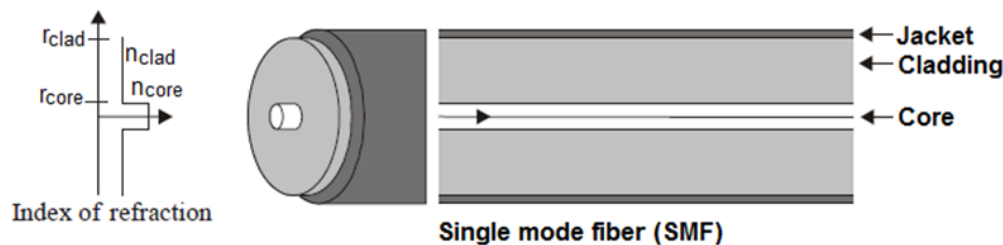


Fig. 2.2. Light propagation in a step-index single-mode (SMF) optical fiber. [11]

2.1.2 Mechanism of Light Propagation in Optical Fibers; Total Internal Reflection

To consider the propagation of light within an optical fiber utilizing the ray theory

model, it is necessary to take into account the refractive index of the dielectric medium [9, 14, 15]. The refractive index of a medium is defined as $n=c/v$, where c is the velocity of light in vacuum and v is the velocity of light in the medium. A ray of light travels more slowly in an optically dense medium than in one less dense, and the refractive index gives a measure of this effect.

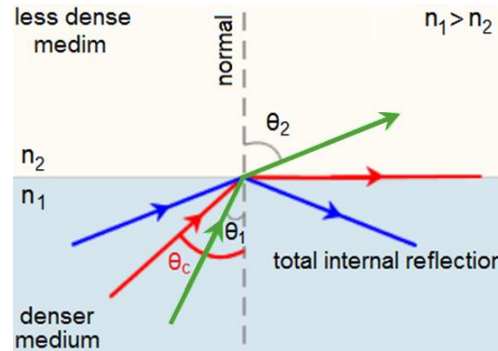


Fig.2.3 Refraction of light from a dense medium to a less dense optical medium. If light propagates from a denser medium to a less dense medium, it will refract away from the normal (green line). Red line corresponds to the light propagation for the critical angle where the incidence light leads to a 90° angle of reflection. Blue line corresponds to the total internal reflection.

When a ray is incident on the interface of a denser medium to a less dense medium, refraction occurs as illustrated in Figure 2.3. According to Snell’s Law which states that the ratio of the sines (sin) of the angles of incidence and refraction is equivalent to the ratio of the indices of refraction:

$$\frac{\sin \theta_1}{\sin \theta_2} = \frac{n_2}{n_1} \quad (2.3)$$

if light propagates from a denser medium to a less dense medium, it will refract away from the normal (see Fig. 2.3, green line). In Eq. (2.3) θ_1 is the angle subtended between the incident ray and the normal to the interface, and θ_2 is the angle subtended between the refracted ray and the normal to the interface. The quantities n_1 and n_2 are termed the *refractive indices* of media 1 and 2, respectively.

When the angle of incidence leads to a 90 degree angle of refraction, then it is called critical angle (see Fig. 2.3, red line) and it is defined as:

$$\sin \theta_c = \frac{n_2}{n_1} \quad \rightarrow \quad \theta_c = \sin^{-1} \left(\frac{n_2}{n_1} \right) \quad (2.4)$$

When the ray of the incidence light while propagating through the denser medium approaches the less denser medium at an angle greater than the critical angle then total internal reflection (TIR) takes place (see Fig. 2.3, blue line). By this way, the light cannot exit the medium and is effectively “trapped” in the denser medium.

Total internal reflection is the basic phenomenon responsible for guiding of light in optical fibers [9]. As shown in Figure 2.4 the black light ray, denoted as A, corresponds to the light ray refracted at air-core interface and then transmitted to the core of the fiber. Afterwards it is propagating through the fiber due to total internal

reflection between the core and the cladding of the optical fiber.

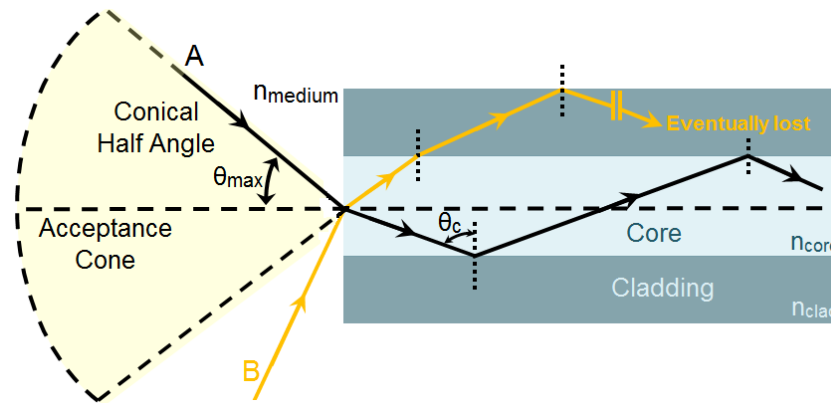


Fig. 2.4. The acceptance angle θ_{max} when launching light into an optical fiber. Black ray light (A) corresponds to the light ray refracted at air-core interface and transmitted to the core of the fiber and propagated in the fiber due to total internal reflection between the core and the cladding of the optical fiber. Any rays which are incident into the optical fiber core at an angle greater than θ_{max} (to the fiber axis) will be partially reflected and transmitted to the core-cladding interface and after some reflections their energy will be eventually lost (see orange ray light (B) [9] .

Rays incident into the optical fiber core at an angle greater than θ_{max} (to the fiber axis) will be partially reflected and partially transmitted out through the boundary towards the cladding. After many such reflections, the energy in these rays will eventually be lost (see orange ray light noted as B). Thus rays that will be transmitted by total internal reflection within the fiber core must be incident on the fiber core within the acceptance cone. Hence θ_{max} is the maximum angle to the fiber axis, at which light may enter the optical fiber in order to be propagated and is referred as conical half angle or total acceptance angle.

2.1.3 Numerical Aperture of optical fiber

It is possible to obtain a relationship between the acceptance angle and the refractive indices of the three media involved, namely the core, cladding and medium by continue the ray theory analysis. This leads to the definition of a more generally used term, the numerical aperture of the optical fiber (NA) [9, 12, 15], which can be defined by the following equation:

$$NA = n_{medium} \sin \theta_{max} = \sqrt{n_{core}^2 - n_{clad}^2} \quad (2.5)$$

The NA may also be given in terms of the relative refractive index difference Δ between the core and the cladding (see Eq. (2.1)) which is defined as [7]:

$$NA = n_{core} (2\Delta)^{\frac{1}{2}} \quad (2.6)$$

The Equations (2.5) and (2.6) for the numerical aperture, are a very useful measure of the light-collecting ability of an optical fiber. They are independent of the fiber core

diameter and are valid for core diameters as small as 8 μm . However, for smaller diameters they break down as the geometric optics approach is invalid. This is because the ray theory model is only a partial description of the character of light. It describes the direction of a plane wave component in the fiber but does not take into account interference between such components. When interference phenomena are considered it is found that only rays with certain discrete characteristics propagate in the fiber core. Thus the fiber will only support a discrete number of guided modes. This becomes critical in small core diameter fibers which only support one or a few modes. Hence electromagnetic mode theory must be applied in these cases.

2.1.4 Material and doping

For the purpose of low-loss transmission and easy fabrication, the material of optical fibers consisted of pure silica glass synthesized by fusing SiO_2 molecules. The refractive-index difference between the core and the cladding is realized by the selective use of dopants during the fabrication process.

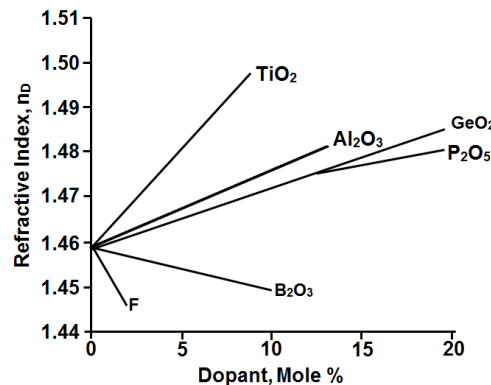


Fig. 2.5. Influence of different dopant mole percentages on refractive index of silica glass. [12]

Materials such as GeO_2 , Al_2O_3 and P_2O_5 raises the refractive index and are suitable to be used as doping for the fiber core. Moreover GeO_2 can enhance photosensitivity, Al_2O_3 enhance the solubility of active rare-earth dopants and P_2O_5 reduces glass viscosity. On the other hand B_2O_3 reduces the refractive index and increases the expansion coefficient, and F reduces the refractive index and glass viscosity, therefore they are used for doping the cladding [12, 15, 16]. Additional dopants can be used depending on specific applications. For example, to make fiber amplifiers and lasers, the core of silica fibers is co-doped with rare-earth ions using dopants such as ErCl_3 and Nd_2O_3 .

2.1.5 Fiber Losses

While light propagates within an optical fiber loses power over distance. The loss of power depends on the wavelength of the light and on the propagating material. For silica glass, the shorter wavelengths are attenuated the most.

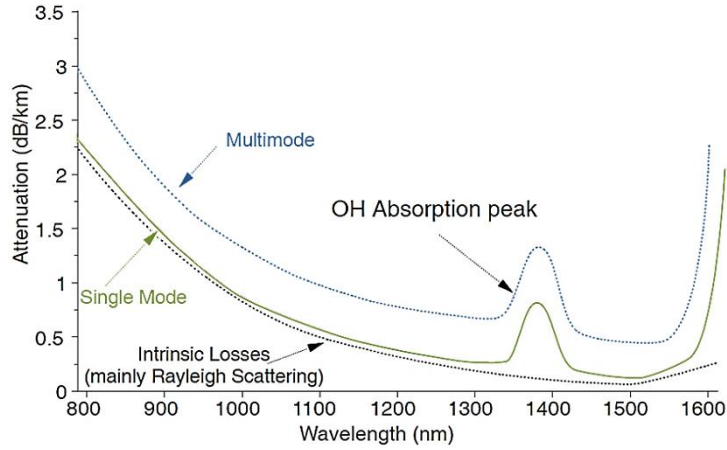


Fig.2.6. Typical fiber attenuation spectrum in infrared region. The green solid curve shows the characteristics of a single-mode fiber made from silica containing about 4% of germanium dioxide (GeO_2) dopant in the core. The blue dashed curve is for graded index multimode fiber. Attenuation in multimode fibers is higher than in single-mode fibers due to higher levels of dopant that are used. The peak at around 1400 nm is due to the effects of traces of water in the glass.[15]

The lowest loss occurs at the wavelength of 1550 nm, which is commonly used for long-distance transmissions. Typical total losses for an optical fiber, at the three different transmission windows are 2 – 3 dB/km at 800 nm, less than 0.5 dB/km at 1300 nm and less than 0.2 dB/km at 1550 nm. These numbers are for single mode fibers (SMF). From Fig. 2.6 it can be seen that multimode fibers (MMF) have slightly higher losses than those of SMF due to higher levels of dopant that are used. There are many different loss mechanisms that reduces the intensity of incident light that travels in an optical fiber and they will be discussed in details in the following sections (2.1.5a and 2.1.5b)

2.1.5a Attenuation losses in optical fibers

Attenuation in fiber optics, also known as transmission loss, is the reduction of the intensity of the incident light, with respect to distance during transmission through the optical fiber [8, 11]. If P_0 is the power launched at the input of an optical fiber of length L , the transmitted power P_T is given by:

$$P_T = P_0 \exp(-\alpha L) \quad (2.7)$$

where the attenuation constant α is a measure of total fiber losses from all sources. In order to express α in units of dB/km one has to use the following equation:

$$\alpha_{dB} = -\frac{10}{L} \log \left(\frac{P_T}{P_0} \right) = 4.343\alpha \quad (2.8)$$

Nowadays fused silica fibers have losses of less than 0.15 dB/km at 1.55 μm , corresponding to more than 97% transmission over 1 km. The mechanisms responsible for the attenuation are the material absorption and Raleigh scattering dominantly. We discuss the loss mechanisms in detail in Section 2.1.6.

2.1.5b Fiber loss mechanisms

There are two basic categories of sources that contribute to the light loss in fiber optical systems, namely those of intrinsic and extrinsic losses [8, 10].

The intrinsic fiber losses are those associated with the material of the optical fiber itself and the total loss is proportional to length L . Absorption and scattering phenomena are the primary causes of intrinsic losses.

Absorption losses in an optical fiber tend to be an exponential function of length. They are caused by the presence of impurities such as traces of metal ions (e.g., Cu^{2+} , Fe^{3+}) and hydroxyl (OH^-) ions [8, 10, 15]. The absorption of these materials is defined in a vicinity of wavelengths corresponding to their natural oscillation frequencies. In modern fibers, absorption losses are almost entirely due to OH^- ions which appear a fundamental absorption peak at $\lambda = 2.73 \mu\text{m}$ and dominant peaks at $\sim 1.4 \mu\text{m}$ and at $\sim 1.24 \mu\text{m}$ a smaller one, shown in Figure 2.7. It is possible to employ dehydration techniques during manufacturing to reduce presence of OH^- ions. In state-of-the-art fibers, the peak near $1.4 \mu\text{m}$ can be reduced to below the 0.5 dB level. It virtually disappears in the so-called “dry” fibers [8].

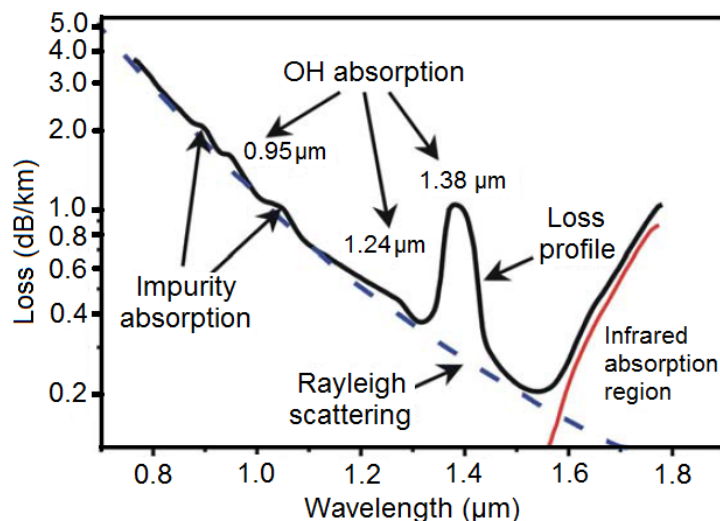


Fig. 2.7. Measured loss spectrum (black solid) of a single mode silica fiber. The blue dashed curve shows the attenuation losses due to Rayleigh scattering while red solid curve illustrate the loss profile arising from infrared absorption. [17]

Scattering losses in an optical fiber are caused from density fluctuations frozen into the fused silica during manufacture or irregularities between the junction and cladding. These imperfections result a fluctuation in the refractive index. If the scale of these fluctuations is on the order of $\lambda/10$ or less, each irregularity acts as a scattering center.

This is a form of Rayleigh scattering and is characterized by an effective absorption coefficient that is proportional to λ^{-4} [8, 10, 15]. Rayleigh scattering can be caused by the existence of tiny dielectric inconsistencies in the glass. The resulting inhomogeneous refractive index scatters light in all directions. The addition of dopants into the fiber results in higher inhomogeneities in the refractive index

distribution, which increases the Rayleigh scattering loss. Figure 2.7 shows the measured loss spectrum of a single-mode silica fiber. Fiber losses increase rapidly as wavelength decreases and reach a level of a few dB/km in the visible region, which is caused by the Rayleigh scattering. The absorption at wavelengths longer than 1.6 μm comes from infrared absorption by silicon-oxygen bonds in the glass; as the plot shows, the absorption increases sharply with longer wavelengths in the near infrared.

The extrinsic fiber losses are caused by geometric characteristics and handling of the optical fibers. There are three different types, namely bending, launching and connector losses.

If the fiber has been improperly cabled or installed, bending losses can arise. Bending losses are divided into micro and macro-bending losses [10, 15, 18]. Micro-bending losses are due to nanometer size deviations in the fiber, while macro-bending losses are due to visible bends in the fiber, as presented in Figure 2.9.

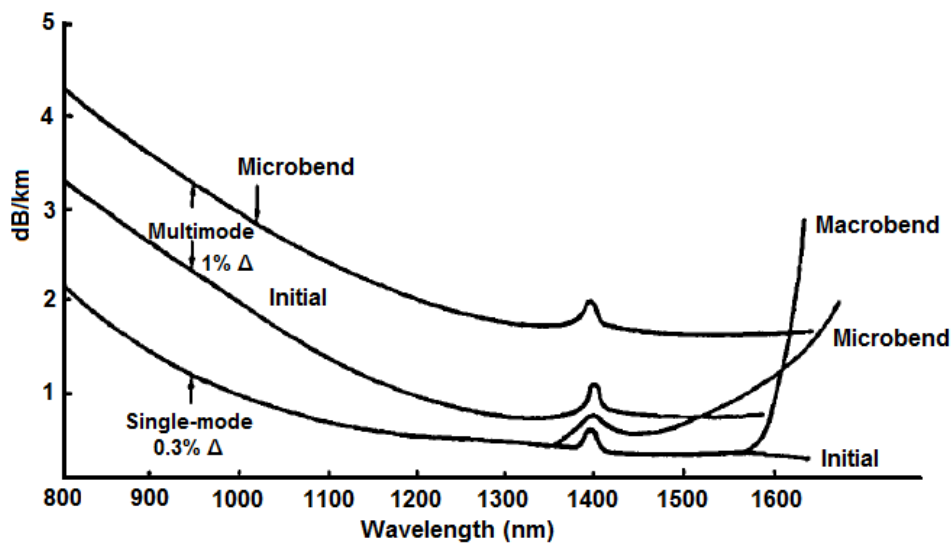


Fig. 2.8. Bend-induced losses of optical fibers. [12]

Micro-bending losses are induced in the process of jacketing, where the fiber is subjected to microscopic deviations of the fiber axis from the straight condition. Moreover, micro-bends could be occurred when the fiber is pressed onto an irregular surface [10, 15]. As it can be observed in Figure 2.8, bending losses are more significant in multimode fibers, than in single mode fibers.

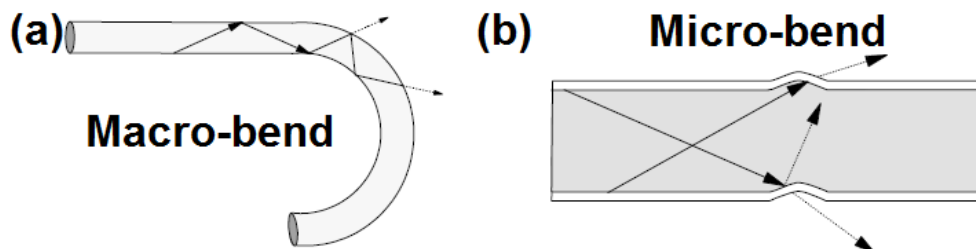


Fig. 2.9. Bends introduced to optical fibers. (a) Macro-bend and (b) micro-bend.[15]

The term launching loss refers to an optical fiber, not being able to propagate all the incoming light rays from an optical source [10, 18]. These occur during the

process of coupling light into the fiber (e.g., losses at the interface stages). Rays launched outside the angle of acceptance excite only dissipative radiation modes in the fiber.

Connector losses are associated with the coupling of the output of one fiber with the input of another fiber, or couplings with detectors or other components. The significant losses may arise in fiber connectors and splices of the cores of the joined fibers having unequal diameters or misaligned centers, or if their axes are tilted [18, 19]. There are other connection losses such as offsets or tilts or air gaps between fibers, and poor surface finishes. Some of these are illustrated in Figure 2.10.

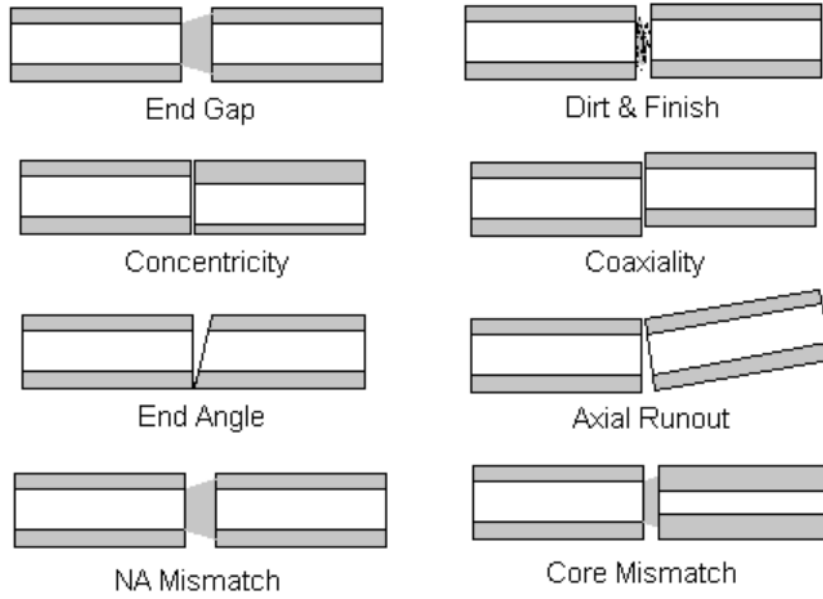


Fig. 2.10. Connection mish-matches. [20]

2.2 Electromagnetic Wave Theory for Optical Fibers

Light propagation in optical fibers is based on electromagnetic wave theory. By applying Maxwell's equations, a model that describes the electromagnetic wave propagation of light in cylindrical geometry, optical fibers can be obtained [7, 9, 14, 21, 22]. Below, some basic equations that can describe the propagation of light as an electromagnetic wave in a step-index fiber will be presented. The analytic steps and description that leads from the one equation to the other and at the final solutions can be found in the literature [7, 14, 21-24]. We consider a step index fiber like the one presented in Figure 2.1, consisting of a homogeneous and lossless dielectric medium. Maxwell's equations are:

$$\nabla \times \mathbf{E} = -\frac{\partial \mathbf{B}}{\partial t} = -\mu \frac{\partial \mathbf{H}}{\partial t} \quad (2.9)$$

$$\nabla \times \mathbf{H} = \mathbf{J} + \frac{\partial \mathbf{D}}{\partial t} = -\varepsilon \frac{\partial \mathbf{E}}{\partial t} \quad (2.10)$$

$$\nabla \cdot \mathbf{D} = \rho_f = 0 \quad (2.11)$$

$$\nabla \cdot \mathbf{B} = 0 \quad (2.12)$$

where \mathbf{E} and \mathbf{H} are electric and magnetic field vectors, respectively, and \mathbf{D} and \mathbf{B} are corresponding electric and magnetic flux densities. The current density vector \mathbf{J} and the charge density ρ_f represent the sources for the electromagnetic field. In the absence of free charges in a medium such as optical fibers, $\mathbf{J} = 0$ and $\rho_f = 0$. The flux densities \mathbf{D} and \mathbf{B} arise in response to the electric and magnetic fields \mathbf{E} and \mathbf{H} propagating inside the medium and are related to them through the constitutive relations given by

$$\mathbf{D} = \varepsilon \mathbf{E} + \mathbf{P} \quad (2.13)$$

$$\mathbf{B} = \mu \mathbf{H} + \mathbf{M} \quad (2.14)$$

where ε and μ denote the permittivity and permeability of the medium while, \mathbf{P} and \mathbf{M} are the induced electric and magnetic polarizations. For a nonmagnetic medium such as an optical fibers, $\mathbf{M} = 0$ and moreover $\mathbf{P} = 0$. The ε and μ are related to their respective values in vacuum ε_0 and μ_0 by

$$\varepsilon = \varepsilon_0 n^2 \quad (2.15)$$

$$\mu = \mu_0 \quad (2.16)$$

where $\varepsilon_0 = 8.854 \times 10^{-12}$ (F/m) and $\mu_0 = 4\pi \times 10^{-7}$ (H/m), while n is the refractive index. Then, the wavenumber of the light in the medium can be expressed as

$$\Gamma = \omega \sqrt{\varepsilon \mu} = \omega \sqrt{\varepsilon_0 \mu_0} = kn \quad (2.17)$$

In Equation (2.17), ω is an angular frequency of the sinusoidally varying electromagnetic fields, with respect to time and k is the wavenumber in a vacuum, which is related to the angular frequency ω by

$$k = \omega \sqrt{\varepsilon_0 \mu_0} = \frac{\omega}{c} \quad (2.18)$$

where c is the light velocity in vacuum. The wavelength of the electromagnetic wave for a frequency f , is obtained by $\lambda = c/f = (\omega/k)/f = 2\pi/k$, with $\omega = 2\pi f$.

By taking the curl of Equations (2.9) and (2.10) one can obtain

$$\nabla^2 \mathbf{E}(r, t) - \varepsilon \mu \frac{\partial^2}{\partial t^2} \mathbf{E}(r, t) = 0 \quad (2.19)$$

$$\nabla^2 \mathbf{H}(r, t) - \varepsilon \mu \frac{\partial^2}{\partial t^2} \mathbf{H}(r, t) = 0 \quad (2.20)$$

Consider an electromagnetic wave with angular frequency ω and propagating in the z direction with propagation constant β , the electric and magnetic fields can be

expressed as

$$\mathbf{E}(r, t) = \mathbf{E}(r, \varphi)e^{i(\omega t - \beta z)} \quad (2.21)$$

$$\mathbf{H}(r, t) = \mathbf{H}(r, \varphi)e^{i(\omega t - \beta z)} \quad (2.22)$$

where r denotes the position in the plane transverse to the z -axis. For the analysis of wave propagation in optical fibers, which are axially symmetric, Maxwell's equations are written in terms of cylindrical coordinates:

$$\frac{1}{r} \frac{\partial \mathbf{E}_z}{\partial \theta} + i\beta \mathbf{E}_\varphi = -i\omega\mu_0 \mathbf{H}_r \quad (2.23a)$$

$$-\frac{\partial \mathbf{E}_r}{\partial r} - i\beta \mathbf{E}_r = -i\omega\mu_0 \mathbf{H}_\varphi \quad (2.23b)$$

$$\frac{1}{r} \frac{\partial}{\partial r} (r \mathbf{E}_\varphi) - \frac{1}{r} \frac{\partial \mathbf{E}_r}{\partial \theta} = -i\omega\mu_0 \mathbf{H}_z \quad (2.23c)$$

$$\frac{1}{r} \frac{\partial \mathbf{H}_z}{\partial \varphi} + i\beta \mathbf{H}_\varphi = i\omega\mu_0 \varepsilon_0 n^2 \mathbf{E}_r \quad (2.23d)$$

$$-\frac{\partial \mathbf{H}_z}{\partial r} - i\beta \mathbf{H}_r = i\omega\varepsilon_0 n^2 \mathbf{E}_\varphi \quad (2.23e)$$

$$\frac{1}{r} \frac{\partial}{\partial r} (r \mathbf{H}_\varphi) - \frac{1}{r} \frac{\partial \mathbf{H}_r}{\partial \varphi} = i\omega\varepsilon_0 n^2 \mathbf{E}_z \quad (2.23f)$$

Maxwell's Equations (2.23a-f) do not determine the electromagnetic field completely. Out of the infinite possibilities of solutions of Maxwell's equations, one must select those that also satisfy the boundary conditions of the respective problem. The most common type of boundary condition occurs when there are discontinuities in the dielectric constant (refractive index), as shown in Fig. 2.1. At the boundary the tangential components of the electric field and magnetic field should satisfy the conditions

$$\mathbf{E}_t^{(1)} = \mathbf{E}_t^{(2)} \quad (2.24)$$

$$\mathbf{H}_t^{(1)} = \mathbf{H}_t^{(2)} \quad (2.25)$$

where the subscript t denotes the tangential components to the boundary and the superscripts (1) and (2) indicate the medium, respectively. Equations (2.24) and (2.25) denote that the tangential components of the electromagnetic fields must be continuous at the boundary. There are also natural boundary conditions that require the electromagnetic fields to be zero at infinity.

The two sets that are obtained for the wave equations by substituting Equations (2.21) and (2.22) into Equations (2.23a-f) are

$$\frac{\partial^2 \mathbf{E}_z}{\partial r^2} + \frac{1}{r} \frac{\partial \mathbf{E}_z}{\partial r} + \frac{1}{r^2} \frac{\partial^2 \mathbf{E}_z}{\partial \varphi^2} + [k^2 n(r, \varphi)^2 - \beta^2] \mathbf{E}_z = 0 \quad (2.26a)$$

$$\frac{\partial^2 \mathbf{H}_z}{\partial r^2} + \frac{1}{r} \frac{\partial \mathbf{H}_z}{\partial r} + \frac{1}{r^2} \frac{\partial^2 \mathbf{H}_z}{\partial \varphi^2} + [k^2 n(r, \varphi)^2 - \beta^2] \mathbf{H}_z = 0 \quad (2.26b)$$

In axially symmetric optical fibers, the refractive-index distribution is not dependent on φ and is expressed by $n(r)$. Then the transverse electromagnetic fields are related to \mathbf{E}_z and \mathbf{H}_z as follows:

$$\mathbf{E}_r = -\frac{i}{[k^2 n(r)^2 - \beta^2]} \left(\beta \frac{\partial \mathbf{E}_z}{\partial r} + \frac{\omega \mu_0}{r} \frac{\partial \mathbf{H}_z}{\partial \varphi} \right) \quad (2.27a)$$

$$\mathbf{E}_\varphi = -\frac{i}{[k^2 n(r)^2 - \beta^2]} \left(\frac{\beta}{r} \frac{\partial \mathbf{E}_z}{\partial \varphi} + \omega \mu_0 \frac{\partial \mathbf{H}_z}{\partial r} \right) \quad (2.27b)$$

$$\mathbf{H}_r = -\frac{i}{[k^2 n(r)^2 - \beta^2]} \left(\beta \frac{\partial \mathbf{H}_z}{\partial r} + \frac{\omega \varepsilon_0 n(r)^2}{r} \frac{\partial \mathbf{H}_z}{\partial \varphi} \right) \quad (2.27c)$$

$$\mathbf{H}_\varphi = -\frac{i}{[k^2 n(r)^2 - \beta^2]} \left(\frac{\beta}{r} \frac{\partial \mathbf{H}_z}{\partial \varphi} + \omega \varepsilon_0 n(r)^2 \frac{\partial \mathbf{H}_z}{\partial r} \right) \quad (2.27d)$$

The azimuthal dependency of the electromagnetic fields in axially symmetric fibers is expressed by $\cos(n\varphi + \psi)$ or $\sin(n\varphi + \psi)$, where n is an integer and ψ denotes the phase. The modes in an optical fiber consists of TE modes ($\mathbf{E}_z = 0$), TM modes ($\mathbf{H}_z = 0$) and hybrid modes ($\mathbf{E}_z \neq 0$ and $\mathbf{H}_z \neq 0$) respectively.

In the following, electromagnetic fields, dispersion equations, and propagation characteristics of optical fibers are described in detail for step-index fibers as shown in Figure 2.1, which has a uniform refractive index in the core denoted as n_{core} and a core radius of r_{core} , while the cladding refractive index is n_{clad} . The wave number in core and cladding along the transversal direction z are defined as

$$\kappa = \sqrt{k^2 n_{core}^2 - \beta^2} \quad (2.28a)$$

$$\sigma = \sqrt{\beta^2 - k^2 n_{clad}^2} \quad (2.28b)$$

Moreover, the normalized transverse wave numbers are defined as

$$u = \kappa r_{core} = r_{core} \sqrt{k^2 n_{core}^2 - \beta^2} \quad (2.29a)$$

$$w = \sigma r_{core} = r_{core} \sqrt{\beta^2 - k^2 n_{clad}^2} \quad (2.29b)$$

Transverse wave numbers u and w are related from Equations (2.33a-b) as

$$u^2 + w^2 = k^2(n_{core}^2 - n_{clad}^2)r_{core}^2 = v^2 \quad (2.30)$$

2.2.1 Wave theory for TE modes of step-index fibers

When $E_z = 0$ in Equations (2.26a-b) and (2.27a-d) and by taking into account that for a step-index optical fiber at the boundary of the core ($n(r_{core}) = n_{core}$) the refractive index is not equal to the refractive index of the cladding n_{clad} , and for this reason the integer n should be zero, then one can obtain the following sets of equations for the TE mode:

$$\frac{\partial^2 H_z}{\partial r^2} + \frac{1}{r} \frac{\partial H_z}{\partial r} + [k^2 n(r)^2 - \beta^2] H_z = 0 \quad (2.31)$$

and

$$E_\varphi = \frac{i\omega\mu_0}{[k^2 n(r)^2 - \beta^2]} \frac{\partial H_z}{\partial r} \quad (2.32a)$$

$$H_r = -\frac{i\beta}{[k^2 n(r)^2 - \beta^2]} \frac{\partial H_z}{\partial r} \quad (2.32b)$$

$$E_r = H_\varphi = 0 \quad (2.32c)$$

By using the 0th – order of Bessel functions and the modified Bessel functions I_0 and K_0 one can finally obtain that the magnetic fields for the TE mode are given by

$$H_z = \begin{cases} AJ_0(\kappa r) & 0 \leq r \leq r_{core} \\ BK_0(\sigma r) & r \geq r_{core} \end{cases} \quad (2.33a)$$

$$\quad (2.33b)$$

where A and B are constants. The boundary conditions are given for H_z and E_φ to be continuous at $r = r_{core}$

$$AJ_0(\kappa r_{core}) = BK_0(\sigma r_{core}) \quad (2.34a)$$

$$\frac{A}{\kappa} J_0'(\kappa r_{core}) = -\frac{B}{\sigma} K_0'(\sigma r_{core}) \quad (2.34b)$$

Then one can obtain

$$\frac{J_0'(u)}{uJ_0(u)} = -\frac{K_0'(w)}{wK_0(w)} \quad (2.34)$$

Based on the Bessel function formulas where

$$J_0'(u) = -J_1(u) \quad (2.35a)$$

$$K'_0(w) = -K_1(w) \quad (2.35b)$$

The Equation (2.34) can be rewritten as

$$\frac{J_1(u)}{uJ_0(u)} = -\frac{K_1(w)}{wK_0(w)} \quad (2.36)$$

When the normalized frequency v is given, the transverse wave numbers u and w are determined from Eqs. (2.36) and (2.30). Substituting Equations (2.33a-b) and (2.34a) into (2.32a-c), the electromagnetic fields for TE mode are obtained;

$$\mathbf{E}_r = \mathbf{E}_z = \mathbf{H}_\varphi = 0 \quad (2.37)$$

while the fields in the core ($0 \leq r \leq r_{\text{core}}$):

$$E_\varphi = -i\omega\mu_0 \frac{r_{\text{core}}}{u} AJ_1\left(\frac{u}{r_{\text{core}}}r\right) \quad (2.38a)$$

$$H_r = i\beta \frac{r_{\text{core}}}{u} AJ_1\left(\frac{u}{r_{\text{core}}}r\right) \quad (2.38b)$$

$$H_z = AJ_0\left(\frac{u}{r_{\text{core}}}r\right) \quad (2.38c)$$

and the fields in the cladding ($r > r_{\text{core}}$):

$$E_\varphi = i\omega\mu_0 \frac{r_{\text{core}}}{w} \frac{J_0(u)}{K_0(w)} AK_1\left(\frac{w}{r_{\text{core}}}r\right) \quad (2.39a)$$

$$H_r = -i\beta \frac{r_{\text{core}}}{w} \frac{J_0(u)}{K_0(w)} AK_1\left(\frac{w}{r_{\text{core}}}r\right) \quad (2.39b)$$

$$H_z = \frac{J_0(u)}{K_0(w)} AK_0\left(\frac{w}{r_{\text{core}}}r\right) \quad (2.39c)$$

2.2.2 Wave theory for TM modes of step-index fibers

When \mathbf{E}_z is set to be $\mathbf{E}_z = 0$ in Equations (2.26a-b) and (2.27a-d) and by taking into $n=0$ then one can obtain the following sets of equations for the TM mode:

$$\frac{\partial^2 \mathbf{E}_z}{\partial r^2} + \frac{1}{r} \frac{\partial \mathbf{E}_z}{\partial r} + [k^2 n(r)^2 - \beta^2] \mathbf{E}_z = 0 \quad (2.40)$$

and

$$\mathbf{E}_r = -\frac{i\beta}{[k^2 n(r)^2 - \beta^2]} \frac{\partial \mathbf{E}_z}{\partial r} \quad (2.41a)$$

$$\mathbf{H}_\varphi = -\frac{i\omega \epsilon_0 n^2}{[k^2 n(r)^2 - \beta^2]} \frac{\partial \mathbf{H}_{\mathbf{E}_z}}{\partial r} \quad (2.41b)$$

$$\mathbf{E}_\varphi = \mathbf{H}_r = 0 \quad (2.41c)$$

By using the 0th – order of Bessel functions and the modified Bessel functions I_0 and K_0 one can finally obtain that the electric fields for the TM mode are given by

$$\mathbf{E}_z = \begin{cases} AJ_0(kr) & 0 \leq r \leq r_{core} \\ BK_0(\sigma r) & r \geq r_{core} \end{cases} \quad (2.42a)$$

$$(2.42b)$$

where A and B are constants. The boundary conditions are given for \mathbf{E}_z and \mathbf{H}_φ to be continuous at $r = r_{core}$

$$\frac{J'_0(u)}{uJ_0(u)} = - \left(\frac{n_{clad}}{n_{core}} \right)^2 \frac{K'_0(w)}{wK_0(w)} \quad (2.43)$$

Based on the Bessel function formulas presented in Equations (2.35a-b) the Equation (2.43) can be rewritten as

$$\frac{J_1(u)}{uJ_0(u)} = - \left(\frac{n_{clad}}{n_{core}} \right)^2 \frac{K_1(w)}{wK_0(w)} \quad (2.44)$$

The electromagnetic fields for TM mode are obtained;

$$\mathbf{E}_\varphi = \mathbf{H}_r = \mathbf{H}_z = 0 \quad (2.45)$$

while the fields in the core ($0 \leq r \leq r_{core}$):

$$E_r = i\beta \frac{r_{core}}{u} AJ_1\left(\frac{u}{r_{core}}r\right) \quad (2.46a)$$

$$E_z = AJ_0\left(\frac{u}{r_{core}}r\right) \quad (2.46b)$$

$$H_\varphi = i\omega\epsilon_0 r_{core}^2 AJ_1\left(\frac{u}{r_{core}}r\right) \quad (2.46c)$$

and the fields in the cladding ($r > r_{core}$):

$$E_r = -i\beta \frac{r_{core}}{w} \frac{J_0(u)}{K_0(w)} AK_1\left(\frac{w}{r_{core}}r\right) \quad (2.47a)$$

$$E_z = \frac{J_0(u)}{K_0(w)} AK_0\left(\frac{w}{r_{core}}r\right) \quad (2.47b)$$

$$H_\varphi = -i\omega\epsilon_0 r_{clad}^2 \frac{r_{core}}{w} \frac{J_0(u)}{K_0(w)} AK_1\left(\frac{w}{r_{core}}r\right) \quad (2.47c)$$

2.2.3 Wave theory for hybrid modes of step-index fibers

The solutions of the wave equations (2.26a) and (2.26b) for the hybrid modes of a

step-index fiber are given by the product of the n^{th} - order of Bessel functions $J_n(\kappa r)$ and the modified Bessel functions of $K_n(\kappa r)$. Moreover, \mathbf{E}_z and \mathbf{H}_z should be continuous at $r = r_{core}$. It is also known from Equations (2.27a-d) that $\partial \mathbf{E}_z / \partial r$ and $\partial \mathbf{H}_z / \partial \varphi$ (or $\partial \mathbf{E}_z / \partial \varphi$ and $\partial \mathbf{H}_z / \partial r$) have the same φ dependencies. Taking this into consideration, the z -components of the electromagnetic field are expressed by

$$\mathbf{E}_z = \begin{cases} A J_n \left(\frac{u}{r_{core}} r \right) \cos(n\varphi + \psi) & 0 \leq r \leq r_{core} \\ A \frac{J_n(u)}{K_n(w)} K_n \left(\frac{w}{r_{core}} r \right) \cos(n\varphi + \psi) & r \geq r_{core} \end{cases} \quad (2.48a)$$

$$\mathbf{E}_z = \begin{cases} A J_n \left(\frac{u}{r_{core}} r \right) \cos(n\varphi + \psi) & 0 \leq r \leq r_{core} \\ A \frac{J_n(u)}{K_n(w)} K_n \left(\frac{w}{r_{core}} r \right) \cos(n\varphi + \psi) & r \geq r_{core} \end{cases} \quad (2.48b)$$

$$\mathbf{H}_z = \begin{cases} C J_n \left(\frac{u}{r_{core}} r \right) \sin(n\varphi + \psi) & 0 \leq r \leq r_{core} \\ C \frac{J_n(u)}{K_n(w)} K_n \left(\frac{w}{r_{core}} r \right) \sin(n\varphi + \psi) & r \geq r_{core} \end{cases} \quad (2.49a)$$

$$\mathbf{H}_z = \begin{cases} C J_n \left(\frac{u}{r_{core}} r \right) \sin(n\varphi + \psi) & 0 \leq r \leq r_{core} \\ C \frac{J_n(u)}{K_n(w)} K_n \left(\frac{w}{r_{core}} r \right) \sin(n\varphi + \psi) & r \geq r_{core} \end{cases} \quad (2.49b)$$

Where A and C are constants. The transverse components are obtained by substituting Equations (2.48a-b) and (2.49a-b) into (3.27a-d) as follows:

For the core region ($0 \leq r \leq r_{core}$):

$$E_r = -\frac{ir_{core}^2}{u^2} \left[A\beta \frac{u}{r_{core}} J_n' \left(\frac{u}{r_{core}} r \right) + C\omega\mu_0 \frac{n}{r} J_n \left(\frac{u}{r_{core}} r \right) \right] \cos(n\varphi + \psi) \quad (2.50a)$$

$$E_\varphi = -\frac{ir_{core}^2}{u^2} \left[-A\beta \frac{n}{r} J_n \left(\frac{u}{r_{core}} r \right) - C\omega\mu_0 \frac{u}{r_{core}} J_n' \left(\frac{u}{r_{core}} r \right) \right] \sin(n\varphi + \psi) \quad (2.50b)$$

$$H_r = -\frac{ir_{core}^2}{u^2} \left[A\omega\varepsilon_0 n_{core}^2 \frac{n}{r} J_n \left(\frac{u}{r_{core}} r \right) + C\beta \frac{u}{r_{core}} J_n' \left(\frac{u}{r_{core}} r \right) \right] \sin(n\varphi + \psi) \quad (2.50c)$$

$$H_\varphi = -\frac{ir_{core}^2}{u^2} \left[A\omega\varepsilon_0 n_{core}^2 \frac{u}{r_{core}} J_n' \left(\frac{u}{r_{core}} r \right) + C\beta \frac{n}{r} J_n \left(\frac{u}{r_{core}} r \right) \right] \cos(n\varphi + \psi) \quad (2.50d)$$

For the cladding region ($r > r_{core}$):

$$E_r = \frac{ir_{core}^2}{w^2} \left[A\beta \frac{w}{r_{core}} K_n' \left(\frac{w}{r_{core}} r \right) + C\omega\mu_0 \frac{n}{r} K_n \left(\frac{w}{r_{core}} r \right) \right] \frac{J_n(u)}{K_n(w)} \cos(n\varphi + \psi) \quad (2.51a)$$

$$E_\varphi = \frac{ir_{core}^2}{w^2} \left[-A\beta \frac{n}{r} K_n \left(\frac{w}{r_{core}} r \right) - C\omega\mu_0 \frac{w}{r_{core}} K_n' \left(\frac{w}{r_{core}} r \right) \right] \frac{J_n(u)}{K_n(w)} \sin(n\varphi + \psi) \quad (2.51b)$$

$$H_r = \frac{ir_{core}^2}{w^2} \left[A\omega\varepsilon_0 n_{clad}^2 \frac{n}{r} K_n \left(\frac{w}{r_{core}} r \right) + C\beta \frac{w}{r_{core}} K_n' \left(\frac{w}{r_{core}} r \right) \right] \frac{J_n(u)}{K_n(w)} \sin(n\varphi + \psi) \quad (2.51c)$$

$$H_\varphi = \frac{ir_{core}^2}{w^2} \left[A\omega\varepsilon_0 n_{clad}^2 \frac{w}{r_{core}} K_n' \left(\frac{w}{r_{core}} r \right) - C\beta \frac{n}{r} K_n \left(\frac{w}{r_{core}} r \right) \right] \frac{J_n(u)}{K_n(w)} \cos(n\varphi + \psi) \quad (2.51d)$$

The boundary condition at $r = r_{core}$ that E_φ and H_φ should be continuous gives two relations, namely Equations (2.52) and (2.53), the first one according to Equations (2.50b) and (2.51b) while the second one according to Equations (2.50d) and (2.51d) respectively and are

$$A\beta \left(\frac{1}{u^2} + \frac{1}{w^2} \right) n = -C\omega\mu_0 \left[\frac{J_n'(u)}{uJ_n(u)} + \frac{K_n'(w)}{wK_n(w)} \right] \quad (2.52)$$

$$A\omega\varepsilon_0 \left[\frac{J_n'(u)}{uJ_n(u)} n_{core}^2 + \frac{K_n'(w)}{wK_n(w)} n_{clad}^2 \right] = -C\beta \left(\frac{1}{u^2} + \frac{1}{w^2} \right) \quad (2.53)$$

The dispersion equation delivered from Equations (2.52) and (2.53) is

$$\left[\frac{J_n'(u)}{uJ_n(u)} + \frac{K_n'(w)}{wK_n(w)} \right] \left[\frac{J_n'(u)}{uJ_n(u)} n_{core}^2 + \frac{K_n'(w)}{wK_n(w)} n_{clad}^2 \right] = \frac{\beta^2}{k^2} \left(\frac{1}{u^2} + \frac{1}{w^2} \right) n^2 \quad (2.54)$$

Substituting the following relation, which is derives from Equation (2.29)

$$\frac{\beta^2}{k^2} \left(\frac{1}{u^2} + \frac{1}{w^2} \right) n^2 = \frac{n_{core}^2}{u^2} + \frac{n_{clad}^2}{w^2} \quad (2.55)$$

Equation (2.54) may be rewritten as

$$\left[\frac{J_n'(u)}{uJ_n(u)} + \frac{K_n'(w)}{wK_n(w)} \right] \left[\frac{J_n'(u)}{uJ_n(u)} + \frac{K_n'(w)}{wK_n(w)} \frac{n_{clad}^2}{n_{core}^2} \right] = n^2 \left(\frac{1}{u^2} + \frac{1}{w^2} \right) \left[\frac{1}{u^2} + \frac{1}{w^2} \frac{n_{clad}^2}{n_{core}^2} \right] \quad (2.56)$$

The constant C in the electromagnetic field expressions (2.50) and (2.51) can be written from Equation (2.52) as

$$C = -A \frac{\beta}{\omega\mu_0} s \quad (2.57)$$

where

$$S = \frac{n\left(\frac{1}{u^2} + \frac{1}{w^2}\right)}{\left[\frac{J'_n(u)}{uJ_n(u)} + \frac{K'_n(w)}{wK_n(w)}\right]} \quad (2.58)$$

By applying the following recurrence relations for the Bessel functions

$$J'_n(z) = \frac{1}{2}[J_{n-1}(z) - J_{n+1}(z)] \quad (2.59a)$$

$$\frac{n}{z}J_n(z) = \frac{1}{2}[J_{n-1}(z) - J_{n+1}(z)] \quad (2.59b)$$

$$K'_n(z) = -\frac{1}{2}[K_{n-1}(z) - K_{n+1}(z)] \quad (2.59c)$$

$$\frac{n}{z}K_n(z) = \frac{1}{2}[K_{n-1}(z) - K_{n+1}(z)] \quad (2.59b)$$

to the Equations (2.50a-d) and (2.51a-d) one can obtain for the axis of propagation the E_z and H_z as

For the core region ($0 \leq r \leq r_{core}$):

$$E_z = AJ_n\left(\frac{u}{r_{core}}r\right)\cos(n\varphi + \psi) \quad (2.60a)$$

$$H_z = -A\frac{\beta}{\omega\mu_0}SJ_n\left(\frac{u}{r_{core}}r\right)\sin(n\varphi + \psi) \quad (2.560b)$$

For the cladding region ($r \geq r_{core}$):

$$E_z = A\frac{J_n(u)}{K_n(w)}K_n\left(\frac{w}{r_{core}}r\right)\cos(n\varphi + \psi) \quad (2.61a)$$

$$H_z = -A\frac{\beta}{\omega\mu_0}S\frac{J_n(u)}{K_n(w)}K_n\left(\frac{w}{r_{core}}r\right)\sin(n\varphi + \psi) \quad (2.61b)$$

The propagation constant of the hybrid modes is calculated by solving Equation (2.56) using the u - w relation of Equation (2.49). Although Eq. (2.56) is the strict solution of the hybrid modes in step-index fibers, it is rather difficult to investigate the propagation properties of optical fibers with Equation (2.56). In practical fibers, the refractive-index difference Δ is of the order of 1%, so one can approximate $n_{core} \cong n_{clad}$ in some cases. In these cases Equation (2.56) can be simplified and much practical and useful information is obtained.

2.2.4 Linearly polarized modes (LP) for weakly guiding approximation

The analysis of fibers based on the approximation with $n_{\text{core}} / n_{\text{clad}} \cong 1$ was first presented by Snyder [24]. Afterwards such mode groups with the approximation $n_{\text{core}} / n_{\text{clad}} \cong 1$ were designated LP (linearly polarized) modes by Gloge [23]. Since an LP mode is derived by the approximation of $n_{\text{core}} / n_{\text{clad}} \cong 1$, it means that the light confinement in the core is not so tight. Therefore this approximation is called weakly guiding approximation [25]. The LP modes will be presented below.

The strict solution for the TE modes is adopted as it was presented in Equation (2.36). For the TM modes the weakly guiding approximation ($n_{\text{core}} / n_{\text{clad}} \cong 1$) is applied to the rigorous dispersion Equation (2.44) and the approximate resulted form is the same to Equation (2.36).

For the hybrid modes when weakly guiding approximation $n_{\text{core}} / n_{\text{clad}} \cong 1$ is applied into the strict dispersion equation (2.56) the pair of equations that are obtained are:

$$\frac{J'_n(u)}{uJ_n(u)} + \frac{K'_n(w)}{wK_n(w)} = \pm n \left(\frac{1}{u^2} + \frac{1}{w^2} \right) \quad (2.62)$$

where $n \geq 1$. This equation is rewritten by using the recurrence relation of Bessel functions (3.59a) and (3.59c) into

$$\frac{J_{n+1}(u)}{uJ_n(u)} = -\frac{K_{n+1}(w)}{wK_n(w)} \quad (2.63)$$

and

$$\frac{J_{n-1}(u)}{uJ_n(u)} = \frac{K_{n-1}(w)}{wK_n(w)} \quad (2.64)$$

where Eq. (2.63) is obtained from the plus sign of Eq. (2.61), and Eq. (2.64) is obtained from the negative sign of Eq. (2.62), respectively. The modes corresponding to the plus sign of Eq. (2.62) are called EH modes, while those corresponding to the negative sign are called HE modes.

Integer n is a mode order in the azimuthal ϕ direction and ℓ is a mode order in the radial direction ($\ell \geq 1$), respectively. More precisely, ℓ represents the ℓ^{th} solution of each dispersion equation. Moreover

$$m = \begin{cases} 1 & \text{TE and TM modes} \\ n + 1 & \text{EH mode} \\ n - 1 & \text{HE mode} \end{cases}$$

It is known from that the mode which has the same mode parameter m and n has the identical eigenvalue under the weakly guiding approximation. Of course, since they are not the strict modes, the eigenvalues are slightly different in the rigorous dispersion equations. Therefore LP modes are approximate modes classified by the

eigenvalues. Using these information one can draw the electric field vectors and intensity profiles of LP modes and conventional modes. For the weakly guiding approximation the optical power carried in the core and the cladding could be calculated by the following equations:

For TE and TM modes:

$$P_{core} = \frac{\pi}{2} \omega \mu_0 \beta |A|^2 \frac{r_{core}^4}{u^2} J_1^2(u) \left[1 + \frac{w^2}{u^2} \frac{K_0(w)K_2(w)}{K_1^2(w)} \right] \quad (2.65a)$$

$$P_{clad} = \frac{\pi}{2} \omega \mu_0 \beta |A|^2 \frac{r_{core}^4}{u^2} J_1^2(u) \left[\frac{K_0(w)K_2(w)}{K_1^2(w)} - 1 \right] \quad (2.65b)$$

and the total power is

$$P = P_{core} + P_{clad} = \frac{\pi}{2} \omega \mu_0 \beta |A|^2 \frac{r_{core}^4 v^2}{u^4} J_1^2(u) \frac{K_0(w)K_2(w)}{K_1^2(w)} \quad (2.66)$$

Therefore the ratios of the power confinement ratios to the total power in core and cladding are expressed as

$$\frac{P_{core}}{P} = 1 - \frac{u^2}{v^2} [1 - \xi_1(w)] \quad (2.67a)$$

$$\frac{P_{clad}}{P} = \frac{u^2}{v^2} [1 - \xi_1(w)] \quad (2.67b)$$

where

$$\xi_m(w) = \frac{K_m^2(w)}{K_{m-1}(w)K_{m+1}(w)} \quad (2.68)$$

The optical power of the EH mode is

$$P_{core} = \frac{\pi}{2} \omega \varepsilon_0 \beta n_{core}^2 |A|^2 \frac{r_{core}^4}{u^2} J_{n+1}^2(u) \left[1 + \frac{w^2}{u^2} \frac{1}{\xi_{n+1}(w)} \right] \quad (2.69a)$$

$$P_{clad} = \frac{\pi}{2} \omega \varepsilon_0 \beta n_{clad}^2 |A|^2 \frac{r_{core}^4}{u^2} J_{n+1}^2(u) \left[\frac{1}{\xi_{n+1}(w)} - 1 \right] \quad (2.69b)$$

and the total power is

$$P = P_{core} + P_{clad} = \frac{\pi}{2} \omega \varepsilon_0 \beta n_{core}^2 |A|^2 \frac{r_{core}^4}{u^4} J_{n+1}^2(u) \frac{v^2}{\xi_{n+1}(w)} \quad (2.70)$$

The ratios of the power confinement ratios to the total power in core and cladding are expressed as

$$\frac{P_{core}}{P} = 1 - \frac{u^2}{v^2} [1 - \xi_{n+1}(w)] \quad (2.71a)$$

$$\frac{P_{clad}}{P} = \frac{u^2}{v^2} [1 - \xi_{n+1}(w)] \quad (2.71b)$$

The optical power of the HE mode is

$$P_{core} = \frac{\pi}{2} \omega \varepsilon_0 \beta n_{core}^2 |A|^2 \frac{r_{core}^4}{u^2} J_{n-1}^2(u) \left[1 + \frac{w^2}{u^2} \frac{1}{\xi_{n-1}(w)} \right] \quad (2.72a)$$

$$P_{clad} = \frac{\pi}{2} \omega \varepsilon_0 \beta n_{clad}^2 |A|^2 \frac{r_{core}^4}{u^2} J_{n-1}^2(u) \left[\frac{1}{\xi_{n-1}(w)} - 1 \right] \quad (2.72b)$$

and the total power is

$$P = P_{core} + P_{clad} = \frac{\pi}{2} \omega \varepsilon_0 \beta n_{core}^2 |A|^2 \frac{r_{core}^4}{u^4} J_{n-1}^2(u) \frac{v^2}{\xi_{n-1}(w)} \quad (2.73)$$

The ratios of the power confinement ratios to the total power in core and cladding are expressed as

$$\frac{P_{core}}{P} = 1 - \frac{u^2}{v^2} [1 - \xi_{n-1}(w)] \quad (2.74a)$$

$$\frac{P_{clad}}{P} = \frac{u^2}{v^2} [1 - \xi_{n-1}(w)] \quad (2.74b)$$

Otherwise by using the parameter m

$$\frac{P_{core}}{P} = 1 - \frac{u^2}{v^2} [1 - \xi_m(w)] \quad (2.75a)$$

$$\frac{P_{clad}}{P} = \frac{u^2}{v^2} [1 - \xi_m(w)] \quad (2.75b)$$

Figure 2.11 shows the relation between the electric field vectors and intensity profiles for the LP modes and conventional modes of LP₀₁-(HE₁₁), LP_{11(even)}-(TM₀₁, HE_{21(even)}), LP_{11(odd)}-(TE₀₁, HE_{21(odd)}), LP_{21(even)}-(EH_{11(even)}, HE_{31(even)}) and LP_{21(odd)}-(EH_{11(odd)}, HE_{31(odd)}). [26]

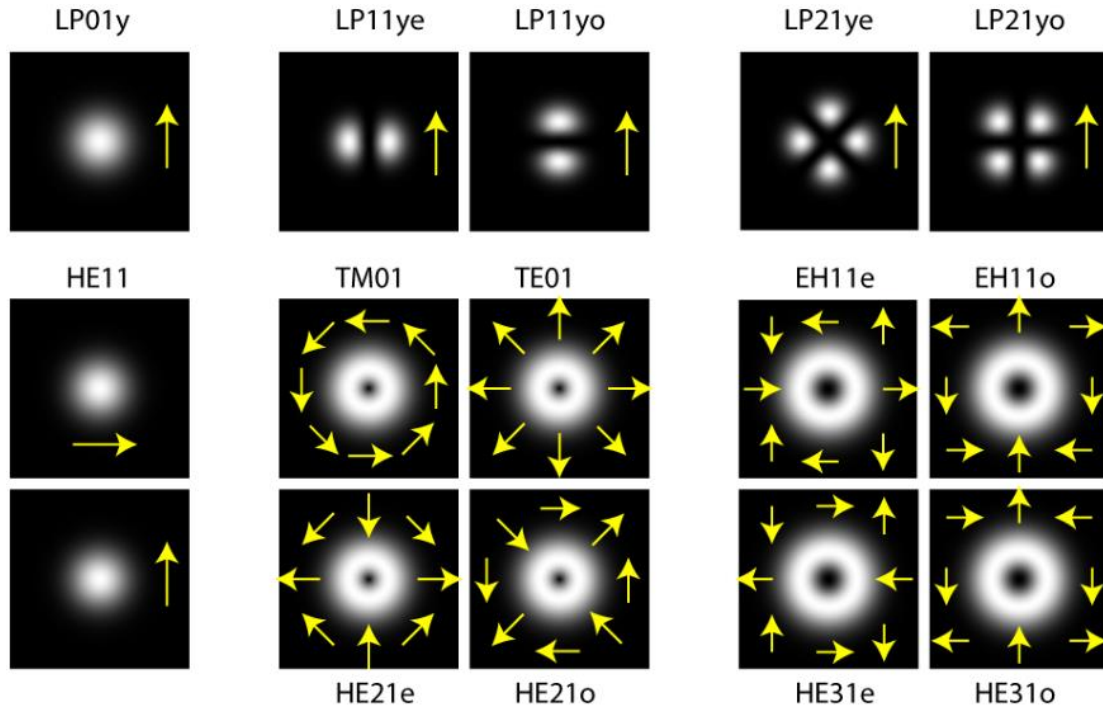


Fig. 2.11. (Top) LP and (Bottom) vector modes (HE, EH, TM, TE) used in this paper. Different angular orientations of degenerate modes, namely even and odd are labeled with 'e' and 'o' respectively. For the LP modes, only the vertical polarization is shown; the horizontal polarizations have the same intensity profiles. (This figure is taken from [26]).

2.3 Tapered optical fibers

Tapered optical fiber otherwise known as optical micro or nanofibers (MNF), have received great attention due to their unique guiding properties. In a standard optical fiber, the intensity of the evanescent wave field (EWF) is almost zero at the outer surface of the cladding. Thus, light propagating in these fibers is insensitive to the surroundings. With the tapered optical fiber, light can be guided along the tapered section as an electromagnetic wave [27], within the visible and near infrared spectral ranges. Due to the small waist diameter the amount of the penetration depth and intensity of the evanescent wave field can be significantly enhanced [28]. This makes them highly sensitive to the refractive index changes of the surrounding medium. The fabrication of a uniform waist and moreover taper transitions which characterized by low losses are the main requirements for a tapered optical fiber. Due to their extended evanescent modal fields tapered fibers are used to couple light to systems such as microresonators [29-36], to form microcavities themselves [37-42] or to be used at many different applications [43-51].

2.3.1 Fabrication and characteristics of tapered optical fibers

Many different processes have been reported in literature for the fabrication of tapered fibers, using flames [52, 53], focused CO₂ laser beams [54, 55], a micro furnace and an electronic arc formed between a pair of electrodes, such as a fusion splicer [56] or chemical etching using hydrofluoric acid [57]. The most common way for the fabrication of tapered fibers is by heating and stretching a section of standard

optical fiber in a flame. By this way the tapered fiber that is formed and presented in Figure 2.12, comprising a narrow stretched filament, namely the taper waist. Each end of the taper waist is linked to un-stretched fiber by a conical tapered section which is named taper transition.

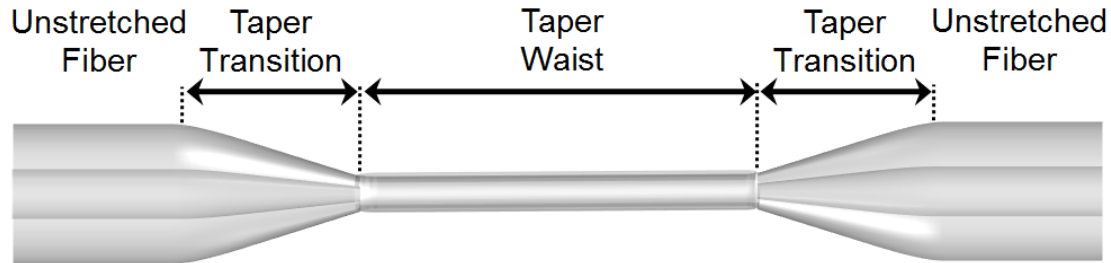


Fig.2.12. Design of a tapered fiber. Taper waist and taper transition regions are depicted in the figure.

Depending on the pulling conditions (pulling speed, length of the heated zone, pulling temperature, etc), one can fabricate tapers with different shapes and thus light transmission properties. When the optical fiber is tapered, the core – cladding interface is redefined in such a way that the light propagation inside the core penetrates to the cladding, which plays the role of the new core, and the external medium is the new cladding. Fiber tapers may be divided into two distinct categories: adiabatic and non-adiabatic.

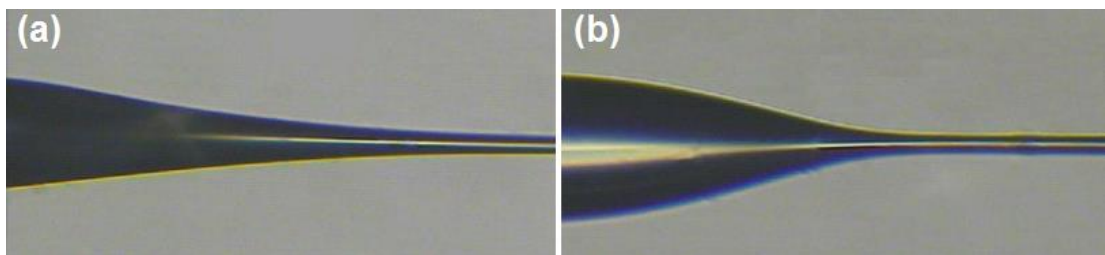


Fig. 2.13. (a) Adiabatic and (b) non-adiabatic tapered fibers. (This figure is taken from [47])

A single-mode tapered fiber can be considered adiabatic if the main portion of the power remains in the fundamental mode (LP_{01}) and does not couple to higher order modes as it propagates along the taper. To avoid coupling between the fundamental mode and higher order modes, the taper local length scale must be much larger than the coupling length between these two modes. In other words, the relative local change in the taper radius has to be very small (small taper angle), as shown in Figure 2.13a [58].

The non-adiabatic fiber tapers, presented in Figure 2.13b, can be made so that coupling occurs primarily between the fundamental mode of the un-stretched single-mode fiber and the first two modes of the taper waveguide (LP_{01} , LP_{02}), where, due to the large difference of the refractive index of air and glass, the taper normally supports more than one mode. The light propagates at the air–cladding interface of the taper’s waist region, in which case the single-mode fiber (SMF) is converted to multimode fiber (MMF). The result of back and forth coupling between the single mode of the fiber and the two (or more) modes of the taper is oscillations in the

spectral response of the taper, which means that the transmission is high for certain wavelengths and low for others (typically, transmission versus wavelength shows periodic behavior) [59].

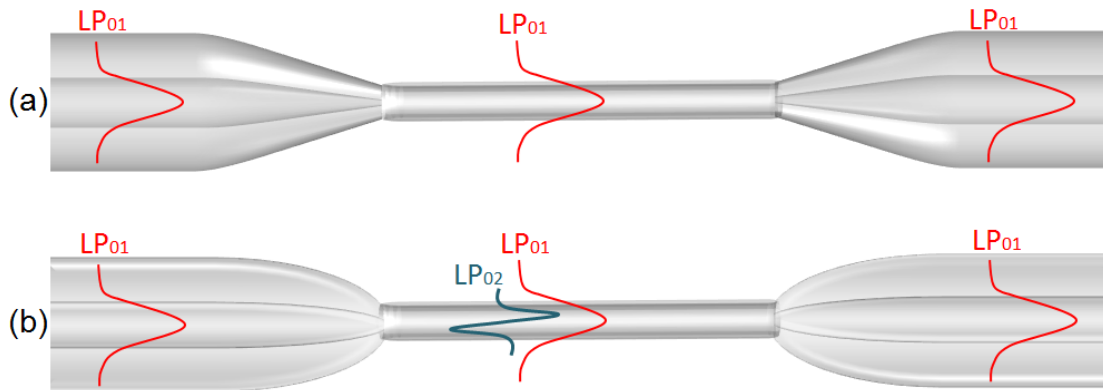


Fig. 2.14. Guiding modes in (a) adiabatic and (b) non-adiabatic tapers.

However, in order the transformation to be characterized by low losses of light from the fundamental mode, the shape of the taper transitions must be adiabatic. On the other hand, it is desirable for the transition to be as short as possible, allowing the resulting component to be compact and insensitive to environmental degradation. The theoretical shape of the shortest taper satisfying the adiabatic criterion for a particular fiber has been described by Love and Henry, and this was shown to be very much shorter than an equivalent sinusoidal taper [60]. There is, though, no indication of how such an optimal taper may be fabricated in practice. The shape of an optical fibertaper is of great importance and had been studied extensively, firstly by Birks and Li [58].

2.3.2 The shape of tapered optical fibers

According to the application, the shape of the taper fiber is significant. Below the theoretical description about the shape of the tapered optical fibers, based on Birks study, will be presented [58]. Figure 2.15 presents the terminology used to describe the shape of a tapered fiber. It is assumed that the taper is formed symmetrically, resulting identical taper transitions.

The radius of the un-tapered fiber is r_0 . The radius of the tapered region is r_w , while taper waist has length l_w . Both taper transitions have length z and a shape described by a decreasing local radius function $r(z)$, where z is a longitudinal coordinate. The starting point for z is considered to be at the beginning of the taper transition point V (left-hand transition in Fig. 2.15), hence $r(0) = r_0$, and $r(z_0) = r_w$. The taper extension x is the net distance through which the taper has been stretched and it is equal to the distance VY minus the distance VY before tapering commenced.

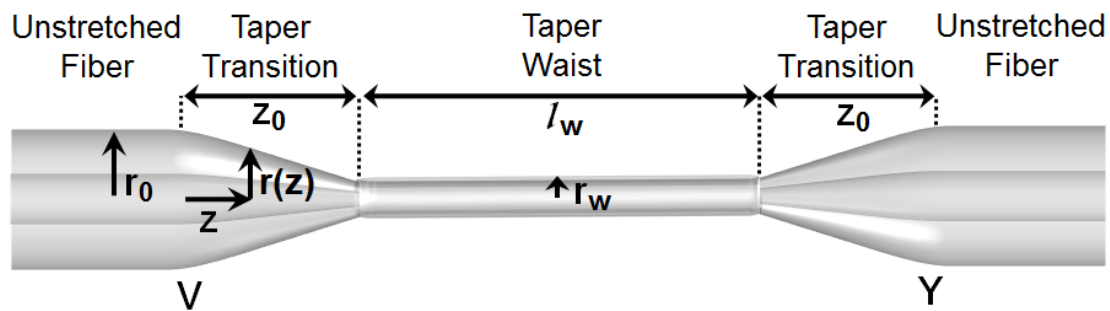


Fig.2.15. The design of a tapered fiber. The figure presents the terminology used in text.

Typically, the variation of x with time t is determined directly by the relative velocity of the two translation stages which pull the ends of the optical fiber apart, during the fabrication. All of these quantities can be apply either to the instantaneous states of the taper as it is being elongated or to the finished taper. The final extension when the taper is finished and elongation ceases is denoted by x_f .

Referring now to Figure 2.16a, at any time t during taper elongation, a symmetrically length L of the taper waist is uniformly heated (the “hot-zone” AB). Due to the heating, the AB part is a deformable cylinder of low viscosity glass. The particular temperature and viscosity values are unimportant, though the hot glass is assumed always to be soft enough to be stretched, while not being so soft that the taper sags under its own weight. Outside the hot-zone AB the glass is cold and solid. The ends of the taper are steadily pulled apart, so that at time $t+\delta t$ the hot glass cylinder stretches to form a narrower cylinder AB of length $L+\delta x$ (see Fig. 2.16b). The hot-zone length is changed to $L+\delta L$ in the same time, where δL may be negative. As the taper is elongated, the AA' and B'B sections of the stretched heated cylinder, leave the hot-zone and solidify, forming the taper transitions. The portion A'B' of the taper waist that is still within the hot-zone remains deformable and will be further stretched and narrowed.

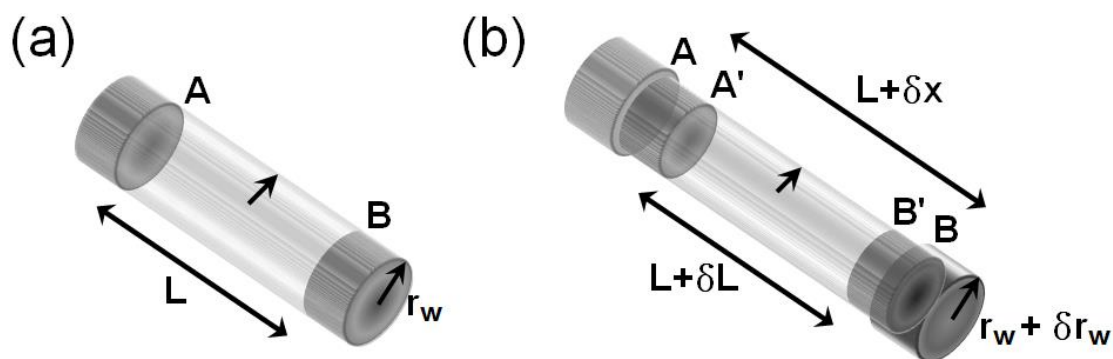


Fig. 2.16. Schematic diagrams of cylindrical tapers waist. (a) At time t the part AB of the taper waist is uniformly heated. (b) The same sample at time $(t+\delta t)$ where AB has been stretched through a distance δx to form a narrower cylindrical taper waist, while at the same time its part A'B' is still heated.

The length L is changed by the appropriate control of the heat source and may vary arbitrarily. However, herein, the variation of L depends on two constraints:

$$L \geq 0 \quad (2.76a)$$

$$\frac{\delta L}{\delta x} \leq 1 \quad (2.76b)$$

The Equation (2.76b) ensures that the heated section of glass is always cylindrical. The instantaneous length l_w , of the taper waist at time t is equal to the hot-zone length at that time so

$$l_w(t) = L(t) \quad (2.77)$$

The final waist length therefore equals to the final hot-zone length. The volume of the stretched glass cylinder AB at time $t+\delta t$ must equal the volume of the heated glass cylinder AB at time t

$$\pi(r_w + \delta r_w)2(L + \delta x) = \pi r_w^2 L \quad (2.78)$$

where δr_w is the change in the cylinder's radius and is negative. In the limit $\delta t \rightarrow 0$, this can be arranged to give a differential equation -the "volume law"- governing the variation of waist radius r_w with extension x

$$\frac{\delta r_w}{\delta x} = -\frac{r_w}{2L} \quad (2.79)$$

L may vary and may in general be regarded as being a function of x , since x is an increasing function of time t .

The second fundamental equation relates the instantaneous taper transition length z_0 , to the taper extension x . From Figure 2.17, comparing the total length VY of the tapered fiber with the initial distance VY at $t = 0$, we obtain the "distance law"

$$2z_0 + L = x + L_f \quad (2.80)$$

where L can be a function of x and L_0 at its initial value, at $x = 0$. According to the model, the local radius $r(z)$ at a general point z along the taper transition is equal to the waist radius $r_w(z)$ as that point was pulled out of the hot-zone. The extension $x(z)$ corresponding to this event is given by the distance law with $z_0 = z$

$$2z = x_0 + L_0 - L \quad (2.81)$$

where x in this expression is specifically the extension at which the point z was pulled out of the hot-zone. This is the generalized distance law. The solution $x(z)$ of this equation depends on how L varies with x . Thus the taper profile $r(z)$ can be determined by substituting this $x(z)$ into the $r_w(x)$ found from the volume law.

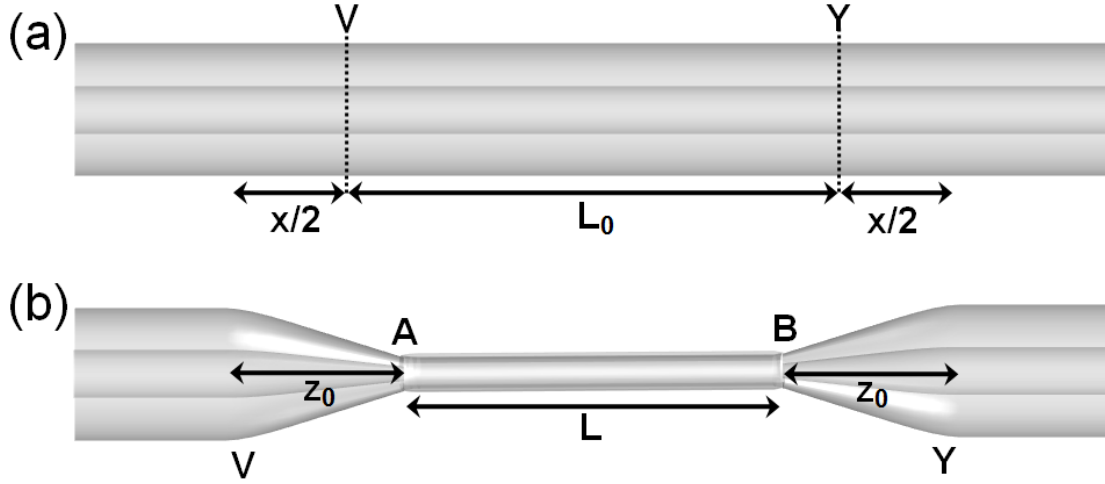


Fig. 2.17. (a) A fiber at time $t = 0$ at the start of tapering. A section VY of length L_0 , is heated. (b) The fiber at time t during tapering. V and Y are further separated by a distance x . The distance VY is also equal to $2x_f + L$.

These are the “forward problem,” in which the elongation conditions are specified and the resultant taper shape is to be found, and the “reverse problem,” in which a particular taper shape is specified and the conditions to produce it need to be found.

2.3.2a Determining the taper shape by the specified elongation conditions

$L(x)$ and x_f are given and l_w , r_w , z_o , and $r(z)$ are to be found. $L(x)$ must satisfy the conditions (2.76a-b). The length of the taper waist is given straight away from (2.77)

$$l_w = L(x_f) \quad (2.82)$$

The variation of the waist radius r_w with x is obtained by integrating the volume law (2.79), with the initial condition $r_w(0) = r_0$

$$\int_{r_0}^{r_w} \frac{dr'_w}{r'_w} = -\frac{1}{2} \int_0^x \frac{dx'}{L(x')} \quad (2.83)$$

giving the general expression

$$r_w(x) = r_0 \exp \left[-\frac{1}{2} \int_0^x \frac{dx'}{L(x')} \right] \quad (2.84)$$

Since $L(x)$ is known, $r_w(x)$ can be found, and the final waist radius is simply $r_w = r_w(x_f)$. The distance law (2.80) gives the taper transition length z as a function of x

$$z(x) = \frac{1}{2} [x + L_0 - L(x)] \quad (2.85)$$

The final transition length z_o is thus $z(x_f)$. To obtain $r(z)$ it is necessary to invert (2.85) to find $x(z)$. This may be achieved analytically or numerically, depending on the particular functional form of $L(x)$. The taper profile function is then found by substituting this $x(z)$ into (2.84) for $r_w(z)$

$$r(z)=r_w(x(z)) \quad (2.86)$$

By this way the complete taper shape has been found.

2.3.2b Determining the conditions in order to produce a specific taper shape

In this case, the desired taper shape (defined by l_w , r_w , z_o , and $r(z)$, where $r(0) = r_o$, and $r(z_o) = r_w$ is given, and $L(x)$ and x_f are required. The solution of this problem is less compact than the previous one. The volume law can be arranged to give

$$-\frac{2L}{r} = \frac{dx}{dr} \quad (2.87)$$

where dx/dr is unknown but, by differentiating the distance law (2.80), can be written as

$$\frac{dx}{dr} = 2 \frac{dz}{dr} + \frac{2L}{dr} \quad (2.88)$$

substitution into (2.87) gives a first-order linear differential equation for L as a function of r , with dz/dr a known function since $r(z)$ is given

$$\frac{2L}{dr} + \frac{2}{r}L + 2 \frac{dz}{dr} = 0 \quad (2.89)$$

With initial conditions $r = r_o$, and $L = L_o$ for $z = 0$, this equation integrates to

$$L(z) = \frac{r_o^2}{r^2(z)}L_o - \frac{2}{r^2(z)} \int_{r_o}^z r^2 \frac{dz}{dr} = 0 \quad (2.90)$$

where $L(z)$ is the hot-zone length as point z was pulled out of the hot-zone. L_o is as yet unknown, but can be determined by evaluating (2.90) at $z = z_o$, since $L(z_o) = l_w$ is given. Hence (2.90) becomes

$$L(z) = \frac{r_w^2}{r^2(z)}l_w - \frac{2}{r^2(z)} \int_z^{z_o} r^2 (z') dz' \quad (2.91)$$

$L(z)$ is now completely known, and so the distance law (2.80) gives x as a known function of z

$$x(z) = 2z + L(z) - L_o \quad (2.92)$$

This function is inverted to give $z(x)$. Again, this may be done analytically or numerically, depending on the functional form of $r(z)$. $L(x)$ then follows from the distance law again

$$L(x) = x + L_o - 2z(x) \quad (2.93)$$

Finally, x_o is found from the distance law with $z = z_o$

$$x_f = 2 z_o + l_w - L_0 \quad (2.94)$$

Equations (2.93) and (2.94), solved using $z(x)$ found from (2.92) and $L(z)$ from (2.91), constitute the complete solution of the problem.

2.3.3 Penetration depth of evanescent field at tapered fibers

As it is known, light in the fiber propagates in total internal reflection way and extend to the cladding region. Maxwell equation defines the wave extending to the cladding region as standing wave, namely the evanescent wave [7]. The penetration depth is a fraction of the wavelength if the incident light is perpendicular to the interface and can be extended to several wavelengths if the incident angle is at the critical angle [28, 61]. The penetration depth along a plane refractive index discontinuity d_p is given by:

$$d_p = \frac{\lambda}{2\pi \sqrt{(n_{core}^2 \sin^2 \theta - n_{clad}^2)}} \quad (2.95)$$

where λ is the wavelength of incident light, n_{core} the refractive index of core and n_{clad} the refractive index of the cladding region and θ the incident angle measured from the normal at the interface of the core and cladding.

In the case of single mode tapered fibers that the radius of the taper waist is of the order of 1 - 1.5 μ m, the core of the fibers at the taper waist is considered to be collapsed, and the light is propagating through the cladding [60]. Thus, the power fraction of the evanescent wave into the surrounding region increases [62, 63]. The penetration depth then is given by:

$$d_{p(taper)} = \frac{\lambda}{2\pi \sqrt{(n_{clad}^2 \sin^2 \theta_{int} - n_{medium}^2)}} \quad (2.96)$$

and it depends on the refractive index of the surrounding medium (n_{medium}) and the incident angle (θ_{int}) [28].

2.4 Fabry-Perot interferometers

The Fabry-Perot interferometer (FPI) was invented by the physicists Charles Fabry and Alfred Perot in 1899 [64]. These optical resonators are usually consist of two (single FP cavity), or, more parallel mirrors (multilayer FP cavities), facilitating multiple light interference via multiple back and forward reflections. These interferometers were usually used in absorption spectroscopy, optical spectrum analyzers, laser cavities etc. During late 80s, fiber optic sensors based on Fabry-Perot interferometers have been introduced. After that time, numerous optical fiber sensors

have been proposed [65-78], as they are simple in fabrication and interrogation, versatile in terms of spectral design, and immune to environmental noise. Since the theory for the Fabry-Perot interferometers has been extensively studied and published in literature [79], below will be presented basic parameters of the Fabry-Perot interferometers.

2.4.1 Principle of Fabry-Perot interferometers

A Fabry-Perot interferometer, or etalon, can be considered as the simplest type of optical resonator [79]. In its simplest configuration consists of two parallel dielectric reflection surfaces of refractive index n_1 and separated by a medium of thickness d and refractive index n_2 .

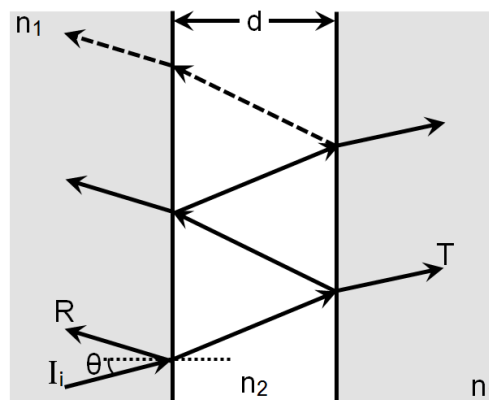


Fig. 2.18. Fabry-Perot cavity consisting of two parallel dielectric reflection surfaces separated with distance d .

The intensity of reflected electromagnetic radiation at the boundary between two dielectric media is given by the reflectance

$$R = \frac{(n_2 - n_1)^2}{(n_2 + n_1)^2} \quad (2.97)$$

while the transmittance is given by

$$T = \frac{4n_1n_2}{(n_1 + n_2)^2} \quad (2.98)$$

If the incident intensity is taken as unity and the fraction of the incident intensity that is reflected is

$$|r|^2 = \frac{4R\sin^2\varphi}{(1-R)^2 + 4R\sin^2\varphi} \quad (2.99)$$

while the transmitted fraction is

$$|t|^2 = \frac{(1-R)^2}{(1-R)^2 + 4R\sin^2\varphi} \quad (2.100)$$

Moreover, both transmittance and reflectance are periodic functions of φ with a period

of π , where φ equals to

$$\varphi = \frac{2\pi}{\lambda} n d \cos\theta \quad (2.101)$$

where n is the refractive index of the medium, d is the thickness of the medium and θ is the incident ray angle to the medium.

Figure 2.19 presents the interference spectra of Fabry-Perot cavities with different finesse (that will be defined later in section 2.4.3)

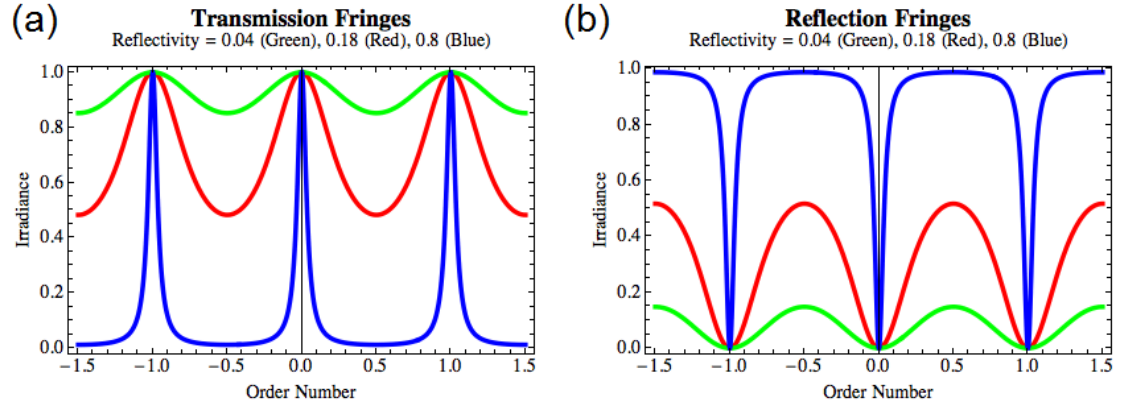


Fig. 2.19. The (a) transmission and (b) reflection of a Fabry-Perot interferometer, as a function of wavelength. A high-finesse etalon (blue curve) shows sharper peaks and lower transmission minima than a low-finesse etalon (green curve). [80]

The difference in wavelength between consecutive interference fringes is defined as the free spectral range (FSR) of a Fabry-Perot interferometer and is given as

$$FSR = \Delta\lambda = \frac{\lambda_1 \lambda_2}{2nd} \quad (2.102)$$

where λ_1 and λ_2 are the wavelengths where the two interference fringes appear their maxima (or minima points at reflection spectrum), n is the refractive index of the medium and d is the thickness of the cavity [81]. It is denoted in Figure 2.19 as $\Delta\lambda$.

Finesse is a factor given to quantify the performance of a Fabry-Perot interferometer and can be thought as the number of interfering beams within the Fabry-Perot cavity [79, 82].

$$\mathcal{F} = \frac{\pi\sqrt{R}}{1-R} = \frac{FSR}{\delta\lambda} \quad (2.103)$$

A higher finesse value, indicating a greater number of interfering beams, results in a more complete interference process and therefore higher resolution measurements. In Figure 2.19 are presented the spectra of two Fabry-Perot cavities with different finesse and the $\delta\lambda$ is denoted within the Figure.

One can also use a quality factor which is defined as the central wavelength of the resonance divided by the full width at half maximum [83].

$$Q = \frac{\lambda}{\delta\lambda} \quad (2.104)$$

This quality factor shows the energy stored in the cavity per the energy dissipated per radian.

2.5 Whispering-gallery modes resonators

Beyond the conventional Fabry-Perot resonators, also microcavities supporting whispering-gallery modes (WGMs) have attracted the interest since they provide a high level of light localization along a closed optical path, thus, sensitivity to opto-geometric properties of the supporting cavities. Usually WGM resonance is achieved in circular symmetry cavities such as microspheres, toroids, ring resonators and cylindrical beams. The first who studied WGM resonance was Lord Rayleigh who studied the propagation of sound over a curved gallery surface [84, 85], while Debye derived equations for the resonant eigenfrequencies of free dielectric and metallic spheres. The first observations of WGMs in optics can be attributed to solid state WGM lasers. Laser action was studied in Sm:CaF₂ crystalline resonators [86]. The size of the resonators was in the millimeter range. One of the simplest geometries of WGM resonators is a ring, where light is guided and circulated into this confined high index closed loop waveguide. Below the basic theory of WGM ring resonators will be presented based on the analysis of [87].

2.5.1 Light propagation in single ring WGM resonator

The simplest configuration that one can study in case of ring resonators is that consisting of a single ring waveguide resonator (green colour) with radius r and a bus waveguide (blue colour) which will be used to couple the light to the resonator in a unidirectional coupling way. This basic configuration is presented in Figure 2.20.

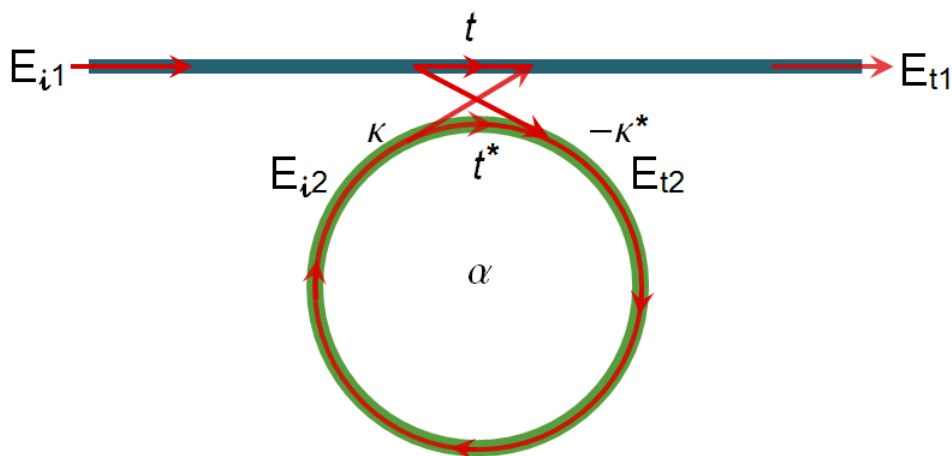


Fig. 2.20. Model of a single ring resonator coupled with one waveguide. (Based on [87])

In order to simplify the problem and ensure that a single unidirectional mode of the resonator is excited, one has to make some assumptions. Firstly, it is considered that the coupling is lossless. Another assumption is that a single polarization is used

and none of the waveguide segments or coupler elements couple light of different polarization to the resonator. Finally, if the various kinds of losses occurring along the propagation of light in the ring resonator are incorporated in the attenuation constant, then the interaction can be described by the matrix relation:

$$\begin{pmatrix} E_{t1} \\ E_{t2} \end{pmatrix} = \begin{pmatrix} t & \kappa \\ -\kappa^* & t^* \end{pmatrix} \begin{pmatrix} E_{i1} \\ E_{i2} \end{pmatrix} \quad (2.105)$$

The complex mode amplitudes E are normalized and their squared magnitude corresponds to the modal power. The coupler parameters t and κ depend on the specific coupling mechanism between the bus and ring waveguide. The star symbol ($*$) denotes the conjugated complex value of t and κ , respectively.

The matrix is symmetric because the networks under consideration are reciprocal. Therefore

$$|\kappa^2| + |t^2| = 1 \quad (2.106)$$

In order to further simplify the model, the input E_{i1} is chosen to be equal to 1. Then the round trip in the ring is given by

$$E_{i2} = \alpha \cdot e^{i\varphi} E_{t2} \quad (2.107)$$

where α is the loss coefficient of the ring. Loss factor α includes all the corresponding loss mechanisms related to scattering, optical absorption and curvature. For zero losses $\alpha = 1$. Moreover $\varphi = \omega L/c$ where L being the circumference of the ring which is given by $L = 2\pi r$, c is the phase velocity of the ring mode ($c = c_0/n_{\text{eff}}$) and the fixed angular frequency $\omega = kc_0$, with c_0 equals to the vacuum speed of light. As it was already mentioned r is the radius of the ring measured from the center of the ring.

From Equations (2.105) and (2.107) one can obtain that

$$E_{t1} = \frac{-\alpha + t \cdot e^{-i\varphi}}{-\alpha t^* + e^{-i\varphi}} \quad (2.108)$$

$$E_{i2} = \frac{-\alpha \kappa^*}{-\alpha t^* + e^{-i\varphi}} \quad (2.109)$$

$$E_{t2} = \frac{-\kappa^*}{1 - \alpha t^* \cdot e^{-i\varphi}} \quad (2.110)$$

The propagation constant β equals to

$$\beta = kn_{\text{eff}} = \frac{2\pi n_{\text{eff}}}{\lambda} \quad (2.111)$$

where k is the vacuum wavenumber ($k = 2\pi/\lambda$) and n_{eff} is the effective refractive index. By this way

$$\varphi = \frac{\omega L}{c} = \frac{kc_0 L}{c} = k2\pi r n_{eff} = \frac{2\pi}{\lambda} 2\pi r n_{eff} = 4\pi^2 n_{eff} \frac{r}{\lambda} \quad (2.112)$$

By this way, the transmittance is given by the formula [88, 89]

$$T = \frac{\alpha^2 + r^2 - 2\alpha r \cos\varphi}{1 - r^2 \alpha^2 - 2\alpha r \cos\varphi} \quad (2.113)$$

Using the Equation (2.108), the transmission power P_{t1} for the output of the waveguide equals to

$$P_{t1} = |E_{t1}|^2 = \frac{\alpha^2 + |t|^2 - 2\alpha |t| \cos(\varphi + \varphi_{coupler})}{1 + \alpha^2 |t|^2 - 2\alpha |t| \cos(\varphi + \varphi_{coupler})} \quad (2.114)$$

where $t = |t| \exp(i\varphi_{coupler})$, with $|t|$ representing the coupling losses and $\varphi_{coupler}$ the phase of the coupler.

The circulating power P_{i2} in the ring is given by

$$P_{i2} = |E_{i2}|^2 = \frac{\alpha^2 (1 - |t|^2)}{1 + \alpha^2 |t|^2 - 2\alpha |t| \cos(\varphi + \varphi_{coupler})} \quad (2.115)$$

On resonance $(\varphi + \varphi_{coupler}) = 2\pi m$, where m is an integer, it follows that

$$P_{t1} = |E_{t1}|^2 = \frac{(\alpha - |t|)^2}{(1 - \alpha |t|)^2} \quad (2.116)$$

$$P_{i2} = |E_{i2}|^2 = \frac{\alpha^2 (1 - |t|^2)}{(1 - \alpha |t|)^2} \quad (2.117)$$

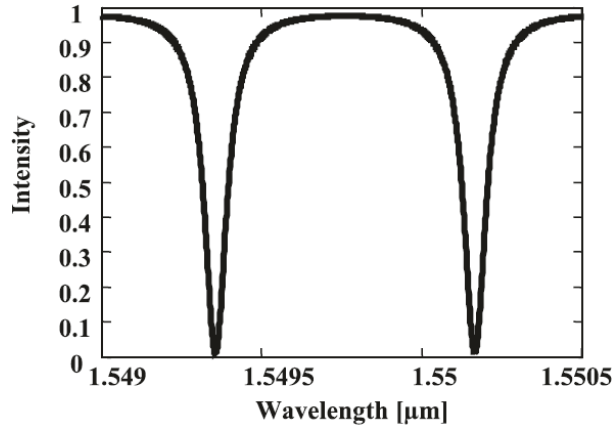


Fig. 2.21. Characteristic spectrum of a single ring resonator. [87]

In Figure 2.21 the interference spectrum of a single ring resonator is presented in the blue curve.

When the internal losses equal to the coupling losses ($\alpha = |t|$) then the transmission power becomes zero. This is known as critical coupling condition where destructive interference takes place, and transmission minima extinction ratio

maximizes.

The difference in wavelength between consecutive interference fringes in the WGM resonators is given as

$$FSR = \Delta\lambda = \frac{\lambda_1\lambda_2}{2\pi r n_{eff}} \quad (2.118)$$

where λ_1 and λ_2 are the wavelengths where the two fringes appear, r is the radius of the ring resonator, n_{eff} is the effective refractive index [87].

Finesse in WGM resonators is defined as the ratio of the FSR and the width of a resonance for a specific wavelength

$$\mathcal{F} = \frac{FSR}{FWHM} = \frac{\Delta\lambda}{\delta\lambda} \quad (2.119)$$

The quality factor Q of a resonance is a measure of the sharpness of the resonance. It is defined as the ratio of the operation wavelength and the resonance width

$$Q = \frac{\lambda}{\delta\lambda} = \frac{n_{eff}L}{\lambda} \mathcal{F} \quad (2.120)$$

This quality factor can also be regarded as the stored energy divided by the power lost per optical cycle.

2.5.2 Light propagation in parallel coupled double ring WGM resonators

A configuration of parallel coupled double ring resonators is presented in Figure 2.21. In this case, both rings are coupled to the waveguide, while the rings are usually separated by a distance D . In case of double ring resonators all the resonators must be resonant at a common wavelength, namely, exhibit the same opto-geometrical characteristics. The resonators are indirectly coupled to each other by the optical path length along the waveguide that interconnects them, and through their coupling between evanescent waves of the two rings. Multiple peaks, or ripples in the optical spectrum indicated nonaligned resonant frequencies. An example of the interference spectrum in transmission mode of parallel coupled double ring resonators is presented in Figure 2.21 (red curve).

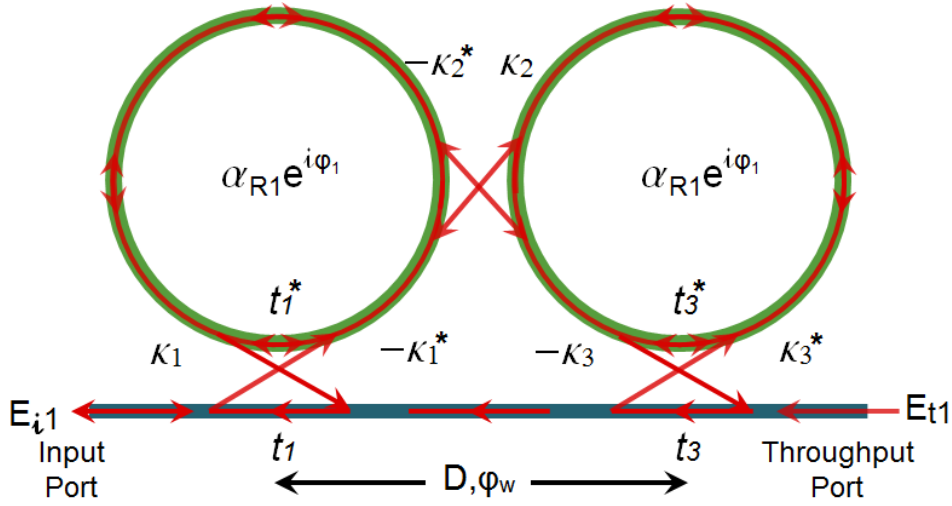


Fig. 2.22. Model of parallel coupled double ring resonators with one waveguide. (Based on [87])

In Figure 2.22, φ_w denoted is the phase shift introduced by the segment of length D with effective refractive index n_{weff} of the waveguide joining both ring resonators. α_{R1} and α_{R2} represent the round trip loss coefficients of the first and second ring resonator respectively.

A simplified expression for the reflectivity at port E_{i1} is obtained for the lossless case and symmetric coupled coefficients between the ring resonator and the waveguide ($\kappa = \kappa_1 = \kappa_3$).

$$R_{i1} = |E_{i1R}|^2 = \frac{4 \left(\frac{\kappa_2 \kappa^2}{2t} \right)^2 \left(\cos \varphi - \frac{t_2(1+t^2)}{2t} \right)^2}{\left[\left(\cos \varphi - \frac{t_2(1+t^2)}{2t} \right)^2 + \left(\frac{\kappa_2 \kappa^2}{2t} \right)^2 \right]^2} \quad (2.121)$$

The phase factor for the distance D between the rings does not appear directly and therefore does not have an influence on the transfer characteristic, except a mismatching phase for achieving maximum coupling. Different reflectivity profiles can be realized using appropriate coupling coefficients. Weakly coupled ring resonators lead to single reflection peaks in the reflectivity function where the height of the peak depend on the value of the coupling coefficients. In order to realize a maximally flat response with a single peak, the coupling coefficients have to obey the following equation:

$$\kappa_2 = \frac{\kappa^2}{\sqrt{2}(1+t^2+t\sqrt{2})} \quad (2.122)$$

The reflectivity at port E_{i1} incorporating loss parameter α is given by

$$R_{i1(\text{loss})} = |E_{i1R(\text{loss})}|^2 = \frac{\left(\frac{\kappa_2 \kappa^2 (\alpha^2 + 1)}{2\alpha t} \right)^2 \left(\cos \varphi - \frac{t_2(1+t^2)}{2t} \right)^2}{\left[\left(\cos \varphi - \frac{t_2(1+\alpha^2 t^2)}{2\alpha t} \right)^2 + \left(\frac{\kappa_2(1-\alpha^2 t^2)}{2\alpha t} \right)^2 \right]^2}$$

$$\times \left[\left(\cos\varphi - \frac{t_2(1+\alpha^2 t^2)}{2\alpha t} + \frac{t_2}{2\alpha t} \frac{(1-\alpha^2)(1-\alpha^2 t^2)}{1+\alpha^2} \right)^2 + \left(\frac{1-\alpha^2}{1+\alpha^2} \right) \sin^2\varphi \right] \quad (2.123)$$

2.6 Multi-photon Polymerization Technique

Although two-photon absorption was originally predicted by Maria Göppert-Mayer in 1931 in her doctoral dissertation, the first experimental verification came thirty years later by Isaac Abella, after the invention of the laser [90]. Initially, this principle found limited application, for example as a spectroscopic tool, due to the extremely small two-photon absorption cross-section of most materials. In 1965, two-photon polymerization was experimentally reported for the first time by Pao and Rentzepis, as the first example of multi-photon excitation-induced photochemical reactions. After that work, no particular efforts were devoted to two photon photopolymerization until this technology found value as a micro-fabrication tool with the use of femtosecond lasers.

Today, direct laser writing by multi-photon polymerization technique is used for the fabrication of micron optical components [91], photonic crystals [92] and many complicated 3D patterning for biological and medical applications [93, 94]. As substrates one can use common microscope slides or cover-glasses, Si wafers and optical fibers.

Due to the fact that Multi-photon polymerization technique is a well-known technology nowadays with many references in literature [90, 95], the basic theory will be presented below.

2.6.1 Sequential and simultaneous two-photon absorption (TPA)

Two-photon absorption (TPA) is a popular multiple-photon excitation approach to the initiation of photo-chemical changes. There are two different mechanisms of TPA: sequential and simultaneous two-photon excitation [90, 95, 96]. The sequential excitation involves the excitation of the absorbing species to a real intermediate state (S_1) (see Figure 2.23b). This first excited state becomes populated by the first absorbed photon and has a well-defined lifetime, typically 10^{-4} to 10^{-9} seconds. Then a second photon is absorbed, as illustrated in Figure 2.23(b). The other mechanism is shown in Figure 2.23(c). In this case there is no real intermediate state, but a virtual intermediate state is created by the interaction of the absorbing species with the first photon. Only if the second photon arrives within the virtual state lifetime, about 10^{-15} seconds, it can be absorbed. Therefore, in the second case higher intensities are required.

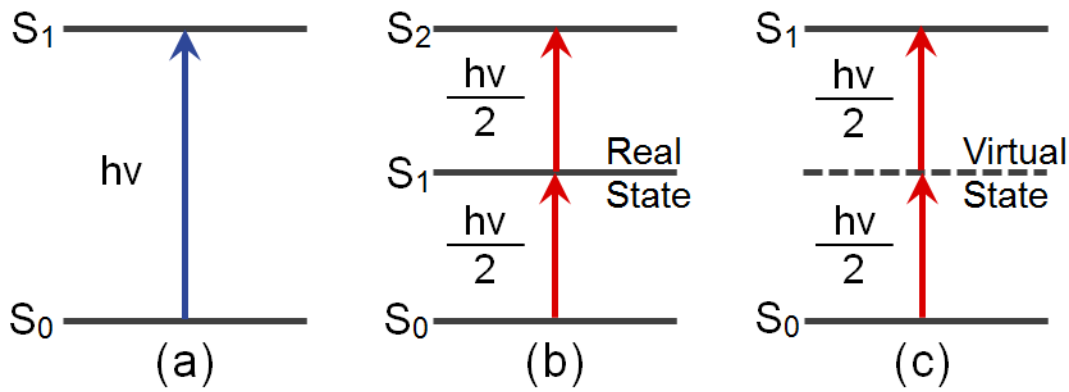


Fig.2.23. (a) Single-photon excitation, (b) Two-photon sequential excitation and (c) Two-photon simultaneous excitation.

In case of single-photon absorption (see Figure 2.23a), the absorbing species is raised from the ground state (S_0) to an excited state (S_1) when it absorbs the energy of the single-photon, which is equal to $h\nu = E_1 - E_0$, where h is Planck's constant and ν the frequency of the incident light, while E_0 and E_1 are the energy levels ($E_0 < E_1$) of the absorbing species.

In the case of TPA, two photons, each with half energy of the gap between the two energy levels, namely $h\nu/2$, induce the electron transition. Ti: sapphire lasers are widely used for the inducing TPA because they produce ultrahigh peak power with a very short pulse width of approximately 100 femtoseconds (fs) or less. Furthermore, these lasers are very useful for TPP because of their central wavelength of approximately 800nm, which is close to half of the wavelength of the polymerization. This enables easy control of the polymerization threshold energy.

2.6.2 Cross-section in the focused spot for single and multi-photon absorption

When a laser beam is closely focused with a high NA objective lens into a volume of photo-curable resin, as shown in Figure 2.24a, photon-density-profiles are formed, with a constant total number of photons at every cross-section in the focused spot.

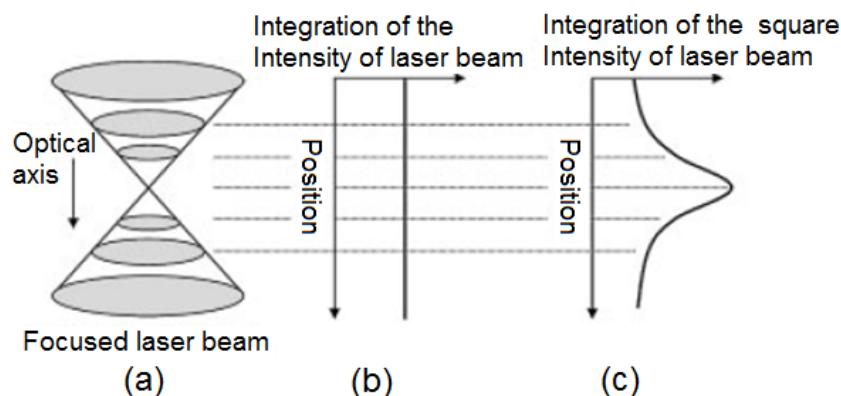


Fig. 2.24. Comparison of TPA with single photon absorption generated by a tightly focused laser beam: (a) schematic diagram of focused laser beam; (b) total single photon absorption per transverse plane; (c) total two photon absorption per transverse plane, which is calculated by integrating the square intensity over the plane with respect to the optical axis. (Taken from [97])

The constant number of photons at every cross-section precludes optical sectioning by exploiting the linear response of materials to the light intensity based on the single photon absorption (see Fig. 2.24b). However, if the material response is proportional to the square of the photon density, the integrated material response is greatly enhanced at the focal point, as illustrated in Figure 2.24c. The two photon transition rate is extremely small in general, so a very high spatial resolution can be obtained.

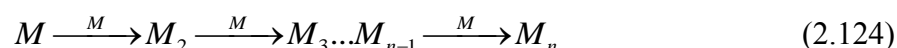
2.6.3 Description of polymerization based on radical initiators

Photopolymerization is one of the most important types of photochemical reaction that have been used for laser fabrication. This is because the material resins undergo a significant phase transition after laser irradiation, from liquid to solid, and non-polymerized liquid is easily removed by a developing process so that the solidified 3D structures stand out. The basic components of the starting liquid material are monomers and oligomers. Upon light excitation, the monomers or oligomers may be solidified by two means: polymerization and crosslinking [96].

An important difference of these two kinds of reaction lies in their quantum yield, which is defined as the ratio of number of polymerized monomer units to the number

In the case of photo-crosslinking, addition of each monomer unit requires absorption of a photon, leading to a quantum yield less than one.

In contrast, photo-polymerization is realized via chain reactions as shown in equation (2.124), so the quantum yield can reach several thousands.



Here M is the monomer or oligomer unit, and M_n , the macromolecule containing n monomer units. The quantum yield of general monomers and oligomers is low. In order to increase the initiating efficiency, one or several low-weight molecules that are more sensitive to light irradiation are added. They form initiating species of radicals or cautions by absorbing photons. Such small molecules are called photo-initiators:



where I denote the photo-initiator, $R \cdot$ the free radicals and I^* an intermediate state of the photo-initiator after absorbing the photons. Therefore the polymerization process is more precisely described by the following equation:



The photo-produced radicals react with monomers or oligomers, producing monomer radicals, which combine with new monomers, and so on; so the monomer radicals expand in chain reaction, until two radicals meet with each other. This chain propagation stops in either of the following channels:

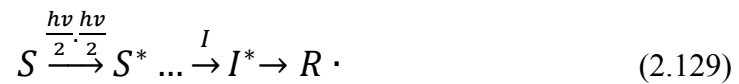


Therefore the polymerization process consists of three steps: (I) photo-initiation, (ii) chain propagation, and (iii) termination.

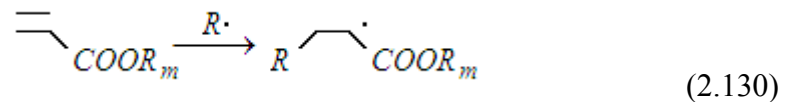
A good photo-initiator should be easily reduced to an initiating species upon light irradiation, and provide photo-produced radicals or cautions active enough to react with monomers or oligomers.

The nonlinear response of photo-polymerization is caused by highly reactive oxygen molecules absorbed by resin. Oxygen molecules inhibit polymerization reaction at the beginning of polymerization, because oxygen molecules scavenge the radicals that generate the polymerization reaction. Accordingly, when the intensity of light is adequately low polymerization reaction does not propagate, because almost all the photons are consumed by the oxygen molecules.

A photo-sensitizer is a molecule that absorbs light and then transfers the energy to a photo-initiator. With such a scheme, the photo-initiation process is expressed as



where S is the photo-sensitizer. A co-initiator itself does not absorb light, but it is involved in the production of radical species. Reactions that are typically used for laser fabrication are double-bond addition of acrylates (radical-type)



For a radical type initiator, benzoyl is the most widely used chromophore, which must have the initiator, since it exhibits good absorption in the UV region.

After polymerization, the oligomer constitutes the backbone of the polymer network. The physical, chemical and mechanical properties of the solidified resin in strictly depend on the nature and structure of the oligomer. Oligomers generally contain at least two reactive groups, from which both cross-linking and polymerization could occur.

Monomers have a much smaller molecular weight and consist of one or several reactive groups. They polymerize similarly to oligomers and are an important factor in determining the efficiency of polymerization. In addition, monomers are also useful for diluting resins so that the polymer is easier to handle for a particular use.

For 3D micro-nanolithography, a suitable viscosity is of particular importance due to the opposite requirements in different steps of processing: a high viscosity is needed for keeping early produced volumes where they are created; while a low viscosity facilitates removal of unsolidified resin from intervals. For a successful fabrication the following behaviors are preferred: i) high polymerization efficiency

upon light irradiation, (ii) lower shrinkage after polymerization, (iii) fast reaction time and low dark polymerization.

2.7 Summary

In this chapter, the theoretical background and the basic principles of the materials and techniques that are required for the experimental processes were presented and discussed. The categories of the optical fibers, their characteristics and the propagation of light in them as electromagnetic wave were presented. Moreover, two different kinds of resonators were presented, those of Fabry-Perot interferometers and Whispering Gallery Mode resonators. Finally, the basic principles of the multi-photon polymerization technique were discussed.

References

- [1] <http://onlinelibrary.wiley.com/doi/10.1002/andp.19103370802/abstract>.
- [2] J. Hecht, *City of Light: The Story of Fiber Optics*. New York: Oxford University Press, 1999.
- [3] "<http://onlinelibrary.wiley.com/doi/10.1002/andp.19103370802/abstract>."
- [4] H. H. Hopkins and N. S. Kapany, "A Flexible Fibrescope, using Static Scanning," *Nature*, vol. 173, p. 39, 01/02/online 1954.
- [5] D. Payne and W. A. Gambling, "New silica-based low-loss optical fibre," *Electronics Letters*, vol. 10, pp. 289-290, 1974.
- [6] "http://digital-library.theiet.org/content/journals/10.1049/el_19870719."
- [7] K. Okamoto, "Wave Theory of Optical Waveguides," in *Fundamentals of Optical Waveguides (Second Edition)*, ed Burlington: Academic Press, 2006.
- [8] G. P. Agrawal, "Chapter 1 - Introduction," in *Nonlinear Fiber Optics (Fourth Edition)*, ed San Diego: Academic Press, 2006, pp. 1-24.
- [9] J. M. Senior, *Optical Fiber Communications Principles and Practice*: Prentice Hall, 2009.
- [10] H. Elen, "Optical Loss," in *The Measurement, Instrumentation and Sensors Handbook*, J. G. Webster, Ed., ed: CRC Press LLC, 1999.
- [11] M. Johnson, *Handbook - Optical Fibres, Cables and Systems*: ITU, 2009.
- [12] U. L. Österberg, "Chapter 1 - Optical Fiber, Cable, and Connectors," in *Handbook of Fiber Optic Data Communication (Second Edition)*, ed San Diego: Academic Press, 2002, pp. 3-40.
- [13] "SMF-28e Fiber product information. URL: <http://www.princetel.com/datasheets/SMF28e.pdf>."
- [14] M. J. Adams, *An Introduction to Optical Waveguides*. New York: Wiley, 1981.
- [15] H. J. R. Dutton, *Understanding Optical Communications*: International Business Machines Corporation, 1998.
- [16] J. Ballato and P. Dragic, "Materials Development for Next Generation Optical Fiber," *Materials*, vol. 7, p. 4411, 2014.
- [17] R. Zhang, "Propagation of ultrashort light pulses in tapered fibers and photonic crystal fibers," Doctor of Philosophy PhD Thesis, Mathematisch-

Naturwissenschaftlichen Fakultät, Rheinischen Friedrich-Wilhelms-Universität Bonn, Bonn, Germany, 2006.

- [18] A. D. Yablon, *Optical Fiber Fusion Splicing*: Springer, 2005.
- [19] D. Marcuse, "Loss analysis of single-mode fiber splices," *The Bell System Technical Journal*, vol. 56, pp. 703-718, 1977.
- [20] "<http://users.otenet.gr/~mlazos/opticalfiber.htm>."
- [21] G. P. Agrawal, "Chapter 2 - Pulse Propagation in Fibers," in *Nonlinear Fiber Optics (Fourth Edition)*, ed San Diego: Academic Press, 2006, pp. 25-50.
- [22] A. S. Julius., *Electromagnetic Theory*. New York: Mcgraw Hill Book Company, 1941.
- [23] D. Gloge, "Weakly Guiding Fibers," *Applied Optics*, vol. 10, pp. 2252-2258, 1971/10/01 1971.
- [24] A. W. Snyder, "Asymptotic Expressions for Eigenfunctions and Eigenvalues of a Dielectric or Optical Waveguide," *IEEE Transactions on Microwave Theory and Techniques*, vol. 17, pp. 1130-1138, 1969.
- [25] K. Thyagarajan, A. K. Ghatak, and A. Sharma, "Vector modes of an optical fiber in the weakly guiding approximation," *Journal of Lightwave Technology*, vol. 7, pp. 51-54, 1989.
- [26] F. K. Fatemi and G. Beadie, "Rapid complex mode decomposition of vector beams by common path interferometry," *Optics Express*, vol. 21, pp. 32291-32305, 2013/12/30 2013.
- [27] X. Jin, "Optical Fiber Index Taper—Theoretical Analysis and Experiment Demonstration," *International Journal of Infrared and Millimeter Waves*, vol. 19, pp. 875-886, 1998/06/01 1998.
- [28] M. Ahmad and L. L. Hench, "Effect of taper geometries and launch angle on evanescent wave penetration depth in optical fibers," *Biosensors and Bioelectronics*, vol. 20, pp. 1312-1319, 2005/01/15/ 2005.
- [29] K. Milenko, I. Konidakis, and S. Pissadakis, "Silver iodide phosphate glass microsphere resonator integrated on an optical fiber taper," *Optics Letters*, vol. 41, pp. 2185-2188, 2016/05/15 2016.
- [30] Y. Wang, H. Y. Li, L. Y. Zhao, B. Wu, S. Q. Liu, Y. J. Liu, *et al.*, "A review of droplet resonators: Operation method and application," *Optics and Laser Technology*, vol. 86, pp. 61-68, Dec 2016.
- [31] Z. P. Liu, Y. Li, Y. F. Xiao, B. B. Li, X. F. Jiang, Y. Qin, *et al.*, "Direct laser writing of whispering gallery microcavities by two-photon polymerization," *Applied Physics Letters*, vol. 97, p. 3, Nov 2010.
- [32] H. M. Wei and S. Krishnaswamy, "Direct Laser Writing Polymer Micro-Resonators for Refractive Index Sensors," *Ieee Photonics Technology Letters*, vol. 28, pp. 2819-2822, Dec 2016.
- [33] J. X. Song, J. T. Lin, J. L. Tang, Y. Liao, F. He, Z. H. Wang, *et al.*, "Fabrication of an integrated high-quality-factor (high-Q) optofluidic sensor by femtosecond laser micromachining," *Optics Express*, vol. 22, pp. 14792-14802, Jun 2014.

- [34] J. M. Ward, Y. Yang, and S. N. Chormaic, "Glass-on-Glass Fabrication of Bottle-Shaped Tunable Microlasers and their Applications," *Scientific Reports*, vol. 6, p. 8, Apr 2016.
- [35] J. C. Knight, G. Cheung, F. Jacques, and T. A. Birks, "Phase-matched excitation of whispering-gallery-mode resonances by a fiber taper," *Optics Letters*, vol. 22, pp. 1129-1131, Aug 1997.
- [36] G. Bahl, J. Zehnpfennig, M. Tomes, and T. Carmon, "Stimulated optomechanical excitation of surface acoustic waves in a microdevice," *Nature Communications*, vol. 2, p. 6, Jul 2011.
- [37] M. Sumetsky, Y. Dulashko, J. M. Fini, and A. Hale, "Optical microfiber loop resonator," *Applied Physics Letters*, vol. 86, p. 161108, 2005.
- [38] M. Sumetsky, Y. Dulashko, J. M. Fini, A. Hale, and D. J. DiGiovanni, "The microfiber loop resonator: Theory, experiment, and application," *Journal of Lightwave Technology*, vol. 24, pp. 242-250, Jan 2006.
- [39] L. Shi, Y. Xu, W. Tan, and X. Chen, "Simulation of Optical Microfiber Loop Resonators for Ambient Refractive Index Sensing," *Sensors*, vol. 7, p. 689, 2007.
- [40] X. Wu, "Optical microfibers and nanofibers," *Nanophotonics* vol. 2(5-6), pp. 407-428, 2013.
- [41] L. M. Tong, R. R. Gattass, J. B. Ashcom, S. L. He, J. Y. Lou, M. Y. Shen, *et al.*, "Subwavelength-diameter silica wires for low-loss optical wave guiding," *Nature*, vol. 426, pp. 816-819, Dec 2003.
- [42] Y. Ren, R. Zhang, C. Ti, and Y. Liu, "Tapered optical fiber loops and helices for integrated photonic device characterization and microfluidic roller coasters," *Optica*, vol. 3, pp. 1205-1208, 2016/11/20 2016.
- [43] J. M. Corres, F. J. Arregui, and I. R. Matias, "Design of Humidity Sensors Based on Tapered Optical Fibers," *Journal of Lightwave Technology*, vol. 24, pp. 4329-4336, 2006.
- [44] M. I. Zibaii, H. Latifi, Z. Saeedian, and Z. Chenari, "Nonadiabatic tapered optical fiber sensor for measurement of antimicrobial activity of silver nanoparticles against Escherichia coli," *Journal of Photochemistry and Photobiology B: Biology*, vol. 135, pp. 55-64, 2014/06/05/ 2014.
- [45] Y. Tian, W. Wang, N. Wu, X. Zou, and X. Wang, "Tapered Optical Fiber Sensor for Label-Free Detection of Biomolecules," *Sensors*, vol. 11, p. 3780, 2011.
- [46] T. Hwang, W. H. Cheng, and Y. K. Su, "Characteristics and Applications of Tapered Fiber Optical Sensors for 1310 nm Wavelength," *Japanese Journal of Applied Physics*, vol. 52, Jun 2013.
- [47] H. Latifi, M. I. Zibaii, S. M. Hosseini, and P. Jorge, "Nonadiabatic tapered optical fiber for biosensor applications," *Photonic Sensors*, vol. 2, pp. 340-356, December 01 2012.
- [48] G. J. Pendock, H. S. MacKenzie, and F. P. Payne, "Dye lasers using tapered optical fibers," *Applied Optics*, vol. 32, pp. 5236-5242, 1993/09/20 1993.

- [49] T. A. Birks, W. J. Wadsworth, and P. S. J. Russell, "Supercontinuum generation in tapered fibers," *Optics Letters*, vol. 25, pp. 1415-1417, 2000/10/01 2000.
- [50] S. Korposh, S. James, R. Tatam, and S.-W. Lee, "Fibre-Optic Chemical Sensor Approaches Based on Nanoassembled Thin Films: A Challenge to Future Sensor Technology," in *Current Developments in Optical Fiber Technology*, S. W. Harun and H. Arof, Eds., ed Rijeka: InTech, 2013, p. Ch. 09.
- [51] G. Chen, M. Ding, T. P. Newson, and G. Brambilla, *A Review of Microfiber and Nanofiber based Optical Sensors* vol. 7, 2013.
- [52] A. Felipe, G. Espíndola, H. J. Kalinowski, J. A. S. Lima, and A. S. Paterno, "Stepwise fabrication of arbitrary fiber optic tapers," *Optics Express*, vol. 20, pp. 19893-19904, 2012/08/27 2012.
- [53] H. Yu, Q. Huang, and J. Zhao, "Fabrication of an Optical Fiber Micro-Sphere with a Diameter of Several Tens of Micrometers," *Materials*, vol. 7, p. 4878, 2014.
- [54] G. Kakarantzas, T. E. Dimmick, T. A. Birks, R. Le Roux, and P. S. J. Russell, "Miniature all-fiber devices based on CO₂ laser microstructuring of tapered fibers," *Optics Letters*, vol. 26, pp. 1137-1139, 2001/08/01 2001.
- [55] M. Sumetsky, Y. Dulashko, and A. Hale, "Fabrication and study of bent and coiled free silica nanowires: Self-coupling microloop optical interferometer," *Optics Express*, vol. 12, pp. 3521-3531, 2004/07/26 2004.
- [56] L. Shi, X. F. Chen, H. J. Liu, Y. P. Chen, Z. Q. Ye, W. J. Liao, *et al.*, "Fabrication of submicron-diameter silica fibers using electric strip heater," *Optics Express*, vol. 14, pp. 5055-5060, Jun 12 2006.
- [57] E. J. Zhang, W. D. Sacher, and J. K. S. Poon, "Hydrofluoric acid flow etching of low-loss subwavelength-diameter biconical fiber tapers," *Optics Express*, vol. 18, pp. 22593-22598, Oct 11 2010.
- [58] T. A. Birks and Y. W. Li, "The Shape of Fiber Tapers," *Journal of Lightwave Technology*, vol. 10, pp. 432-438, Apr 1992.
- [59] M. I. Zibaii, H. Latifi, Z. Saeedian, and Z. Chenari, "Nonadiabatic tapered optical fiber sensor for measurement of antimicrobial activity of silver nanoparticles against *Escherichia coli*," *Journal of Photochemistry and Photobiology B-Biology*, vol. 135, pp. 55-64, Jun 2014.
- [60] J. D. Love, W. M. Henry, W. J. Stewart, R. J. Black, S. Lacroix, and F. Gonthier, "Tapered single-mode fibres and devices. I. Adiabaticity criteria," *IEE Proceedings J - Optoelectronics*, vol. 138, pp. 343-354, 1991.
- [61] L. w. Li and X. h. Sun, "Investigation on the Tapered Fiber Evanescent-Field Sensor Based on the Comsol Software," in *2012 Symposium on Photonics and Optoelectronics*, 2012, pp. 1-3.
- [62] S. E. Skelton, M. Sergides, R. Patel, E. Karczewska, O. M. Maragó, and P. H. Jones, "Evanescent wave optical trapping and transport of micro- and nanoparticles on tapered optical fibers," *Journal of Quantitative Spectroscopy and Radiative Transfer*, vol. 113, pp. 2512-2520, 2012/12/01/ 2012.

- [63] J. Bures and R. Ghosh, "Power density of the evanescent field in the vicinity of a tapered fiber," *Journal of the Optical Society of America A*, vol. 16, pp. 1992-1996, 1999/08/01 1999.
- [64] A. Perot, "On the Application of Interference Phenomena to the Solution of Various Problems of Spectroscopy and Metrology," *Astrophysical Journal*, vol. 9, p. 87, 1899.
- [65] J. H. Chen, X. G. Huang, J. R. Zhao, J. Tao, W. X. He, and S. H. Liu, "Fabry-Perot interference-based fiber-optic sensor for small displacement measurement," *Optics Communications*, vol. 283, pp. 3315-3319, Sep 2010.
- [66] X. Chen, F. Shen, Z. Wang, Z. Huang, and A. Wang, "Micro-air-gap based intrinsic Fabry-Perot interferometric fiber-optic sensor," *Applied Optics*, vol. 45, pp. 7760-7766, 2006/10/20 2006.
- [67] S. Dong, S. Pu, and J. Huang, "Magnetic field sensing based on magneto-volume variation of magnetic fluids investigated by air-gap Fabry-Perot fiber interferometers," *Applied Physics Letters*, vol. 103, Sep 9 2013.
- [68] F. Farahi, T. P. Newson, J. D. C. Jones, and D. A. Jackson, "Coherence multiplexing of remote fibre optic fabry-perot sensing system," *Optics Communications*, vol. 65, pp. 319-321, 1988/03/01/ 1988.
- [69] M. Islam, M. Ali, M.-H. Lai, K.-S. Lim, and H. Ahmad, "Chronology of Fabry-Perot Interferometer Fiber-Optic Sensors and Their Applications: A Review," *Sensors*, vol. 14, p. 7451, 2014.
- [70] V. R. Machavaram, R. A. Badcock, and G. F. Fernando, "Fabrication of intrinsic fibre Fabry-Perot sensors in silica fibres using hydrofluoric acid etching," *Sensors and Actuators A: Physical*, vol. 138, pp. 248-260, 2007/07/20/ 2007.
- [71] V. Melissinaki, M. Farsari, and S. Pissadakis, "A Fiber-Endface, Fabry-Perot Vapor Microsensor Fabricated by Multiphoton Polymerization," *Ieee Journal of Selected Topics in Quantum Electronics*, vol. 21, p. 10, Jul-Aug 2015.
- [72] V. Melissinaki, I. Konidakis, M. Farsari, and S. Pissadakis, "Fiber endface Fabry-Perot microsensor with distinct response to vapors of different chlorinated organic solvents," *IEEE Sensors Journal*, vol. PP, pp. 1-1, 2016.
- [73] V. Melissinaki, M. Farsari, and S. Pissadakis, "A Fiber Optic Fabry-Perot Cavity Sensor for the Probing of Oily Samples," *Fibers*, vol. 5, p. 1, 2017.
- [74] S. Pevec and D. Donlagic, "All-fiber, long-active-length Fabry-Perot strain sensor," *Optics Express*, vol. 19, pp. 15641-15651, 2011/08/01 2011.
- [75] S. Pevec and D. Donlagic, "Miniature all-fiber Fabry-Perot sensor for simultaneous measurement of pressure and temperature," *Applied Optics*, vol. 51, pp. 4536-4541, Jul 2012.
- [76] Z. L. Ran, Y. J. Rao, W. J. Liu, X. Liao, and K. S. Chiang, "Laser-micromachined Fabry-Perot optical fiber tip sensor for high-resolution temperature-independent measurement of refractive index," *Optics Express*, vol. 16, pp. 2252-2263, Feb 2008.

- [77] Y. J. Rao, M. Deng, D. W. Duan, and T. Zhu, "In-line fiber Fabry-Perot refractive-index tip sensor based on endlessly photonic crystal fiber," *Sensors and Actuators a-Physical*, vol. 148, pp. 33-38, Nov 2008.
- [78] T. Zhu, T. Ke, Y. Rao, and K. S. Chiang, "Fabry-Perot optical fiber tip sensor for high temperature measurement," *Optics Communications*, vol. 283, pp. 3683-3685, 2010/10/01/ 2010.
- [79] P. Yeh, *Optical waves in layered media*. Hoboken, N.J. ; [Great Britain]: Wiley-Interscience, 1998.
- [80] "http://wyant.optics.arizona.edu/MultipleBeamInterference/MultipleBeamInterferenceNotes.html."
- [81] K. Betzler. *Fabry-Perot Interferometer*, URL: <http://www.fen.bilkent.edu.tr/~aykutlu/msn513/fibersensors/fabryperot.pdf>.
- [82] F. Hadjaj, *Study of a Fabry Perot resonator*, 2013.
- [83] G. W. Chantry, "The use of Fabry-Perot interferometers, etalons and resonators at infrared and longer wavelengths-an overview," *Journal of Physics E: Scientific Instruments*, vol. 15, p. 3, 1982.
- [84] L. Rayleigh, "IX. Further applications of Bessel's functions of high order to the Whispering Gallery and allied problems," *The London, Edinburgh, and Dublin Philosophical Magazine and Journal of Science*, vol. 27, pp. 100-109, 1914/01/01 1914.
- [85] L. Rayleigh, "CXII. The problem of the whispering gallery," *The London, Edinburgh, and Dublin Philosophical Magazine and Journal of Science*, vol. 20, pp. 1001-1004, 1910/12/01 1910.
- [86] C. G. B. Garrett, W. Kaiser, and W. L. Bond, "Stimulated Emission into Optical Whispering Modes of Spheres," *Physical Review*, vol. 124, pp. 1807-1809, 12/15/ 1961.
- [87] D. G. Rabus, *Integrated Ring Resonators The Compendium*. New York: Springer, 2007.
- [88] G. N. Tsigaridas, "A study on refractive index sensors based on optical micro-ring resonators," *Photonic Sensors*, vol. 7, pp. 217-225, September 01 2017.
- [89] W. Bogaerts, "Silicon microring resonators," *Laser Photonics Reviews*, vol. 6, pp. 47-73, 2012.
- [90] H.-B. Sun and S. Kawata, "Two-Photon Photopolymerization and 3D Lithographic Microfabrication," in *NMR • 3D Analysis • Photopolymerization*, N. Fatkullin, T. Ikehara, H. Jinnai, S. Kawata, R. Kimmich, T. Nishi, *et al.*, Eds., ed Berlin, Heidelberg: Springer Berlin Heidelberg, 2004, pp. 169-273.
- [91] M. Malinauskas, A. Zukauskas, V. Purlys, A. Gaidukeviciute, Z. Balevicius, A. Piskarskas, *et al.*, "3D microoptical elements formed in a photostructurable germanium silicate by direct laser writing," *Optics and Lasers in Engineering*, vol. 50, pp. 1785-1788, Dec 2012.
- [92] I. Sakellari, E. Kabouraki, D. Gray, V. Purlys, C. Fotakis, A. Pikulin, *et al.*, "Diffusion-Assisted High-Resolution Direct Femtosecond Laser Writing," *Acs Nano*, vol. 6, pp. 2302-2311, Mar 2012.

- [93] V. Melissinaki, A. A. Gill, I. Ortega, M. Vamvakaki, A. Ranella, J. W. Haycock, *et al.*, "Direct laser writing of 3D scaffolds for neural tissue engineering applications," *Biofabrication*, vol. 3, p. 045005, 2011.
- [94] C. Schizas, V. Melissinaki, A. Gaidukeviciute, C. Reinhardt, C. Ohrt, V. Dedoussis, *et al.*, "On the design and fabrication by two-photon polymerization of a readily assembled micro-valve," *International Journal of Advanced Manufacturing Technology*, vol. 48, pp. 435-441, May 2010.
- [95] *3D Laser Microfabrication: Principles and Applications*: Wiley-VCH Verlag GmbH & Co, 2006.
- [96] F. Maria, V. Maria, and N. C. Boris, "Multiphoton polymerization of hybrid materials," *Journal of Optics*, vol. 12, p. 124001, 2010.
- [97] K. S. Lee, D. Y. Yang, S. H. Park, and R. H. Kim, "Recent developments in the use of two-photon polymerization in precise 2D and 3D microfabrications," *Polymers for Advanced Technologies*, vol. 17, pp. 72-82, Feb 2006.

Chapter 3

Materials and Methods

The last few years new inorganic-organic hybrid photosensitive materials, synthesized by sol-gel method [1, 2], have been used for the fabrication of micro-optical elements onto optical fibers [3, 4]. These hybrid composites have attracted intense academic and industrial interest, because they combine the dissimilar properties of the two components, those of inorganic glass (hardness, transparency, chemical resistance) and organic polymeric materials (control of composite properties, low processing temperatures, porosity etc.). As a result, they exhibit good optical and mechanical properties [5, 6], as well as, surface functionalization [7] and biocompatibility capabilities. The development of these multi-functional advanced materials has a major impact on future applications in fields such as optics and photonics, electronics, mechanics, membranes, protective coatings, catalysis, sensors and biology.

The experimental apparatuses used for fabrication and characterization, the preparation processes of the optical fiber samples, as well as, the direct laser writing (DLW) protocol followed in this thesis will be presented in this chapter. In the first section of the chapter, the synthesis of the materials that had been used for the fabrication of the Fabry-Perot (FP) microresonators and the Whispering Gallery Mode (WGM) microresonators will be presented. The second section focuses on the preparation of the optical fibers for both FP fiber endface microsensors and WGM ring resonators onto tapered fibers, including the preparation of the optical samples for the multiphoton polymerization process; the DLW set-up that had been used in each case are also described.

3.1 Hybrid materials

Hybrid organic–inorganic materials can be defined as nanocomposites made of organic and inorganic components combined over length scales ranging from a few Ångströms to a few tens of nanometers. The development of hybrid organic–inorganic materials is mainly due to the development of soft inorganic chemistry processes, especially sol–gel processes, where synthetic conditions allow access to chemically designed combinations of inorganic domains obtained via inorganic polymerization reactions with organic or even bioactive molecules. The inorganic part of these composites is derived from metallic alkoxides, which upon hydrolysis and condensation, form an inorganic network. The organic part comprises monomer units, which carry photopolymerizable functional groups that are attached to the inorganic network. The linear and non-linear photosensitivity of these materials arises from the use of appropriate photoinitiators. Such molecules have the ability of initiating polymerization of the organic part, when treated with specific wavelength radiation, resulting the formation of an organic-inorganic network.

3.1.1 Synthesis of hybrid materials

The materials used for the microstructure fabrication onto the fibers, were organic-inorganic hybrid composites [7, 8]. They were produced by adding zirconium propoxide (ZPO, 70% in propanol) to methacryloxypropyltrimethoxysilane (MAPTMS). The zirconium propoxide was used for the formation of the inorganic network. MAPTMS carries a trialkoxysilane functional group, which can undergo hydrolysis and condensation and is thus attached to the inorganic network, while bearing a polymerizable methacrylate moiety. This methacrylate moiety of MAPTMS and 2-(dimethylamino)ethyl methacrylate (DMAEMA) were used as the organic photopolymerizable monomers. All the chemicals were obtained from Sigma-Aldrich without any further purification. Michler's ketone, 4,4-bis(diethylamino) benzophenone (BIS), was used as a photoinitiator.

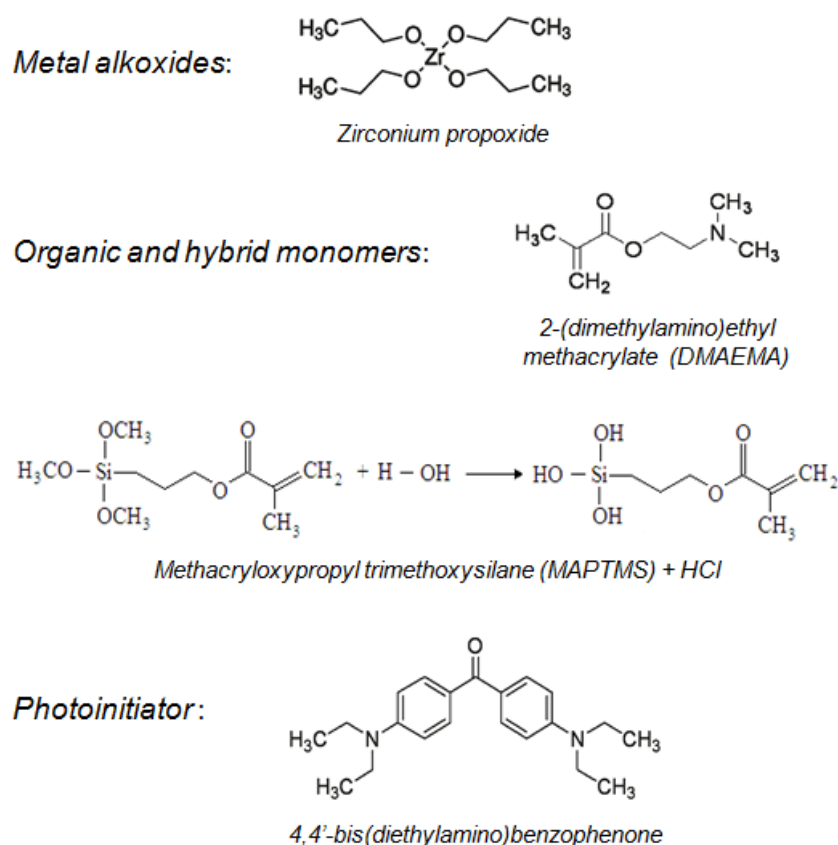


Fig. 3.1. Chemical formulas of the precursor molecules used for the synthesis of the hybrid materials.

The final material consists of an inorganic network chemically attached via the Si atoms to the polymer matrix. The Zr and Si atoms are randomly connected to each other. The polymerized material has a functional amino group on the polymer matrix (see Figure 3.2), which can be used in case of further functionalization of the fabricated structures is needed.

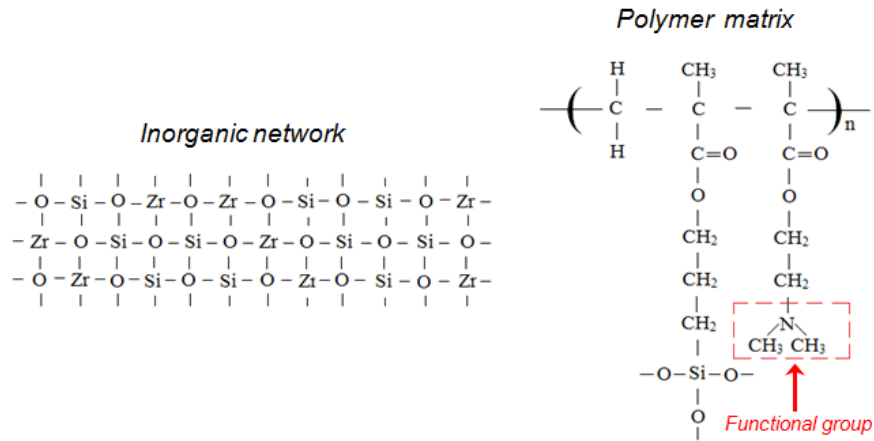


Fig. 3.2. Inorganic network (left) and polymer matrix (right) of the polymerized hybrid materials. In the red dash line the functional amino group of the polymer matrix is presented.

3.1.1a Synthesis of the hybrid material for the fabrication of the endface Fabry-Perot microresonators

For the fabrication of the endface Fabry-Perot microresonators the inorganic-organic hybrid material was synthesized as follows. MAPTMS was first hydrolyzed using HCl solution (0.1 M) at a 1:0.1 ratio, while ZPO was mixed with DMAEMA. After 15 minutes of stirring, the hydrolyzed MAPTMS was added to the zirconium solution at a 8:2 molar ratio and was left stirring for 10 minutes. The (MAPTMS+ZPO):DMAEMA molar ratio was 9:1. Finally, the photoinitiator was added to the mixture at a 1% w/w concentration with respect to the monomers. The final solution was magnetically stirred for 15 minutes before being filtered using a 0.22 μm pore size syringe filter.

3.1.1b Synthesis of the hybrid material for the fabrication of Whispering Gallery Mode (WGM) microring resonators onto tapered fibers

In order to minimize scattering and absorption losses and ensure efficient light trapping through WGM microring resonance, a multiphoton polymerization resin resulting to smooth optical interfaces was developed.

In order to have a material that will be polymerized easier, the inorganic-organic hybrid composite was synthesized in a similar way to that which was used for the fabrication of the endface Fabry-Perot microresonators (see paragraph 3.1.1a), with the difference estimated in the molar ratio of (MAPTMS+ZPO) to DMAEMA. As it was mentioned before (see paragraph 3.1 Hybrid materials), the inorganic part of the hybrid composite is responsible for the hardness of the final synthesized material. In the previous case of Fabry-Perot microresonators the molar ratio of (MAPTMS+ZPO):DMAEMA was 9:1 (see paragraph 3.1.1a), while for the fabrication of the WGM microring resonators onto tapered fibers, this ratio was determined to be 7:3. The reduction of the inorganic composites and at the same time the increase of the organic part results to a synthesized hybrid material with lower polymerization threshold. This means that for the same laser power and the same scanning speed, the second material will have lower resolution than the first one,

providing smoother surfaces.

3.2 Optical fiber preparation and DLW process

One of the goals of this thesis is the fabrication of optical microstructures onto the endfaces or onto the thinned cladding of optical fibers; thus, a thorough preparation, handling, positioning and demounting of the optical samples was necessary. Specifically the technical challenge was to handle and position the optical fiber with respect to the resin and the objective used for laser delivery and imprinting. Below is presented in detail the preparation of the samples and related experimental apparatus for both the fiber endface Fabry-Perot microresonators and the WGM microring resonators onto tapered fibers.

3.2.1 Preparation of optical fiber samples for the fabrication of the endface Fabry-Perot microresonators

For the fabrication of the endface Fabry-Perot microresonators, a commercially available telecom optical fiber, SMF-28e (Corning, USA), with core diameter of 8.2 μm and cladding diameter of 125 μm was used. A special designed base was used to host the optical fiber and the photosensitive material (see Fig. 3.3). The optical fiber was firstly stripped from its polymeric jacket and endface cleaved using a high precision diamond blade cleaver (Photon Kinetics FK11) (see Fig. 3.4a); then, it was mounted on the translation stage (see Fig. 3.4b). This stage consists of a single axis micrometer translation stage and a metallic hollow plate, which is fixed above the translation stage and serve as the base of the photosensitive hybrid material.

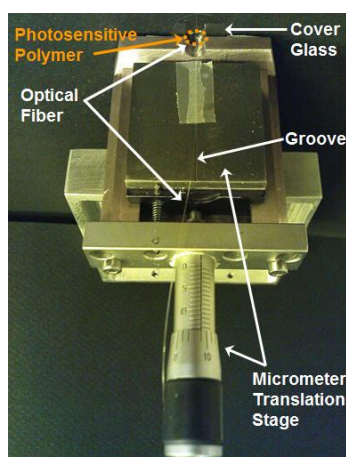


Fig. 3.3. Special designed base used for the DLW fabrication of the endface FP microresonators.

Then, the photopolymer was drop-cast on a thin cover glass substrate (100 μm) and left for 10 minutes at ambient conditions to gelate (see Fig. 3.4c). Afterwards, it was placed on the metallic hollow plate and the fiber tip was immersed in the photopolymer droplet, at the appropriate distance from the glass substrate, depending on the structuring requirements (see Fig. 3.4d). The precise control of the distance between the fiber tip and the resin glass substrate enabled high accuracy fabrication (see Fig. 3.4c). After immersion of the optical fiber endface sample in the resin, it was

left at ambient conditions for 24 hours to ensure slow and crack-free solvent evaporation (gelation of hybrid material). All the processes are being presented schematically in Figure 3.4. Finally, the sample was placed at the DLW set-up and the details for the fabrication process are presented in detail in paragraph 3.2.3a.

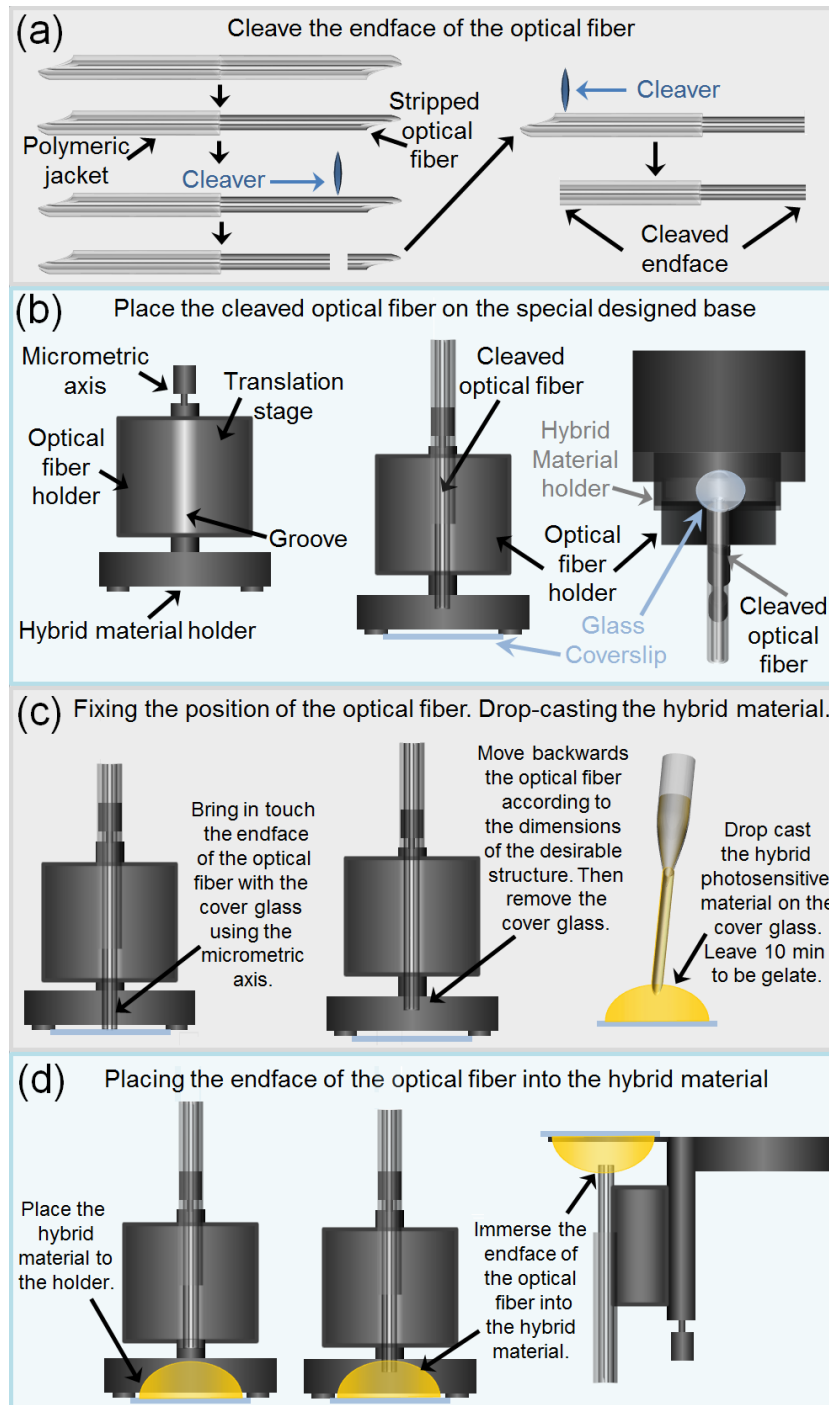


Fig. 3.4. Schematic presentation of the preparation process of the samples for the fabrication of the FP microresonators. (a) Stripping and cleaving the SMF-28e optical fiber. (b) Place the cleaved optical fiber onto the special designed stage. (c) Adjust the appropriate distance of the endface of the fiber to the cover glass substrate. (d) Immerse the endface of the optical fiber into the photosensitive material.

3.2.2 Preparation of optical fiber tapered samples for the fabrication of the WGM microring resonators onto them.

The optical fiber used for the fabrication of the WGM microring resonators was also the commercially available telecom fiber SMF-28e. For these experiments, the optical fiber had to be tapered before the polymerization process takes place. By tapering the optical fiber, the light propagating through it, evanesces at the tapered region into the environment where the microring resonator was fabricated/attached, allowing light coupling and excitation of the whispering gallery modes [9, 10].

In order to taper down the single mode fiber a Vytran (GPX-3000) glass fiber processor was employed [11]. A piece of approximately 1 m length of the aforementioned optical fiber was used. Firstly the fiber was stripped off from its plastic polymeric jacket in the middle area of its length and then it was mounted to the Vytran processor (see Fig. 3.6b). The holders-mounts secured the fiber while the area that had to be tapered was suspended between the mounds (see Fig. 3.5 left and Fig. 3.6b). The desirable taper waist and length the appropriate parameters were loaded to the Vytran processor. The filament-based furnace incorporated to the processor was heating up the area that had to be tapered and at the same time the mounds were moved at opposite directions straining the fiber (see Fig. 3.6b). The procedure was real time monitored through a high-resolution microscopic imaging system coupled with a high-resolution digital CCD camera. After the end of the process, a specially designed “fork” was used in order to remove the tapered fiber from the Vytran processor (see Fig. 3.6b) and place it precisely onto the glass substrate (see Fig. 3.5 right, Fig. 3.6c). This fork had two fingers that secured strained the tapered fiber, and two micrometer translation stages that could be used to move the fiber in x and z axis and a third micrometer translation stage connected to a base that could be used in order to control precisely the inclination of the fiber (see Fig. 3.5 right).

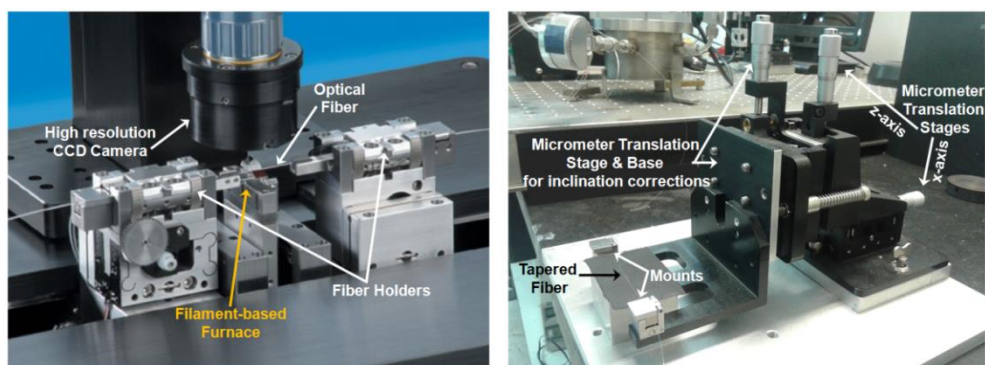


Fig. 3.5. Vytran processor GPX-3000 (left), Special designed “fork” (right).

After the optical fiber had been tapered, it was moved with the special fork onto a glass substrate. A UV glue (Norland Optical Adhesive 81) was used to secure the tapered fiber on the glass (see Fig. 3.6c). As glass substrate were used microscope slides of 1 mm thickness. On the top of one microscope slides had been placed at both edges and secured by the same UV glue pieces of ~1 cm length (see Fig. 3.6a). This

way, the fiber was placed and glued on these two pieces of glass while the tapered region was suspended between the gap. Afterwards, an amount of the hybrid material was drop-cast on the top of the tapered fiber, until a drop that surrounded the tapered region was formed (see Fig. 3.6d).

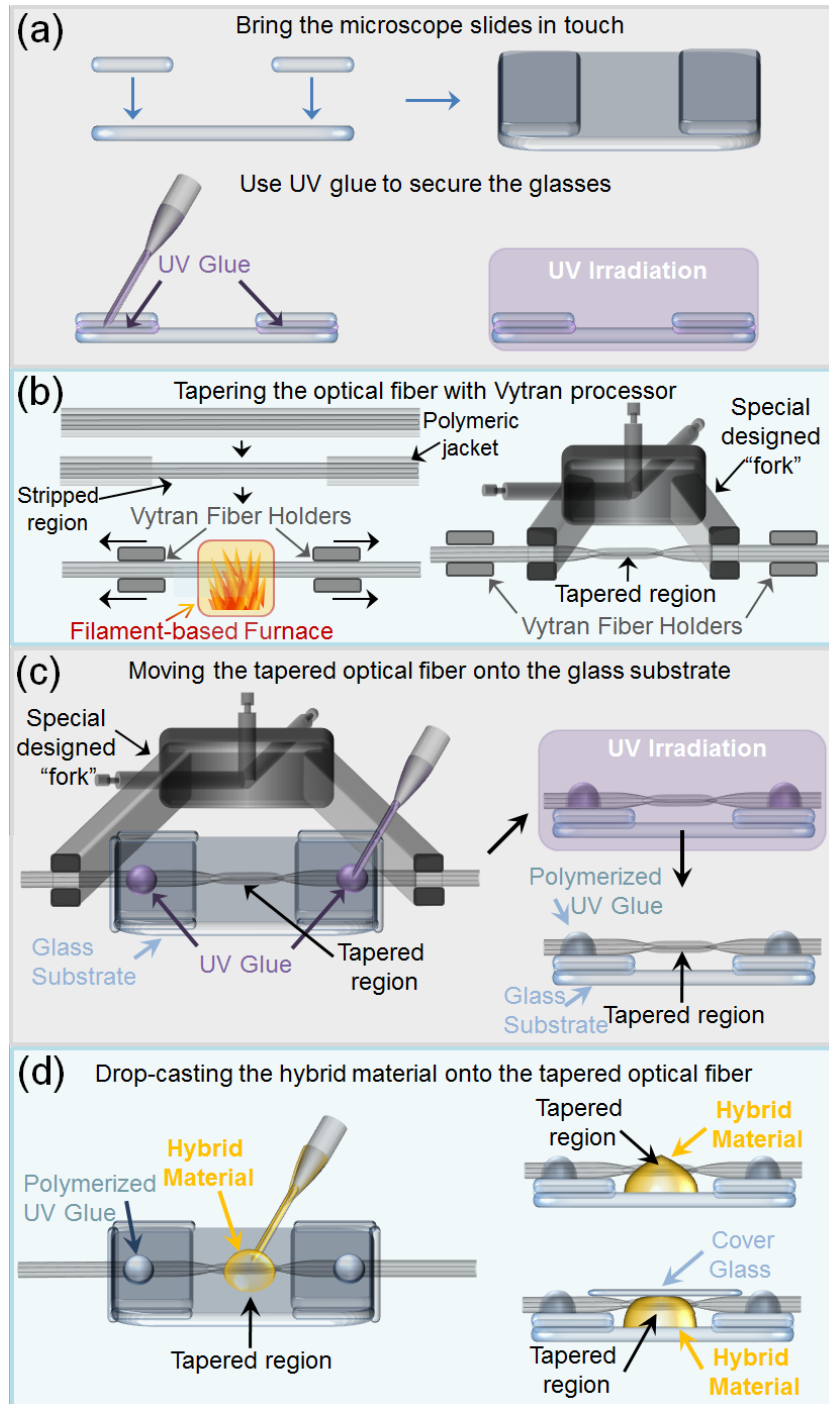


Fig. 3.6. Schematic presentation of the preparation process of the samples for the fabrication of the ring microresonators onto tapered fibers. (a) Preparation of glass substrates. (b) Taper the SMF-28e optical fiber and move it from Vytran processor with the specially designed "fork". (c) Place the tapered optical fiber onto the glass substrate and secure it using UV glue. (d) Drop-cast the photosensitive material on the tapered area of the SMF-28e optical fiber.

The hybrid material had been left before in ambient conditions to gelate. Finally, a small glass substrate of $\sim 100\mu\text{m}$ thickness was placed on the top of the droplet, in order to be used during the DLW process for the alignment (see Fig. 3.6d). The sample was left under vacuum conditions (22inHg) for at least 4 days to ensure solvent evaporation. All the processes are being presented schematically in Figure 3.6. The details for the fabrication process are presented in details in paragraph 3.2.3b.

3.2.3 Direct Laser Writing (DLW) set-up and processes

The fabrication procedure of Direct Laser Writing (DLW) has been described extensively in literature from many different groups and for a variety of applications [4, 5, 12-14]. The experimental set-up employed herein is presented schematically in Fig. 3.7. A Ti:Sapphire femtosecond laser was employed as light source. The laser beam was guided through optics on a x-y galvanometric mirror digital scanner (Scanlabs Hurryscan II). A high numerical aperture microscope objective lens (40x, N.A. = 0.95, Zeiss, Plan Apochromat), which was placed below the galvanometric scanners was used for the focusing of the beam onto the sample. To achieve better focusing, the laser beam was expanded 3x using a telescope lens arrangement. Z-axis scanning and larger-scale x-y movements were carried out using a high-precision three-axis linear translation stage (PI). Beam intensity was controlled by a mechanical shutter (Uniblitz) and a motorized attenuator (Altechna). The galvanometric scanners were controlled by SAMLIGHT (SCAPS) software, while the whole DLW setup was computer controlled using a National Instruments LabVIEW program. The fabrication process was monitored by a CCD camera mounted behind a dichroic mirror.

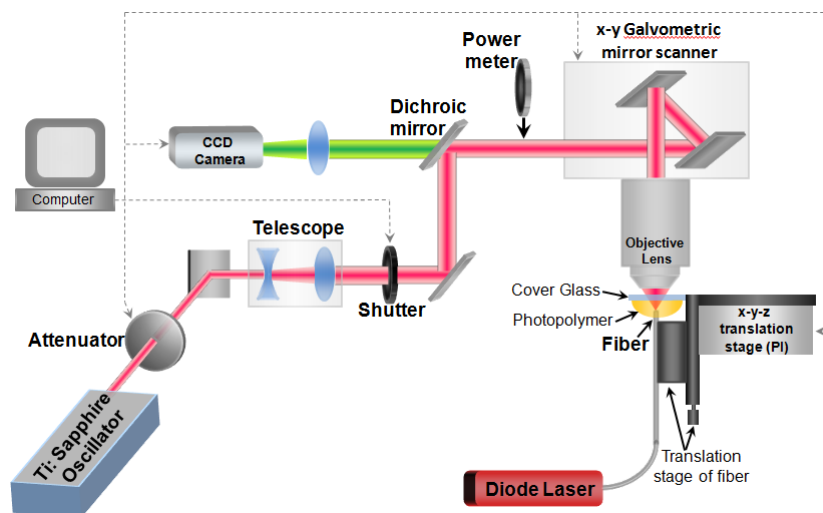


Fig. 3.7. Direct laser writing (DLW) set-up.

3.2.3a DLW set-up and process for the fabrication of the endface Fabry-Perot microresonators

For the fabrication of the optical fiber endface Fabry-Perot microresonators a Femtolasers Fusion Ti:Sapphire femtosecond laser was used as light source, (wavelength 800 nm, repetition rate of 75 MHz, pulse duration < 20 fs, 450 mW

maximum output power).

When the samples that were prepared as it was described previously in paragraph 3.2.1 were ready for the DLW fabrication process, they were moved to the set-up. The special designed base that accommodated the fiber and the hybrid material was placed on the x-y-z linear transition PI stage as presented in Figure 3.5. In order to align the fiber core with the microscope objective, a diode laser operating at 635 nm (Optronics EYT) was coupled to the free end of the fiber (see Fig 3.7). In this way, the light emerging out from the endface of the fiber, which was immersed in the photopolymer, enabled the fiber core to be clearly imaged with the CCD camera and to be aligned to the reflection of the laser writing beam by moving the PI stages.

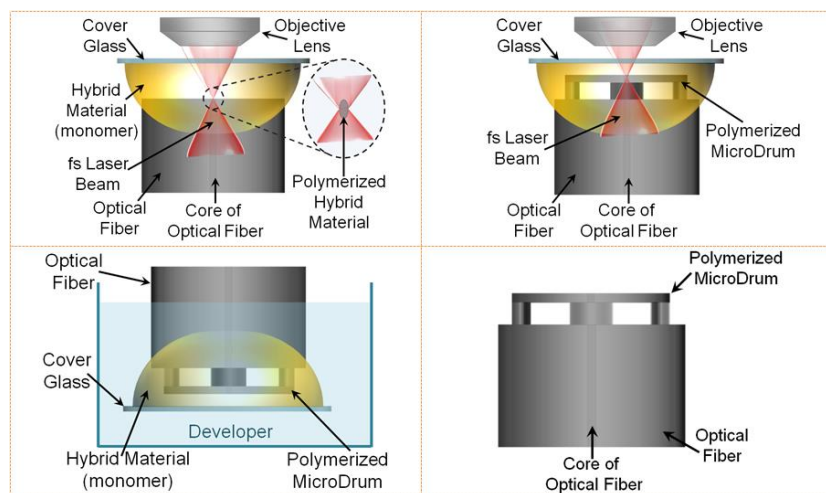


Fig. 3.8. Schematic representation of the DLW fabrication process on the endface of the fiber. The laser beam is focusing in the cleaved fiber-hybrid material interface where the photopolymerization begins and takes place only at the focal point of the laser beam (left-up). The polymerization takes place in a layer-by-layer fashion (right-up). After the end of the polymerization the sample is getting immersed in the appropriate solvents in order the unpolymerized material to be washed off (bottom-left). The desirable polymerized structure is obtained on the endface of the optical fiber.

After the alignment, the laser writing beam was focused onto the fiber-hybrid material interface and the photopolymerization began in a layer-by-layer fashion, with the first layer being fabricated on the surface of the fiber (see Fig. 3.8). After the completion of the fabrication process, the sample was developed for 1 hour into a 70:30 solution of 1-propanol and isopropanol, and, it was further rinsed with isopropanol in order the unpolymerized material to be washed off.

3.2.3b DLW set-up and process for the fabrication of WGM microring resonators onto tapered fibers

For these experiment another Ti:Sapphire fs laser was used obtained from Spectra-Physic (Tsunami, Model 3960-L3S, wavelength 790 nm, repetition rate of 80 MHz, pulse duration <100 fs, 700 mW average power).

Here, the sample was loaded directly onto the x-y-z linear transition PI stage. Initially, the sample was moved in z direction towards the focal point of the laser beam using the PI stages. When the reflection of the cover glass was imaged through

the CCD camera, the sample was moved in x and y directions in order the tapered region of optical fiber to be visible through the CCD camera and then be aligned to the laser writing beam. When the tapered region was aligned to the laser beam and placed at the focal point of the beam, the polymerization took place in a single layer fashion (see Fig. 3.9) directly onto the optical fiber. Depending on the desirable thickness of the ring, the beam was scanned inside the material in homocentric circles of 20 nm difference in their radius, with the biggest radius be that of the desirable dimension of the ring microresonator. After the end of the polymerizing process, the sample was immersed in a 70:30 solution of 1-propanol: isopropanol for at least 3 hours. When the most of the unpolymerized material was washed off, the upper cover glass was removed and the sample was left in the developer further for 30 minutes, in order all the unpolymerized material to be washed of. Finally, the sample was further rinsed with isopropanol.

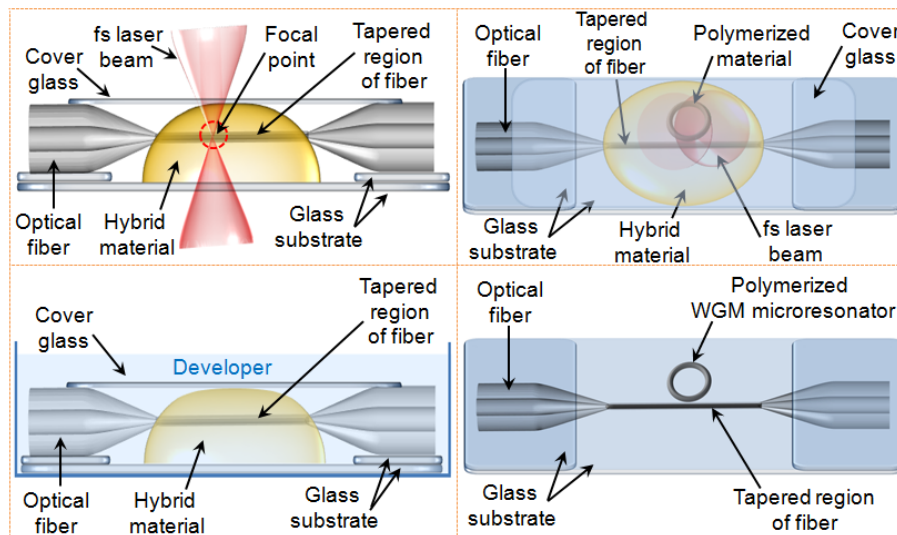


Fig. 3.9 .Schematic representation of the DLW fabrication process directly onto the tapered optical fiber. The laser beam is focusing on the tapered fiber-hybrid material interface where the photopolymerization begins and takes place only at the focal point of the laser beam (left-up). The polymerization takes place in a single layer fashion (right-up). After the end of the polymerization the sample is getting immersed in the appropriate solvents in order the unpolymerized material to be washed off (bottom-left). The desirable polymerized structure is obtained onto the tapered optical fiber.

In this case the development process took more time, due to that the hybrid material was enclosed between two glass substrates, and moreover, a larger volume of the material was used in this case. After the end of the development process, the WGM microring resonator was attached onto the air suspended tapered optical fiber.

3.3 Summary - Conclusions

The synthesis of the hybrid organic-inorganic materials, as well as the preparation of the samples for the fabrication of both endface Fabry-Perot microresonators and Whispering Gallery Mode microring resonators onto tapered fibers were described above. In order to fabricate the microresonators two different sample preparation processes were developed.

In case of Fabry-Perot microresonators, a special designed stage was fabricated (see Fig. 3.3) to host both the cleaved fiber and the hybrid material. The design of this stage was inspired from the work of H. E. Williams [13], and was modified in order to fit to the needs of our experiments. The precise control of the immersion of fiber tip into the hybrid material, achieved by the use of the translation micrometric stage, enabled high accuracy fabrication. The first challenge that was faced during the direct laser writing process was to "find" the optical fiber (125 μm diameter) inside the volume of the droplet of the hybrid material ($\sim 4\text{mm}$ diameter and $\sim 1.5\text{mm}$ height). For these reason a diode laser was coupled to the free end of the fiber and the light immersed from the endface of the fiber immersed in the hybrid material helped to find and align the optical fiber to the laser beam (see Section 3.2.3a and Fig. 3.7). The second challenge was to align correctly the endface of the optical fiber to the fs laser beam in order to be perpendicular. For achieving efficient interference between the reflection surfaces of the FP cavity, the reflectors have to be parallel. The fabricated microstructure (2nd reflection surface) would be non-parallel to the endface of the optical fiber (1st reflection surface of the FP cavity), in case of a small introduced inclination during the alignment. For this reason the alignment of the endface of the fiber to the laser beam (through the base that the sample is placed on the translation PI stages, see Fig. 3.7 took place for more than three or four times for each sample. Another challenge at these experiments was to ensure the correct "viscosity" of the hybrid material in order to start the photopolymerization process. Before the photopolymerization the samples were left at ambient conditions in order the solvents that were used during the synthesis of the material to be evaporated (gelation of the material). When the hybrid material was not sufficiently gelled the optical fiber was observed to "move" inside the volume of the material during the photopolymerization process, affecting the quality of the structure. On the other hand, when the hybrid material was over-gelated, it was hard to remove the unpolymerized material during the development. Even a remained thin layer of unpolymerized resin on the Fabry-Perot reflectors, affected the quality of the interference spectrum. For these reason different samples were prepared and remained for different time at ambient conditions to be gelled. Afterwards were used for the photopolymerization process in order to find the optimum conditions for gelation time (see Section 3.2.1).

On the contrary, the processes for the fabrication of the microring resonators directly onto tapered fibers by multiphoton polymerization technique had been developed for the very first time during the experiments of the present PhD thesis. Until today, no research group of the community, working in the fields of WGM microresonators or direct laser writing, had managed to fabricate directly onto tapered optical fibers microring resonators, to the best of our knowledge. The first challenge in these experiments was to prepare the appropriate substrate which had to host the tapered fiber and serve all the steps of the experiments (photopolymerization, development, spectrum characterization etc.). For this reason, different glass substrates had been use and tested. The conclusion obtained from these experiments, was that a spacing was necessary between the glass substrate and the tapered region. The absence of this spacing led to problems with the development of the samples

after the photopolymerization. The non-polymerized material did not wash off properly and residues of the hybrid material and solvent remained on the tapered fibers and the microring, affecting the light propagation. For this reason, microscope slides (15 mm x 20 mm and thickness of ~ 1mm) were used as spacers and fixed on a microscope slide using UV glue (see Fig. 3.6a). The second challenge was to place the tapered fiber on the glass substrate and glue it, in order to remain stretched. For this reason a special designed "fork" was developed and used to remove the tapered fiber from the Vytran processor and place it on the glass substrate (see Fig. 3.5, Fig. 3.6b and Fig. 3.6c). After fixing the tapered fiber with the UV glue on the glass substrate the fiber was released from the "fork". When the tapered fiber was not stretched the photopolymerization process was difficult to succeed and after the development the tapered region was attached to the microscope slide. On the other hand, when the tapered fiber was more tensioned, it would easily break during the dopcasting of the hybrid material or when the sample was removed from the developer. Another challenge was again the correct "viscosity" of the hybrid material. Herein, the hybrid material was left in ambient conditions to gelate after its synthesis in order to be more viscous. This way the material was easier to be drop-cast on the tapered fiber, since the droplet had to have a height of at least ~1.2mm (the fiber had a space from the microscope slide of approximately of 1mm) in order to enclose the tapered fiber inside her volume (see Fig. 3.6d). The biggest challenge here was to find the tapered fiber of ~2.4 μm diameter inside the volume of the hybrid material and then find the appropriate position on the tapered fiber in order to fabricate the microring. The microring had to be polymerized as near to the outer surface of the tapered region as possible and symmetrically to the center of the tapered fiber at z axis (perpendicular to the diameter of the tapered region). At the same time one had to ensure that the connection point between the tapered fiber and the microring was not at the edge of the tapered fiber, otherwise after the development, the microring would drop-off. Moreover, at the parallel couple microresonators, the rings were fabricated one by one, because the tapered fiber presented differences at its positioning even within a 30 μm length. That is why the microrings that will be presented in Chapters 6 and 7 will present slight differences at the positioning onto the tapered fiber.

To conclude, even though there were a lot of challenges that we had to face and overcome, new processes were developed and used in order to successfully fabricate, directly onto optical fibers for the very first time, two different kind of microresonators, namely those of FP and WGM, by the multiphoton polymerization technique. The spectral characterization of the photopolymerized microresonators that will be presented in the next Chapters, show that both the developed processes are able to fabricate functional and robust microstructures that can be used in order to develop new optical fiber sensors for a variety of different applications.

References

- [1] G. Kickelbick, "Introduction to Hybrid Materials," in *Hybrid Materials*, ed: Wiley-VCH Verlag GmbH & Co. KGaA, 2007, pp. 1-48.
- [2] H. Schmidt, "Inorganic-Organic Composites by Sol-Gel Techniques," *MRS Proceedings*, vol. 171, 2011.
- [3] M. Schumann, T. Buckmann, N. Gruhler, M. Wegener, and W. Pernice, "Hybrid 2D-3D optical devices for integrated optics by direct laser writing," *Light Sci Appl*, vol. 3, p. e175, 06/06/online 2014.
- [4] M. Malinauskas, A. Zukauskas, V. Purlys, A. Gaidukeviciute, Z. Balevicius, A. Piskarskas, *et al.*, "3D microoptical elements formed in a photostructurable germanium silicate by direct laser writing," *Optics and Lasers in Engineering*, vol. 50, pp. 1785-1788, Dec 2012.
- [5] A. Ovsianikov, S. Z. Xiao, M. Farsari, M. Vamvakaki, C. Fotakis, and B. N. Chichkov, "Shrinkage of microstructures produced by two-photon polymerization of Zr-based hybrid photosensitive materials," *Optics Express*, vol. 17, pp. 2143-2148, Feb 2009.
- [6] F. Mammeri, E. L. Bourhis, L. Rozes, and C. Sanchez, "Mechanical properties of hybrid organic-inorganic materials," *Journal of Materials Chemistry*, vol. 15, pp. 3787-3811, 2005.
- [7] K. Terzaki, N. Vasilantonakis, A. Gaidukeviciute, C. Reinhardt, C. Fotakis, M. Vamvakaki, *et al.*, "3D conducting nanostructures fabricated using direct laser writing," *Optical Materials Express*, vol. 1, pp. 586-597, Aug 2011.
- [8] I. Sakellari, E. Kabouraki, D. Gray, V. Purlys, C. Fotakis, A. Pikulin, *et al.*, "Diffusion-Assisted High-Resolution Direct Femtosecond Laser Writing," *Acs Nano*, vol. 6, pp. 2302-2311, Mar 2012.
- [9] T. A. Birks and Y. W. Li, "The Shape of Fiber Tapers," *Journal of Lightwave Technology*, vol. 10, pp. 432-438, Apr 1992.
- [10] J. M. Ward, A. Maimaiti, V. H. Le, and S. N. Chormaic, "Contributed Review: Optical micro- and nanofiber pulling rig," *Review of Scientific Instruments*, vol. 85, p. 10, Nov 2014.
- [11] "GPX-3000 Series, Optical Fiber Glass Processors," URL: http://www.optoscience.com/maker/vytran/pdf/datasheet_gpx_3000_series.pdf.
- [12] I. Sakellari, A. Gaidukeviciute, A. Giakoumaki, D. Gray, C. Fotakis, M. Farsari, *et al.*, "Two-photon polymerization of titanium-containing sol-gel composites for three-dimensional structure fabrication," *Applied Physics a-Materials Science & Processing*, vol. 100, pp. 359-364, Aug 2010.
- [13] H. E. Williams, D. J. Freppon, S. M. Kuebler, R. C. Rumpf, and M. A. Melino, "Fabrication of three-dimensional micro-phonic structures on the tip of optical fibers using SU-8," *Optics Express*, vol. 19, pp. 22910-22922, Nov 2011.
- [14] T. Gissibl, M. Vieweg, M. M. Vogel, M. A. Ahmed, T. Graf, and H. Giessen, "Preparation and characterization of a large mode area liquid-filled photonic crystal fiber: transition from isolated to coupled spatial modes," *Applied Physics B-Lasers and Optics*, vol. 106, pp. 521-527, Mar 2012.

Chapter 4

Fabry-Perot optical fiber endface microresonators

Optical fiber sensors based on Fabry–Perot (FP) interferometers have been implemented in a wide range of applications since 80's [1]. They have been extensively studied, due to their operational advantages such as high sensitivity, low cost, immunity to electromagnetic radiation, corrosion resistance etc. Several techniques have been developed to fabricate FP cavities either on the cladding, or, on the endface of optical fibers. The most common techniques that have been extensively used are laser micromachining methods [2-6], chemical etching [7-9], fusion splicing of single mode fibers (SMF) with photonic-crystal fibers (PCF) [10] or microstructured optical fibers (MOF) [11] and dip-coating methods [12].

Herein, we demonstrate the fabrication of FP microresonators on the endface of commercially available single mode fibers by Direct Laser Writing (DLW) with multiphoton polymerization technique using a homemade hybrid inorganic organic photosensitive material. The use of multiphoton polymerization technique provides the flexibility of fabricating fully functional devices, by changing easily and straightforwardly, either the dimensions or the design of the FP cavity according to the requirements of the experiment planned, resulting in robust light localization structures of tailored performance that can be reused several times.

Three different designs of endface FP microresonators will be introduced in this chapter and their principle of operation will be explained in details. Moreover, their spectral response as well as simulated spectra through two-beam optical interference approximation and finite difference time domain (FDTD) will be presented.

4.1 Micro-drum FP optical fiber endface resonator; design and principle of operation

The design of the first proposed FP endface microresonator is presented in Figure 4.1. It consists of a thin, flat membrane suspended on four pillars attached on the endface of a cleaved single mode optical fiber (SMF-28e) [13]. This architecture allows the formation of a small air cavity, of length D , between the endface of the fiber and the flat membrane (thickness d) of the fabricated microstructure, which acts as multiple FP resonator, due to the reflection surfaces 1 (endface of the optical fiber), 2 (inner surface of the fabricated membrane) and 3 (outer surface of the fabricated membrane), respectively, shown in Figure 4.1(a). Liquid or gaseous media can readily penetrate the empty cavity of the microstructured resonator, allowing straightforward detection of refractive index or adsorption changes in reflection mode.

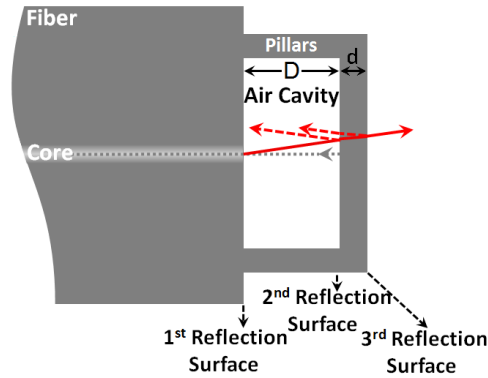


Fig. 4.1. Design and principle of operation of the multiple FP microdrum resonator fabricated on the endface of a single mode SMF-28e optical fiber. Grey dashed line corresponds to the reflected light that is recording. Red solid line and red dashed line corresponds to the guided light for the maximum angle of the Numerical Aperture (NA) of the core of the optical fiber and the reflected light from both the fabricated reflection surfaces of the microstructure respectively.

4.1.1 Spectral characterization of the optical fiber endface FP micro-drum resonator

The optical microscope image (see Fig. 4.2(a)) and the scanning electron microscope image (SEM) (Fig. 4.2(b)) present the fabricated microdrum structure [13]. For the fabrication of this resonator by the multiphoton polymerization technique, the laser power was adjusted to 18 mW, measured before the objective, while the laser scanning speed was set at 100 $\mu\text{m/s}$. The specific cavity demonstrated herein consists of a $\sim 14 \mu\text{m}$ air gap formed between the fiber endface and the photopolymerized structure, while the membrane thickness is $\sim 9.6 \mu\text{m}$. The FP resonator has been optimized for operation in the spectral region spanning between 1440 nm and 1660 nm. The interference spectrum, measured in reflection mode, of this microdrum endface multiple FP resonator is presented in Fig. 4.2(c), characterized with a periodic modulation of notches of $\sim 23 \text{ dB}$ in amplitude strength and a free spectral range for the deepest notches of $\sim 80 \text{ nm}$.

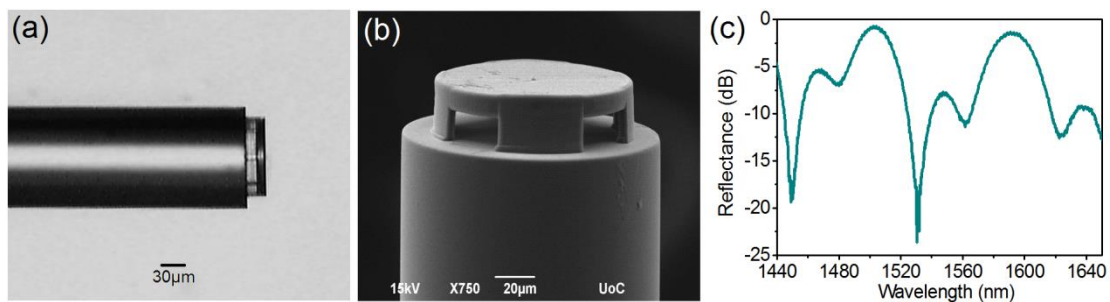


Fig. 4.2. Microdrum FP resonator fabricated on the endface of a single mode SMF-28e optical fiber. (a) Optical microscope image of the fabricated structure. (b) Scanning electron microscope (SEM) image. (c) Interference spectrum of the multiple FP microdrum resonator.

A simple set-up (presented in Figure 4.3), was used in order the interference spectrum of the microresonator to be recorded in reflection mode, while being interrogated using a 50/50 AFC/PC angle coupler. The measurements were performed using an optical fiber pigtailed superluminescence source (QPhotonics) and an Optical Spectrum Analyzer (OSA) ANDO AQ6317B.

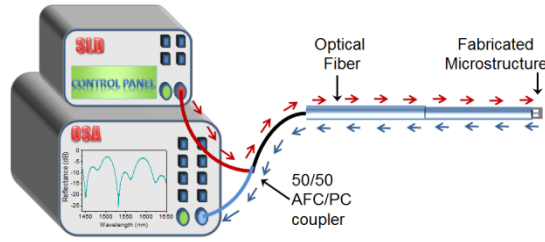


Fig. 4.3. Set-up that was used to record the interference spectrum of the endface microresonators in reflection mode. The red arrows show the propagation of the light from the light source to the endface of the optical fiber and the microresonator through the 50/50 angle coupler, while the blue arrows show the reflected light from the resonator that was recorder to the optical spectrum analyzer (OSA).

4.1.2 Simulating the reflection spectrum of the multiple FP optical fiber microdrum resonator using two-beam optical interference approximation

The goal herein is to develop a simulation model of the reflected electric field, which will predict the interference FP spectrum of a microdrum FP resonator. The design of the endface FP microdrum resonator was already presented in Figure 4.1. As it was mentioned it consists of a thin, flat, suspended on four pillars attached on the endface of a cleaved single mode optical fiber (SMF-28e). By this way a multiple FP resonator is formed, consisting of three reflection mirrors, shown in schematic image of Figure 4.4(a), labeled as 1st, 2nd and 3rd reflection surface respectively. Reflection surfaces 1 and 2 form the 1st cavity of length D and refractive index n_m , reflection surfaces 2 and 3 form the 2nd FP cavity of length d and refractive index of n_s and finally the 3rd cavity is formed form 1st and 3rd reflection surfaces of length $D + d$. The refractive index of the core of the optical fiber is labeled as n_c , while this of the cladding of the optical fiber is denoted as $n_{cladding}$.

Due to the low reflectivity of the three reflective surfaces, the sensor can be simplified as a low finesse device, and thus can be modeled using the two-beam optical interference approximation [2, 3, 14-16]. Figure 4.4(b) shows the electric field amplitude coefficients at the three reflection surfaces. The reflection coefficient of electric fields towards the detector, E_r , is given approximately by the sum of all the reflection coefficients of the electric fields from the three surfaces. $R_1 = R_{r1}R_{s1}$, $R_2 = R_{r2}R_{s2}$ and $R_3 = R_{r3}R_{s3}$, where R_{r1} , R_{r2} and R_{r3} correspond to the power reflection coefficients at surfaces 1, 2 and 3 respectively, while R_{s1} , R_{s2} and R_{s3} to the Rayleigh scattering loss coefficients. T_1 , T_2 and T_3 are the transmission loss factors at reflection surfaces 1, 2 and 3 respectively, which are due to the surface imperfections (e.g. roughness). Moreover, α is the air cavity loss factor and L_s is the membrane loss factor, which are mainly caused by diffraction and scattering in the air cavity (Cavity 2) and the membrane (Cavity 3). The refractive index of the optical fiber core equals to $n_c = 1.4682$, this of the fabricated microdrum equals to $n_s = 1.52$ while the refractive index n_m equals to the refractive index of the medium in the Cavity 1. Therefore, in case that $n_m < n_s$ there is a π -phase shift at reflection surface 2, since

light is reflected from an optically denser medium. The power reflection coefficients R_{r1} , R_{r2} and R_{r3} at the reflection surfaces 1, 2 and 3, respectively, can be calculated using the following Fresnel equations:

$$R_{r1} = \left(\frac{n_c - n_m}{n_c + n_m}\right)^2, R_{r2} = \left(\frac{n_m - n_s}{n_m + n_s}\right)^2, R_{r3} = \left(\frac{n_s - n_m}{n_s + n_m}\right)^2. \quad (4.1)$$

The losses due to the Rayleigh scattering are inverse proportional to the fourth power of the wavelength ($1/\lambda^4$). The attenuation coefficient $\alpha_c(\lambda)$, in dB/km, due to the Rayleigh scattering is given by the following equation :

$$\alpha_c(\lambda) = \alpha_0 \frac{\lambda_0^4}{\lambda^4}. \quad (4.2)$$

where α_0 is the attenuation coefficient in dB/km at wavelength λ_0 . R_{s1} , R_{s2} and R_{s3} can be calculated by means of the attenuation coefficients and the Beer's Law that says that the transmitted power decays exponentially with the propagation distance L , (in km) through the optical fiber, thus :

$$R_{s1} = \exp(-\tilde{a}L), R_{s2} = f_{s2}R_{s1}, R_{s3} = f_{s3}R_{s1} \quad (4.3)$$

where \tilde{a} is the attenuation coefficient in km^{-1} and is correlated to α_c as $\alpha_c \left[\frac{\text{dB}}{\text{km}}\right] = \frac{10}{L} \log\left(\frac{1}{R_{s1}}\right) = 4.343 \tilde{a} \left[\frac{1}{\text{km}}\right]$. For simplicity, Rayleigh scattering loss coefficients R_{s2} and R_{s3} considered to be proportional to R_{s1} by factors of f_{s2} and f_{s3} , respectively. These factors are changing depending on the characteristics (e.g. roughness) of the fabricated microstructure, since every photopolymerized microstructure exhibits different surface roughness and porosity, depending upon exposure conditions.

The total reflected electric field, $E_{r(MD)}$, is thus given by Equation (4.4):

$$E_{r(MD)} = \sqrt{R_1}E_0 + (1 - T_1)(1 - R_1)(1 - a)\sqrt{R_2}E_0e^{-i2D\varphi_1+i\pi} \\ + (1 - T_1)(1 - T_2)(1 - R_1)(1 - R_2)(1 - a)(1 - L_s)\sqrt{R_3}E_0e^{-i2(D\varphi_1+d\varphi_2)} \quad (4.4)$$

where E_0 is the input field and φ_1 and φ_2 are the round-trip propagation phase shifts, and are equals to $\varphi_1 = 2\pi n_s/\lambda$ and $\varphi_2 = 2\pi n_m/\lambda$. From Eq. (4.4), we obtain the normalized reflection spectrum $R_{(MD)}(\lambda)$ as follows:

$$R_{(MD)}(\lambda) = |E_r/E_0|^2 \\ = R_1 + R_2(1 - T_1)^2(1 - R_1)^2(1 - a)^2 \\ + R_3(1 - T_1)^2(1 - T_2)^2(1 - R_1)^2(1 - R_2)^2(1 - a)^2(1 - L_s)^2 \\ - 2\sqrt{R_1R_2}(1 - T_1)(1 - R_1)(1 - a) \cos\left(\frac{4\pi n_s D}{\lambda}\right) \\ + 2\sqrt{R_1R_3}(1 - T_1)(1 - T_2)(1 - R_1)(1 - R_2)(1 - a)(1 - L_s) \cos\left(\frac{4\pi n_s D}{\lambda} + \frac{4\pi n_m d}{\lambda}\right) \\ - 2\sqrt{R_2R_3}(1 - T_1)^2(1 - T_2)(1 - R_1)^2(1 - R_2)(1 - a)^2(1 - L_s)^2 \cos\left(\frac{4\pi n_m d}{\lambda}\right) \quad (4.5)$$

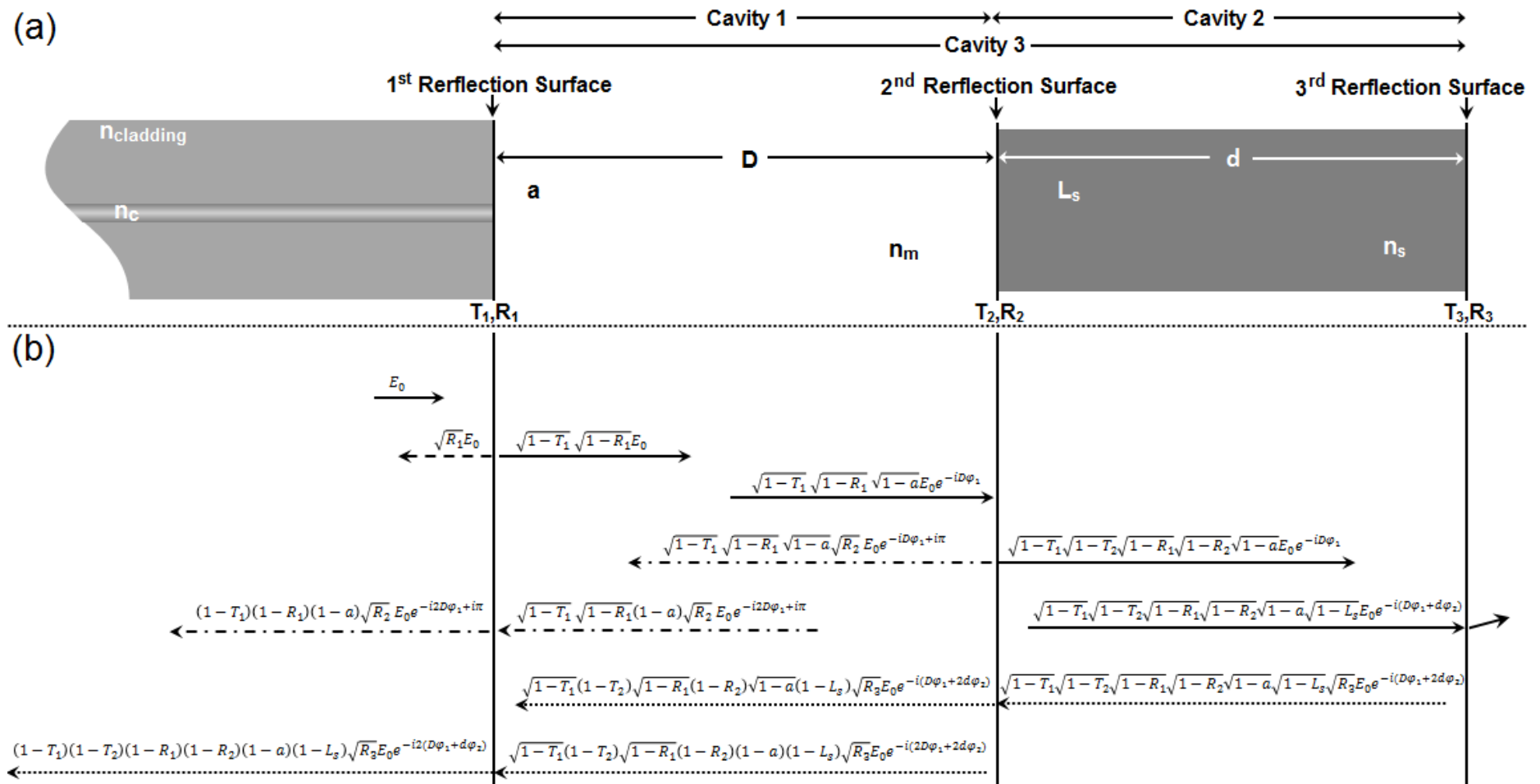


Fig. 4.4. Microdrum FP resonator model for two-beam optical interference approximation. (a) Schematic design of the FP cavity, where are presented the three reflection surfaces as well as the formed FP cavities and their characteristics. (b) The field amplitudes at the three reflection surfaces.

The simulated spectra according to Eq. (4.4), as well as the recorded spectrum at ambient air conditions of the microdrum FP resonator are presented in Figure 4.5. In order to simulate the reflectance spectrum in dB scale, one has to plot the $10\log R_{(MD)}(\lambda)$. The blue curve corresponds to the recorded experimental results. The red dashed curve corresponds to the simulated spectrum using as cavities lengths the effective lengths of the cavities $D_{\text{eff}} = 13.96 \mu\text{m}$ and $d_{\text{eff}} = 9.15 \mu\text{m}$, as they had been calculated from the experimental interference spectrum. The green curve corresponds to the simulated spectrum using as cavities lengths the $D_{\text{SEM}} = 13.9 \mu\text{m}$ and $d_{\text{SEM}} = 9.6 \mu\text{m}$ the value through SEM imaging. The main reason for the deviation of the values extracted from the SEM images, from those calculated through the recorded Fabry-Perot spectra, is the observation angle from which the samples were examined during SEM inspection, resulting in slightly erroneous thickness values. Moreover, the transmission loss factors used for the simulations were $T_1 \approx 0.035$ calculated according to the optical fiber characteristics [17], while considered to be $T_2 = 0.05$ since we assumed that the polymerized hybrid material the transmission losses will be higher than those of the optical fiber, as a multi-composite material. Moreover, for the Rayleigh scattering loss coefficients, $\alpha_o = 0.23 \text{ dB/km}$ at $\lambda_o = 1550 \text{ nm}$ according to the optical fiber characteristics [17], while Rayleigh scattering factors herein equals to $f_{s2} = 2$ and $f_{s3} = 14$ for the reflection surfaces 2 and 3 respectively. The air cavity loss factor was considered to be $a = 0.01$ [3] and the membrane loss factor considered to be $L_s = 0.03$. Finally, the dispersion of the photopolymerised material was not considered in the calculation of the theoretical spectral of Fig. 4.5, introducing an additional parameter that leads to deviatios with respect to the experimental data.

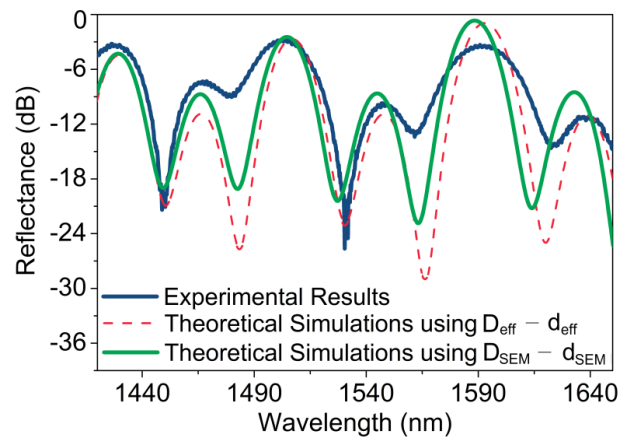


Fig. 4.5. Interference spectra of the microdrum FP resonator fabricated on the endface of SMF-28e, while it was exposed to ambient air conditions. The blue curve corresponds to the experimental results, while dashed red and green curves correspond to the simulation results using the two-beam optical interference approximation for $D_{\text{eff}} - d_{\text{eff}}$ and $D_{\text{SEM}} - d_{\text{SEM}}$ respectively.

The simulated results seem to be in relatively good agreement with the experimental interference spectrum. The differences observed at the amplitude strength of the spectra are due to the loss factors that cannot be precisely defined, since the actual loss factors of the photopolymerised resin and the cleaved surface are practically unknown. Nevertheless, the simulation model that was deployed herein can be used

for predicting a first image of the expected spectrum of a multi-layer FP microdrum resonator.

4.1.3 Simulating the reflection spectrum of the multiple FP optical fiber microdrum resonator using the Finite - Difference Time - Domain (FDTD) method

Finite-difference time-domain (FDTD) or Yee's method is a numerical analysis technique used for modeling computational electrodynamics, finding approximate solutions to the associated system of differential equations. The FDTD method belongs in the general class of grid-based differential numerical modeling methods. The novelty of Kane Yee's FDTD scheme, presented in his seminal 1966 paper was to apply centered finite difference operators on staggered grids in space and time for each electric and magnetic vector field component in Maxwell's curl equations [18]. The descriptor "Finite-difference time-domain" and its corresponding "FDTD" acronym were originated by Allen Taflove in 1980.

Herein, the OptiFDTD software, developed by the Optiwave Systems Inc., was used to simulate the microdrum FP resonator [19]. For the simulation modeling design was based on the microdrum FP resonator presented in Fig. 4.2. The effective lengths of the cavities as they had been calculated from the experimental interference spectrum (see Fig. 4.2(c)) had been used for the design, namely $D_{\text{eff}} = 13.96 \mu\text{m}$ and $d_{\text{eff}} = 9.15 \mu\text{m}$ corresponding to the air cavity and the membrane respectively. The refractive index of the core of the optical fiber was set to be equal to $n_c = 1.4682$ while its cladding as $n_{\text{cladding}} = 1.4677$. The refractive index of the fabricated microdrum was equal to $n_s = 1.52$, while air was used as surrounding medium ($n_m = 1$). A wafer of $130 \mu\text{m}$ length and $140 \mu\text{m}$ width was used at the Optiwave program. For the input field a Gaussian modulated continuous wave was used. For running a 2D simulation the Mesh Delta parameters were set at $0.09 \mu\text{m}$, while it was running for 4850 time steps.

The FDTD simulation results are presented in Figure 4.6. Figure 4.6(a) shows how the standing modes are confined and changing in spatial frequency within the individual cavities, as the light is propagating through the FP structure. As it is observed in Fig. 4.6 the standing waves formed are expanding as light propagates outside the optical fiber to the air cavity, and then are again get compressed as the light penetrate the photopolymerized membrane; this corresponds to the optical path of each section.

Figure 4.5(b) presents the reflection spectrum, of the FDTD simulations (red curve). The experimental spectrum is also presented in the diagram of Fig, 4.5(b) (blue curve) for comparison reasons. As it can be observed, the simulation spectrum is in a quite good agreement with the experimental one. The discrepancies that are observed are due to the differences of the real structure to the simulation design, since the reflection surfaces of the photopolymerized resonator present imperfections such as roughness etc. that cannot be inserted to the simulation design.

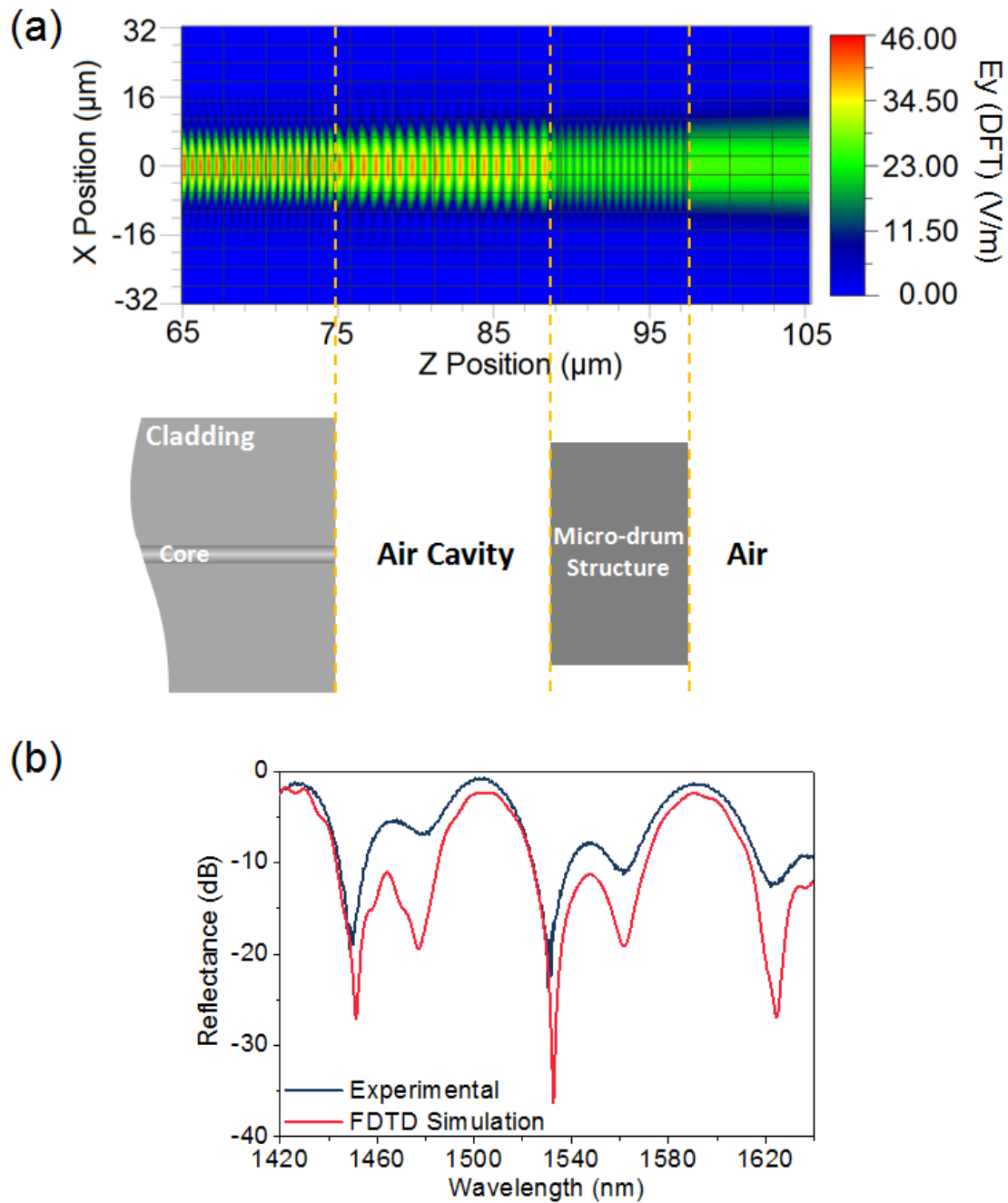


Fig. 4.6. FDTD simulations according to the microdrum FP endface resonator. (a) The image of the modes as the light is propagating through the optical fiber to the FP resonator. The dashed orange lines are denoting the cavities of the FP resonator on the color diagram, while the sketch of the microdrum endface FP resonator is presented below. (b) Interference reflection spectrum of the microdrum FP resonator fabricated on the endface of SMF-28e. Red curve corresponds to the FDTD simulation results, while blue curve corresponds to the experimental results.

4.2 Microfunnel FP optical fiber endface resonator; design and principle of operation

In order to avoid the multiple FP resonance between the two surfaces of the thin membrane, which in turn complicates the interrogated spectrum, a different microstructure was designed and fabricated, with an inclination of approximately 20° forming a funnel-shape structure, homocentrically with the membrane (see Fig. 4.7, see 3rd reflection surface) [13]. Calculations based on Shell's law were used to

determine the suitable inclination that had to be used for the design and fabrication of the microfunnel defect. This inclination directs the reflected light of the outer FP surface, outside the numerical aperture (NA) of the optical fiber [17]; thus, interference effects related to this surface were fully suppressed, resulting single FP interrogation spectra.

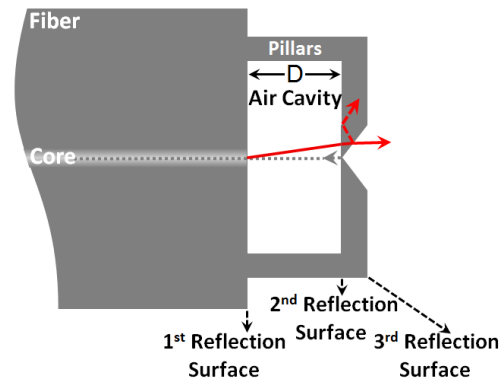


Fig. 4.7. Design and principle of operation of the FP microfunnel resonator fabricated on the endface of a single mode SMF-28e optical fiber. Grey dashed line corresponds to the reflected light that is recording. Red solid line and red dashed line corresponds to the guided light for the maximum angle of the Numerical Aperture (NA) of the core of the optical fiber and the reflected light from the fabricated funnel and the surfaces of the microstructure respectively.

4.2.1 Spectral characterization of the endface FP microfunnel resonator

Figures 4.8(a) and 4.8(b) present an optical microscope image and an SEM image respectively of the fabricated microfunnel resonator on the endface of the optical fiber [13]. For the fabrication of this resonator, the laser power was adjusted to 18 mW, measured before the objective, while the laser scanning speed was set at 100 $\mu\text{m/s}$. The specific cavity demonstrated herein consists of $\sim 15.9\mu\text{m}$ air cavity, resulting a periodic modulation of the reflected optical spectrum by notches of $\sim 11\text{dB}$ in amplitude strength with a free spectral range of $\sim 80\text{nm}$. Moreover, the photopolymerized membrane thickness is 10.4 μm . The problem in this case is that the fiber core has to be aligned precisely to the microfunnel, otherwise the single FP interference spectrum turns to a multiple FP resonance spectrum.

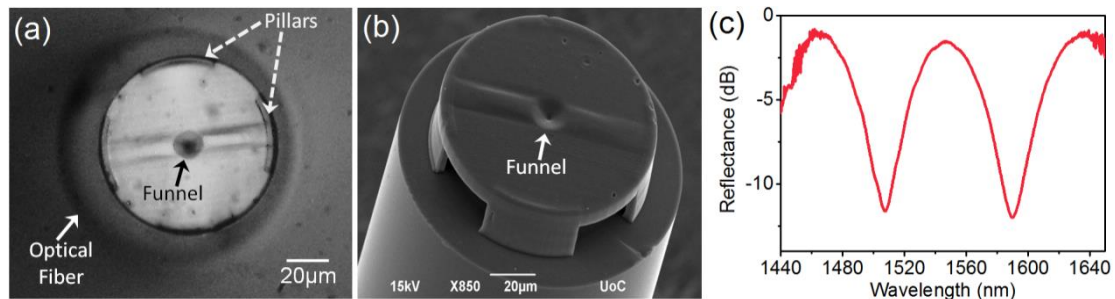


Fig. 4.8. Microfunnel FP resonator fabricated on the endface of a single mode SMF-28e optical fiber. (a) Optical microscope image of the fabricated structure. (b) Scanning electron microscope (SEM) image. (c) Interference spectrum of the single FP microfunnel resonator.

4.2.2 Simulating the reflection spectrum of the multiple FP optical fiber endface microfunnel resonator using two-beam optical interference approximation

In order to predict the interference spectrum of the microfunnel FP resonator another model based on two-beam optical interference approximation was developed. In this case a single FP resonating cavity of length D is formed, between the 1st and the 2nd reflection surfaces, labeled as Cavity 1 in Figure 4.9(a).

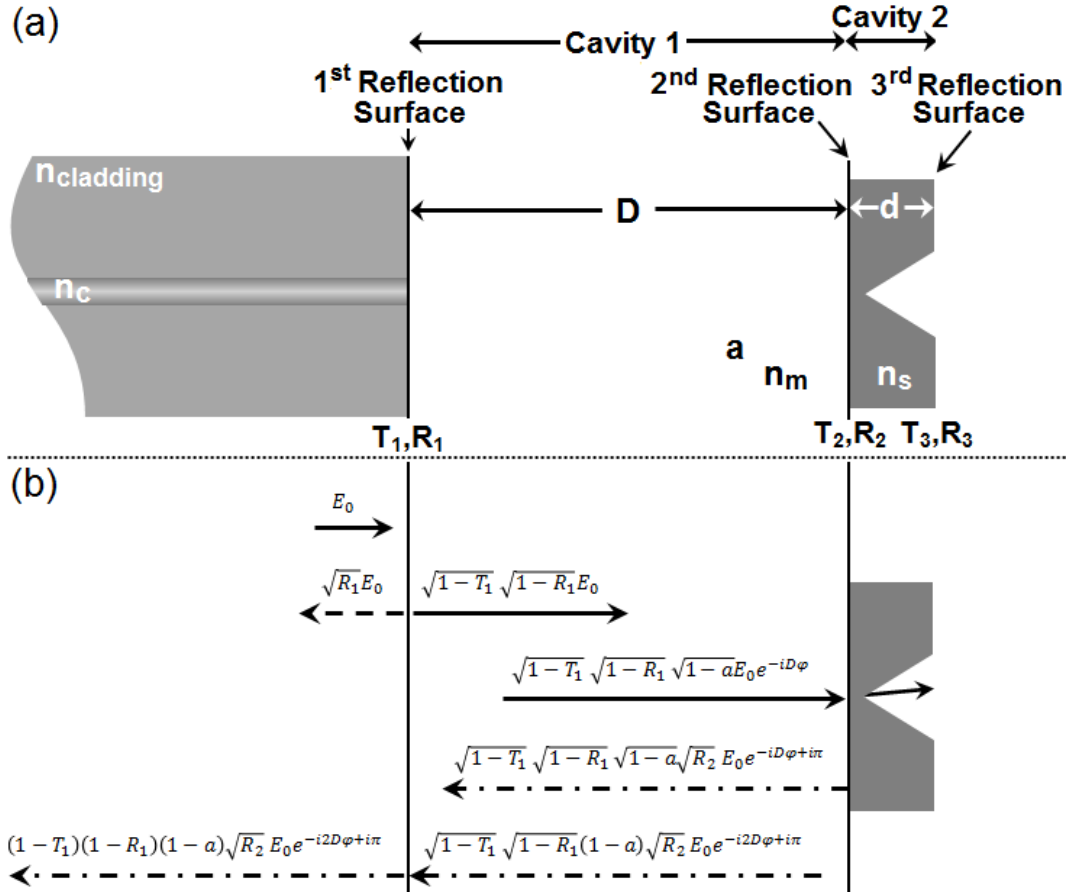


Fig. 4.9. Microfunnel FP resonator model for two-beam optical interference approximation. (a) Schematic design of the FP cavity, where are presented the three reflection surfaces as well as the formed FP cavities and their characteristics. (b) The field amplitudes at the two reflection surfaces.

The refractive index of the Cavity 1, namely n_m , is equal to the refractive index of the medium filling the cavity. The Cavity 2 which is formed by the reflection surfaces 2 and of length d refractive index of n_s , does not contribute in the electric field, since the inclination of the 3rd reflection surface directs the reflected light away from the NA of the core (see Fig. 4.7). The refractive index of the core of the optical fiber is labeled as n_c , while this of the cladding of the optical fiber is denoted as $n_{cladding}$. Again $R_1 = R_{r1}R_{s1}$, $R_2 = R_{r2}R_{s2}$ and $R_3 = R_{r3}R_{s3}$. R_{r1} , R_{r2} and R_{r3} correspond to the power reflection coefficients at surfaces 1, 2 and 3 respectively and are calculated according to Eq. (4.1), while R_{s1} , R_{s2} and R_{s3} are the Rayleigh scattering loss coefficients calculated using Eq. (4.2). T_1 , T_2 and T_3 are the transmission loss factors at reflection surfaces 1, 2 and 3 respectively, which are due to the surface imperfections (e.g., roughness). Finally, α is the air cavity loss factor caused by

diffraction in the air cavity (Cavity 1).

Figure 4.9(b) shows the electric fields at the 1st and 2nd reflection surfaces. The total reflected electric field at the detector, $E_{r(MF)}$, is given by the sum of all the reflected electric fields from these two surfaces and it is equal to:

$$E_{r(MF)} = \sqrt{R_1}E_0 + (1 - T_1)(1 - R_1)(1 - a)\sqrt{R_2}E_0e^{-i2D\varphi+i\pi} \quad (4.6)$$

where E_0 is the input field and φ is the round-trip propagation phase shift, which is equal to $\varphi = 2\pi n_s/\lambda$. From Eq. (4.7), we obtain the normalized reflection spectrum $R_{(MF)}(\lambda)$ as follows:

$$\begin{aligned} R_{(MF)}(\lambda) &= |E_r/E_0|^2 \\ &= R_1 + R_2(1 - T_1)^2(1 - R_1)^2(1 - a)^2 \\ &\quad - 2\sqrt{R_1R_2}(1 - T_1)(1 - R_1)(1 - a) \cos\left(\frac{4\pi n_s D}{\lambda}\right) \end{aligned} \quad (4.7)$$

According to Eq. (4.7) the simulated spectra for the microfunnel FP resonator presented in Figure 4.8, are presented in Figure 4.10, by plotting the $10\log R_{(MF)}(\lambda)$.

The blue curve corresponds to the recorded experimental results. The red dashed curve corresponds to the simulated spectrum using as cavity length the effective length $D_{\text{eff}} = 14.325 \mu\text{m}$ as it had been calculated from the experimental interference spectrum. The green curve corresponds to the simulated spectrum using as cavity length the $D_{\text{SEM}} = 15.92 \mu\text{m}$, extracted through SEM imaging. As it was already mentioned, the main reason for the deviation of these values is the observation angle from which the sample was examined during SEM observation. Again the transmission loss factors used for the simulations were $T_1 \approx 0.035$ and $T_2 = 0.05$ (see section 4.1.2), while the Rayleigh scattering factor for the reflection surface 2 equals to $f_{s2} = 13$. Finally, the air cavity loss factor was considered again to be $a = 0.01$ [3].

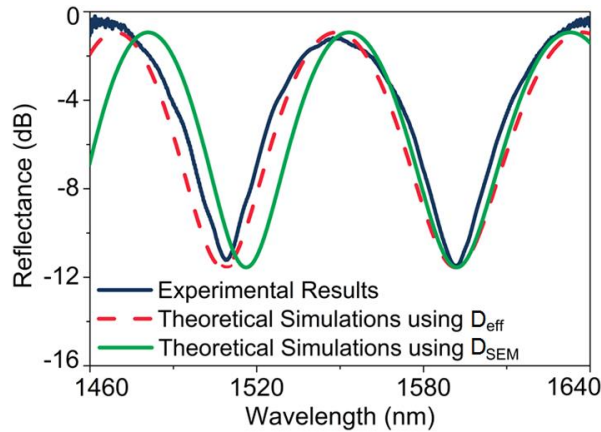


Fig. 4.10. Interference spectra of the microdrum FP resonator fabricated on the endface of SMF-28e, while it was exposed to ambient air conditions. The blue curve corresponds to the experimental results, while dashed red and green curves correspond to the simulation results using the two-beam optical interference approximation for D_{eff} and D_{SEM} respectively. The main reason for the deviation of the values extracted from the SEM images, from those calculated through the recorded FP spectra, is the observation angle from which the samples were examined during SEM observation.

As it is observed from Figure 4.10, the two-beam optical interference approximation model that was developed for the microfunnel FP endface resonator can correctly predict the characteristics of the interference spectrum giving simulated results that are in good agreement with the experimental interference spectrum.

4.2.3 Simulating the reflection spectrum of the multiple FP microfunnel resonator using the Finite - Difference Time - Domain (FDTD) method

In order to simulate the microfunnel FP endface resonator, the applied design to the OptiFDTD software was based on the microfunnel FP resonator presented in Fig. 4.8. As length of the air cavity (Cavity 1) was used the effective length calculated from the experimental interference spectrum (see Fig. 4.8(c)), namely $D_{\text{eff}} = 14.325 \mu\text{m}$ while for the photopolymerized membrane (Cavity 2) as length was used the value extracted from SEM imaging, namely $d_{\text{SEM}} = 10.4 \mu\text{m}$. The refractive index of the core of the optical fiber was set to be equal to $n_c = 1.4682$ while for its cladding as $n_{\text{cladding}} = 1.4677$. The refractive index of the photopolymerized microfunnel was equal to $n_s = 1.52$, while air was used as surrounding medium ($n_m = 1$). The wafer that was used at the OptiFDTD had $130 \mu\text{m}$ length and $140 \mu\text{m}$ width. Again a Gaussian modulated continuous wave was used as input field, while Mesh Delta parameters were set at $0.09 \mu\text{m}$ for running a 2D simulation. 4850 time steps were used for the simulations.

The FDTD simulation results are presented in Figure 4.11. The modes behavior while the light is propagating through the FP cavity is presented Figure 4.11(a). The sketch of the microfunnel FP resonator on the endface of the optical fiber, existing below the color diagram highlights with orange dust lines the orientations of the FP cavities. As it is observed the modes are expanding as light propagates outside the optical fiber to the air cavity, and then as the light propagates through the photopolymerized membrane, the inclined walls of the fabricated microfunnel direct the light away from the air cavity. Actually, as it is observed in Figure 4.11(a), the reflected light from the outer surface of the membrane (3rd reflection surface), is totally reflected within the photopolymerized membrane.

Figure 4.11(b) presents the interference reflection spectrum, as it is obtained for the FDTD simulations (red curve), while blue curve corresponds to the experimental recorded spectrum. As it can be observed, the simulated FDTD spectrum is in a good agreement with the experimental one. The discrepancies that are observed again are due to the surface characteristics and porosity of the photopolymerized structure that cannot be explicitly inserted into the simulation design.

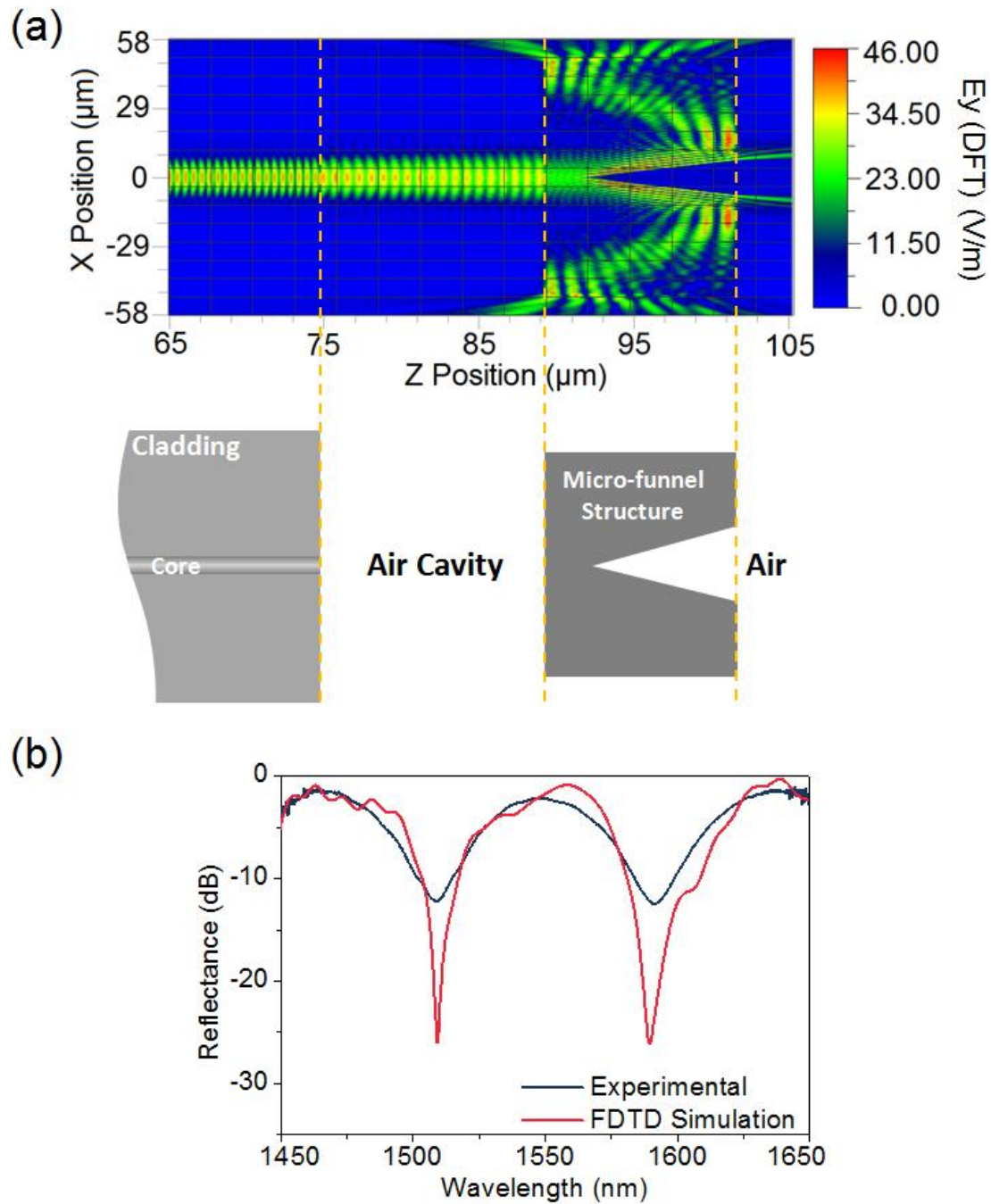


Fig. 4.11. FDTD simulations according to the microfunnel FP endface resonator. (a) The image of the modes as the light is propagating through the optical fiber to the FP resonator. The dashed orange lines are denoting the cavities of the FP resonator on the color diagram, while the sketch of the microfunnel endface FP resonator is presented below. (b) Interference reflection spectrum of the microfunnel FP resonator fabricated on the endface of SMF-28e. Red curve corresponds to the FDTD simulation results, while blue curve corresponds to the experimental results.

4.3 Microprism FP endface resonator; design, principle of operation and spectral characterization

A third microresonator was designed in order to overcome the alignment problems of the microfunnel FP resonator with respect to the core of the optical fiber. This time a 20° inclination was given all across the outer surface of the FP structure, resulting in a “prism”-like shape (see Fig. 4.12). Again, the inclination of the outer

surface directs the reflected light outside the numerical aperture (NA) of the fiber [17], ensuring a single FP interrogation spectrum [13, 20-22].

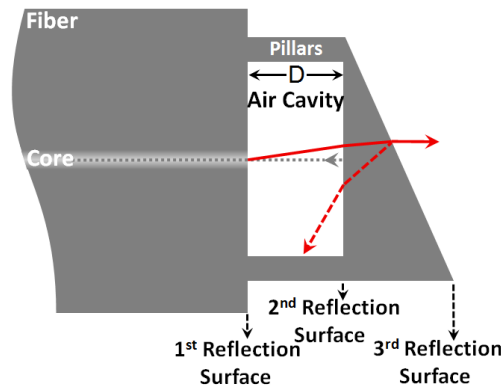


Fig. 4.12. Design and principle of operation of the FP microprism resonator fabricated on the endface of a single mode SMF-28e optical fiber. Grey dashed line corresponds to the reflected light that is recording. Red solid line and red dashed line corresponds to the guided light for the maximum angle of the Numerical Aperture (NA) of the core of the optical fiber and the reflected light from the outer reflection surface of the microstructure respectively.

4.3.1 Spectral characterization of the endface FP microprism resonator

The specific cavity presented in Figures 4.13(a) and 4.13(b) through an optical microscope image and a SEM image respectively, consists of a $17.9\mu\text{m}$ air cavity, resulting a periodic modulation of the reflected optical spectrum by notches of $\sim 22\text{dB}$ in amplitude strength with a free spectral range of $\sim 68\text{nm}$. For the fabrication of the resonator, the laser power was adjusted to 18 mW, measured before the objective, while the laser scanning speed was set at $100\ \mu\text{m/s}$. The inclination of the outer surface of the photopolymerized structure derived from the SEM image is $\sim 16^\circ$. This microprism design ensures the single FP interference of the light between the 1st and the 2nd reflection surfaces, even if the microstructure is not aligned precisely to the core of the optical fiber.

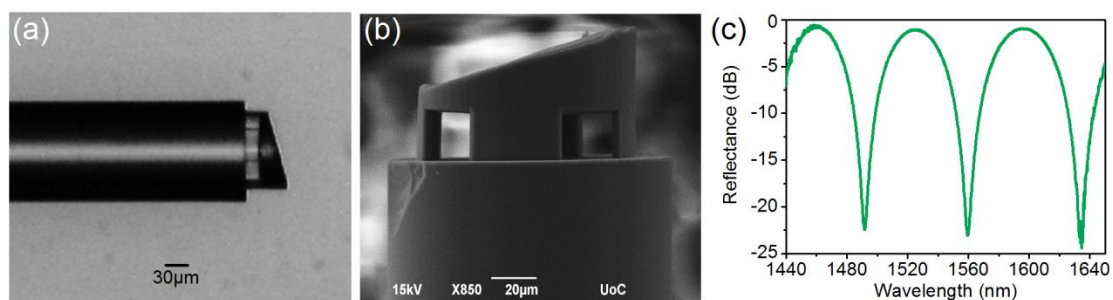


Fig. 4.13. Microprism FP resonator fabricated on the endface of a single mode SMF-28e optical fiber. (a) Optical microscope image of the fabricated structure. (b) Scanning electron microscope (SEM) image. (c) Interference spectrum of the single FP microprism resonator.

4.3.2 Simulating the reflection spectrum of the multiple FP microprism resonator using two-beam optical interference approximation

The two-beam optical interference approximation was used also in this case to develop a simulation model which will predict the interference spectra of the

microprism FP resonators. A single FP resonating cavity of length D and n_m refractive index is formed between the 1st and the 2nd reflection surfaces, labeled as Cavity 1 in Figure 4.14(a). As previously n_m equals to the refractive index of the medium immersed in FP Cavity 1. The Cavity 2, formed by the 2nd and 3rd reflection surfaces does not contribute in the electric field, since the inclination of the 3rd reflection surface directs the reflected light away from the NA of the core (see Fig. 4.12). The refractive index of the photopolymerized structure is n_s . Moreover, the refractive index of the core of the optical fiber is labeled as n_c , while this of the cladding of the optical fiber is denoted as $n_{cladding}$.

As in previous presented FP resonators, $R_1 = R_{r1}R_{s1}$, $R_2 = R_{r2}R_{s2}$ and $R_3 = R_{r3}R_{s3}$. R_{r1} , R_{r2} and R_{r3} correspond to the power reflection coefficients at surfaces 1, 2 and 3 respectively and are calculated according to Eq. (4.1), while R_{s1} , R_{s2} and R_{s3} are the Rayleigh scattering loss coefficients calculated using Eq. (4.2). T_1 , T_2 and T_3 are the transmission loss factors at reflection surfaces 1, 2 and 3 respectively, which are due to the surface imperfections (e.g., roughness). Finally, α is the air cavity loss factor caused by diffraction in the air cavity (Cavity 1).

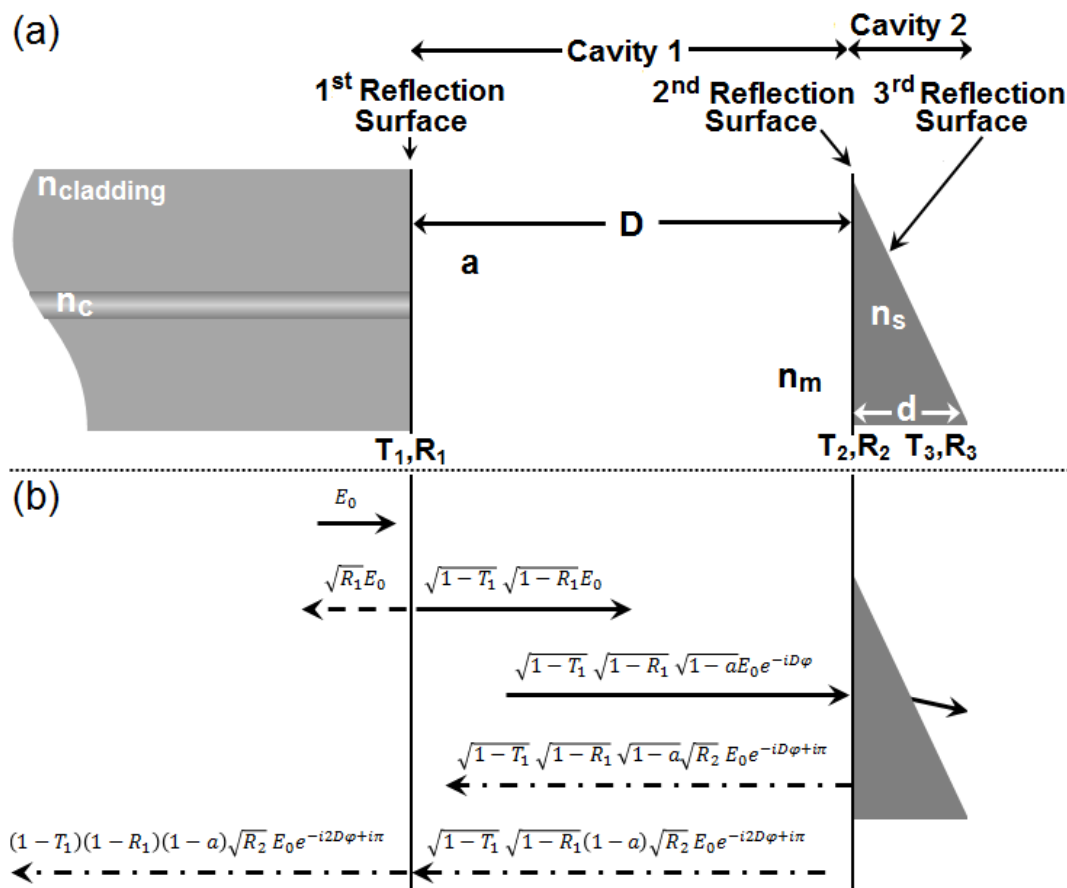


Fig. 4.14. Microprism FP resonator model for two-beam optical interference approximation. (a) Schematic design of the FP cavity, where are presented the three reflection surfaces as well as the formed FP cavities and their characteristics. (b) The field amplitudes at the two reflection surfaces.

Figure 4.14(b) shows the electric fields at the 1st and 2nd reflection surfaces. As it is observed, the electric field components presented in the microprism FP resonator

are the same like those presented in the microfunnel FP resonator (see Fig. 4.9). This was expected since the characteristics of the reflection surfaces in both cases are common, and furthermore the 3rd reflection surface did not participate at the interference process. The total reflected electric fields at the detector, $E_{r(MP)}$, is given by the sum of all the reflected electric fields from these two surfaces and it is equal to:

$$E_{r(MP)} = \sqrt{R_1}E_0 + (1 - T_1)(1 - R_1)(1 - a)\sqrt{R_2}E_0e^{-i2D\varphi+i\pi} \quad (4.8)$$

where E_0 is the input field and φ is the round-trip propagation phase shift, which is equal to $\varphi = 2\pi n_s/\lambda$. From Eq. (4.8), we obtain the normalized reflection spectrum $R_{(MF)}(\lambda)$ as follows:

$$\begin{aligned} R_{(MF)}(\lambda) &= |E_r/E_0|^2 \\ &= R_1 + R_2(1 - T_1)^2(1 - R_1)^2(1 - a)^2 \\ &\quad - 2\sqrt{R_1R_2}(1 - T_1)(1 - R_1)(1 - a) \cos\left(\frac{4\pi n_s D}{\lambda}\right) \end{aligned} \quad (4.9)$$

The experimental and the simulated interference spectra of four different fabricated microprism resonators, exposed to ambient air conditions, are shown in Figure 4.15. The simulation model was applied for all the D_{eff} values and only for two cases of D_{SEM} that were existing SEM data.

The values of the transmission loss factors and the air cavity loss factor a that were used herein were the same like those used in microdrum and microfunnel FP resonators (see section 4.1.2 and 4.2.2). The Rayleigh scattering factor f_{s2} for the reflection surface 2 was varying between 8 and 15 depending on the surface microstructure.

In the case where D_{eff} equals to 17.1 μm the corresponding value through SEM imaging was measured at $D_{\text{SEM}} = 17.9 \mu\text{m}$, while for the case of D_{eff} equals to 32.3 μm the D_{SEM} value equals to 33.1 μm .

Another physically expected observation emerging from Figure 4.15 is that an increase in the fabricated cavity length D is followed by an increase of the number of fringes that appear within a given spectral range, with a simultaneous decrease of the corresponding free spectral range (FSR) of the fringes. For a 7.3 μm fabricated cavity length, the FSR equals 162.14 nm with a fringe visibility of about 15 dB, while in the case of a 32.3 μm cavity length, the FSR is 35.86 nm and the fringe visibility about 22 dB.

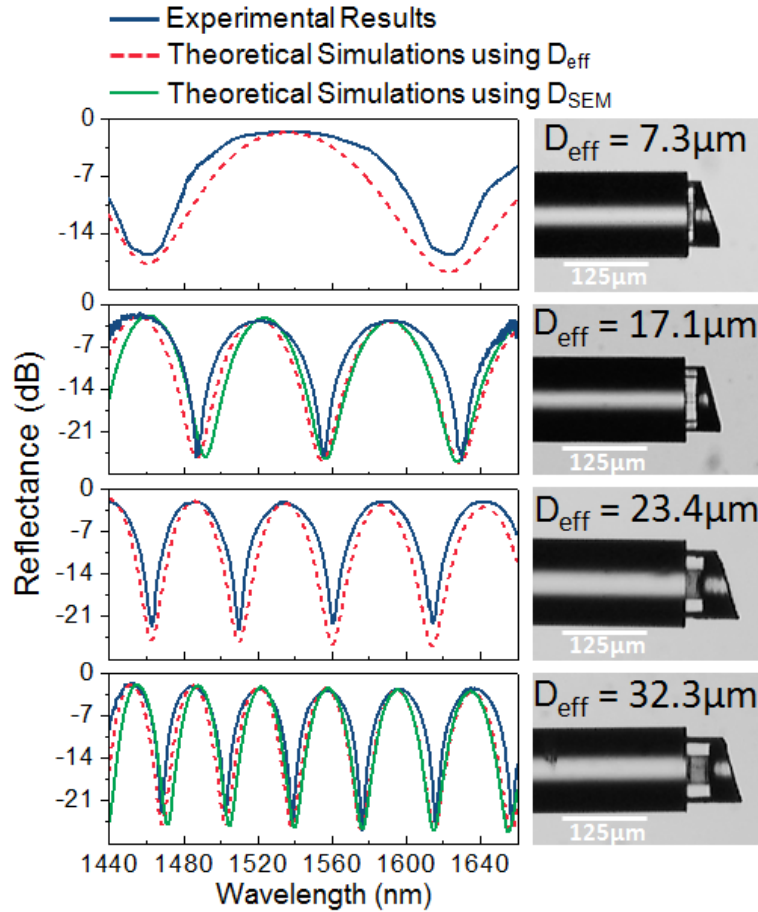


Fig. 4.15. Experimental and simulated interference spectra of four different fabricated microprism FP resonators on the endface of optical fiber, exposed to ambient conditions. At the right are also presented optical microscope images of these FP cavities. The blue curve corresponds to the experimental results, while dashed red and green curves correspond to the simulation results using the two-beam optical interference approximation for D_{eff} and D_{SEM} respectively. The theoretical simulations were done for all the D_{eff} values, while the simulation model was used only for two cases that were existing SEM data (D_{SEM}). The main reason for the deviation of the values extracted from the SEM images, from those calculated through the recorded FP spectra, is the observation angle from which the samples were examined during SEM observation.

4.3.3 Simulating the reflection spectrum of the multiple FP microprism resonator using the Finite - Difference Time - Domain (FDTD) method

The design of the microprism FP endface resonator presented in Figure 4.13 was applied to the OptiFDTD software in order to simulate the FP interference spectrum. As length of the air cavity (Cavity 1) was used the effective length calculated from the experimental interference spectrum (see Fig. 4.13(c)), namely $D_{\text{eff}} = 14.84 \mu\text{m}$. For the photopolymerized membrane (Cavity 2) the length of the short side of the triangle of the microprism was set at $d_{\text{SEM}(\text{short})} = 8 \mu\text{m}$ while the long one was set at $d_{\text{SEM}(\text{long})} = 33 \mu\text{m}$. Both values were extracted from the SEM imaging (see Fig. 4.13b). The refractive index of the core of the optical fiber was set to be equal to $n_c = 1.4682$ while for its cladding as $n_{\text{cladding}} = 1.4677$. The refractive index of the photopolymerized microfunnel was equal to $n_s = 1.52$, while air was used as surrounding medium ($n_m = 1$). The wafer dimension used at the OptiFDTD software

was 130 μm length by 140 μm width. A Gaussian modulated continuous wave was used as input field, while Mesh Delta parameters were set at 0.09 μm for running a 2D simulation. 4850 time steps were used for the simulations.

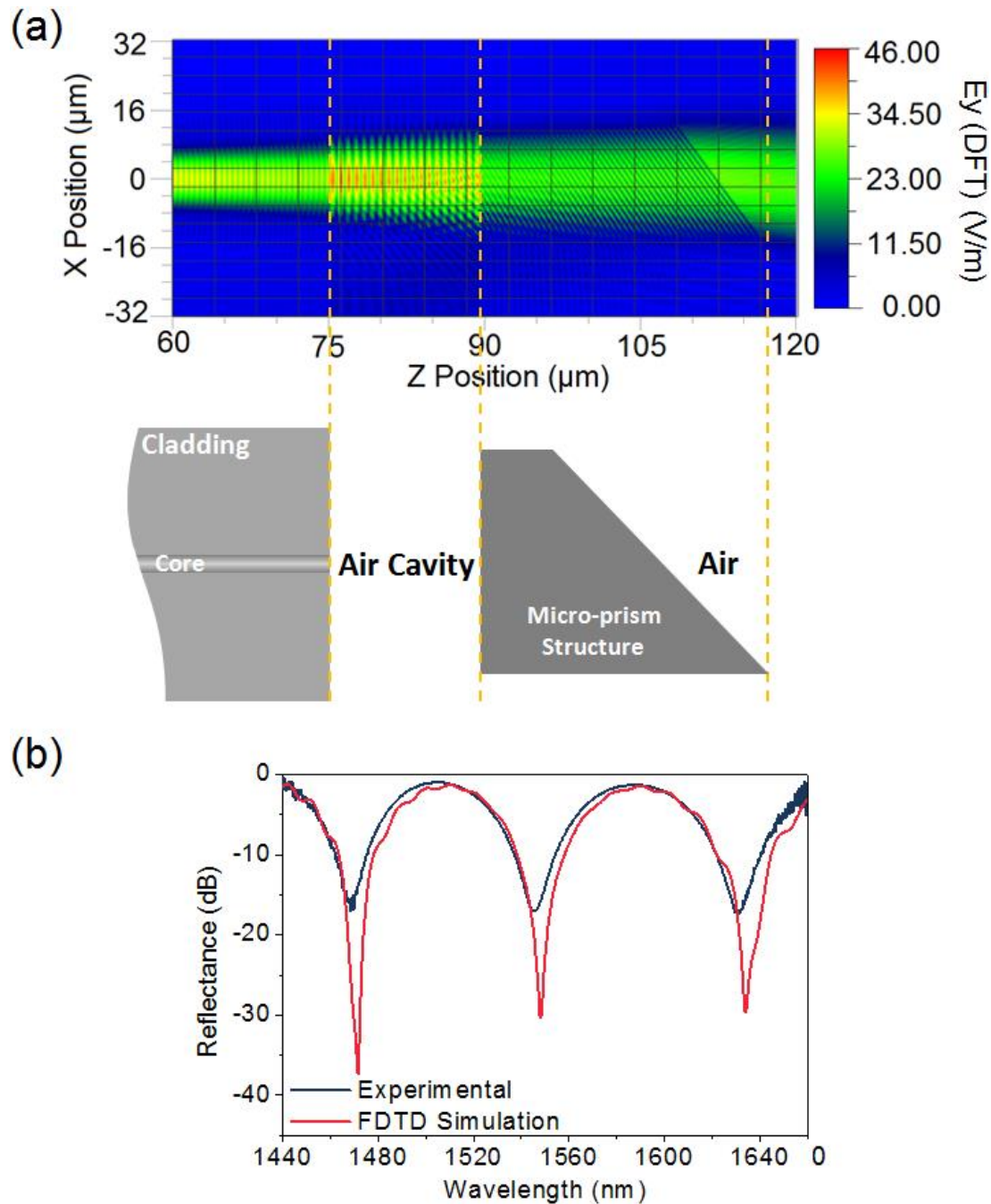


Fig. 4.16. FDTD simulations according to the microprism FP endface resonator. (a) The image of the modes as the light is propagating through the optical fiber to the FP resonator. The dashed orange lines are denoting the cavities of the FP resonator on the color diagram, while the sketch of the microprisms endface FP resonator is presented below. (b) Interference reflection spectrum of the microprism FP resonator fabricated on the endface of SMF-28e. Red curve corresponds to the FDTD simulation results, while blue curve corresponds to the experimental results.

The FDTD simulation results are presented in Figure 4.16. The modes behavior while the light is propagating through the FP cavity is presented Figure 4.16(a). The sketch of the microprism FP resonator on the endface of the optical fiber, below the

color diagram, highlights with orange dashed lines, the orientations of the FP cavities. As it is observed the modes are expanding as light propagates outside the optical fiber to the air cavity. Then as the light propagates through the photopolymerized microprism membrane the inclined of the outer surface direct the light away from the air cavity.

Figure 4.16(b) presents the interference reflection spectrum, as it is obtained for the FDTD simulations (red curve) and the experimental interference spectrum (blue curve). As it can be observed, the simulated FDTD spectrum is in a good agreement with the experimental one. Again discrepancies observed are attributed to the lack of exact information of the surface roughness and porosity of the photopolymerised section.

4.4 Summary

Herein, the three different FP microresonators fabricated by multiphoton polymerization technique on the endface of a standard single mode optical fiber (SMF-28e) were presented and analysed. The first FP resonator, a microdrum shape resonator, was consisting of a thin flat membrane suspended of four pillars, which were attached on the endface of the optical fiber. By this way a multiple FP resonator was developed. In order to avoid this multiple FP cavity, two different designs were fabricated, namely the microfunnel resonator and the microprism resonator. At the first on, an inclination of approximately 20° at a funnel-shape was introduced homocentrically with the membrane, while at the second one the inclination was given all across the outer surface, resulting a prism-like shape. By this way single endface FP resonators were developed diving similar interference spectrum. The difference between these two single FP resonators is that the microfunnel endface resonator has to be precisely aligned to the core of the optical fiber otherwise it gives a multiple FP interference spectrum.

To the best of our knowledge, even if multiphoton polymerization technique had already been used in order optical microstructures to be fabricated on the endface of optical fibers [23-31], it is the first time that this technique was used to fabricate FP resonators. With the present experiments, it is proved that multiphoton polymerization technique can be used to fabricate robust structures that are optically functional and the FP cavities geometry can be easily tuned, by changing either the design or the dimensions of the FP cavity according to the requirements of the experiments.

Moreover, two different simulation methods were used to predict the interference spectrum of the endface FP cavities. The first simulation method that was developed was based on two-beam optical interference approximation resulting special simulating models for each design of endface FP microresonator. The second simulation method was based on Finite-Difference Time-Domain (FDTD) method. A commercially available software, that of OptiFDTD (Optiwave Systems Inc.) was used and simulated the behavior of the modes during the light propagation throughout the FP devices, as well as the reflected interference spectrum.

References

- [1] F. Farahi, T. P. Newson, J. D. C. Jones, and D. A. Jackson, "Coherence multiplexing of remote fibre optic fabry-perot sensing system," *Optics Communications*, vol. 65, pp. 319-321, 1988/03/01/ 1988.
- [2] T. Wei, Y. K. Han, Y. J. Li, H. L. Tsai, and H. Xiao, "Temperature-insensitive miniaturized fiber inline Fabry-Perot interferometer for highly sensitive refractive index measurement," *Optics Express*, vol. 16, pp. 5764-5769, Apr 2008.
- [3] Z. L. Ran, Y. J. Rao, W. J. Liu, X. Liao, and K. S. Chiang, "Laser-micromachined Fabry-Perot optical fiber tip sensor for high-resolution temperature-independent measurement of refractive index," *Optics Express*, vol. 16, pp. 2252-2263, Feb 2008.
- [4] G. Gruca, D. Chavan, J. Rector, K. Heeck, and D. Iannuzzi, "Demonstration of an optically actuated ferrule-top device for pressure and humidity sensing," *Sensors and Actuators a-Physical*, vol. 190, pp. 77-83, Feb 1 2013.
- [5] D. Helie, S. Gouin, and R. Vallee, "Assembling an endcap to optical fibers by femtosecond laser welding and milling," *Optical Materials Express*, vol. 3, pp. 1742-1754, Oct 1 2013.
- [6] C. R. Liao, T. Y. Hu, and D. N. Wang, "Optical fiber Fabry-Perot interferometer cavity fabricated by femtosecond laser micromachining and fusion splicing for refractive index sensing," *Optics Express*, vol. 20, pp. 22813-22818, 2012/09/24 2012.
- [7] V. R. Machavaram, R. A. Badcock, and G. F. Fernando, "Fabrication of intrinsic fibre Fabry-Perot sensors in silica fibres using hydrofluoric acid etching," *Sensors and Actuators A: Physical*, vol. 138, pp. 248-260, 2007/07/20/ 2007.
- [8] X. Chen, F. Shen, Z. Wang, Z. Huang, and A. Wang, "Micro-air-gap based intrinsic Fabry-Perot interferometric fiber-optic sensor," *Applied Optics*, vol. 45, pp. 7760-7766, 2006/10/20 2006.
- [9] S. Pevec and D. Donlagic, "Miniature all-fiber Fabry-Perot sensor for simultaneous measurement of pressure and temperature," *Applied Optics*, vol. 51, pp. 4536-4541, Jul 2012.
- [10] T. Zhu, T. Ke, Y. Rao, and K. S. Chiang, "Fabry-Perot optical fiber tip sensor for high temperature measurement," *Optics Communications*, vol. 283, pp. 3683-3685, 2010/10/01/ 2010.
- [11] A. Lopez-Aldaba, A. Pinto, M. Lopez-Amo, O. Frazão, J. Santos, J. Baptista, *et al.*, "Experimental and Numerical Characterization of a Hybrid Fabry-Pérot Cavity for Temperature Sensing," *Sensors*, vol. 15, p. 8042, 2015.
- [12] X. Y. Zhang, Y. S. Yu, C. C. Zhu, C. Chen, R. Yang, Y. Xue, *et al.*, "Miniature End-Capped Fiber Sensor for Refractive Index and Temperature Measurement," *IEEE Photonics Technology Letters*, vol. 26, pp. 7-10, 2014.

- [13] V. Melissinaki, I. Konidakis, M. Farsari, and S. Pissadakis, "Fiber endface Fabry-Perot vapor microsensors fabricated by multiphoton polymerization technique," in *SPIE OPTO*, 2015, p. 8.
- [14] Y. J. Rao, M. Deng, D. W. Duan, and T. Zhu, "In-line fiber Fabry-Perot refractive-index tip sensor based on endlessly photonic crystal fiber," *Sensors and Actuators a-Physical*, vol. 148, pp. 33-38, Nov 2008.
- [15] S. Pevec and D. Donlagic, "Miniature all-silica fiber-optic sensor for simultaneous measurement of relative humidity and temperature," *Optics Letters*, vol. 40, pp. 5646-5649, Dec 1 2015.
- [16] J. H. Chen, X. G. Huang, J. R. Zhao, J. Tao, W. X. He, and S. H. Liu, "Fabry-Perot interference-based fiber-optic sensor for small displacement measurement," *Optics Communications*, vol. 283, pp. 3315-3319, Sep 2010.
- [17] "SMF-28e Fiber product information. URL: <http://www.princetel.com/datasheets/SMF28e.pdf>."
- [18] Y. Kane, "Numerical solution of initial boundary value problems involving maxwell's equations in isotropic media," *IEEE Transactions on Antennas and Propagation*, vol. 14, pp. 302-307, 1966.
- [19] "Information about OptiFDTD software: URL: <https://optiwave.com/category/products/component-design/optifdtd/>."
- [20] V. Melissinaki, M. Farsari, and S. Pissadakis, "A Fiber-Endface, Fabry-Perot Vapor Microsensor Fabricated by Multiphoton Polymerization," *Ieee Journal of Selected Topics in Quantum Electronics*, vol. 21, p. 10, Jul-Aug 2015.
- [21] V. Melissinaki, I. Konidakis, M. Farsari, and S. Pissadakis, "Fiber endface Fabry-Perot microsensor with distinct response to vapors of different chlorinated organic solvents," *IEEE Sensors Journal*, vol. PP, pp. 1-1, 2016.
- [22] V. Melissinaki, M. Farsari, and S. Pissadakis, "A Fiber Optic Fabry-Perot Cavity Sensor for the Probing of Oily Samples," *Fibers*, vol. 5, p. 1, 2017.
- [23] M. Malinauskas, A. Zukauskas, V. Purlys, A. Gaidukeviciute, Z. Balevicius, A. Piskarskas, *et al.*, "3D microoptical elements formed in a photostructurable germanium silicate by direct laser writing," *Optics and Lasers in Engineering*, vol. 50, pp. 1785-1788, Dec 2012.
- [24] H. E. Williams, D. J. Freppon, S. M. Kuebler, R. C. Rumpf, and M. A. Melino, "Fabrication of three-dimensional micro-photon structures on the tip of optical fibers using SU-8," *Optics Express*, vol. 19, pp. 22910-22922, Nov 2011.
- [25] N. Ma, P. C. Ashok, D. J. Stevenson, F. J. Gunn-Moore, and K. Dholakia, "Integrated optical transfection system using a microlens fiber combined with microfluidic gene delivery," *Biomedical Optics Express*, vol. 1, pp. 694-705, Sep 2010.
- [26] G. S. Sokolovskii, V. Melissinaki, V. V. Dudelev, S. N. Losev, K. K. Soboleva, E. D. Kolykhalova, *et al.*, "Superfocusing of high- M^2 semiconductor laser beams: experimental demonstration," in *SPIE Photonics Europe*, 2014, p. 7.
- [27] G. S. Sokolovskii, V. V. Dudelev, V. Melissinaki, S. N. Losev, K. K. Soboleva, A. G. Deryagin, *et al.*, "Optical trapping with superfocused high- M^2 laser diode beam," in *SPIE LASE*, 2015, p. 7.

- [28] Z. W. Xie, S. F. Feng, P. J. Wang, L. S. Zhang, X. Ren, L. Cui, *et al.*, "Demonstration of a 3D Radar-Like SERS Sensor Micro- and Nanofabricated on an Optical Fiber," *Advanced Optical Materials*, vol. 3, pp. 1232-1239, Sep 2015.
- [29] M. Kowalczyk, J. Haberko, and P. Wasylczyk, "Microstructured gradient-index antireflective coating fabricated on a fiber tip with direct laser writing," *Optics Express*, vol. 22, pp. 12545-12550, May 2014.
- [30] A. Žukauskas, *Improvement of the Fabrication Accuracy of Fiber Tip Microoptical Components via Mode Field Expansion* vol. 9, 2014.
- [31] T. Gissibl, M. Vieweg, M. M. Vogel, M. A. Ahmed, T. Graf, and H. Giessen, "Preparation and characterization of a large mode area liquid-filled photonic crystal fiber: transition from isolated to coupled spatial modes," *Applied Physics B-Lasers and Optics*, vol. 106, pp. 521-527, Mar 2012.

Chapter 5

Fabry-Perot optical fiber endface micro-resonators; devices and processing

Fabry-Perot (FP) interferometers are simple design, photonic elements that can provide decent light localization performance. Their cavity can be used for detecting changes occurring either within the resonance optical path, or loss and phase changes occurring at the reflected surfaces. Fiber-optic FP resonators have been successfully commercialized and widely used for measuring temperature [1], pressure [2, 3], strain [4, 5], refractive index (RI) [6-9], pH [10], displacement [11] etc. Especially, the measurement of RI changes using FP optical fiber sensors has attracted great attention, as they can offer a number of specific advantages over other optical fiber sensors, such as high sensitivity, high measurement range, ability for multi-parameters sensing, rapid response, etc.

Herein, FP hollow cavities photopolymerized onto commercially available telecommunication fiber endfaces have been fabricated and used for simultaneous measurements of refractive index and loss changes of an optical medium along a given optical path. These endface FP probes had been tested as sensing devices for gaseous and liquid species. Their sensing behavior is correlated with adsorption or diffusion effects into the porous photopolymerized reflection surface resulting distinct spectro-temporal response to different species.

The sensing mechanism of the fabricated devices is based on physisorption phenomena. Therefore, the devices were fully recovered, in terms of spectral response to their initial conditions, after each sensing cycle and could be reused several times without reducing their sensitivity and selectivity, always compared to sensors that are based on chemisorption effects.

In this chapter, the FP optical fiber endface design will be tested along different sensing functionalities, depicting the advantages and potential emerging from the specific approach. The chapter structure is as follows: in the first section the experimental apparatuses used for the testing and calibration of the operation of the FP optical fiber endface sensors in gaseous and liquid media will be presented. In the second section, the FP optical fiber endface sensor will be tested with respect to its response to ethanol vapors [12]. In the third section we further progress in order to exploit the sensing ability of the FP optical fiber endface sensor for the detection of three different chlorinated organic solvents, in order to test its potential spectro-temporal distinct response to solvents that their molecules exhibit dissimilar packing abilities [13]. Finally, in the last section, the FP optical fiber endface device will be tested as a liquid sensor this time, with respect to its response to oily samples [14].

5.1 Experimental apparatus used for the characterization of the FP optical fiber endface sensing probes.

The fabricated endface micro-prism FP sensing probes were tested for the detection of both gaseous (vapors) and liquid species. Below are presented in details the experimental set-ups that were used in both cases.

It has to be noted that the FP devices have been optimized for operation in the spectral region spanning between 1440 nm and 1660 nm, while being interrogated in reflection mode using a 50/50 AFC/PC coupler. All the measurements were performed using an optical fiber pigtailed superluminescence source (QPhotonics) and an Optical Spectrum Analyzer (OSA) ANDO AQ6317B (see Fig. 5.1).

5.1.1 Experimental apparatus used for the characterization of the FP microresonators for the detection of vapor species.

In order the fabricated FP probes to be tested as sensing devices for the detection of vapors, a specially designed stainless steel chamber of ~500 ml volume was used (see Fig. 5.1). The sensing head was placed at 3.5 cm above the bottom of the chamber using a fit-through connector. Appropriate inlets and outlets were adjusted on the top and along the perimeter of the chamber, for the injection of the organic solvents in liquid form and nitrogen buffer gas, respectively. Moreover, a manometer was attached to the chamber as presented in Figure 5.1, allowing the observation of changes in pressure due to the evaporation of the solvent. Finally, for easy inspection of the sample during the measurements in the chamber, a plexiglas window was fitted to the top of the chamber.

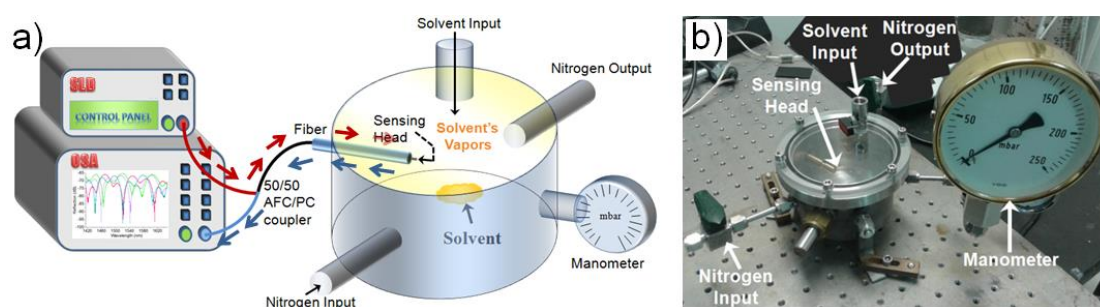


Fig. 5.1. Experimental set-up that was used for vapor measurements with the endface FP sensing devices. (a) Schematic representation. The red arrows show the propagation of the light from the light source to the endface of the optical fiber and the microresonator through the 50/50 angle coupler, while the blue arrows show the reflected light from the resonator that was recorder to the optical spectrum analyzer (OSA). (b) image of the chamber

In order to achieve highest accuracy in the measurements, before the injection of the solvent, the chamber was cleaned using nitrogen flow, eliminating residual humidity. The liquid solvent was injected directly into the chamber at various volumes from 0.002 ml to 0.2 ml, corresponding to 4 ppm to 400 ppm concentrations and was left to evaporate. Following the injection of the desirable solvent volume into the chamber, the FP resonance spectra were recorded in real time, every 2.5 minutes until saturation. All the measurements were performed at ambient conditions ($T = 21.5\text{ }^{\circ}\text{C}$).

5.1.1a Characterization of the first FP sensing device for the detection of organic solvent vapors

As it was already mentioned, the first FP sensing device was tested for measuring the vapors of two organic solvents from two different families, those of ethanol (alcohols) and chloroform (chlorinated organic solvents). These solvents were chosen for their difference in refractive index, (1.36 and 1.445 at 20 °C, respectively) and vapor pressure (44.6mmHg and 160mmHg at 20 °C, respectively). Both solvents were purchased from Sigma Aldrich (purity 99.9%) [15, 16].

The maximum pressure values reached in the chamber due to the evaporation of the solvents at different concentrations are presented in Figure 5.2. For 400 ppm concentration the maximum pressure reached in the chamber due to ethanol evaporation was 63.5 mbar, while in case of chloroform was 90 mbar. According to the Antoine equation [17-19], the experimental saturated vapor pressures are in good agreement with the expected theoretical values. In the case of ethanol, the vapor pressure at saturation was calculated to be 63.7 mbar, while for chloroform, 225 mbar, ($T = 21.5^{\circ}\text{C}$). The small discrepancy between the experimental and the theoretical values in case of ethanol can be explained, if the manometer error is taken into account.

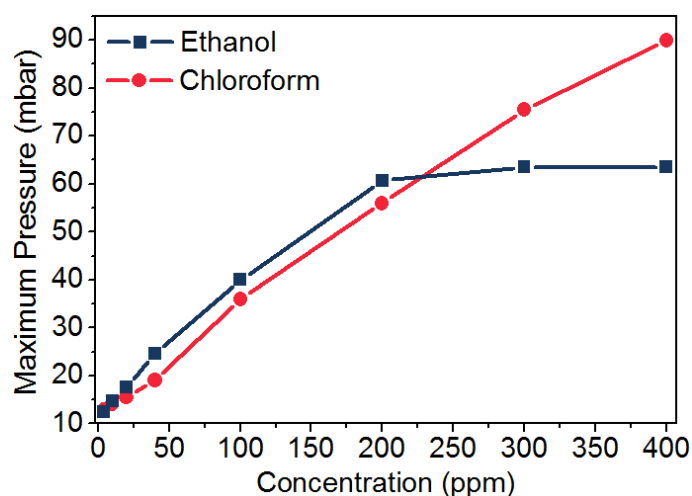


Fig. 5.2. Maximum reached pressure in the chamber due to solvent evaporation. Blue curve corresponds to maximum pressure due to the vapors of different ethanol concentrations, while red curve corresponds to chloroform vapors.

As it is observed from Figure 5.2, and according to the results of the Antoine equation [19], the chamber was considered to be saturated from ethanol vapors, for concentrations of ethanol greater than 200 ppm. Concentrations higher than 200 ppm lead to condensation of ethanol, manifested as a small volume of liquid solvent still existing on the bottom of the chamber. On the contrary, all the injected liquid chloroform was evaporated, even for the higher concentration of 400 ppm, resulting in a pressure of 90 mbar as mentioned before.

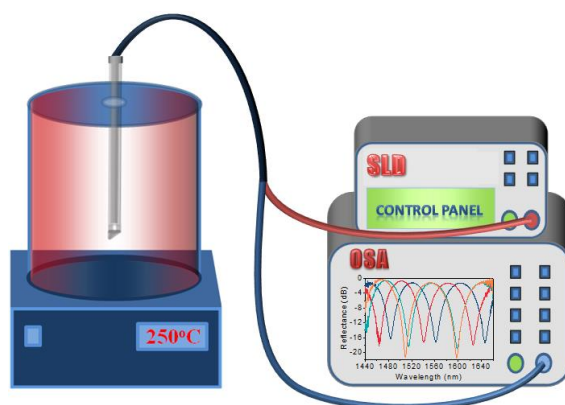


Fig. 5.3. Experimental set-up for the thermal treatment of the sensing head.

Herein, it has to be noted that the device sensitivity was investigated with respect to the reflecting surface porosity of the fabricated micro-prism. For this purpose, the sensing head was placed inside a heating furnace and the temperature was increased gradually in order to investigate the changes of the surface porosity and the effect of these changes to the spectral response of the FP probe (see Fig. 5.3). When the desired temperature was achieved, the device was kept in the furnace for about 30 minutes and then the reflection spectra were once more recorded. This procedure was followed for three different temperature values, namely, 150 °C, 200 °C and 250 °C. During the adjustment of the sensing device in the furnace and at intervals of the heating process, resonant spectra, in reflection mode, were recorded in order the robustness of the sensing head to be confirmed.

5.1.1b Characterization of the FP microresonator for the detection of chlorinated organic solvent vapors (Cl-VOCs)

In order to investigate the sensitivity and the surface affinity of the fabricated optical fiber sensing device, the FP sensing probe was subjected to vapors of three Cl-VOCs with different number of Cl atoms in their molecules, i.e. CH₂Cl₂, CHCl₃, and CCl₄ (listed in Table 5.1). All the chlorinated solvents were purchased from Sigma Aldrich and their purity was 99.9% [16, 20, 21].

Solvent	Refractive index	Vapor pressure (mmHg)	Dipole moment (debye units)
CH ₂ Cl ₂	1.4240	353.2	1.57
CHCl ₃	1.4459	160.0	1.01
CCl ₄	1.4607	91.0	0

Table 5.1. Values of refractive index [16, 20, 21], vapor pressure [16, 20-22], and dipole moment for the three Cl-VOCs studied [23].

As it was mentioned before, in order to achieve highest accuracy, before the injection of the solvent, the chamber was cleaned using nitrogen flow. The liquid solvents were inserted directly into the chamber and were left to evaporate. The

maximum vapor pressures reached in the chamber are presented in Figure 5.4. Following the injection of the desirable solvent volume, FP resonance spectra were recorded in real time, i.e. every 2.5 minutes, while vaporization was progressing. For these experiments as well all measurements were performed at an ambient temperature of 21.5 °C, while the sensing behavior of the probe was tested up to 120 min after its exposure to the Cl-VOCs vapors. For all organic solvents examined, the pressure inside the chamber stabilizes to the 95% of the maximum value recorded within the first 5 min, after the injection of the solvent into the chamber.

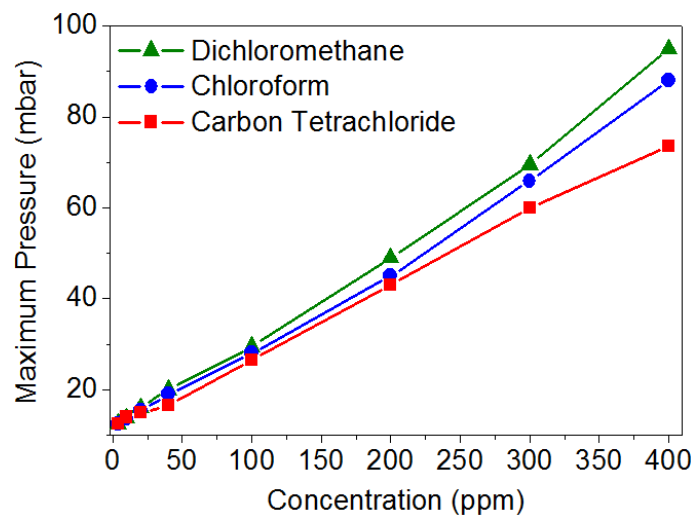


Fig. 5.4. Maximum reached pressure in the chamber due to chlorinated solvent evaporation. Green curve corresponds to maximum pressure due to the vapors of different CH_2Cl_2 concentrations, blue curve corresponds to CHCl_3 vapors and finally red curve corresponds to CCl_4 vapors.

5.1.2 Experimental apparatus used for the characterization of the FP microresonators for the detection of liquid species.

Herein, the FP sensing probe was tested by using different series of refractive index oils, in order to investigate the sensitivity of the FP optical fiber sensing device at the changes of the refractive index inside the microcavity. In the same time was investigated the surface affinity due to the fabricated porous membrane and how this might be affected due to the filling of the pores by liquid materials with different characteristics (i.e., chemical composition, viscosity). For this purpose, three different series of refractive index liquids were used for these experiments, namely SERIES AA, the refractive indices of which range between $n_D = 1.400$ – 1.458 ; SERIES A1 with $n_D = 1.460$ – 1.570 ; and finally SERIES A2 with $n_D = 1.572$ – 1.640 (see Table 5.2). All the aforementioned refractive index liquids were purchased from Cargille Laboratories, Cedar Grove, NJ, USA. Information about the exact ratios between the substances used in these refractive index matching oils were not disclosed by the manufacturing company.

Refractive Index Liquid Series	First Basic Substance	Second Basic Substance	Refractive Indices Range (n_D)
SERIES AA	Mixture of Aliphatic/Alicyclic Hydrocarbons	—	1.400–1.458
SERIES A1	Mixture of Aliphatic/Alicyclic Hydrocarbons	Hydrogenated Terphenyl	1.460–1.570
SERIES A2	Hydrogenated Terphenyl	1-Bromonaphthalene	1.572–1.640

Table 5.2. Series of Cargille refractive index liquids that were used for the experiments.

A simple set-up was used in order to characterize the response of the sensing head to these refractive index oils (Fig.5.5). Some droplets of the desirable oil were drop-casted on a microscope slide which was lying on the experiment table. The optical fiber sensing head was immersed in the oil and the FP resonance spectra were recorded in real time, i.e., every 2.5 min, while the microcavity of the sensing head and as a consequence, the pores of the fabricated membrane were getting filled with the oil. All measurements were performed at an ambient temperature of 21.5 °C, while the sensing behavior of the probe was tested up to 32.5 min after its exposure to the refractive index oils.

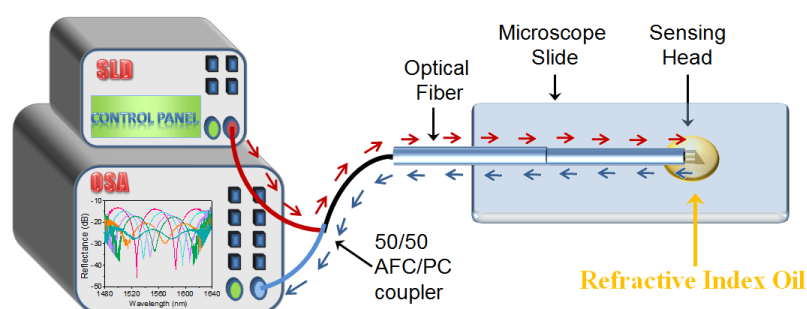


Fig. 5.5. Experimental set-up for Cargille refractive index liquids measurements. The red arrows show the propagation of the light from the light source to the endface of the optical fiber and the microresonator through the 50/50 angle coupler, while the blue arrows show the reflected light from the resonator that was recorder to the optical spectrum analyzer (OSA).

All the series of the Cargille refractive index oily liquids were measured. The step between the refractive index changes from the one oil to the other was 0.01 (e.g., 1.40, 1.41, 1.42 etc.). The sensing head was immersed in 2-propanol for 5 min, after measuring each one of the oils, in order to rinse the refractive index oil and the microcavity to be cleaned for the next measurement. Then, the sensing head was left drying in ambient air for approximately 30 min before the next set of measurements was started. It has to be noted that the same sensing head was used, for all the measurements performed, showing no spectral hysteresis/distortion after repeated oil immersion and isopropanol cleaning process.

5.2 Fiber-endface FP microresonator tested for the detection of organic solvent vapors

The fabricated micro-prism FP resonator was used in order to be tested as sensing

device for the detection of vapors of common organic solvents. Primarily the device was used for the detection of ethanol vapors; however it had also been tested for the detection of chloroform vapor traces. Ethanol was chosen due to its wide use in beverage and food industry related with fermentation processes, as well as, in the automotive fuel sector, wherein ethanol can be mixed with gasoline for tuning octane performance and fuel price. Moreover, the detection of ethanol in ppm concentrations has prominent importance in breath analysis applications. On the other hand, chloroform is extensively used as a cleansing agent and as a solvent for fats, oils, rubber and resins. Furthermore chloroform is used in industry for pesticide formulations and in fire extinguishers.

The wide use of these common organic solvents derived the demand of the production of sensors that are able to detect their presence at low vapor concentrations either for indoor air quality and humans' health, or for the detection of adulterated products. The development of optical fiber endface miniature sensing probes provides a robust optical detection configuration that allows greater functionality integration and can be used for multi-parametric sensing systems.

Herein, the operation of the proposed endface FP sensing probe are investigated for different vapor concentrations and post-fabrication annealing, revealing the role of surface porosity that underlines physisorption effects, affecting the probe performance. It should be noted that, all the following experiments and results were carried out with a single micro-prism resonator, in order to examine in the most realistic way the behavior, the robustness and the sensitivity of the fabricated sensor.

5.2.1 Sensing of ethanol vapors using the endface FP resonator as-fabricated

The fabricated micro-prism endface FP probe device, presented in Figure 5.6(a), was initially tested for measuring vapors of different ethanol concentrations (4 ppm to 400 ppm) in order to be evaluated as sensing device. The experimental procedure was presented in details in section 5.1 (see 5.1.1 and 5.1.1a). The microresonator that was used for these experiments was consisted of a $14.86 \mu\text{m}$ cavity length (d_{eff}). As it was already mentioned the device was operated in reflection mode. The characteristic interference spectra of the device before stimulus (blue curve) and at saturated atmosphere (red curve) for 4 ppm ethanol vapors are displayed in Figure 5.6(b), resulting a 6.38 nm red shift due to the solvent evaporation. The saturated pressure recorded for this ethanol concentration was 12.5 mbar, while as it is observed from the interference spectra the free spectral range (FSR) was $\sim 78 \text{ nm}$ and the notches were about 16 dB in amplitude strength.

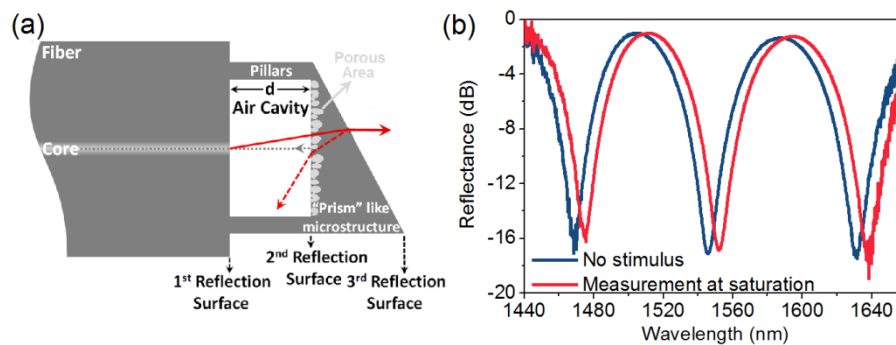


Fig. 5.6. (a) Design of the FP micro-prism resonator onto the endface of the SMF-28e fiber. The porous area on the 2nd reflection surface is presented with light gray "dots". (b) Reflection spectra of the fiber endface FP resonator of measurements before stimulus (blue curve) and at saturation (red curve) due to vapors of ethanol at 4 ppm concentration.

In order to obtain a more detailed picture of the sensing process and understand the operating mechanism of the device, the reflection mode was recorded in real time every 2.5min. The wavelength shifts of the central minimum in time, for four different ethanol concentrations are presented in Figure 5.7(a), while Figure 5.7(b) presents the ratio of the wavelength shift ($\Delta\lambda$) to the changes of pressure in the chamber during the measurements due to the evaporation of the ethanol (ΔP), namely $\Delta\lambda/\Delta P$ versus time.

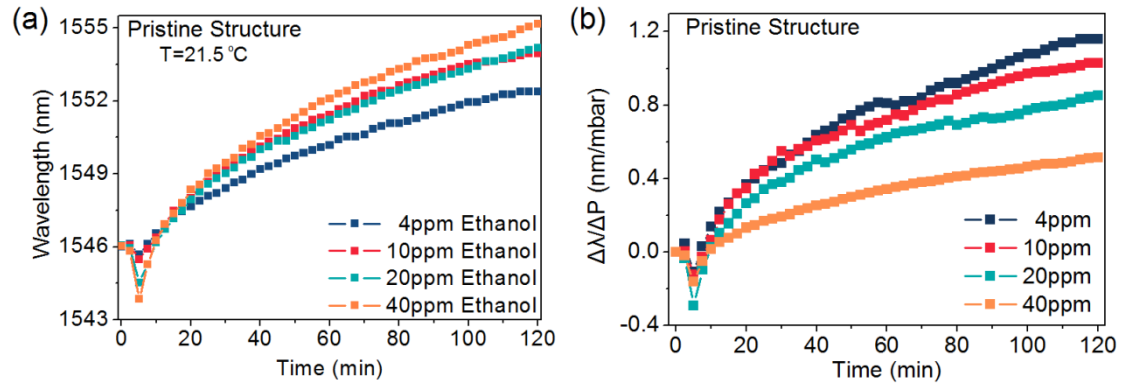


Fig. 5.7. (a) Shift in wavelength versus time for 4ppm, 10ppm, 20ppm and 40ppm of ethanol concentration. (b) The ratio of wavelength shift ($\Delta\lambda$) to the changes of the pressure in the chamber during the measurements due to the evaporations of ethanol (ΔP) versus time for 4ppm, 10ppm, 20ppm and 40ppm of ethanol concentration. The experiments were held with the micro-prism endface FP sensor at 21.5 °C.

Initially, when the sensing head was exposed to ethanol vapors, a blue wavelength shift was observed until the 5th minute and then it was sharply reversed to red shift (see Fig. 5.7(a)). As the ethanol vapor concentration was increased, the blue shift increased as well, namely 0.33 nm for 4 ppm and 2.2 nm for 40 ppm of ethanol vapor concentration. This non-monotonic spectral shift effect could be attributed to physisorption effects that took place on the porous surface of the photopolymerized structure.

Generally, when gas molecules adhere onto a solid surface, existing porosity can affect the progression of population of the adsorbed sites. Namely, in the case of porous surfaces, negative slopes characterizing adsorption progression and its physical manifestations (in the current case F-P notch wavelength shift), are possibly attributed to the immediate filling of pores after the solvent vapors are injected into the chamber [24, 25]. Therefore, the initial, anomalous wavelength shift behavior observed for the endface FP resonator under ethanol vapor exposure is associated with such a pores filling effect and adsorption layer generation, modifying the effective optical path of the hollow FP cavity. Once the surface pores had been filled with ethanol vapors, the notches of the FP resonators shifted to longer wavelengths (red shift) resulting positive slopes (see Fig. 5.7(a)).

In addition, data presented in Figure 5.7(b) show that the ration $\Delta\lambda/\Delta P$ in time decreases till the 5th minute and then is sharply reverse to higher values. As it can be observed this ration decreases in time as the concentration of ethanol vapors increases. Namely, for 4ppm of ethanol concentration the ratio decreases to -0.11 nm/mbar within the first five minutes and then increases up to 1.16 nm/mbar, while in

case of 40 ppm these values are -0.16 nm/mbar and 0.52 nm/mbar respectively.

5.2.1a Simulating the results of the micro-prism endface FP optical fiber resonator as-fabricated

In order to explain and quantify these spectral shifts of the sensing probe that are likely attributed to pores filling and the physisorption processes on the reflection surfaces, a multilayer Fabry-Perot model was used. The model was applied in the data for 40 ppm of ethanol vapors, where a full cycle of blue and red spectral shifts took place within the 120 min that the device was exposed to the vapors.

The miniaturized fabricated structure on the endface of the optical fiber did not allowed us to perform direct AFM studies on the photopolymerized surface (either on the 2nd or 3rd reflection surfaces (see Fig. 5.6(a)), in order to have an accurate determination of its pores size. However previous studies, in which similar organic-inorganic materials were used for the fabrication of photopolymerized structures by DLW, revealed an average pores size of approximately 30 nm [26]. Therefore, this value of pores size will be used in our model.

For this simulating model, four different stages were considered, depending on the vapors sensing progression. The first stage was corresponding to $t = 0$ min, where no stimulus were existed in the chamber (see Fig. 5.8(a)). The second stage (Phase I) correlated with the time that the blue shift had the maximum value, namely $t = 5$ min, (see Fig. 5.8(b)). The third stage (Phase II) corresponding to the time that the pressure in the chamber due to ethanol evaporation had been stabilized, namely $t = 17.5$ min (see Fig. 5.8(c)). Finally the fourth stage (Phase III) corresponding to the last measurement of the exposure to ethanol vapors, at $t = 120$ min (see Fig. 5.8(d)).

In the first stage, the photopolymerized micro-prism reflection surface was divided into two layers, since we assumed that the porous layer was responsible for the blue shift response of the fabricated FP sensing device. The first layer was an outer thin porous layer with a nominal thickness d_p of the order of the roughness of the material (namely $d_p = 30$ nm) [26], while the second layer was a thick non-porous layer (see 5.8(a), right sketch). Therefore, a three layer FP optical interference approximation model was used for fitting the data of the FP resonator in ambient atmosphere. The equation for the normalized total reflective intensity $I_{R(3LM)}(\lambda)$ for the 3 layer FP model, using the two-beam optical interference approximation [12, 27] was:

$$\begin{aligned}
 I_{R(3LM)}(\lambda) = & (L_1)^2 + (L_2)^2 + (L_3)^2 \\
 & + 2L_1L_2 \cos\left(\frac{4\pi n_c d}{\lambda}\right) - 2L_1L_3 \cos\left[\left(\frac{4\pi n_c d}{\lambda}\right) + \left(\frac{4\pi n_p d_p}{\lambda}\right)\right] \\
 & + 2L_2L_3 \cos\left(\frac{4\pi n_p d_p}{\lambda}\right)
 \end{aligned} \tag{1}$$

where:

$$L_1 = \sqrt{R_1}$$

$$L_2 = (1 - T_1)(1 - R_1)(1 - a)\sqrt{R_2}$$

$$L_3 = (1 - T_1)(1 - T_2)(1 - R_1)(1 - R_2)(1 - a)\sqrt{R_3}$$

with $R_1 = R_{r1}R_{s1}$, $R_2 = R_{r2}R_{s2}$ and $R_3 = R_{r3}R_{s3}$ while R_{r1} , R_{r2} and R_{r3} correspond to the power reflection coefficients at surfaces 1, 2 and 3 respectively and R_{s1} , R_{s2} and R_{s3} to the Rayleigh scattering loss coefficients [28, 29]. T_1 and T_2 are the transmission loss factors at reflection surfaces 1 and 2 respectively, α is the air cavity loss factor (all the aforementioned coefficients and loss factors were presented in details in Chapter 4, sections 4.2.2 and 4.3.2). Moreover n_c corresponds to the refractive index of the medium in the open FP cavity with length d , while n_p corresponds to the refractive index of the porous layer with d_p thickness.

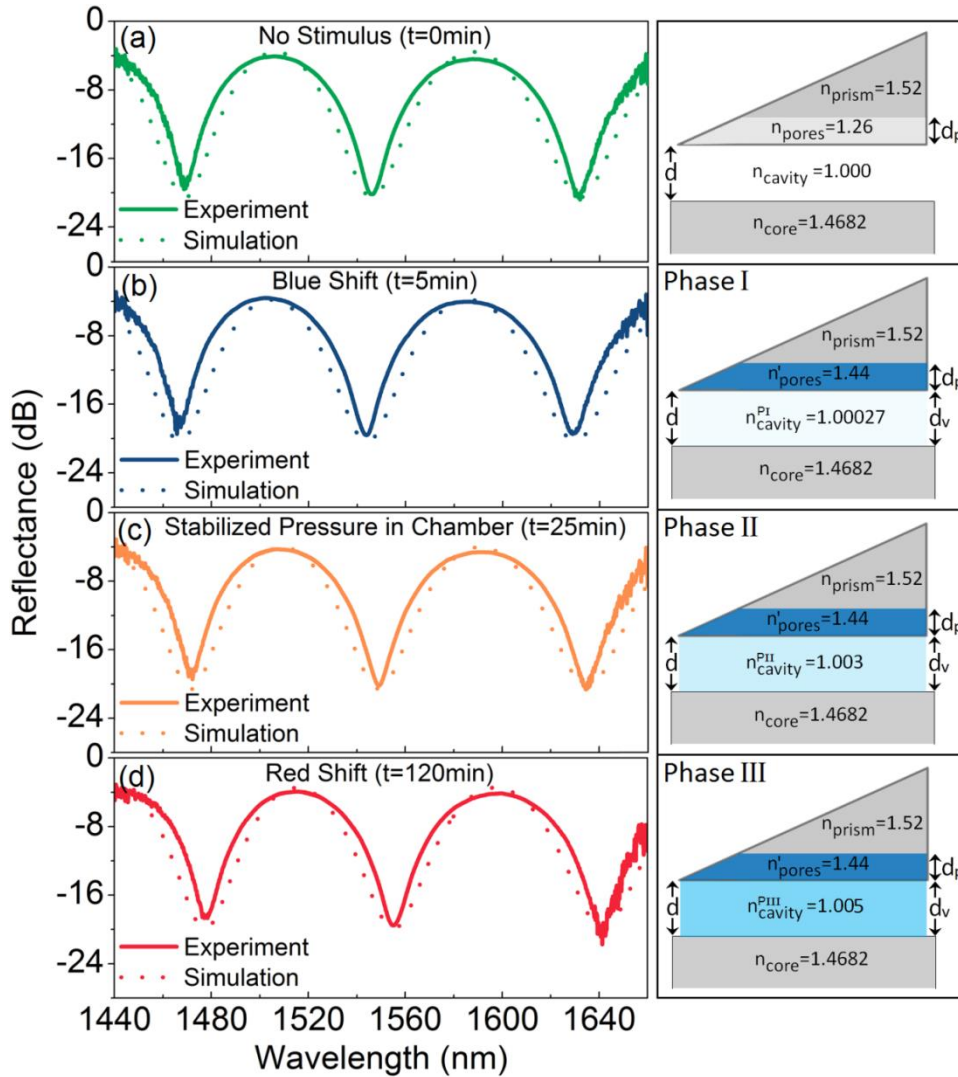


Fig. 5.8. Simulation spectra of 40 ppm Ethanol for four different instances of the sensing process; (a) for $t=0$ min, (b) for $t=5$ min that the blue shift had its maximum value, (c) for $t=17.5$ min where the pressure in the chamber due to ethanol evaporation had been stabilized and (d) for $t=120$ min. On the right, are being presented the schematic representations with the characteristic parameters for each applied theoretical model (see text). Experimental spectra are also included for the sake of comparison.

Since at $t = 0$ min no solvent had been injected in the chamber, the refractive index of the FP cavity was set to be $n_{\text{cavity}} = 1$, while the refractive index of the thick non-porous layer was equal to the refractive index of the hybrid photopolymerized material, namely $n_{\text{prism}} = 1.52$ (see Fig. 5.8(a), right). The effective index value for the n_{pores} is expected to rest between that of air and the photopolymerized material, since there will be voids of empty space and peaks of the solid matrix. Using the aforementioned three layer FP optical interference approximation model (Eq. (1)), the effective refractive index of the porous thin layer was calculated to be $n_{\text{pores}} = 1.26$. From this effective refractive index value a filling ratio G of this porous layer was extracted, which was estimated to be 0.5 for the experimental data fitted. This filling factor ratio is characteristic for each photopolymerized structure, while being dependent upon the photosensitive epoxy composition the laser exposure and the wet development conditions.

On the following phase (Phase I), the ethanol solvent was injected into the chamber and vapors were generated, thus, exposing the FP sensing probe. Within the first five minutes of the exposure, the vapors were adsorbed on the available sites within the porous layer, and filled the pores on the reflection surface of the photopolymerized micro-prism with condensed organic solvent. Moreover, in the same time the refractive index of the FP cavity was increased due to the vapors introduction until the saturation point (see Fig. 5.8(b)). The refractive index of the porous layer at this stage was estimated according to the filling ratio G , emerged from the first stage at $t = 0$ min. In order the effective refractive index n'_{pores} of the organic vapor filled layer to be calculated, the refractive index of the ethanol [15] and this of the photopolymerized resin ($n_{\text{resign}}=1.52$) were used, resulting a $n'_{\text{pores}}=1.44$. Applying again the three layer FP optical interference approximation model (Eq. (1)) a blue wavelength shifts of the FP spectral notches was observed, which was in good agreement with the experimental findings (Fig. 5.8(b), $t=5$ min). The effective index within the FP cavity due to the ethanol vapors at this stage was calculated to be equal to $n_{\text{cavity}}^{\text{PI}}=1.00027$.

During the second phase (Phase II) the pressure in the chamber was noticed to be stabilized for first time, while the FP notches were observed to shift to red. The three layer FP optical interference approximation model (Eq. (1)) was applied again. This time the effective refractive index of the porous layer considered to be again $n'_{\text{pores}} = 1.44$ since the pores were already filled with the vapors of ethanol, while the effective index of the open FP cavity was considered to be increased since the ethanol solvent continued to be evaporated. A red wavelength shifts of the FP spectral notches was observed this time, which was in good agreement with the experimental findings (Fig. 5.8(c), $t=17.5$ min), with the effective index within the FP cavity at this stage calculated to be equal to $n_{\text{cavity}}^{\text{PII}}=1.003$.

At the final phase (Phase III), even though the pressure in the chamber had been stabilized and one could expect that the refractive index within the open cavity should be stabilized, it seemed that this was not the case here. We assume that this happened

due to the fact that the solvent vapors probably interact somehow with the chamber itself. Since the surfaces of the chamber's walls are porous themselves that could emerge different phenomena for example absorption and liquefaction that could affect the refractive index within the chamber and as a consequence within the hollow FP cavity. By applying again the three layer FP optical interference approximation model (Eq. (1)) with effective refractive index of the porous layer to be again $n'_{\text{pores}} = 1.44$, a further red wavelength shifts of the FP spectral notches was observed with the effective index within the FP cavity at this phase be calculated equal to $n_{\text{cavity}}^{\text{PIII}}=1.005$, resulting good agreement with the experimental findings (Fig. 5.8(d), $t=120$ min).

5.2.1b Confirming the sensing mechanism using the micro-funnel endface FP optical fiber resonator as-fabricated

Similar to the above, non-monotonic spectral behavior has been observed when the micro-funnel endface FP resonator was tested with ethanol vapors under the same experimental conditions. In Figure 5.9 the wavelength shifts of the FP spectral notches versus exposure time to ethanol vapors are presented. For this endface FP sensing device also a blue shift was observed initially within the first five minutes and then reversed to a red shift. The slight differences that were observed in the slopes between the two endface FP sensing devices (see Fig. 5.7(a) for micro-prism device and Fig. 5.9 for micro-funnel device) were due to the differences of the fabricated surface porosity during the photopolymerization process.

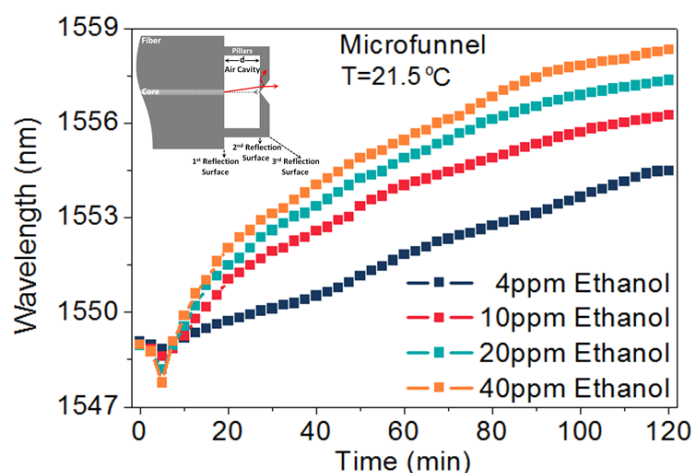


Fig. 5.9. Shift in wavelength versus time for 4ppm, 10ppm, 20ppm and 40ppm of ethanol concentration. The experiments were held with the micro-funnel endface FP sensor at 21.5 °C.

5.2.1c Testing the as-fabricated micro-prism endface FP optical fiber resonator at slightly higher temperature

When the experiments of the micro-prism sensing device were held at a room temperature of 23.1 °C instead of 21.5 °C, a slightly different behavior at the spectral response was observed (see Fig. 5.10).

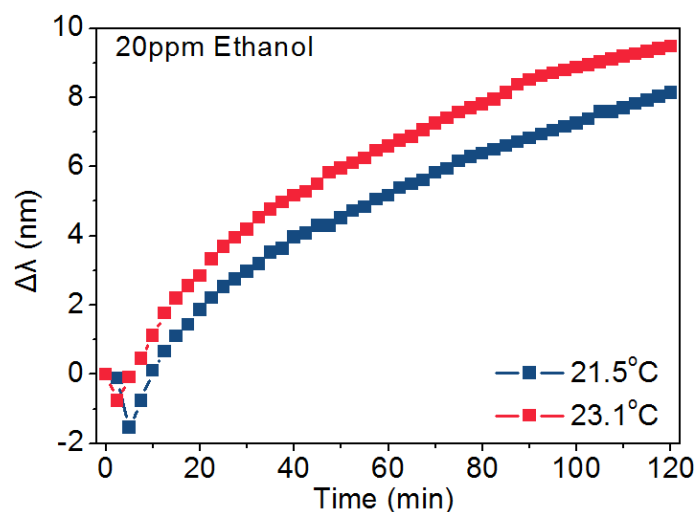


Fig. 5.10. Shift of the FP fringes versus time for 20 ppm ethanol concentration, for two different temperatures, namely 21.5°C (blue curve) and 23.1°C (blue curve). The experiments were held with the micro-prism endface FP optical fiber sensor.

In this case, the blue shift was observed within the first 2.5 minutes of the exposure to ethanol vapors and then was reversed to red shift, while for the experiments at 21.5 °C the blue shift was observed within the first 5 minutes. This could be explained if someone take into account that the ethanol evaporates faster in higher temperature. Considering that, due to the faster evaporation the porous got filled in shorted time resulting a shallower blue shift in comparison with that one recorded at 21.5 °C, namely 0.76 nm and 1.54 nm for 20 ppm ethanol vapors concentration at 23 °C and 21.5 °C respectively.

5.2.1d Recovery of the endface FP optical fiber resonator after ethanol measurements by flushing the chamber with nitrogen

It has to be noted here, that in all the aforementioned experiments, upon flushing the chamber with pure nitrogen, ethanol desorption takes place, while progressing substantially faster, compared to the physisorption built up process. Typical characteristic recovery times were of the order of 5 min and 12.5 min (see Fig. 5.11). This recovery behavior provides more evidence that the sensing probe is based on physisorption phenomena, where adsorbed molecules are weakly bound on the hosting surface. Similar results, although with slightly longer recovery times (up to 20 min), are obtained when the sensor is exposed to ambient air.

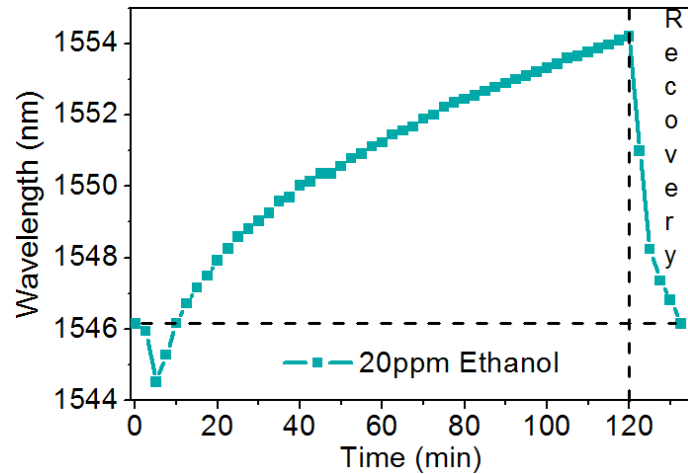


Fig. 5.11. Shift in wavelength versus time and recovery of the endface micro-prism FP optical fiber sensor upon flushing the chamber with nitrogen.

5.2.2 Annealing process of the micro-prism endface FP resonator

In order to investigate further how the surface porosity of the fabricated micro-prism cavity affects the sensing behavior of the probe, improve the performance of the device and potentially addressing ways for controlling the porosity of the photopolymerized optical structures, the optical fiber endface device was annealed following specific annealing cycles. The experimental procedure was described in details in section 5.1 (see paragraph 5.1.1a).

It had been shown by others that typical photopolymerized organic-inorganic structures can be heated up to ~ 300 °C without deteriorating their shape and optical properties [30]. After considering the above, the optical fiber endface FP sensing probe was consecutively annealed at 150 °C, 200 °C and 250 °C for 30 min. After every thermal treatment the sensing head was placed again in the chamber and all measurements for the different concentrations of ethanol vapors were repeated under the same temperature conditions. The spectra recorded after each thermal treatment cycle, are presented in Figure 5.12(a).

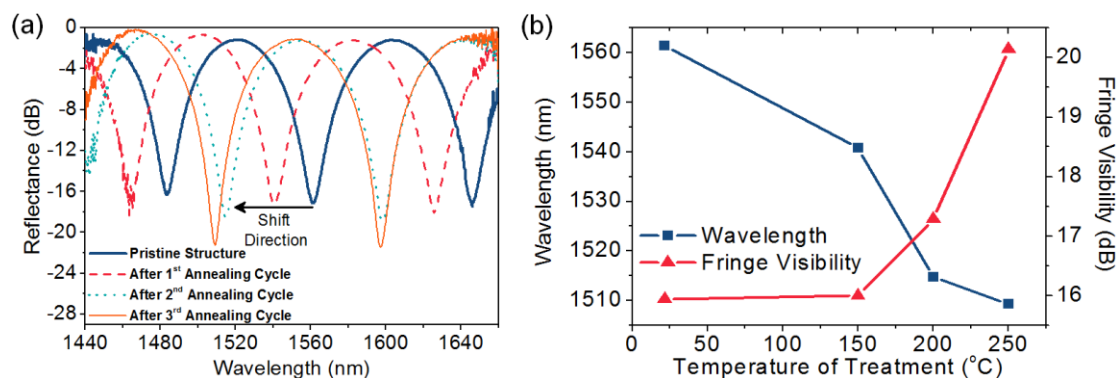


Fig. 5.12 a) Reflection spectra at ambient air, before and after each thermal treatment (1st Annealing Cycle at $T = 150$ °C, 2nd Annealing Cycle at $T = 200$ °C and 3rd Annealing Cycle at $T = 250$ °C). b) Wavelength shift (blue curve) and fringe visibility (red curve) to temperature of annealing treatment.

As it was observed, after each thermal treatment a blue shift of the FP spectrum

was observed simultaneously with an increase of the fringe strength visibility (see Fig. 5.12(b)). This indicates that the thermal treatment reduces the scattering and absorption losses at the photopolymerized surface, predominantly, by possible collapsing of the pore size. The resultant fringe visibility increased from 15 dB that was recorded at the as-fabricated microstructure to 20 dB after the last annealing treatment cycle at 250 °C.

As aforementioned, after each annealing treatment cycle, the sensing device was placed in the chamber and exposed to ethanol vapors (see paragraph 5.1.1a), for identifying the role of porosity in the sensing performance. The results for a 20 ppm ethanol concentration after each annealing treatment are presented in Figure 5.13.

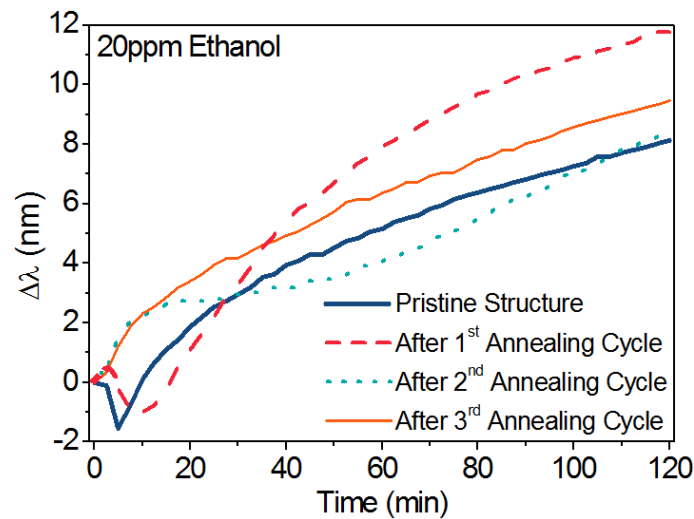


Fig. 5.13. FP notch spectral shift versus time, of 20 ppm of ethanol, after each thermal treatment (1st Annealing Cycle at $T = 150$ °C, 2nd Annealing Cycle at $T = 200$ °C and 3rd Annealing Cycle at $T = 250$ °C).

As it is observed, the temporal sensing behavior of the probe was modified after every thermal annealing cycle. Namely, the initial blue wavelength shift in time that had been observed in the as-fabricated device (see Fig. 5.7), was translated to longer time scales, while being reduced in terms of absolute wavelength shift $\Delta\lambda$; the last took place up to the last annealing treatment (3rd in row), where the blue shift was no longer observable within the time scale of our measurements (see Fig. 5.13, orange solid curve).

The above experimental results constitute an additional evidence on the role of surface porosity of the photopolymerized structure and the spectro-temporal sensing performance of the device. The reduction of pores size after each thermal treatment cycle reduced or even prevented the ethanol diffusion and pores filling phenomena that took place on the flat reflection surface of the micro-prism structure, which in turn distorted the operation of the sensing device.

In order to evaluate the sensing performance of the optical fiber endface FP device after the last annealing cycle at 250 °C, where the blue shift was no longer observed, the results of ethanol vapor measurements for different concentrations were examined (see Fig. 5.14(a)).

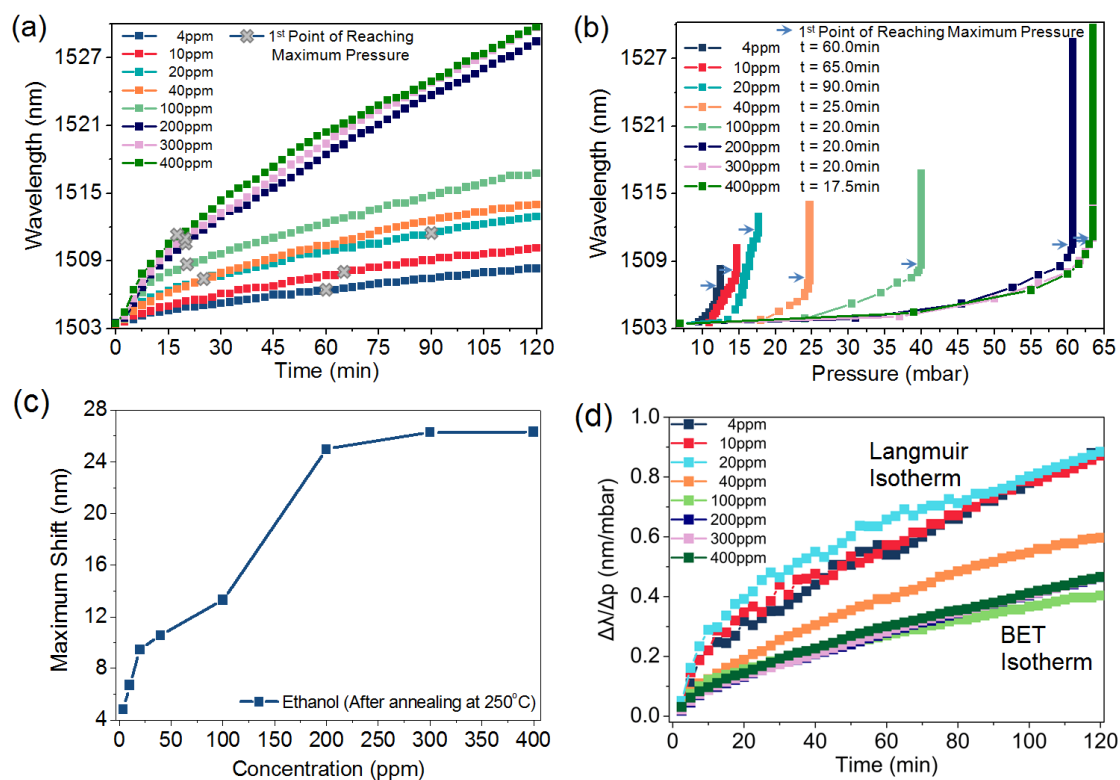


Fig. 5.14. (a) Shift in wavelength to time and (b) shift in wavelength to pressure in the chamber for different concentrations of ethanol vapors, after thermal treatment at 250 °C. (c) Maximum shift of the interference notches for the examined concentrations after thermal treatment at 250 °C. (d) The ratio of wavelength shift ($\Delta\lambda$) to the changes of the pressure in the chamber (ΔP) during the measurements due to the evaporations of ethanol, versus time for the examined concentrations. For 4 ppm to 100 ppm the endface device follows Langmuir isotherm, while for concentrations higher of 200 ppm the endface device follows the BET isotherm.

The first observation is that the shift of the FP notches follow a monotonic red shift behavior versus exposure time to the ethanol vapors for all the examined concentrations (see Fig. 5.14(a)). Moreover, the shift in wavelength was increased as the concentration of the ethanol vapors in the chamber increased, namely for 4 ppm of ethanol vapors the maximum shift that was recorded was 4.84 nm, while for 400 ppm the maximum shift was 26.31 nm (see Fig. 5.14(c)).

According to Antoine equation [19], concentrations greater than 200 ppm leads to saturated vapor pressures (see section 5.1.1a and Fig. 5.2). This was also observed during the experimental process, while for volumes greater than 100 μl , which corresponded to ethanol vapor concentrations greater than 200 ppm, a small volume of the injected solvent into the chamber did not evaporated completely. The data presented in Figures 5.14(a) and 5.14(b) show that for concentrations greater than 200 ppm the device exhibited an “almost” identical sensing behavior. This happened due to the heavily saturated atmosphere of ethanol vapors into the chamber. This phenomenon lead to fast adsorption of the ethanol vapors onto the reflection surfaces and then to liquefaction of the evaporated solvent on the reflection surfaces, resulting similar shifts in wavelength for volumes higher than 200 ppm (see Fig. 5.14(b) and 5.14(d)). Thus, the sensor presented herein is not potentially suitable for measuring ethanol vapor concentrations greater than ~ 100 ppm. In case of 100 ppm ethanol

concentration the notches of the FP shifted up to ~ 7 nm, leading to a pressure figure of ~ 0.11 nm/mbar. The sensitivities that were obtained from these data, defined as $S = \Delta\lambda/\Delta n$, was calculated to be $\sim 1.5 \times 10^3$ nm/RIU [6, 9, 31, 32].

Another finding emerging from the data presented in Figure 5.14(b) is that even if the pressure in the chamber was stabilized, the FP notches continued to be shifted towards longer wavelengths. The continuous red-shift of the FP notches versus the exposure time in ethanol vapors is also presented in Figure 5.14(a). The last finding can be explained considering the BET isotherm model [23, 25]. According to this model, when surfaces are exposed to vapors, a monolayer of vapors is formed onto the existing adsorption sites; then, when the pressure is saturated, the molecules of the vapors are adhering onto the initial monolayer, towards the formation of thicker layer of the condensated vapor. Therefore, until the pressure due to the ethanol evaporation was stabilized for concentrations higher than 200 ppm, the spectral shift was a result of both the formation of the adsorbed monolayer on the photopolymerized reflection surface and the cleaved surface of the SMF-28e fiber, as well as the change of the refractive index within the FP cavity of the device. After the pressure stabilization, the spectra shift was due to the additional adsorbed layers on the reflection surfaces of the FB cavity.

According to the previous results presented in Figure 5.14(b) and 5.14(d), the sensing mechanism of the fabricated sensing head for vapor concentrations up to 100 ppm resulting low vapor pressures in the chamber (see Fir. 5.2 in section 5.1.1a), relies on Langmuir isotherm forming an adsorbed monolayer on the reflection surfaces [33, 34], while for vapor concentrations higher than 200 ppm the sensing mechanism relies on BET isotherm [25, 34] forming a multilayer.

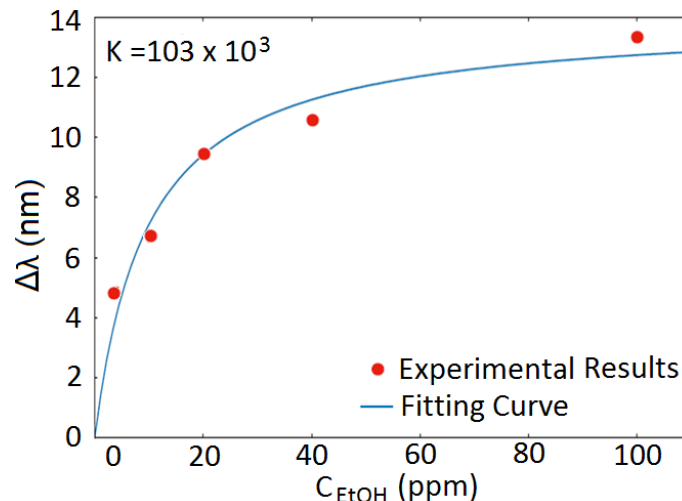


Fig. 5.14. Fitting of experimental data of maximum shift of ethanol vapors, at concentrations lower than 100 ppm, with a Langmuir isotherm. Red dots correspond to the experimental data, while blue curve corresponds to the fitting curve according to Equation (2).

By fitting the maximum shift data presented in Figure 5.14(c) for volumes up to 100 ppm with the equation for Langmuir isotherm [23, 35]:

$$\Delta\lambda = \Delta\lambda_{\max} \frac{K C_{\text{EtOH}}}{10^6 + K C_{\text{EtOH}}} \quad (2)$$

one can extract the equilibrium constant K . The results of the fitting data with the Equation (2) are presented in Figure 5.15, resulting an equilibrium constant $K=103 \times 10^3$.

In order to calculate the thickness of the formed BET overlayer at $t = 120$ min for 400 ppm ethanol concentration, three different stages were considered, depending on the vapors sensing progression. The first stage was corresponding to $t = 0$ min, where no stimulus were existed in the chamber (see Fig. 5.15(a)). The second stage (Phase I) corresponding to the time that the pressure in the chamber due to ethanol evaporation had been stabilized, namely $t = 17.5$ min (see Fig. 5.15(b)). Finally, the third stage (Phase II) corresponding to the last measurement of the exposure to ethanol vapors, at $t = 120$ min (see Fig. 5.15(c)).

In the first stage, the refractive index of the photopolymerized micro-prism was equal to the refractive index of the photosensitive resin since the porosity on the photopolymerized reflection surface after the annealing treatment at 250°C had vanished ($n_{\text{prism}}=1.52$). The refractive index of the FP cavity was equal to that of air since no stimulus were existed in the chamber ($n_{\text{cavity}}=1.00$).

For this stage a 2 layer FP model using the two-beam optical interference approximation [12, 27] was used. The equation for the normalized total reflective intensity $I_{R(2LM)}(\lambda)$ for the 2 layer FP model is:

$$I_{R(2LM)}(\lambda) = (L_1)^2 + (L_2)^2 + 2L_1L_2 \cos\left(\frac{4\pi n_v d_v}{\lambda}\right) \quad (3)$$

where:

$$L_1 = \sqrt{R_1}$$

$$L_2 = (1 - T_1)(1 - R_1)(1 - a)\sqrt{R_2}$$

with $R_1 = R_{r1}R_{s1}$ and $R_2 = R_{r2}R_{s2}$, while R_{r1} and R_{r2} correspond to the power reflection coefficients at surfaces 1, 2 and 3 respectively and R_{s1} and R_{s2} to the Rayleigh scattering loss coefficients [28, 29]. T_1 and T_2 are the transmission loss factors at reflection surfaces 1 and 2 respectively and α is the air cavity loss factor (all the aforementioned coefficients and loss factors were presented in details in Chapter 4, sections 4.2.2 and 4.3.2). Moreover n_v in this stage corresponds to the refractive index in the open FP cavity that equals to the refractive index of air (see Fig. 5.15(a)). The results show that the simulated data are in a good agreement with the experimental results.

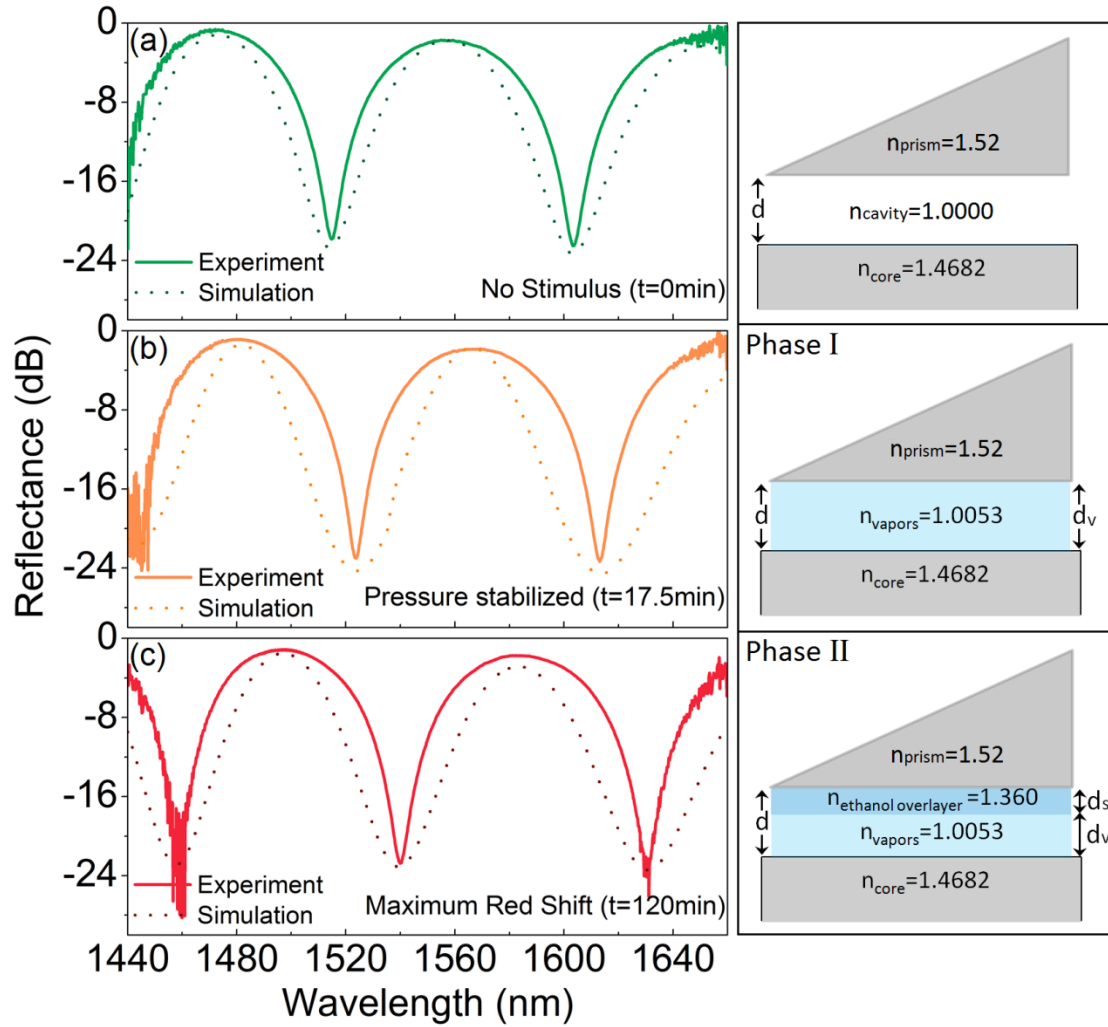


Fig. 5.15. Simulation spectra of 400 ppm ethanol for three different instances of the sensing process; (a) for $t=0$ min, (b) for $t=17.5$ min when the pressure in the chamber due to ethanol evaporation had been stabilized and (c) for $t=120$ min. On the right, are being presented the schematic representations with the characteristic parameters for each applied theoretical model (see text). Experimental spectra are also included for the sake of comparison.

The second stage (Phase I) (see Fig. 5.15(b)), corresponds to $t = 17.5$ min, when the pressure in the chamber was stabilized (see Fig. 5.13(b)). At that time the open FP cavity was filled with the ethanol vapors resulting the spectral shift of the FP notches. The refractive index change due to the presence of ethanol vapors in the FP cavity was calculated using the interference spectra presented in Figure 5.15(a) and 5.15(b), since $\Delta n = (\Delta\lambda/\lambda_{t=0\text{min}})n_{t=0\text{min}}$ and therefore $n_{\text{vapors}} = n_{t=0\text{min}} + \Delta n \approx 1.0053$ (see Fig. 5.15(b), right). Using the equation (3) where $n_v=1.0053$ the experimental and the simulated results seems to be in good agreement.

In the third stage (Phase II) (see Fig. 5.15(c)), after the stabilization of the pressure the shift of the notches of the interference spectra to longer wavelengths was due to the formation of the overlayer on the photopolymerized flat surface of the micro-prism. The refractive index of the overlayer was considered to be equal to that of the refractive index of ethanol, namely $n_s = 1.360$ [15], since we considered that the vapors had been condensed, while the thickness of the overlayer was defined as d_s . Finally, the FP cavity length d at $t = 120$ min was considered to be defined as $d =$

$d_v + d_s$, where d_v was the thickness of the vapor layer inside the FP open cavity, while d_s was the thickness of the formed overlayer of the condensed ethanol vapors onto the photopolymerized flat surface of the micro-prism and inside the open FP cavity (see Fig. 5.15(c)). The equation for the normalized total reflective intensity $I_{R(3LM)}(\lambda)$ for the 3 layer FP model, using the two-beam optical interference approximation [12, 27] was:

$$\begin{aligned}
I_{R(3LM)}(\lambda) = & (L_1)^2 + (L_2)^2 + (L_3)^2 \\
& + 2L_1L_2 \cos\left(\frac{4\pi n_v d_v}{\lambda}\right) - 2L_1L_3 \cos\left[\left(\frac{4\pi n_v d_v}{\lambda}\right) + \left(\frac{4\pi n_s d_s}{\lambda}\right)\right] \\
& - 2L_2L_3 \cos\left(\frac{4\pi n_s d_s}{\lambda}\right)
\end{aligned} \tag{4}$$

where:

$$\begin{aligned}
L_1 &= \sqrt{R_1} \\
L_2 &= (1 - T_1)(1 - R_1)(1 - \alpha)\sqrt{R_2} \\
L_3 &= (1 - T_1)(1 - T_2)(1 - R_1)(1 - R_2)(1 - \alpha)\sqrt{R_3}
\end{aligned}$$

with $R_1 = R_{r1}R_{s1}$, $R_2 = R_{r2}R_{s2}$ and $R_3 = R_{r3}R_{s3}$ while R_{r1} , R_{r2} and R_{r3} correspond to the power reflection coefficients at surfaces 1, 2 and 3 respectively and R_{s1} , R_{s2} and R_{s3} to the Rayleigh scattering loss coefficients [28, 29]. T_1 and T_2 are the transmission loss factors at reflection surfaces 1 and 2 respectively and α is the air cavity loss factor (all the aforementioned coefficients and loss factors were presented in details in Chapter 4, sections 4.2.2 and 4.3.2). Moreover n_v corresponds to the refractive index in the open FP cavity due to the ethanol vapors which occupy a length of d_v (see Fig. 5.15(c)), while n_s corresponds to the refractive index of the ethanol liquefied overlayer within the FP cavity of thickness d_s .

Calculations performed using the three-layer FP model (Eq. 4) revealed that for the 400 ppm concentration, such an ethanol adhered overlayer can built up to ~50 nm thickness, after 120min of exposure to the organic vapor. It has to be noted here that the thickness of the adsorbed ethanol estimated using the model above, is assumed to be formed only onto the photopolymerised surface. This is actually not true, since this total layer is divided to both the photopolymerised micro-prism surface and the cleaved endface of the optical fiber.

5.2.3 Sensing of chloroform vapors using the endface FP resonator

The optical fiber endface FP sensing device was also exposed, to chloroform vapors, in order to investigate its sensitivity and possible specificity of the device. As it was already mentioned in section 5.1.1a, chloroform was chosen since it is an organic solvent, with greater refractive index and higher vapor pressure than ethanol.

The optical fiber endface FP sensing device was exposed to chloroform vapors

before the thermal treatment and after each annealing cycle, exactly like as for the case of ethanol vapors. Figure 5.16 presents the results of the pristine structure, at 20 ppm of chloroform vapors (red curve). In the same diagram the corresponding results for ethanol vapors appear in order to compare the sensing response of the device for both examined solvents. In contrary to ethanol vapors that had presented a sharp blue shift within the first five minutes, the response of the device to chloroform vapors was somewhat different. In this case, the blue shift that was observed, presented a slower progression in time, and moreover was shallower in terms of wavelength shift values; namely for ethanol vapors the FP notches blue wavelength shift was 1.54 nm while for chloroform vapors that was 0.88 nm.

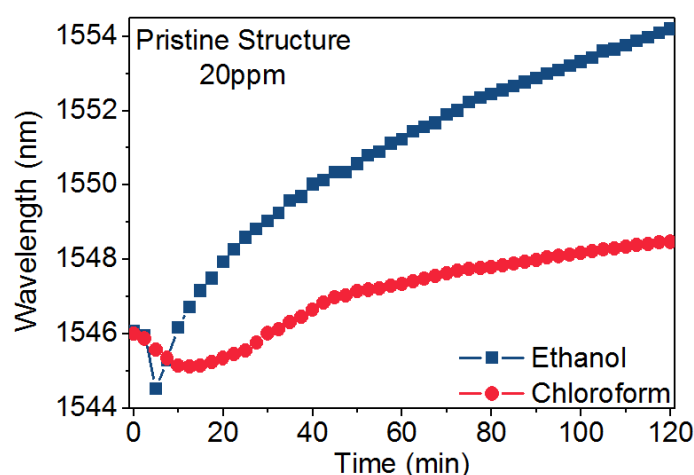


Fig. 5.16. Shift of FP notches in wavelength versus time, due to the presence of 20 ppm ethanol concentration (blue curve) and chloroform (red curve). The measurements were performed with the endface micro-prism FP optical fiber sensor as-fabricated.

These differences in the spectral response of the device are attributed to the packing ability of the two solvents onto the reflection surfaces of the FP sensing probe [36]. Ethanol ($\text{CH}_3\text{CH}_2\text{-OH}$), as an alcohol with an OH group attached, has a higher packing ability in comparison to chloroform (CHCl_3) which is a molecule exhibiting tetrahedral type of symmetry. In the case of chloroform, the packing ability of the molecules in the FP cavity and on the reflection surfaces is reduced, because of the large size of the three chlorine atoms and the repulsive forces created between chloroform molecules due to the increased electronegativity of chlorine atoms [23]. The above assertion can justify the lower sensitivity of the FP microcavity sensing device to chloroform vapors in comparison to the ethanol case.

The results for 20 ppm chloroform vapors concentration for the as-fabricated structure and after each annealing treatment are presented in Figure 5.17. Similarly to the results measured for ethanol, the blue wavelength shift that had been observed in the as-fabricated structure for chloroform vapors, was shifted to longer time scales after the first annealing cycle. After the second annealing treatment at 200 °C this blue shift was no longer observed and the device presented a monotonic spectral behavior. It has to be noted here that in case of ethanol vapors, this monotonic spectral behavior was observed only after the third annealing treatment at 250 °C (see Figure 5.13). This

could be one more evidence that the sensing response of the FP device is relied on the packing ability of the two solvents, and its correlation with the porosity of the photopolymerised structure.

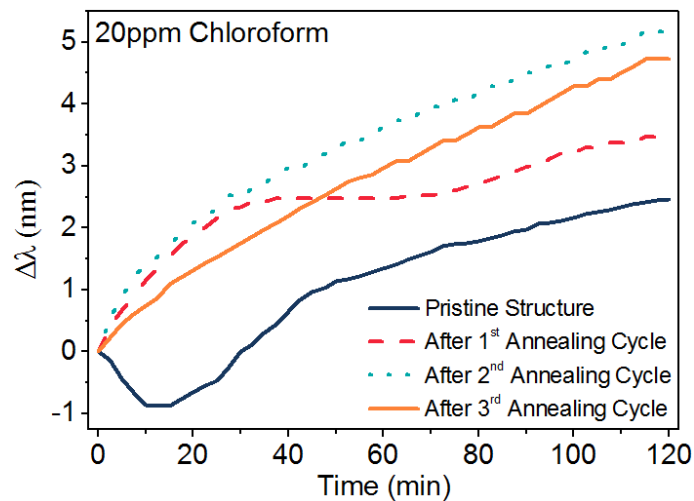


Fig. 5.17. FP notch spectral shift versus time, for 20 ppm of chloroform vapors, after each thermal treatment (1st Annealing Cycle at $T = 150\text{ }^{\circ}\text{C}$, 2nd Annealing Cycle at $T = 200\text{ }^{\circ}\text{C}$ and 3rd Annealing Cycle at $T = 250\text{ }^{\circ}\text{C}$).

Finally, the results of the exposure of the sensing device to 4 ppm concentration chloroform vapors after the final thermal treatment at $250\text{ }^{\circ}\text{C}$ are presented in Figure 5.18 (see red curve). As can be observed from Figure 5.18(a), even for the lowest examined vapors concentration the difference between the spectral response of the FP microsensor to these two organic solvents is obvious. As shown in Figure 5.18(a), the maximum shift in case of chloroform vapors was 3.63 nm while for ethanol was 4.84 nm, resulting detectivity figures of $\Delta\lambda/c_{\text{Chl}} \sim 0.90\text{ nm/ppm}$ and $\Delta\lambda/c_{\text{Eth}} \sim 1.2\text{ nm/ppm}$ respectively ($c_{\text{Chl}} = c_{\text{Eth}} = 4\text{ ppm}$). Although, it is obvious that in both cases the notches of the FP device were shifted even if the pressure in the chamber was stabilized.

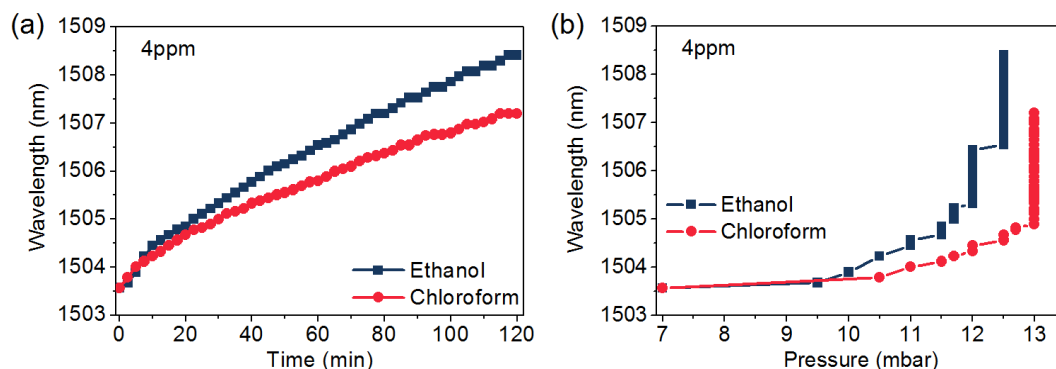


Fig. 5.18. (a) Shift in wavelength versus time and (b) shift in wavelength versus pressure after the third annealing cycle of the endface FP optical fiber sensor at $250\text{ }^{\circ}\text{C}$, at the presence of 4 ppm of ethanol (blue curve) and chloroform (red curve) vapors in the chamber.

Moreover, Figure 5.19 presents the maximum wavelength shifts for both chloroform and ethanol for all the examined vapor concentrations. It is obvious that as

concentration increases the difference between the two solvents becomes more significant. For 400 ppm concentration, the maximum shift was 5.38 nm for chloroform vapors (red curve) while in case of ethanol vapors reached the value of 26.31 nm. This could be explained if one considers the differences that these two solvents presents in their packing abilities. The sensitivity of the sensor to chloroform was estimated to be 1.52×10^3 nm/RIU.

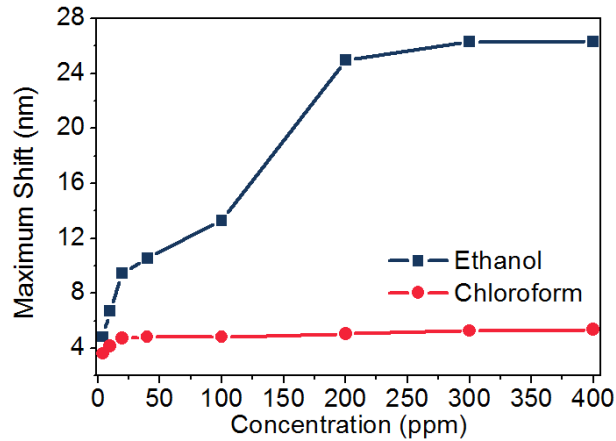


Fig. 5.19. Maximum spectral shift diagram for different concentrations of ethanol (blue curve) and chloroform vapors (red curve).

5.2.4 Operation of the sensing probe under ambient air conditions

All the aforementioned experiments were held out under dry conditions, since before the injection of the solvent the chamber was cleaned with nitrogen flow. Afterwards, the sensor was also tested under ambient air conditions, to reveal the effect of humidity vapors on the sensing performance of the probe. Figure 5.20 presents the sensing response of the device as measured at room temperature for various humidity levels in the chamber with the presence of 4 ppm ethanol (Fig. 5.20, left) or chloroform (Fig. 5.20, right).

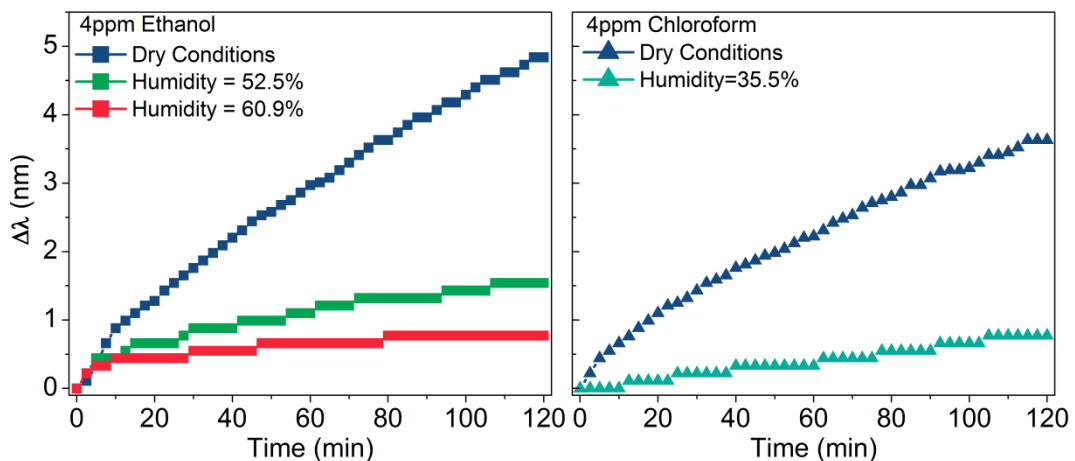


Fig. 5.20. (Left) FP notch spectral shift versus time, of 4 ppm ethanol measured at dry conditions (blue curve) and at ambient conditions with humidity (red and green curves). (Right) Spectral shift versus time, for 4 ppm chloroform at dry conditions (blue curve) and at ambient conditions with humidity (light blue curve). The humidity in the chamber was measured using an automatic humidity controller from ETS (Electro-Tech Systems, inc.), (Model 514).

The results reveal that the presence of water vapors inside the chamber during the sensing process led to smaller sensitivities in both cases (see Fig. 5.20, ethanol-left and chloroform-right), compared with the measurements in dry atmosphere. The existence of vapor species in the chamber could induce a pre-occupation of the available adsorption sites on the photopolymerized reflection surface of the device, allowing a smaller number of ethanol or chloroform species to adhere.

In more detail, considering that water and ethanol are fully miscible liquids, the surface monolayer that was initially formed on the photopolymerized reflection surface could contain both species at the same time, resulting reduced refractive index changes on the reflection interface instead of that in case of pure ethanol. As a consequence a smaller spectral shift was recorded in case of ambient conditions, namely 4.84 nm for dry conditions, 1.54 nm for 52.2 % humidity and 0.77 nm in case of 60.9 % humidity in the chamber (see Fig. 5.18 green and red curves, left).

In case of chloroform, that exhibits a low solubility to water of ~ 0.8 g/100 mL, the spectral shift was reduced by a factor of almost 5x, even for low humidity levels, namely the spectral shift was 3.63 nm at dry conditions while it was reduced to 0.77 nm in case of 35.5 % humidity presence.

5.3 Fiber-endface FP microresonator with distinct response to different chlorinated organic solvents vapors

Over the last years, different chemical fabrication procedures and technique have been used in order to develop optical fiber sensors with increased sensitivity and selectivity for the detection of gaseous species that are harmful for the environment and the humans' health. Fiber endface, cladding or even the inside walls of the capillaries of photonic crystal fibers (PCF) or microstructured optical fibers (MOF) have been overlaid with suitable transducing materials for attaining sensitivity (and potentially selectivity) to specific gaseous and liquid substances. In most cases, the sensing operation relies on chemisorption processes on the surface of the actuating material and the formation of chemical bonds that consequently affect its optical signature (usually refractive index and/or absorption). Transducing/actuating materials such as fluorescent dyes [37], inorganic oxides [17], vapo-chromic materials [38], graphene [39], polymers [40, 41] and materials prepared by sol-gel process [42] have been used. Consequently, the selectivity of the sensing device enhances significantly due to the chemisorption reactions between the actuation material and the vapors. However, the formation of chemical bonds and the binding of solvent molecules on the surface of the actuation element is often hard to revert without causing damage and/or surface corrosion that reduce the sensing device performance and re-usability.

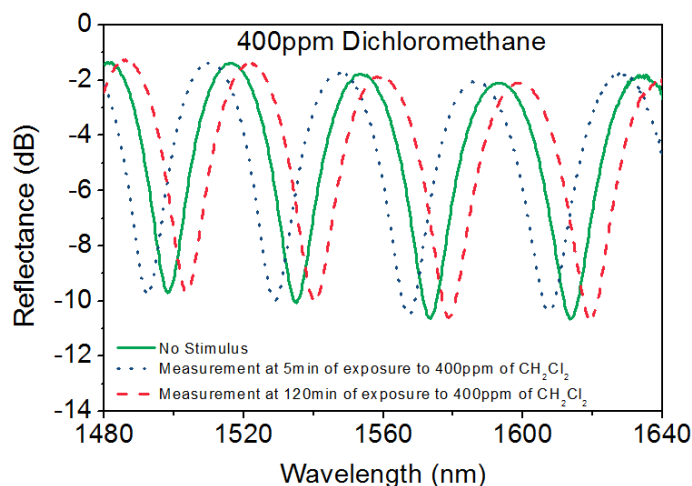
The aforementioned fiber sensors based on actuation element layers or cavities have been used for the detection of chlorinated volatile organic compounds (Cl-VOCs) and solvents, since they are highly toxic for human health and hazardous for the environment.

The differences in the response of the fabricated endface FP optical fiber sensor to

ethanol and chloroform vapors, presented in section 5.2, as well as the fact that its sensing mechanism was based on physisorption effects, motivated us to test the ability of our sensor, to distinguish vapors which belong to the same "family". Thus, herein, the as-fabricated endface FP micro-prism sensing probe was tested for the detection of organic solvent vapors of three different Cl-VOCs, i.e. dichloromethane (CH_2Cl_2), chloroform (CHCl_3) and carbon tetrachloride (CCl_4). In sections 5.2.3 and 5.2.5, it was presented that the sensing mechanism of the fabricated FP micro-prism sensing device, was not dependent only on the optical and vapor pressure characteristics of the solvents, but also on their molecular structure and affinity to the sensing surfaces resulting differences in spectro-temporal response of the device. Therefore, this sensing device is a good candidate for the detection and the distinct response of Cl-VOCs, since the molecules of these solvents exhibit dissimilar packing efficiency due to their molecular size variation, and the variable repulsive forces created between their molecules in accordance to their electronegativity. Below, the results of the experiments will be presented and the sensing principle will be explained in terms of standard physisorption, as well as, molecule packing mechanisms on the porous surface. Moreover, a simple refractometric model was used to describe the physisorption process of the organic vapors onto the photopolymerized structure.

5.3.1 Spectral response of the FP sensing device to Cl-VOCs

The endface FP micro-prism porous device that was used here, consisted of a 31.45 nm cavity length (d_{eff}), resulting a free spectral range (FSR) of 36.96 nm and notches of about 9 dB in amplitude strength. It has to be noted here, that all the measurements that will be presented below were obtained with the same FP device.



5.21. Typical interference reflection spectra of the endface FP device, before stimulus (green solid line), for the measurement where the pores were filled (blue shift, blue dotted line) and at the saturation (red dashed line) for 400ppm of dichloromethane.

Characteristic spectra recorded at the reflection mode before stimulus (green dashed curve) and during the exposure of the sensing device to 400 ppm of dichloromethane are presented in Figure 5.21. As data show, within the first five

minutes of exposure to dichloromethane vapors, the existing pores on the photopolymerized reflection surface were getting filled resulting a 5.72 nm blue shift (blue dashed curve). After the 5th minute and till the end of the measurements at 120th minute, an 11.22 nm red shift was observed (red dashed curve). Consequently, a 5.5 nm total red shift was recorded between the initial measurement before stimulus and the last measurement at saturation in the chamber.

The selectivity performance of this sensing device relied on the filling rate of the pores existing on the photopolymerized reflection surface with the vapors of chlorinated solvents. It had been discussed in section 5.2.1a that based on bibliography [26], we consider a porous layer with an average pores size of approximately 30 nm. Thus, the actual pores size did not have a direct impact on the packing efficiency neither the mechanism of the physisorption process, since several thousands of molecules were required to fully fill the pores on the surface.

To draw a more detailed picture of the sensing mechanism, spectral shift data of the FP notches versus sensing time for different vapor concentrations of the three Cl-VOCs are presented in Figure 5.22. Again, the first observation according to these data is that the sensing device presents a distinct non-monotonic time-dependent spectral response to the vapors of the three different chlorinated organic solvents that was used for these experiments.

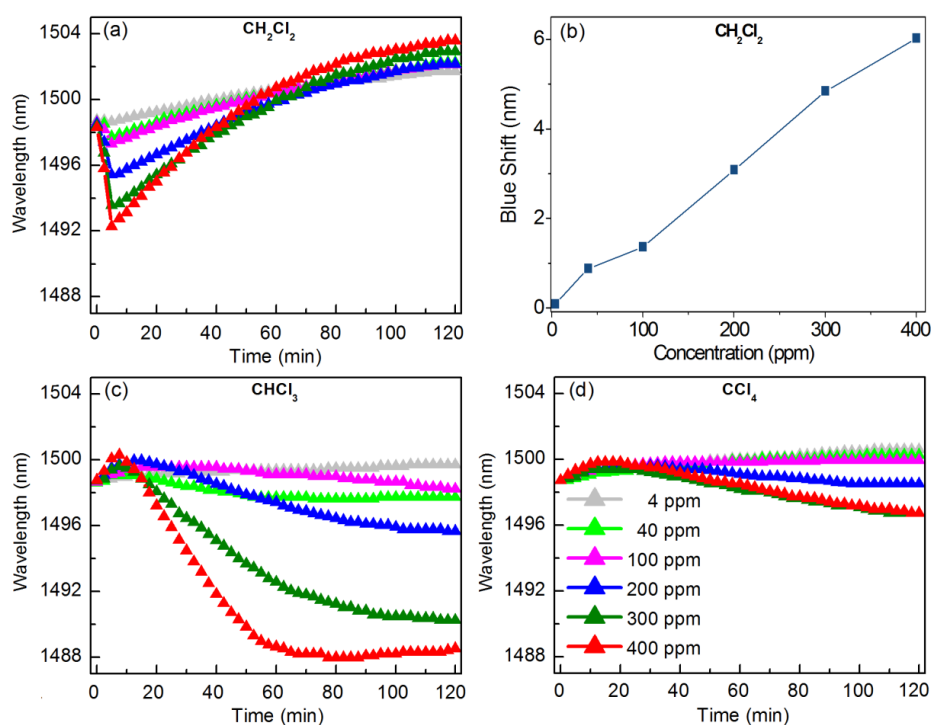


Fig. 5.21. Wavelength shift versus time of exposure profiles for six different concentrations of (a) CH₂Cl₂, (c) CHCl₃, and (d) CCl₄ VOCs respectively. Concentrations are listed in (d). Blue shift observed within the first five minutes of exposure due to vapors of CH₂Cl₂ solvent versus concentration is presented in (b).

In particular, for the case of CH₂Cl₂, when the solvent was injected in the chamber and started to evaporate, rapidly progressing blue shift was obtained within the first five minutes (see Figure 5.21(a)). As the concentration of the vapors was

increased, the magnitude of the blue shift was also increased progressively, as shown in Figure 5.21(b). This was expected since the existence of more vapor molecules in the chamber increases the probability and the required time that the available adhesion sites, within the pores need to be occupied [23]. After the 5th minute, a red spectral shift of the FP notches was observed over the exposure time. This behavior had been observed before, and was discussed in detail, in section 5.2.1, when other similar FP endface sensing probes had been exposed to ethanol vapors (see Fig. 5.7a for micro-prism resonator in section 5.2.1 and Fig. 5.9 for micro-funnel resonator in section 5.2.1b) [12]. In all these cases, this non-monotonic spectral behavior was attributed to the pores filling of the photopolymerized reflection surfaces [24, 25] and it was attributed to physisorption effects, since upon flushing the chamber with nitrogen, the sensing probe fully recovered to its initial spectral characteristics.

Accordingly, when the porous device was exposed to CHCl_3 (see Fig 5.21(c)) and CCl_4 (see Fig. 5.21(d)), the aforementioned blue shift appeared weaker and later in time scale. More specifically, within the first ten minutes of exposure to CHCl_3 vapors a red shift was recorded for all concentrations studied. Following this period, a blue shift was observed with its magnitude being more significant for concentrations higher than 200 ppm. Finally for the case of CCl_4 solvent, for concentrations up to 100 ppm the blue shift was totally absent, and a weak monotonic red shift was observed (see Fig. 5.21(d)). For concentrations higher than 200 ppm, a blue was observed only after several minutes of exposure.

The above spectro-temporal behavior can be explained considering the chlorine coordination/number of the three different chlorinated molecules, as well as, the corresponding differences among their physical properties. CH_2Cl_2 molecules contain only two Cl atoms [36], resulting in greater molecular dipole moment (Debye number) compared to the CHCl_3 and CCl_4 , although the last exhibit higher vapor pressures (see Table 5.1, in section 5.1.1b). Therefore, the greater polarizability, dichloromethane molecules can faster attach and diffuse into the porous photopolymerized reflection surface; the CHCl_3 molecules of lower molecular polarizability appear slower in occupying the porous sites of the sensing probe. Finally, the physisorption process of the non-polar CCl_4 molecules, relies mainly on Van der Waals forces [23, 36], and thus, is much weaker, resulting to minimal refractive index changes in longer exposure times.

Consequently, it has to be noted here, that for the current study, the presence of pores on the photopolymerized reflection surface was critical for the distinct spectral response of the sensing device, since the operation principle was strongly relied on the pores filling with the Cl-VOCs vapor molecules.

5.3.1a Recovery of the endface FP optical fiber resonator after Cl-VOCs measurements, by flushing the chamber nitrogen

In all the aforementioned experiments, upon flushing the chamber with pure nitrogen, the sensing probe fully recovered to its initial spectral characteristics, within 5 min for all the tested Cl-VOCs (see Fig. 5.22), in contrary with the distinctly

different characteristic times of tens of minutes required for their detection response. The fully recover of the device was one more evidence, that the sensing mechanism of the fabricated FP device relied on physisorption phenomena.

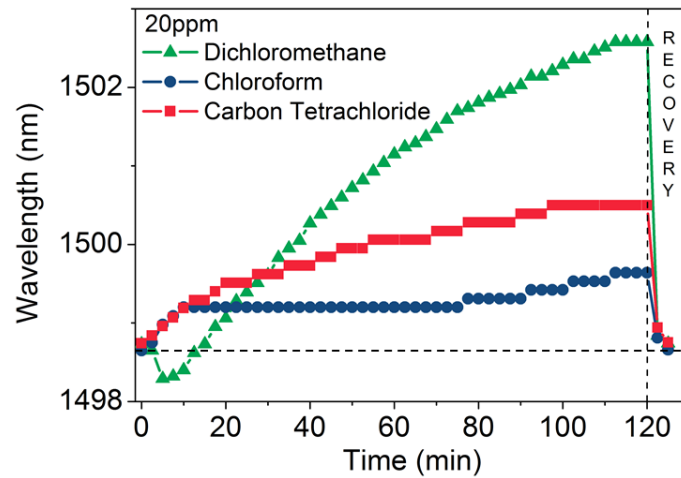


Fig. 5.22. Shift in wavelength versus time and recovery upon flushing the chamber with nitrogen for 20 ppm concentration of CH_2Cl_2 , CHCl_3 , and CCl_4 vapors.

5.3.1b Testing the FP optical fiber resonator at slightly higher temperature

Moreover, sensing experiments were performed for various concentrations of CHCl_3 vapors, for increased ambient temperature at 23.1°C . It has to be noted here, that these experiments were performed with another FP sensing probe fabricated using slightly different energy density conditions, leading to slightly different porosity and spectra profile. Even though, the results clearly demonstrate the effect of temperature on the sensing response of such type of sensing probes. Figure 5.23 presents the results for 400 ppm CHCl_3 concentration at 21.5°C (blue curve) and 23.1°C (red curve).

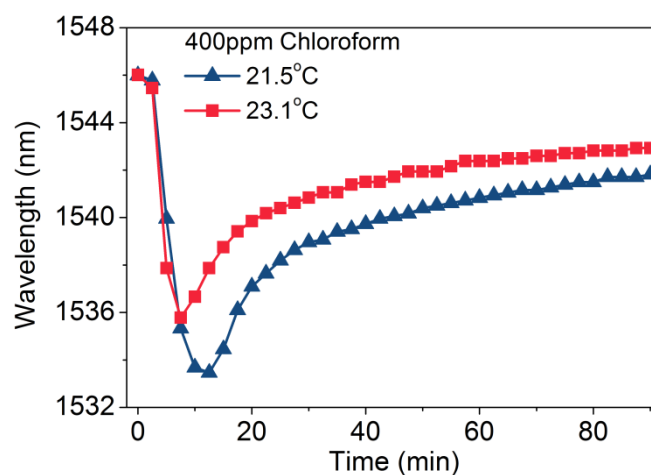


Fig. 5.23. Wavelength shift data for 400ppm concentration of CHCl_3 VOCs using another FP micro-sensor, under two different ambient temperature conditions, namely 21.5°C (blue curve) and 23.1°C (red curve).

As it is observed from data presented in Figure 5.23, an increase of approximately

2 °C at room temperature speeded up the appearance of the blue shift by 5 min, approximately, while the magnitude of the blue shift in wavelength decreased by 2 nm. Moreover, the red shift of the FP fringes increased by approximately 1 nm. Generally, the increase of the temperature reduced pores filling process due to the dependence upon Van der Waals forces [36].

5.3.2 Simulating the sensing performance of the endface FP optical fiber sensor to the presence of dichloromethane vapors

The distinct response of the investigated sensing device relied on the temporal and magnitude differences of the blue shift presented in the spectral response of the sensing probe during the exposure of the photopolymerized cavity to different organic vapors. In order to explain and quantify these spectral shifts of the sensing probe that are likely attributed to pores filling and the physisorption processes on the reflection surfaces, a multilayer Fabry-Perot model was used. The model was applied in the data for 400 ppm of CH_2Cl_2 , where a full cycle of blue and red spectral shifts took place within the 120 min that the device was exposed to the vapors.

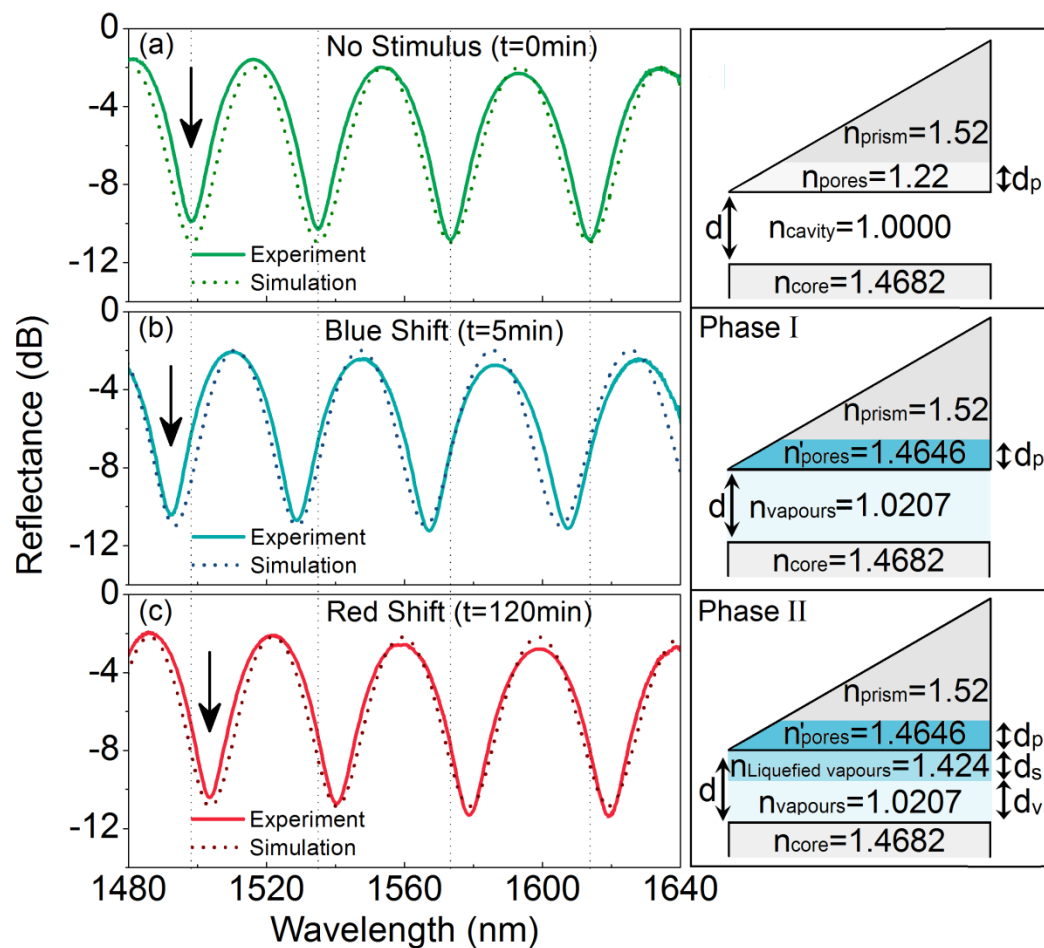


Fig. 5.24. Simulation spectra of 400 ppm CH_2Cl_2 for three different instances of the sensing process; (a) for $t=0$ min, (b) for $t=5$ min and (c) for $t=120$ min, and schematic representation of the applied theoretical model (see text). Experimental spectra are also included for the sake of comparison, while the arrows point out the selected experimental notch plotted in Fig. 5.20(a).

For this simulating model, three different stages were considered, depending on the vapors sensing progression. The first stage was corresponding to $t = 0$ min, where no stimulus were existed in the chamber (see Fig. 5.24(a)). The second stage (Phase I) correlated with the time that the blue shift had the maximum value, namely $t = 5$ min, (see Fig. 5.24(b)). Finally the third stage (Phase II) corresponding to the last measurement of the exposure to CH_2Cl_2 vapors, at $t = 120$ min (see Fig. 5.24(c)).

In the first stage, the photopolymerized micro-prism reflection surface was divided into two layers, since we assumed that the porous layer was responsible for the distinct response of the fabricated FP sensing device. The first layer was an outer thin porous layer with a nominal thickness d_p of the order of the roughness of the material (namely $d_p=30$ nm) [26], while the second layer was a thick non-porous layer (see Fig. 5.24(a), right sketch). Therefore, a three layer FP optical interference approximation model was used for fitting the data of the FP resonator in ambient atmosphere. The normalized total reflective intensity $I_{R(3LM)}(\lambda)$ was calculated using Equation (1) that had been presented in section 5.2.1a.

Since at $t = 0$ min no solvent had been injected in the chamber, the refractive index of the FP cavity was set to be $n_{\text{cavity}} = 1$, while the refractive index of the thick non-porous layer was equal to the refractive index of the hybrid photopolymerized material, namely $n_{\text{prism}} = 1.52$ (see Fig. 5.24(a)). Using the aforementioned three layer FP optical interference approximation model (Eq. (1)), the effective refractive index of the porous thin layer was calculated to be $n_{\text{pores}} = 1.22$ (see Fig. 5.24(a)). From this effective refractive index value a filling ratio G of this porous layer was extracted, which was estimated to be 0.577 for the experimental data fitted.

On the following phase (Phase I), the CH_2Cl_2 organic solvent was injected into the chamber and vapors were generated, thus, exposing the FP sensing probe. Within the first five minutes of the exposure, the vapors were adsorbed on the available sites within the porous layer, and filled the pores on the reflection surface of the photopolymerized micro-prism with condensed organic solvent. Moreover, in the same time the refractive index of the FP cavity was increased due to the vapors introduction until the saturation point (see Fig. 5.24(b)). The refractive index of the porous layer at this stage was estimated according to the filling ratio G , emerged from the first stage at $t = 0$ min. In order the effective refractive index n'_{pores} of the organic vapor filled layer to be calculated, the refractive index of the CH_2Cl_2 (see Table 5.1) and this of the photopolymerized resin were used, resulting a $n'_{\text{pores}} = 1.4646$. Applying again the three layer FP optical interference approximation model (Eq. (1)) a blue wavelength shifts of the FP spectral notches was observed, which was in good agreement with the experimental findings (Fig. 5.24(b), $t=5$ min).

During the last stage (Phase II), the pressure in the chamber was stabilized while the red shift of the FP notches was continued to be observed. As it was already mentioned, in case of ethanol detection in section 5.2.2 where the same spectral response was observed, this phenomenon is based on BET theory [23]. At this stage, the vapors are adhering on the available sites existing on the already formed monolayer on the porous reflection surface (Phase I, $t = 5$ min), forming an additional thick layer (d_s) on the aforementioned monolayer (see Fig. 5.24©). For this reason,

one more layer was added to the theoretical model and the equation for the normalized total reflective intensity $I_{R(4LM)}(\lambda)$ for the 4 layer FP model was:

$$\begin{aligned}
I_{R(4LM)}(\lambda) = & (L_1)^2 + (L_2)^2 + (L_3)^2 + (L_4)^2 \\
& - 2L_1L_2 \cos\left(\frac{4\pi n_v d_v}{\lambda}\right) - 2L_1L_3 \cos\left[\left(\frac{4\pi n_v d_v}{\lambda}\right) + \left(\frac{4\pi n_{LV} d_s}{\lambda}\right)\right] \\
& - 2L_1L_4 \cos\left[\left(\frac{4\pi n_v d_v}{\lambda}\right) + \left(\frac{4\pi n_{LV} d_s}{\lambda}\right) + \left(\frac{4\pi n_p d_p}{\lambda}\right)\right] \\
& + 2L_2L_4 \cos\left(\frac{4\pi n_{LV} d_s}{\lambda}\right) + 2L_2L_4 \cos\left[\left(\frac{4\pi n_{LV} d_s}{\lambda}\right) + \left(\frac{4\pi n_p d_p}{\lambda}\right)\right] \\
& + 2L_3L_4 \cos\left(\frac{4\pi n_p d_p}{\lambda}\right)
\end{aligned} \tag{5}$$

where

$$L_1 = \sqrt{R_1}$$

$$L_2 = (1 - T_1)(1 - R_1)(1 - a)\sqrt{R_2}$$

$$L_3 = (1 - T_1)(1 - T_2)(1 - R_1)(1 - R_2)(1 - a)\sqrt{R_3}$$

$$L_4 = (1 - T_1)(1 - T_2)(1 - T_3)(1 - R_1)(1 - R_2)(1 - R_3)(1 - a)\sqrt{R_4}$$

with T_1 , T_2 and T_3 the transmission loss factors at reflection surfaces 1, 2 and 3 respectively while $R_1 = R_{r1}R_{s1}$, $R_2 = R_{r2}R_{s2}$, $R_3 = R_{r3}R_{s3}$ and $R_4 = R_{r4}R_{s4}$ with R_{r1} , R_{r2} , R_{r3} and R_{r4} correspond to the power reflection coefficients at surfaces 1, 2, 3 and 4 respectively and R_{s1} , R_{s2} , R_{s3} and R_{s4} to the Rayleigh scattering loss coefficients [28, 29]. Moreover a is the air cavity absorption loss factor. All the aforementioned coefficients and loss factors were presented in details in Chapter 4, sections 4.2.2 and 4.3.2. Furthermore n_v corresponds to the refractive index of the vapors in the open FP cavity with length $d_v = d - d_s$ (see Fig. 5.23 Phase II), where d_s was the thickness of the formed overlayer of liquefied vapors within the FP cavity with refractive index of n_{LV} . Additionally n_p corresponds to the refractive index of the porous layer with d_p thickness.

Herein, the refractive indices that were used for the simulation were namely; $n_{\text{vapors}} = 1.0207$ and $n'_{\text{pores}} = 1.4646$. Using the four layer FP optical interference approximation model a red wavelength shifts of the FP notches was confirmed. The simulated results were again in good agreement with the experimental findings presented in Figure 5.23(c). Moreover, using this model, the thickness of the additional liquefied vapors layer was calculated to be ~ 500 nm. During simulations, this layer was assumed to be formed only onto the photopolymerized reflection surface. In fact, this layer should be taking into account that was formed not only on this reflection surface, but also on the cleaved endface of the fiber, which consist the

second reflection surface of the FP cavity, and as a consequence, the thickness of layer should be divided by a factor of $\sim x2$.

5.4 Fiber-endface FP microresonator for probing of oily samples

After the successful test of the fabricated endface FP optical fiber device as a gas sensor, we considered to test it also as a liquid sensor. We would like to observe the differences that we could probably be able to see in its spectral response when operating as liquid sensor, in comparison with the gas sensing.

Moreover, liquid sensors are good candidates to be used in industries for food quality monitoring, including detection of adulteration, genetic modification and micro-organism growth [43-45].

For these reasons, the fabricated FP endface optical fiber device was tested as liquid sensor using oily samples of different refractive indices.

5.4.1 Spectral response of the FP sensing device to oily samples

The endface porous FP device that was used for these experiments was consisted of a $14.86 \mu\text{m}$ cavity length (d_{eff}), resulting an interference spectra of free spectral range (FSR) of 78 nm, while the notches presented a fringe visibility of 16 dB. The characteristic interference spectrum in reflection mode is presented in Figure 5.25.

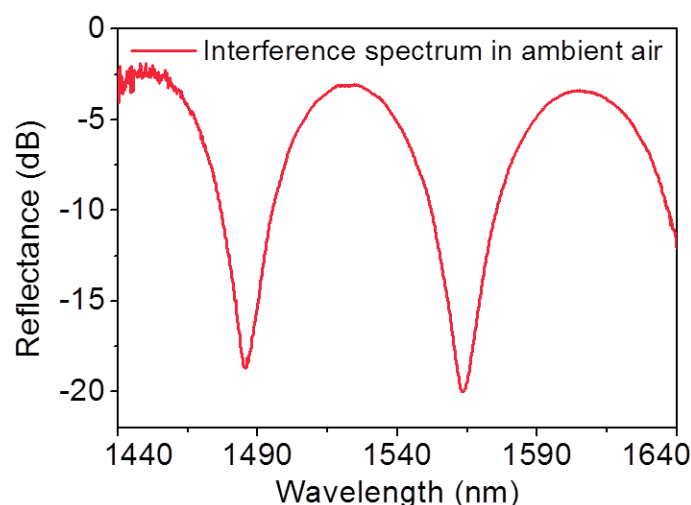


Fig. 5.25. Interference spectrum in reflection mode of the resonant probe in ambient air conditions.

Following the experimental procedure described in section 5.1.2, the sensing head was immersed in the oily liquid sample and the interference spectra in the reflection mode was recorded every 2.5 min. By this way all the refractive index oily liquids from series AA, A1 and A2 had been examined (see Table 5.2 in section 5.1.2).

After each set of measurements for each oil, the sensing head was immersed in 2-propanol for 5 min, to rinse the oil from the FP cavity and the porous surface and then was left to dry in ambient air conditions for approximately 30 min since the same sensing head was used for all the measurements performed. No spectral hysteresis was observed after repeated oil immersion and isopropanol cleaning process.

Figure 5.26 presents the wavelength shift versus immersion time in the oily samples, of the 1563 nm notch of the FP resonator for three oils with the lowest refractive indices from the series AA, A1 and A2.

In this approach, the porous section of the photopolymerized FP resonator was investigated as a diffusion layer for oil based liquid samples. This system is simpler than those presented before, since when the liquid penetrates the open FP cavity, diffuses into the pores of the fabricated reflection surface resulting a blue shift. Since the porous layer is filled with the oily sample, a plateau is observed in the spectral response of the sensing device (see Fig. 5.26).

It was observed that as the refractive index of the oils was increased, more time was required in order the oily liquid to diffuse in the pores of the photopolymerized reflection surface. When the pores and the FP cavity got filled with the oil, the spectral shift was stabilized. Namely, 7.5 min, 12.5 min and 22.5 min required for the spectral stabilization of the oils with refractive indices of 1.40, 1.46 and 1.58 respectively, resulting blue shifts of 1.1 nm, 1.98 nm and 5.72 nm correspondingly. These oils came from different series (namely AA, A1 and A2) and different substances had been used for their synthesis in order to exhibit tailored refractive index values (see table 5.2 in section 5.1.2). The sensitivities that were obtained from these data, for the oils with the lowest refractive indices from the three series (AA, A1 and A2) examined here, were $S_{1.40} = 2.75$ nm/RIU, $S_{1.46} = 4.30$ nm/RIU and $S_{1.58} = 9.86$ nm/RIU respectively.

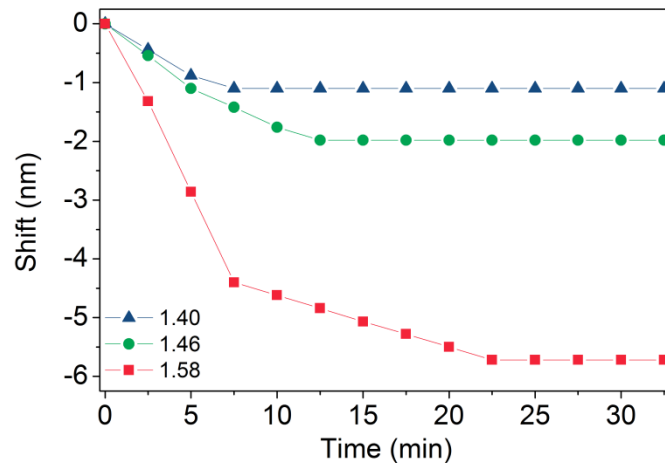


Fig.5.26. Wavelength shift of the fiber enface FP resonator versus immersion time in oily samples, of the 1563 nm notch of the FP resonator for three oils with the lowest refractive indices from the series AA, A1 and A2.

In addition, to the different spectro-temporal behavior of the FP device, fundamental differences in the fringe visibility of the spectral notches were also observed. Figure 5.27(a) presents the characteristic interference spectra recorded when the cavity of the FP optical fiber device were fully filled with the oily liquids with the lowest refractive indices from the series AA, A1 and A2. As it is observed in this figure, for the oil with refractive index 1.40 the fringe visibility was ~28 dB with a FSR of 57.4 nm, while in case of the oil with refractive index 1.58 these values were

~2.6 dB and 50.8 nm respectively, as was expected, since the FSR is inversely proportional to the refractive index of the medium within the FP cavity. For the oil of the series A1, which refractive index (1.46) was approximated the refractive index of the first reflection surface (optical fiber endface), namely $n_{\text{core}} = 1.4682$, the Fresnel's reflections almost vanished and for this reason the fringe visibility presented the lowest value.

Moreover, the 3 layer FP optical interference approximation model was used for fitting the data of the FP resonator. Equation (1) was used to calculate the normalized total reflective intensity $I_{R(3LM)}(\lambda)$. The refractive indices of the porous layer for the three refractive index oils were considered to be $n_{\text{pores}}^{AA} = 1.46$, $n_{\text{pores}}^{A1} = 1.49$ and $n_{\text{pores}}^{A2} = 1.55$ respectively, since the filling ration $G=0.5$.

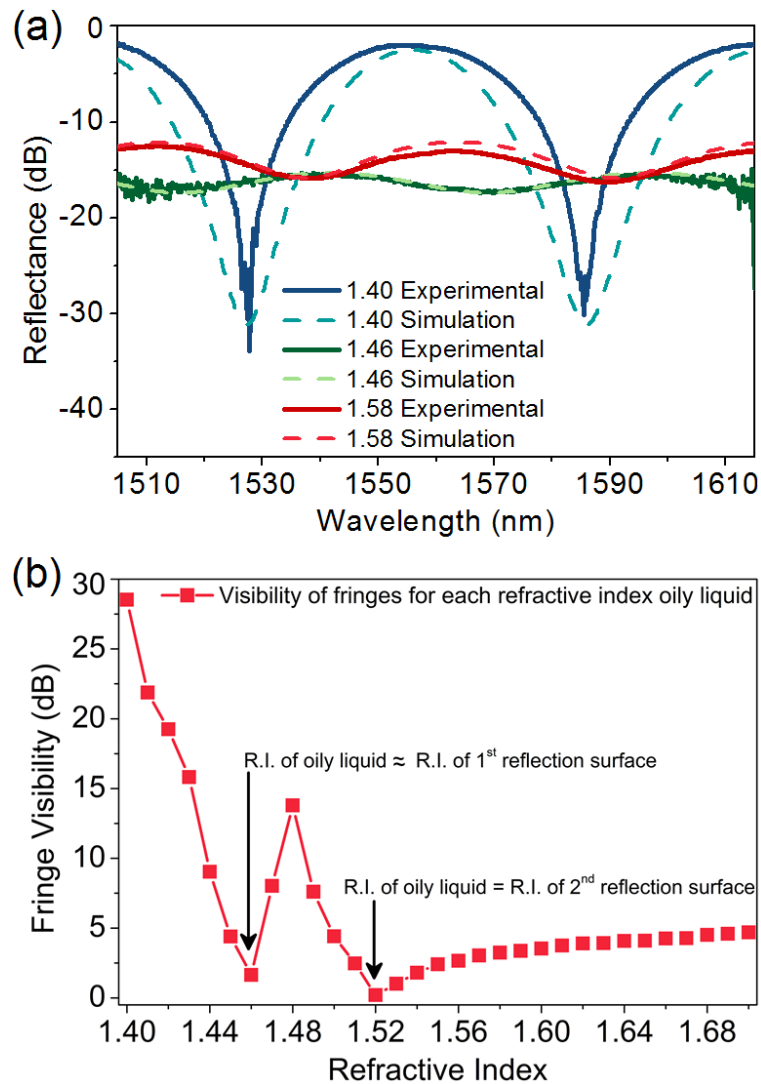


Fig.5.26. (a) Reflection spectra of the device after saturation of the FP cavity with the oily liquids with the lowest refractive indices from the series AA, A1 and A2, and the simulated spectra. (b) Strength visibility of the fringes after saturation versus the refractive index of the oily liquids that were examined.

Figure 5.26(b) presents the strength visibility of the spectral fringes versus the refractive index for all the oily liquids that had been examined after the spectral data

rested to saturation. When refractive index of the oily liquid approximated the refractive index of one of the optical materials constituted the FP cavity (RI of cleaved fiber (1st reflection surface) $n_{\text{core}} = 1.4682$, and RI of photopolymerized porous surface (2nd reflection surface) $n_{\text{prism}} = 1.52$) the fringe visibility reached values close to zero, because the Fresnel's reflections at the corresponding interface almost vanished.

In order to draw a more detailed picture for the changes in spectro-temporal response of the porous FP sensing device to the refractive index oils which belonged to one of the examined series, namely that of A1, the shift of the notches to time was plotted and is presented in Figure 5.27. The results revealed that also in this case that oils came from the same series but they had different ratios of substances, they presented different temporal behavior with respect to the FP notch wavelength shifts. This time-dependent spectral behavior was related to the diffusion effects occurring within the porous photopolymerized reflection surfaces of the FP device. In case of the oil with refractive index equal to 1.46 the recorded blue shift was 1.98 nm, while 12.5 min were required in order the oil to penetrate the FP cavity and be diffused in the porous membrane resulting saturation. For the 1.51 refractive index oil, the corresponding blue shift was 9.24 nm while it was stabilized after 30 min. The sensitivity for the oil with refractive index of 1.46 was calculated to be $S_{1.46} = 4.30$ nm/RIU, while for that of refractive index of 1.51 was calculated at $S_{1.51} = 18.11$ nm/RIU. Accordingly, by considering only the maximum wavelength shift obtained from the sensing head used, a refractive sensitivity of 66 nm/RIU was obtained between the 1.50 and 1.51 refractive index oils.

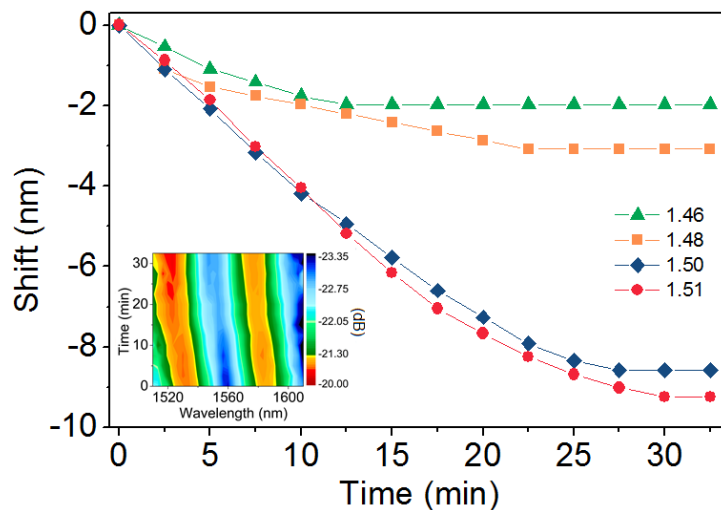


Fig.5.27. Wavelength shift versus immersion time in the oily sample, of the 1563 nm notch of the FP resonator, for four oils with different refractive indices from series A1. The error bars present the resolution of the optical spectrum analyzer during the recording of the measurements. The inset picture presents a contour graph of the wavelength shift of a single FP notch for 1.51 refractive index oil.

Although data of Figures 5.25 and 5.27 referred to an experimentally measured quantity, that of the wavelength shift of the FP resonator notches, this did not constituted a direct physical quantity/parameter that could characterize the effect of the oil diffusion into the porous section of the photopolymerized micro-prism.

Therefore, in order to explain the specific spectro-temporal behavior and predict the diffusion effects in the porous membrane of the fabricated sensing head, as described above, a three-layer Fabry–Perot model was used. Such types of multilayer FP models had been used previously in section 5.3.2, in order to predict the spectral shifts during pores filling with chlorinated solvent vapors, as well as the formation of the physisorption liquid layer on the reflection surface [13]. Here, the three-layer FP model was applied in the data of the lowest refractive indices from each series, namely 1.40, 1.46 and 1.58, for calculating the n_{diffuse} refractive index within the porous layer, due to the diffusion of the oil in the pores of the photopolymerized reflection surface (see Eq. (1) in section 5.2.1a). As n_{diffuse} , an average refractive index of the whole porous section was defined here. While this assumption did not described in full detail the oil diffusion effect into the porous area, it provided a first insight into the physical effect, which could lead to an easy parametrization of the sensing mechanism.

Similar to the interpretation used in section 5.3.2, it was assumed that the photopolymerized porous micro-prism constituted of an outer thin porous layer with thickness of the order of the roughness of the material (namely $d_p = 30$ nm, see Fig. 5.28(b)), and a thick non-porous layer (see the schematic representation of Fig. 5.28(b)). Using the three-layer model, for $n_{\text{cavity}} = n_{\text{air}}$ since initially the FP cavity was exposed to ambient air conditions and the refractive index of the thick non-porous layer to be equal to the refractive index of the hybrid material, namely $n_{\text{prism}} = 1.52$, the refractive index of the porous layer was estimated to be $n_{\text{pores}} = 1.26$. Using this value for the refractive index of the thin porous layer, a filling factor G of 0.5 was resulting, which was described the porosity of the thin diffusion layer.

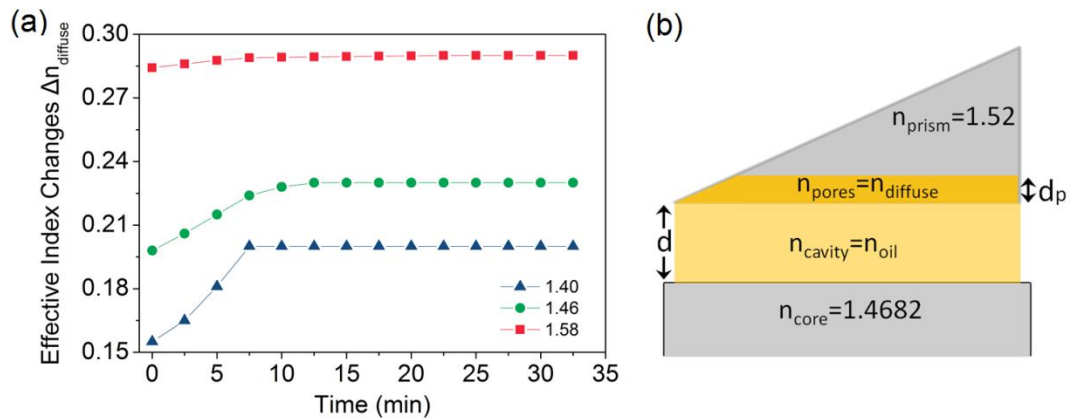


Fig.5.28. (a) Effective index changes versus immersion oily sample, for three oils with the lowest refractive indices from the series AA. (b) Schematic representation of the three-layer FP theoretical model and the refractive indices that were used (see text).

By immersing the sensing head in the refractive index oil, the FP cavity was getting filled with the refractive index oil and consequently the refractive index of the FP cavity was equal to that of the used oil $n_{\text{cavity}} = n_{\text{oil}}$. In the same time, the refractive index oil was gradually diffused in the pores of the porous layer resulting a blue shift in time till the porous layer was saturated and the wavelength depicted with a plateau

of the wavelength shift. From the recorded data in time the average refractive index n_{diffuse} is calculated for each measurement. The changes of the n_{diffuse} versus immersion time into the oil were calculated from the three layer FP theoretical model are presented in Figure 5.28, where $\Delta n_{\text{diffuse}} = n_{\text{diffuse}} - n_{\text{pores}}$. A first quantification of the diffusion was done by fitting the refractive index data of Figure 5.25 using an error function of the form:

$$f(t) = A + B \times \text{erf}(t/t_{\text{Ch}}) \quad (6)$$

where t_{Ch} was the characteristic time of the oil diffusion into the sensing head, and A and B were constant factors. Equation (6) is the most commonly used error function for fitting diffusion data in order to calculate the characteristic time t_{Ch} that a liquid needs to penetrate into a porous medium. The estimation of the characteristic time t_{Ch} for each oil examined was then used in the approximate diffusion equation [46]:

$$d = \sqrt{2Dt_{\text{Ch}}} \quad (7)$$

where d was the diffusion length (in this case the thickness of the porous layer, namely 30 nm), D was the diffusion coefficient and t_{Ch} was the time that the liquid needed to penetrate and fill the length of the diffusion layer [47], namely, the characteristic time t_{Ch} . By using the t_{Ch} from the fitting of the error function to our data and Equation (7), the diffusivities for the three oils with the lowest refractive indices from the series AA, A1 and A2 were calculated to be, $D_{1.40} = 1.021 \times 10^{-14} \text{ cm}^2/\text{s}$, $D_{1.46} = 8.678 \times 10^{-15} \text{ cm}^2/\text{s}$ and $D_{1.58} = 8.870 \times 10^{-15} \text{ cm}^2/\text{s}$, respectively. Since the oily media used were of non-/low-polar nature, and did not react with the photopolymerized porous material, we considered the diffusivities estimated to be constant during the diffusion of the specimens into the porous area [48]. As it is observed, the contaminants of the refractive index oils affected the diffusion process into the porous photopolymerized surface. The addition of Hydrogenated Terphenyl into the mixture of Aliphatic/Alicyclic Hydrocarbons for the synthesis of series A1 (see Table 5.2 in section 5.1.2), introduced a slower diffusion of these oils into the fabricated porous surface. Hydrogenated Terphenyl consist of a long triple aromatic hydrocarbon chain and has a high molecular weight (~238.36 g/mol). These characteristics could make the diffusivities of the oily samples of series A1 into the pores of the reflection surface slower than these of series AA. On the other hand, for the synthesis of series A2, 1-Bromonaphthalene was also added in the mixture of Aliphatic/Alicyclic Hydrocarbons and Hydrogenated Terphenyl. 1-Bromonaphthalene is a halogenated aromatic hydrocarbon with refractive index of approximately 1.65. The existence of the bromide bond in these oily samples possible changed the diffusivity in this case.

5.5 Conclusions

To conclude, in this chapter were presented FP sensing devices fabricated by direct laser writing onto the endface of standard single-mode commercially available telecommunication optical fiber. These devices were tested as vapor and liquid sensors [12-14].

More specifically, the fabricated device was initially tested as vapor sensor for the detection of species of two different organic solvents, those of ethanol and chloroform. Its sensitivity with respect to the surface porosity of the fabricated micro-prism sensing head was studied by reducing the pores size of the photopolymerized reflection surface using annealing treatment processes. Results show the dependence of the sensitivity and selectivity/specificity upon the porosity of the fabricated FP cavity. Moreover, the studies of the two different organic solvents revealed that the operation mechanism of the fabricated sensing device did not depended only on the optical and vapor pressure characteristics of the solvents but also on their molecular structure and affinity to the sensing surfaces. To the end, the fabricated endface FP optical fiber device was able to detect concentrations of vapor traces down to 4 ppm, revealing sensitivities of $\sim 1.5 \times 10^3$ nm/RIU after the annealing treatment at 250°C.

Afterwards, the porous (as-fabricated) FP optical fiber device was further tested as vapors sensor for the detection of traces of three different Cl-VOCs. As it was expected, the physisorption mechanism relied not only on the differences of the refractive indices and the vapor pressures of the chlorinated solvents, but also on the chlorine coordination/number of the three different chlorinated molecules which resulting different polarizabilities. Thus, the experimental results show distinct spectra response versus sensing time, for each chlorinated solvent that was examined herein, even for vapor concentrations down to 4 ppm, without any further chemical analysis needed.

After the successful use of the fabricated endface FP optical fiber device as a vapor sensor, we considered to test it as a liquid sensor. Thus the device was used for the probing of substances of oily media. Their diffusion behavior in the porous fabricated reflection surface was tested and results revealed that each of the oily liquids exhibited a distinct spectral response versus sensing time, depending on the diffusion process of the oily liquid into the photopolymerized porous reflection surface.

In all the previous cases, results show that the sensing mechanism of the devices was based on physisorption phenomena, allowing the full recover of the sensing probes to their initial spectral response and their reuse for several times. This is one more advantage of the fabricated devices since other optical fiber devices based on chemisorption phenomena has limited margins of use.

Additionally, theoretical models, based on two-beam optical interference approximation [12, 27], were used, in order to confirm the experimental results and the sensing mechanism of the fabricated devices.

The fabricated endface FP devices could potentially be used for the development of breath analyzing units based for early detection of high fatality diseases, such as

lung cancer [49-51] or metabolic syndrome [52, 53] through off-line breath analysis protocols [54], environmental and industrial safety (paper, rubber and pesticide industry) monitoring [55], where FP sensing probes such those presented here, can provide distinct response between different chlorinated organic gasses, or at food quality monitoring for the identification of adulterants [56] and plasticizers [57] in edible olive oil.

References

- [1] S. Pevec and D. Donlagic, "High resolution, all-fiber, micro-machined sensor for simultaneous measurement of refractive index and temperature," *Optics Express*, vol. 22, pp. 16241-16253, Jun 30 2014.
- [2] J. Zhu, M. Wang, L. Chen, X. Ni, and H. Ni, "An optical fiber Fabry-Perot pressure sensor using corrugated diaphragm and angle polished fiber," *Optical Fiber Technology*, vol. 34, pp. 42-46, 3// 2017.
- [3] S. Pevec and D. Donlagic, "Miniature fiber-optic sensor for simultaneous measurement of pressure and refractive index," *Optics Letters*, vol. 39, pp. 6221-6224, Nov 2014.
- [4] Y. J. Rao and Z. L. Ran, "Fiber-optic Fabry-Perot sensors take the strain under high temperature," *Laser Focus World*, vol. 47, pp. 71-74, Nov 2011.
- [5] S. Pevec and D. Donlagic, "All-fiber, long-active-length Fabry-Perot strain sensor," *Optics Express*, vol. 19, pp. 15641-15651, 2011/08/01 2011.
- [6] T. Z. Ming Deng, Yun-Jiang Rao and Hong Li, "Miniaturized Fiber-Optic Fabry-Perot Interferometer for Highly Sensitive Refractive Index Measurement," *Journal of Electronic Science and Technology of China*, vol. 6, pp. 365-, 2008.
- [7] S. Pevec and D. Donlagic, "Nanowire-based refractive index sensor on the tip of an optical fiber," *Applied Physics Letters*, vol. 102, p. 213114, 2013.
- [8] J. J. Tian, Y. J. Lu, Q. Zhang, and M. Han, "Microfluidic refractive index sensor based on an all-silica in-line Fabry-Perot interferometer fabricated with microstructured fibers," *Optics Express*, vol. 21, pp. 6633-6639, Mar 2013.
- [9] T. Wei, Y. K. Han, Y. J. Li, H. L. Tsai, and H. Xiao, "Temperature-insensitive miniaturized fiber inline Fabry-Perot interferometer for highly sensitive refractive index measurement," *Optics Express*, vol. 16, pp. 5764-5769, Apr 2008.
- [10] J. Li, F. Albri, R. R. J. Maier, W. Shu, J. Sun, D. P. Hand, *et al.*, "A Micro-Machined Optical Fiber Cantilever as a Miniaturized pH Sensor," *Ieee Sensors Journal*, vol. 15, pp. 7221-7228, Dec 2015.
- [11] J. H. Chen, X. G. Huang, J. R. Zhao, J. Tao, W. X. He, and S. H. Liu, "Fabry-Perot interference-based fiber-optic sensor for small displacement measurement," *Optics Communications*, vol. 283, pp. 3315-3319, Sep 2010.
- [12] V. Melissinaki, M. Farsari, and S. Pissadakis, "A Fiber-Endface, Fabry-Perot Vapor Microsensor Fabricated by Multiphoton Polymerization," *Ieee Journal of Selected Topics in Quantum Electronics*, vol. 21, p. 10, Jul-Aug 2015.

- [13] V. Melissinaki, I. Konidakis, M. Farsari, and S. Pissadakis, "Fiber endface Fabry-Perot microsensors with distinct response to vapors of different chlorinated organic solvents," *IEEE Sensors Journal*, vol. PP, pp. 1-1, 2016.
- [14] V. Melissinaki, M. Farsari, and S. Pissadakis, "A Fiber Optic Fabry-Perot Cavity Sensor for the Probing of Oily Samples," *Fibers*, vol. 5, p. 1, 2017.
- [15] E. s. Sigma_Aldrich,
["https://www.sigmaaldrich.com/catalog/product/aldrich/40210?lang=en®ion=GR."](https://www.sigmaaldrich.com/catalog/product/aldrich/40210?lang=en®ion=GR)
- [16] C. s. Sigma_Aldrich,
["https://www.sigmaaldrich.com/catalog/product/aldrich/528730?lang=en®ion=GR&gclid=EAIaIQobChMIwuOU6O6G2AIVDhHTCh2z1gLnEAAYASAAEgJ1gfD_BwE."](https://www.sigmaaldrich.com/catalog/product/aldrich/528730?lang=en®ion=GR&gclid=EAIaIQobChMIwuOU6O6G2AIVDhHTCh2z1gLnEAAYASAAEgJ1gfD_BwE)
- [17] M. Konstantaki, A. Klini, D. Anglos, and S. Pissadakis, "An ethanol vapor detection probe based on a ZnO nanorod coated optical fiber long period grating," *Optics Express*, vol. 20, pp. 8472-8484, Apr 2012.
- [18] N. J. Choi, J. H. Kwak, Y. T. Lim, T. H. Bahn, K. Y. Yun, J. C. Kim, *et al.*, "Classification of chemical warfare agents using thick film gas sensor array," *Sensors and Actuators B-Chemical*, vol. 108, pp. 298-304, Jul 2005.
- [19] A. E. DDBST GmbH,
["http://ddbonline.ddbst.com/AntoineCalculation/AntoineCalculationCGI.exe."](http://ddbonline.ddbst.com/AntoineCalculation/AntoineCalculationCGI.exe)
- [20] D. s. Sigma_Aldrich,
["https://www.sigmaaldrich.com/catalog/product/aldrich/528749?lang=en®ion=GR&gclid=EAIaIQobChMIIsIue4O-G2AIVIQzTCh0GZwnmEAAYASAAEgJzXPD_BwE."](https://www.sigmaaldrich.com/catalog/product/aldrich/528749?lang=en®ion=GR&gclid=EAIaIQobChMIIsIue4O-G2AIVIQzTCh0GZwnmEAAYASAAEgJzXPD_BwE)
- [21] C. T. s. Sigma_Aldrich,
["https://www.sigmaaldrich.com/catalog/product/sial/34905?lang=en®ion=GR."](https://www.sigmaaldrich.com/catalog/product/sial/34905?lang=en®ion=GR)
- [22] G. L. E. Turner, "CRC Handbook of Chemistry and Physics - A Ready-Reference Book of Chemical and Physical Data, 70th Edition - Weast,RC, Lide,DR," *Annals of Science*, vol. 48, pp. 496-497, Sep 1991.
- [23] P. W. Atkins, *Physical chemistry*, 6th ed. ed. Oxford: Oxford University Press, 1998.
- [24] J. B. Condon, *Surface area and porosity determinations by physisorption, measurements and theory*: Elsevier, 2006.
- [25] K. S. W. Sing, D. H. Everett, R. A. W. Haul, L. Moscou, R. A. Pierotti, J. Rouquerol, *et al.*, "Reporting Physisorption data for gas solid systems with special reference to the determination of surface-area and porosity (recommendations 1984)," *Pure and Applied Chemistry*, vol. 57, pp. 603-619, 1985.
- [26] M. Malinauskas, A. Zukauskas, V. Purlys, K. Belazaras, A. Momot, D. Paipulas, *et al.*, "Femtosecond laser polymerization of hybrid/integrated micro-optical elements and their characterization," *Journal of Optics*, vol. 12, Dec 2010.

- [27] Z. L. Ran, Y. J. Rao, W. J. Liu, X. Liao, and K. S. Chiang, "Laser-micromachined Fabry-Perot optical fiber tip sensor for high-resolution temperature-independent measurement of refractive index," *Optics Express*, vol. 16, pp. 2252-2263, Feb 2008.
- [28] H. Eren. (2000, The measurement, instrumentation and sensors handbook. 1–14. Available: <http://www.crcnetbase.com/doi/abs/10.1201/b15474-3?queryID=>
- [29] R. Ellis. (2007, Explanation of Reflection Features in Optical Fiber as Sometimes Observed in OTDR Measurement Traces. (WP1281). Available: http://www.corning.com/media/worldwide/coc/documents/Fiber/RC-%20White%20Papers/WP-General/WP1281_11-2015.pdf
- [30] B. Lange, J. Wagner, and R. Zentel, "Fabrication of robust high-quality ORMOCER (R) inverse opals," *Macromolecular Rapid Communications*, vol. 27, pp. 1746-1751, Oct 2006.
- [31] Z. F. Yu and S. H. Fan, "Extraordinarily high spectral sensitivity in refractive index sensors using multiple optical modes," *Optics Express*, vol. 19, pp. 10029-10040, May 2011.
- [32] M. D. George Y. Chen, Trevor P. Newson and Gilberto Brambilla, "A Review on Microfiber and Nanofiber Based Optical Sensor " *The Open Optics Journal*, vol. 7, pp. 32-57, 2013.
- [33] Patiha, E. Heraldly, Y. Hidayat, and M. Firdaus, "The langmuir isotherm adsorption equation: The monolayer approach," *IOP Conference Series: Materials Science and Engineering*, vol. 107, p. 012067, 2016.
- [34] J. B. Condon, "Chapter 1 - An Overview of Physisorption," in *Surface Area and Porosity Determinations by Physisorption*, ed Amsterdam: Elsevier Science, 2006, pp. 1-27.
- [35] N. A. Yebo, P. Lommens, Z. Hens, and R. Baets, "An integrated optic ethanol vapor sensor based on a silicon-on-insulator microring resonator coated with a porous ZnO film," *Optics Express*, vol. 18, pp. 11859-11866, May 24 2010.
- [36] J. McMurry, *Organic chemistry*: Brooks/Cole Thomson Learning, 2000.
- [37] T. A. Dickinson, K. L. Michael, J. S. Kauer, and D. R. Walt, "Convergent, self-encoded bead sensor arrays in the design of an artificial nose," *Analytical Chemistry*, vol. 71, pp. 2192-2198, Jun 1 1999.
- [38] C. Bariain, I. R. Matias, I. Romeo, J. Garrido, and M. Laguna, "Detection of volatile organic compound vapors by using a vapochromic material on a tapered optical fiber," *Applied Physics Letters*, vol. 77, pp. 2274-2276, Oct 9 2000.
- [39] S. Some, Y. Xu, Y. Kim, Y. Yoon, H. Qin, A. Kulkarni, *et al.*, "Highly Sensitive and Selective Gas Sensor Using Hydrophilic and Hydrophobic Graphenes," *Scientific Reports*, vol. 3, Jun 5 2013.
- [40] L. Athanasekos, A. El Sachat, S. Pispas, and C. Riziotis, "Amphiphilic Diblock Copolymer-Based Multiagent Photonic Sensing Scheme," *Journal of Polymer Science Part B-Polymer Physics*, vol. 52, pp. 46-54, Jan 1 2014.
- [41] M. Giordano, A. Russo, A. Cusano, and G. Mensitieri, "An high sensitivity optical sensor for chloroform vapours detection based on nanometric film of

- delta-form syndiotactic polystyrene," *Sensors and Actuators B-Chemical*, vol. 107, pp. 140-147, May 27 2005.
- [42] S. J. Mechery and J. P. Singh, "Fiber optic based gas sensor with nanoporous structure for the selective detection of NO₂ in air samples," *Analytica Chimica Acta*, vol. 557, pp. 123-129, Jan 31 2006.
- [43] A. G. Mignani, L. Ciaccheri, C. Cucci, A. A. Mencaglia, A. Cimato, C. Attilio, *et al.*, "EAT-by-LIGHT: Fiber-optic and micro-optic devices for food quality and safety assessment," *Ieee Sensors Journal*, vol. 8, pp. 1342-1354, Jul-Aug 2008.
- [44] M. U. Abdelhaseib, A. K. Singh, M. Bailey, M. Singh, T. El-Khateib, and A. K. Bhunia, "Fiber optic and light scattering sensors: Complimentary approaches to rapid detection of Salmonella enterica in food samples," *Food Control*, vol. 61, pp. 135-145, Mar 2016.
- [45] A. Candiani, M. Sozzi, A. Cucinotta, S. Selleri, R. Veneziano, R. Corradini, *et al.*, "Optical Fiber Ring Cavity Sensor for Label-Free DNA Detection," *Ieee Journal of Selected Topics in Quantum Electronics*, vol. 18, pp. 1176-1183, May-Jun 2012.
- [46] R. W. Balluffi, S. M. Allen, and W. C. Carter, "The Diffusion Equation," in *Kinetics of Materials*, ed: John Wiley & Sons, Inc., 2005, pp. 77-97.
- [47] R. H. Doremus, "Diffusion of water in silica glass," *Journal of Materials Research*, vol. 10, pp. 2379-2389, 1995.
- [48] D. Shamiryan, M. R. Baklanov, P. Lyons, S. Beckx, W. Boullart, and K. Maex, "Diffusion of solvents in thin porous films," *Colloids and Surfaces A: Physicochemical and Engineering Aspects*, vol. 300, pp. 111-116, 6/1/ 2007.
- [49] K. Mitsubayashi, K. Yokoyama, T. Takeuchi, and I. Karube, "Gas-Phase Biosensor For Ethanol," *Analytical Chemistry*, vol. 66, pp. 3297-3302, Oct 15 1994.
- [50] R. F. Machado, D. Laskowski, O. Deffenderfer, T. Burch, S. Zheng, P. J. Mazzone, *et al.*, "Detection of lung cancer by sensor array analyses of exhaled breath," *American Journal of Respiratory and Critical Care Medicine*, vol. 171, pp. 1286-1291, Jun 1 2005.
- [51] J. Rudnicka, M. Walczak, T. Kowalkowski, T. Jezierski, and B. Buszewski, "Determination of volatile organic compounds as potential markers of lung cancer by gas chromatography-mass spectrometry versus trained dogs," *Sensors and Actuators B-Chemical*, vol. 202, pp. 615-621, Oct 2014.
- [52] F. Baldini and A. G. Mignani, "Optical-fiber medical sensors," *Mrs Bulletin*, vol. 27, pp. 383-387, May 2002.
- [53] S. Nair, K. Cope, R. H. Terence, and A. M. Diehl, "Obesity and female gender increase breath ethanol concentration: Potential implications for the pathogenesis of nonalcoholic steatohepatitis," *American Journal of Gastroenterology*, vol. 96, pp. 1200-1204, Apr 2001.
- [54] N. Queralto, A. N. Berliner, B. Goldsmith, R. Martino, P. Rhodes, and S. H. Lim, "Detecting cancer by breath volatile organic compound analysis: a review of array-based sensors," *Journal of Breath Research*, vol. 8, Jun 2014.

- [55] A. McCulloch, "Chloroform in the environment: occurrence, sources, sinks and effects," *Chemosphere*, vol. 50, pp. 1291-1308, 3// 2003.
- [56] G. Fragaki, A. Spyros, G. Siragakis, E. Salivaras, and P. Dais, "Detection of Extra Virgin Olive Oil Adulteration with Lampante Olive Oil and Refined Olive Oil Using Nuclear Magnetic Resonance Spectroscopy and Multivariate Statistical Analysis," *Journal of Agricultural and Food Chemistry*, vol. 53, pp. 2810-2816, 2005/04/01 2005.
- [57] X. Bi, X. Pan, S. Yuan, and Q. Wang, "Plasticizer Contamination in Edible Vegetable Oil in a U.S. Retail Market," *Journal of Agricultural and Food Chemistry*, vol. 61, pp. 9502-9509, 2013/10/02 2013.

Chapter 6

Ring resonators imprinted on tapered fibers

Many different techniques [1-8] have been used in order to fabricate Whispering gallery mode (WGM) microcavities of different designs, like microring [9], microdisk [10], microtoroid [11], microsphere [12, 13], microbottle [7, 14], etc. However, in most of these cases, the excitation of these microcavities is achieved by the use of an external tapered fiber which has to be in touch with the WGM microresonator [7, 15]. These coupling systems are susceptible to environmental disturbance depend upon strict alignment and they lack of robustness. Specifically, a tiny external vibration or a small misalignment can change the optimum coupling conditions and as a consequence the spectral response of the microresonator. Moreover, the use of high-resolution 3D translation stages for the alignment of the tapered fiber to the WGM microresonators would make the system expensive and bulky, eliminating the portability of the device. To overcome these problems, either specific mounts were used to keep the tapered fibers in touch with the resonators [16], or the devices were being packaged after the achievement of the optimum coupling conditions [17, 18].

Herein, we propose the fabrication of microring resonators directly onto tapered single mode telecommunication fibers by employing the multiphoton polymerization technique. This is the first time, in our knowledge, that ring microresonators will be directly fabricated onto tapered fibers. Such an approach will allow the demonstration of integrated and robust tapered optical fiber WGM resonators of straightforward packaging capabilities. These packaged devices will be small and portable, allowing optimum coupling efficiency; thus could be used at different applications, including microsensors, microlasers etc.

In this chapter, the configurations of the ring resonators that have been fabricated directly onto tapered fibers will be presented. In the first section single ring resonators and their spectral characterization as well as simulated results will be discussed, while the second section presents the results of coupled and defected ring resonators.

6.1 Experimental configurations used for the spectral characterization of the microring resonators

To confirm the successful fabrication of the microrings, after photopolymerizing and wet development processing, the spectral response of the single ring microresonators was tested using the set-up presented in Figure 6.1(a). The one input of the fabricated microresonator was coupled to a Superluminescence light source, with a spectral range of 1420 – 1680 nm, while the other edge was connected directly to an optical spectrum analyzer (OSA) using a patchcord. Light was coupled to the fabricated microring successively in both directions of the optical fiber, in order to excite the ring from both orientations and record the differences in the spectral response. For this reason capital letter “A” and “B” will be used to denote the

orientation of the excitation. For example, in the transmittance and polarization spectra, A-B signify that the light source was coupled to A while the OSA was connected to B edge (see Fig. 6.1).

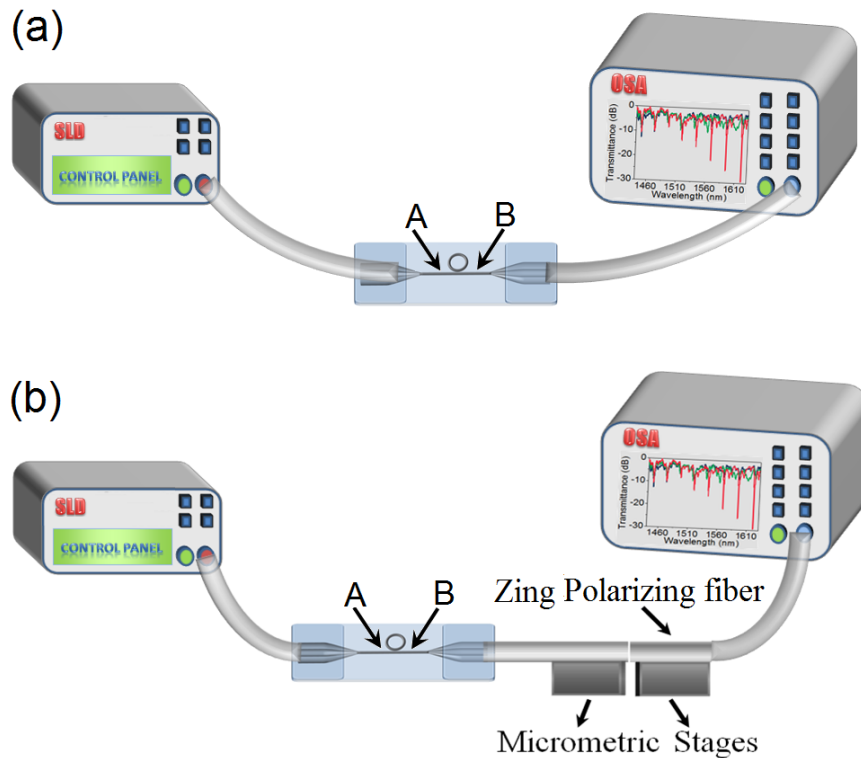


Fig. 6.1. Experimental configurations that were used for the characterization of the fabricated WGM microresonators. (a) Set-up for transmission spectra, (b) Set-up for the polarization spectra in transmission mode.

For further spectral characterization of the single ring microresonators, TE and TM polarization spectra were recorded, using the set-up presented in figure 6.1(b). In this case the input of the fabricated device was connected to the Superluminescence light source, while the other edge of the device was placed on 3D micrometric stages and this was aligned with a Zing polarizing fiber obtained from FiberCore, with a polarization extinction ratio ≥ 30 dB [19]. The other edge of the Zing polarizing fiber was connected directly to the OSA. This Zing polarizing fiber is an all-fiber polarizer in which only a single polarization state is allowed to propagate. In order the light to be correctly propagated through the Zing polarizing fiber, FiberCore recommend 5 meters of the fiber to be used [19]. This was the length of the Zing polarizing fiber that was used in these experiments.

In addition, for the spectral characterization of the coupled microresonators, the same experimental configuration to that which was used in the case of single microresonators was employed. Also in this case, the spectral response was tested in both configurations of the rings, by exciting the WGM of the “molecule” successively from both sides. Herein, in the transmittance and polarization spectra, A-B signify that the light source was coupled to the edge of the fiber that was closer to “A” ring, while the other edge, closer to “B” ring, was coupled to the OSA in order the spectral response to be recorded (see Fig. 6.2(a)).

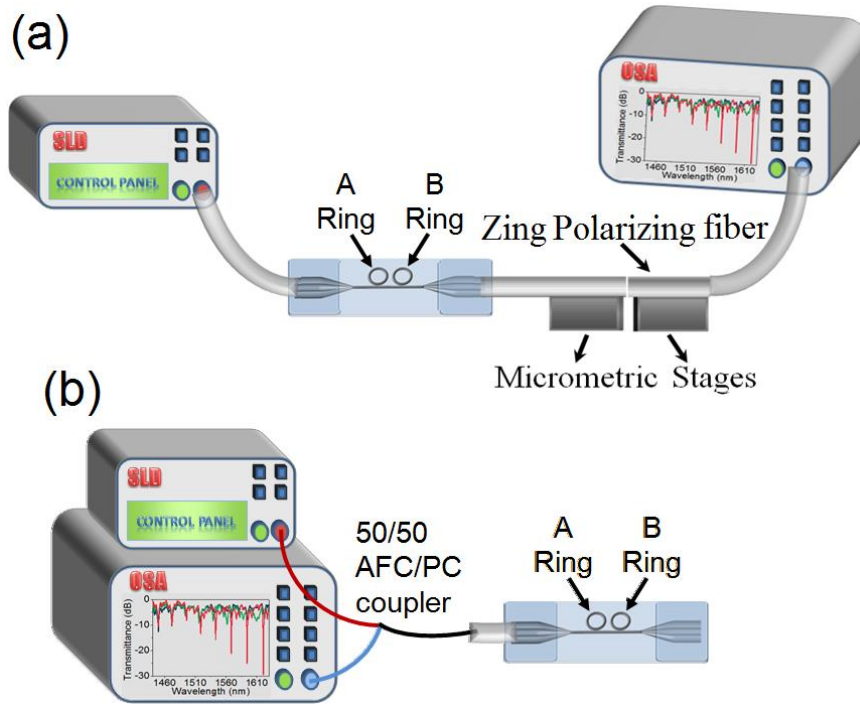


Fig. 6.2. Experimental configurations for the characterization of the coupled fabricated WGM microresonators, onto the tapered fibers. (a) Set-up for transmission spectra (by coupling the second edge of the tapered fiber directly to the OSA), or for the polarization spectra in transmission mode using the set-up as presented in the figure. (b) Set-up for the reflection spectra.

For the case of the photonic molecule, the resonance spectra in reflection mode were also recorded, using a 50/50 AFC/PC optical-fiber coupler (see Fig. 6.2(b)). Again both configurations (Ring “A” and Ring “B”) were tested.

It has to be noted here, that in all the following experiments single mode optical fiber adiabatic tapers were used, of a diameter of $\sim 2.4 \mu\text{m}$. These tapers are supporting the fundamental mode LP_{01} with a power confinement ratio (see section 2.2.4) of the total power in core and cladding to be $P_{\text{core}}/P \approx 0.97\%$. This means that the 97% of the electric field is guiding through the taper waist and only the 3% of the field escape to the surrounding environment. In contrary, the power confinement ratio for the LP_{02} mode is $P_{\text{core}}/P \approx 0.81\%$ resulting an evanescence field of $\sim 19\%$ of the electric field to interact with the surrounding environment of the tapered fiber [20-22].

6.2 Single ring microresonators fabricated onto tapered optical fiber

By employing the set-up presented in Chapter 3 at subsection 3.2.2, single ring microresonators were fabricated directly onto tapered fibers.

6.2.1 First demonstration of single ring on tapered fiber

Figure 6.3 presents Scanning Electron Microscope (SEM) images of a $20 \mu\text{m}$ diameter ring fabricated onto a $2.4 \mu\text{m}$ diameter tapered optical fiber ($n_{\text{eff}} = 1.3776$). For the fabrication of the microring the laser power was adjusted at 55 mW , while the scanning speed was set at $2000 \mu\text{m}/\text{sec}$. The thickness of the ring is approximately 800 nm measured through SEM images, while its height is about $7 \mu\text{m}$.

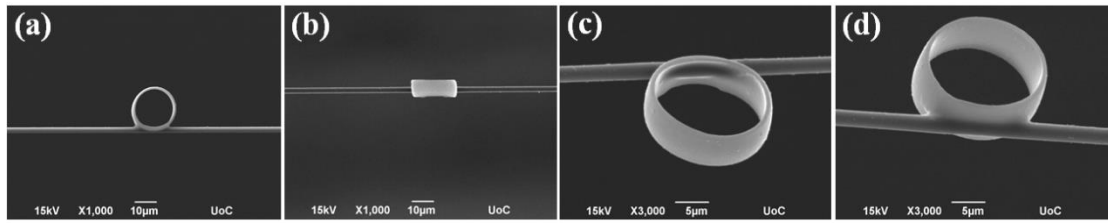


Fig. 6.3. SEM images of 20 μm diameter ring resonator onto 2.4 μm diameter tapered fiber. (a) Top view, (b) Site view, (c) and (d) tilted views.

To confirm the successful fabrication of the microresonator, spectral characterization was carried out using the set-up presented in Figure 6.1(a). The characteristic spectrum of the fabricated WGM microrings is presented in Figure 6.4.

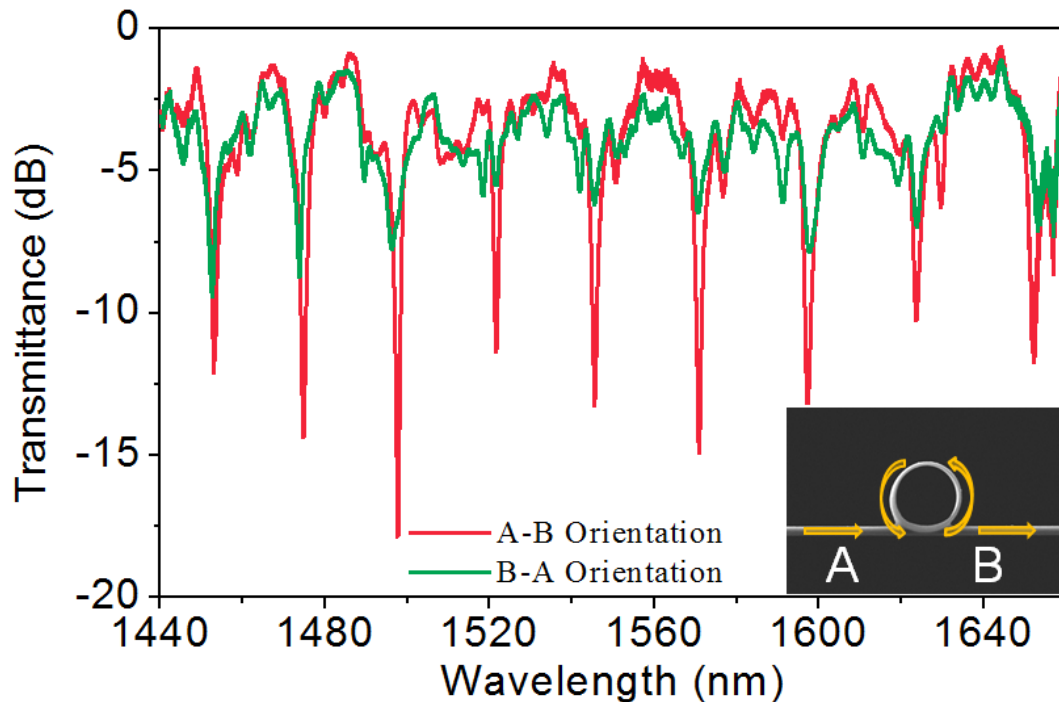


Fig. 6.4. Characteristic transmission spectrum of the fabricated 20 μm diameter WGM microresonator without polarization resolution. Red curve corresponds to the A-B orientation, while green curve corresponds to B-A orientation presented in the inset SEM figure of the fabricated microring resonator onto the tapered optical fiber (2.4 μm diameter) The yellow arrows in the inset figure presents how the light is propagating to the tapered fiber and is coupled to the ring resonator .

The spectral region for this measurements laying between 1440 nm and 1640 nm. As it is presented in Figure 6.4, the transmission spectrum recorded for the A-B orientation reveals a fringe visibility up to approximately 18 dB, while in case of B-A orientation the fringe visibility is ~ 6 dB. The free spectral range (FSR) is ~ 23.8 nm for both orientations.

The differences that are presented in the transmission spectra are emanated from the discrepancies existing on the fabricated microring. As it is presented in Figure 6.3, the ring is slightly deformed and also the thickness of its walls is not totally uniform. For these reasons, the direction of excitation has a significant role at the coupling conditions and as a consequence at the recorded spectra.

Therefore, all the fabricated rings were excited from both sides and according to

the collected spectra we chose the orientation that resulted the best coupling conditions in order to use it and continue the characterization of the fabricated WGM device.

For the specific fabricated WGM ring resonator onto the tapered optical fiber, the A-B orientation was used for further characterization of the device. Figure 6.5 presents the transmission spectrum of the microring resonator, in the spectral region laying between 1440 nm and 1640 nm. Fitting the spectra with a Lorentzian function the Q factor of the fringes was calculated to be of the order of 1.04×10^3 . In comparison with other WGM resonators that present Q factors of the order of 10^6 to 10^8 , this value is not adequate. Nevertheless, this happens due to the fact that our ring resonator is not just in touch with the tapered optical fiber, but a part of it is fabricated inside the "volume" of the optical fiber, resulting a "mismatch" at the refractive indices of the both components. Moreover, the deformation at the shape of the ring constitutes one more reason for the low Q factor. On the other hand, if one finds the optimum fabrication parameters (positioning of the ring onto the fiber, thickness of the ring so it will not be able to deformed but at the same time not be so thick that will support many modes that will result a noisy spectrum) then the value of the Q factor should be increased.

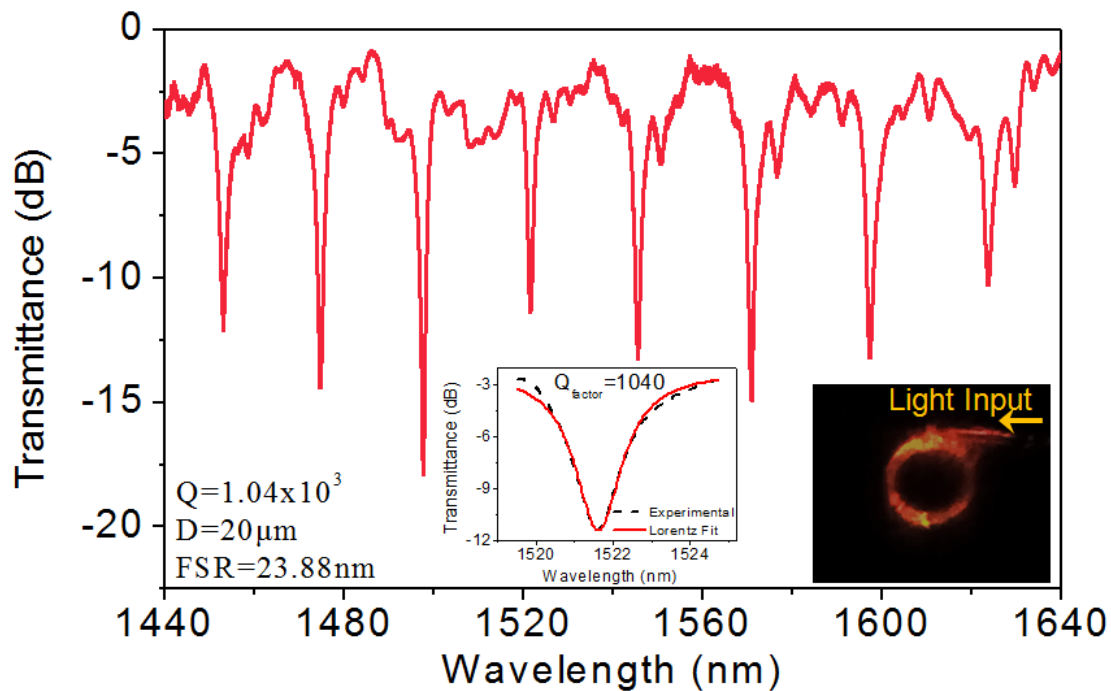


Fig. 6.5. Characteristic transmission spectrum of the fabricated 20 μm diameter WGM microresonator without polarization resolution. The inset diagram presents the Lorentz fit and the Q-factor of a selected WGM resonance, while the inset optical microscope image presents the experimental demonstration of WGM excited by a supercontinuum laser source.

For further spectral characterization, TE and TM polarization spectra were recorded, using the set-up presented in Figure 6.1(b). The TE and TM spectra of the fabricated microresonator are presented in Figure 6.6. As it observed the fringe visibility was $\sim 8\text{dB}$ for the TM polarization, while it was increased up to 29dB in case of TE polarization. This happens because in TE mode the light is propagating across

the circumference of the ring (perpendicular to the ring plane and towards to its radius), where the thickness of the fabricated ring is ~ 800 nm supporting less modes. In contrary, TM polarized light is propagating at the height of the ring, which is ~ 7 μm supporting more modes and consequently reducing the strength of the recording spectrum. Moreover the Q factor was increased up to 1.78×10^3 in case of TE polarization. This reveals that the fabricated WGM microresonator has an increased sensitivity while operates at TE polarization, conclusion that will be taken into account when this microresonating configuration will be used as a sensing device.

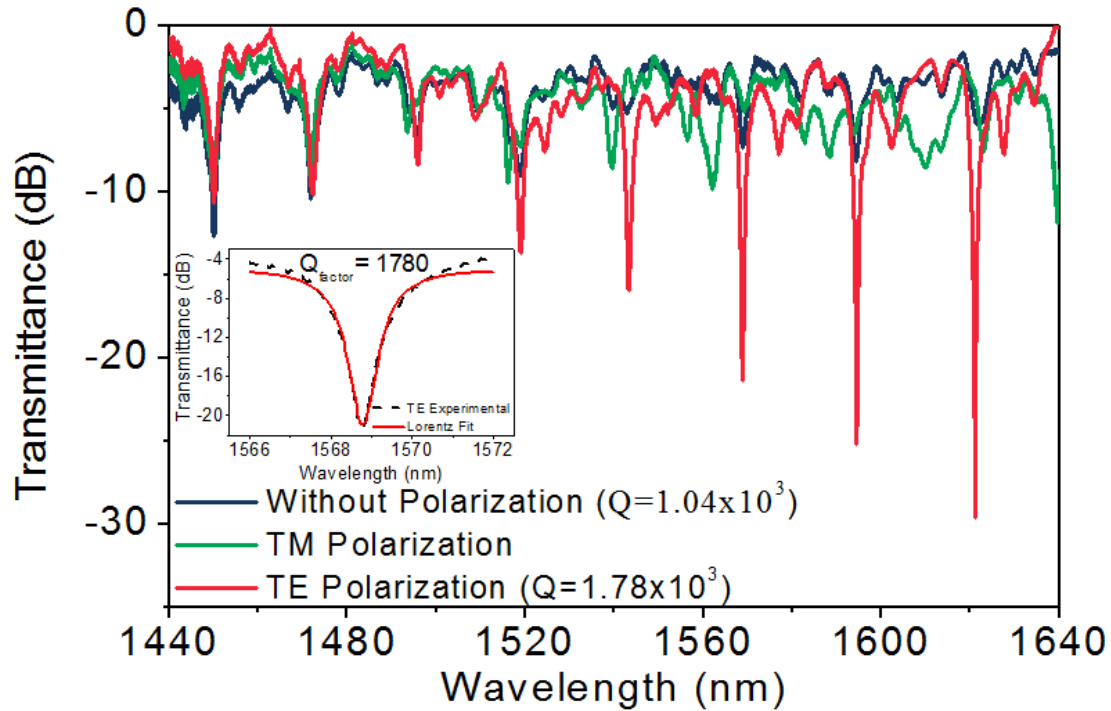


Fig. 6.6. Spectra in transmission mode of the fabricated 20 μm diameter WGM microresonator: Blue curve corresponds to the transmission spectrum without polarization, while green and red curves correspond to the TM and TE polarization spectra respectively.

For the theoretical description of the modal order location of TE polarized resonance pattern, Airy approximation was applied [23, 24].

$$\lambda_{\text{TE}}[q = 1, \ell, R, m] := 2\pi n_s R \left(v + 1.8557v^{1/3} - \frac{m}{\sqrt{m^2 - 1}} + 1.0331v^{-1/3} - \frac{0.6186m^3}{(m^2 - 1)^{3/2}} v^{-2/3} \right)^{-1} \quad [\text{Eq. 1}]$$

Equation 1 describes the wavelength positions of the first order ($q=1$) of TE modes with mode number ℓ . Moreover, n_s is the refractive index of the ring resonator, R is the radius of the ring, $m = n_s/n_e$ is the refractive index contrast at the ring-environment interface, n_e is the refractive index of the environment (in this case air) and $v = \ell + 1/2$. The experimental TE wavelength resonance data presented in Figure 6.7 (red solid line) are in good agreement with those predicted in simulations (black dashed line) and all the modes were characterized by their modal order.

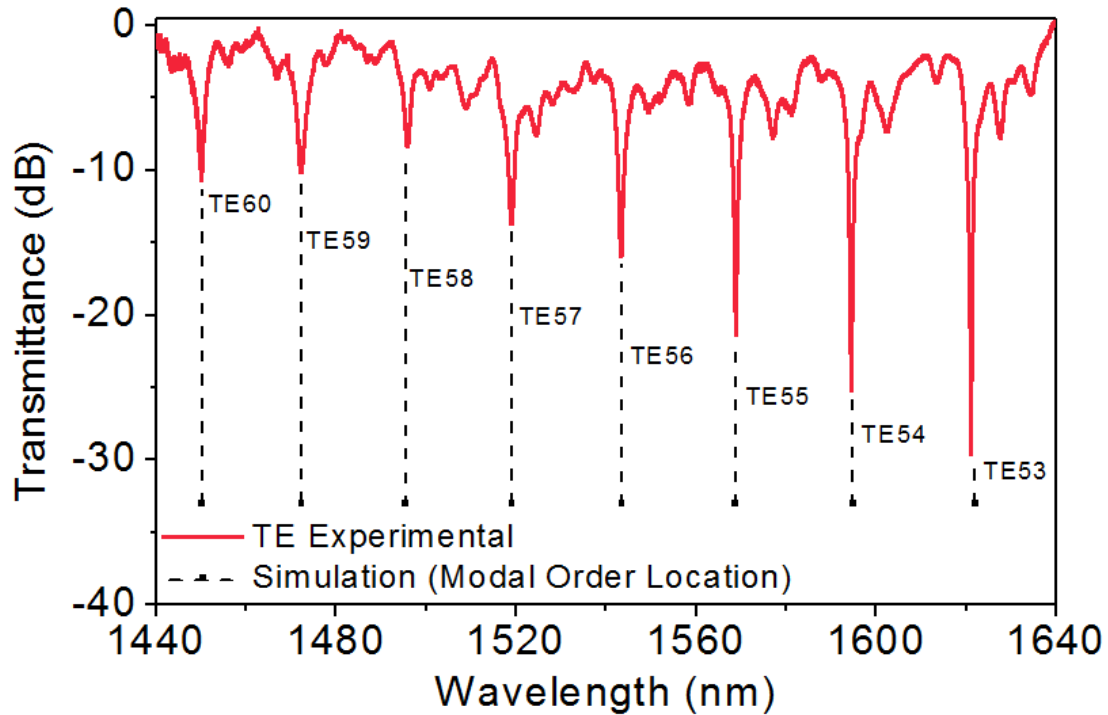


Fig. 6.7. Simulated modal order location of the TE polarization spectrum. Red solid line corresponds to the experimental spectrum, while black dashed line to the simulated modal order location.

Finally, finite-difference time domain (FDTD) simulations were carried out using the Optiwave software [25] and are presented in Figure 6.8. The microresonating device was designed according to the dimensions and the picture of the device presented in SEM images of Figure 6.3, (height of ring $7\ \mu\text{m}$, thickness $800\ \text{nm}$, taper diameter $2.4\ \mu\text{m}$, position of the ring was set the middle of the diameter of the tapered fibers). Moreover, the refractive index of the ring was that of the photopolymerized material, namely $n_{\text{ring}}=1.52$, while the refractive index of the tapered fiber was that of its cladding, namely $n_{\text{cladding}} = 1.4677$, since for $2.4\ \mu\text{m}$ diameter tapered fiber the core has been collapsed [26].

Slight differences are observed between the experimental and the simulating spectra, both at relative intensities of the fringes and at the expected resonance wavelength positions. These differences depend firstly on the discrepancy between the morphology (shape, dimensions, surface characteristics) of the fabricated microring resonator and the designed one to the FDTD software and secondly to the positioning of the fabricated and the simulated microring onto the tapered fiber (see Fig. 6.3 and inset figure of Fig. 6.8).

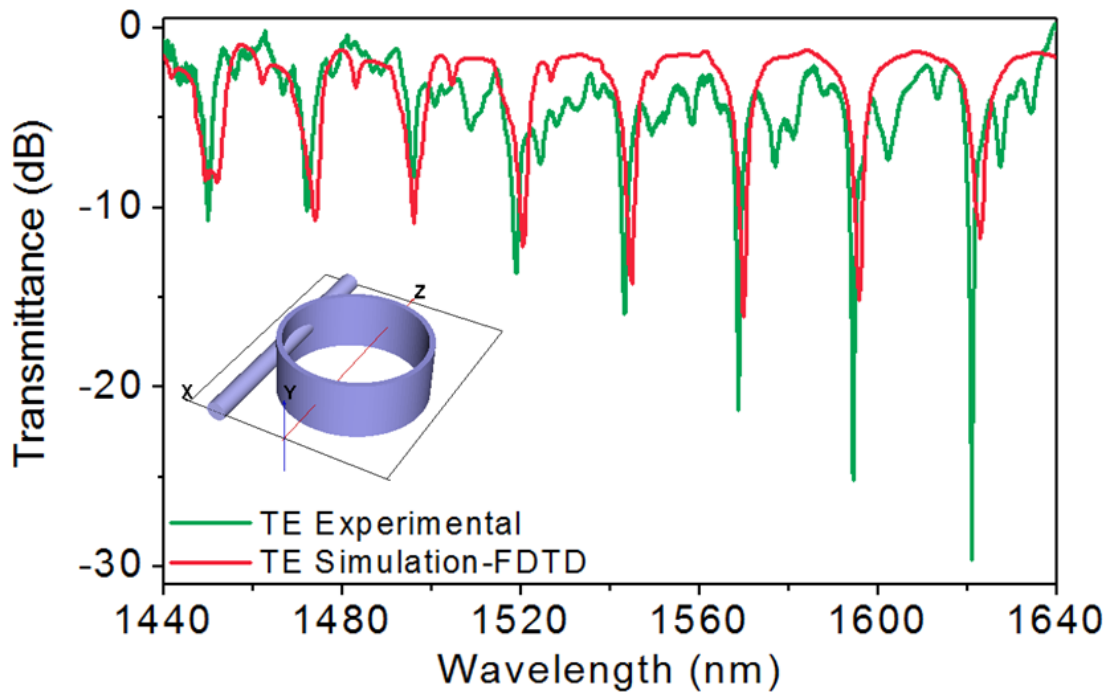


Fig. 6.8. Experimental (green line) and Finite-difference time domain (FDTD) simulations (red line) of the TE polarization spectrum. The inset figure presents the FDTD simulated designed of the microresonator.

6.2.2 Parameterization of the photopolymerization process

Microrings of different diameters, namely 20 μm , 30 μm and 40 μm , were fabricated and characterized in order to test the capability of the photopolymerization method and potential implications related to this imprinting process. The resonance spectra and optical microscope images of three different diameter microrings are presented in Figure 6.9. It has to be noted that for the fabrication of the microrings the scanning speed was set at 2000 $\mu\text{m}/\text{sec}$, while the laser power was adjusted at 55 mW, 60mW and 62mW respectively. These differences in the laser power were necessary in order the microrings to be properly structured. The larger the diameter of the ring, the higher the laser power was needed in order the microrings to be robust and not to be collapsed during the development process.

As expected, an increase in the fabricated ring diameter D is followed by an increase of the number of fringes that appear within a given spectral range, with a simultaneous decrease of the corresponding FSR of the fringes. More specifically, the FSR of the fringes is 25.839 nm, 17.039 nm and 13.904 nm for ring diameter of 20 μm , 30 μm and 40 μm respectively, while the effective diameters where calculated to be 20.854 μm , 30.776 μm and 39.513 μm according to the experimental FSR. Moreover, it is observed that as the ring diameter increases, the resonance spectra became more complicated. This happens due to the fact that as the diameter of the ring resonators increases, a bigger part of the resonator is attached onto the optical fiber, allowing the coupling of more modes within its cavity. The Q factors were calculated to be 1.01×10^3 , 1.58×10^3 and 2.55×10^3 for ring diameter of 20 μm , 30 μm and 40 μm respectively.

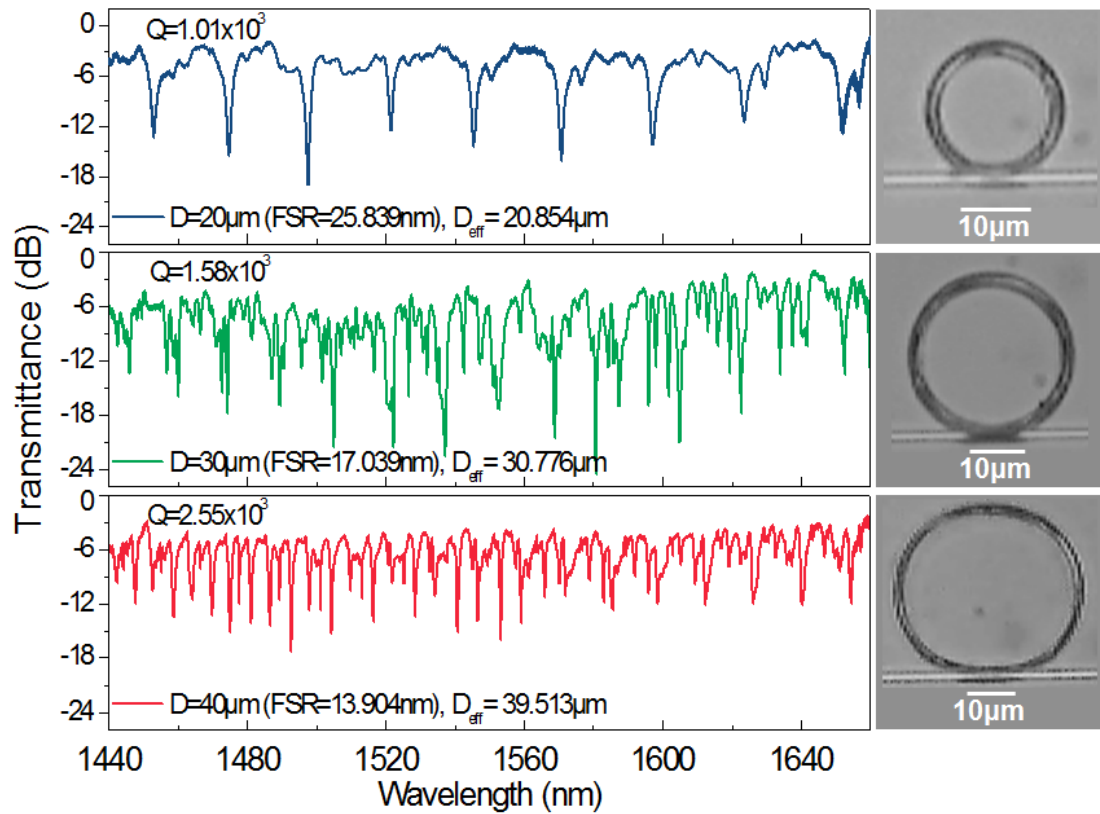


Fig. 6.9. Unpolarized WGM resonance spectra and corresponding optical microscope images of WGM rings fabricated with 20 μm (blue curve), 30 μm (green curve) and 40 μm (red curve) nominal diameter.

6.2.3 Fabrication of microrings with different thickness

The resonance dependence to the thickness of the ring waveguide was also studied. For this purpose, rings with three different thickness were fabricated, by changing the number of scans during the photopolymerization. The scanning speed was set again at 2000 $\mu\text{m}/\text{sec}$ and the laser power was adjusted at 59 mW. The number of scans, in order to have three rings of different thickness, was set at 5 scans, 7 scans and 9 scans. SEM measurements show that the difference in thickness was approximately 100nm, resulting a thickness of $\sim 800\text{nm}$ for the ring of 5 scans, $\sim 900\text{nm}$ for the ring of 7 scans and finally $\sim 1000\text{nm}$ in case of 9 scans ring.

In figure 6.10 are presented in the top left diagram the transmission spectra of the three different microrings, while in top right, bottom left and bottom right diagrams are presented the transmission spectra as well as the TE and TM polarization spectra of 5 scans, 7 scans and 9 scans rings respectively.

As it is observed the highest fringe visibility that equals to 20 dB is obtained from the microring fabricated by 7 scans, while the fringe visibility of 5 scans and 9 scans microrings equals to 12 dB and 10 dB respectively. This could be explained since the 5 scans ring is not so robust and it gets slightly deformed after the wet development process. In contrary, the thickness of the 9 scans ring gets quite thick resulting the coupling of more modes within its cavity that affects the resonant spectrum. In addition, the Q factors for 5 scans rings calculated to be for the fringes of the

transmission spectra 0.38×10^3 , while for the TE polarization spectra it was increased to 0.92×10^3 . In case of 7 scans ring the Q factor for the transmission spectra calculated to be 2.12×10^3 while in TM polarization spectra increased to 3.55×10^3 . For 9 scans the Q factor for the transmission spectra calculated to be 2.93×10^3 , while in TE polarization spectra decreased to 1.19×10^3 .

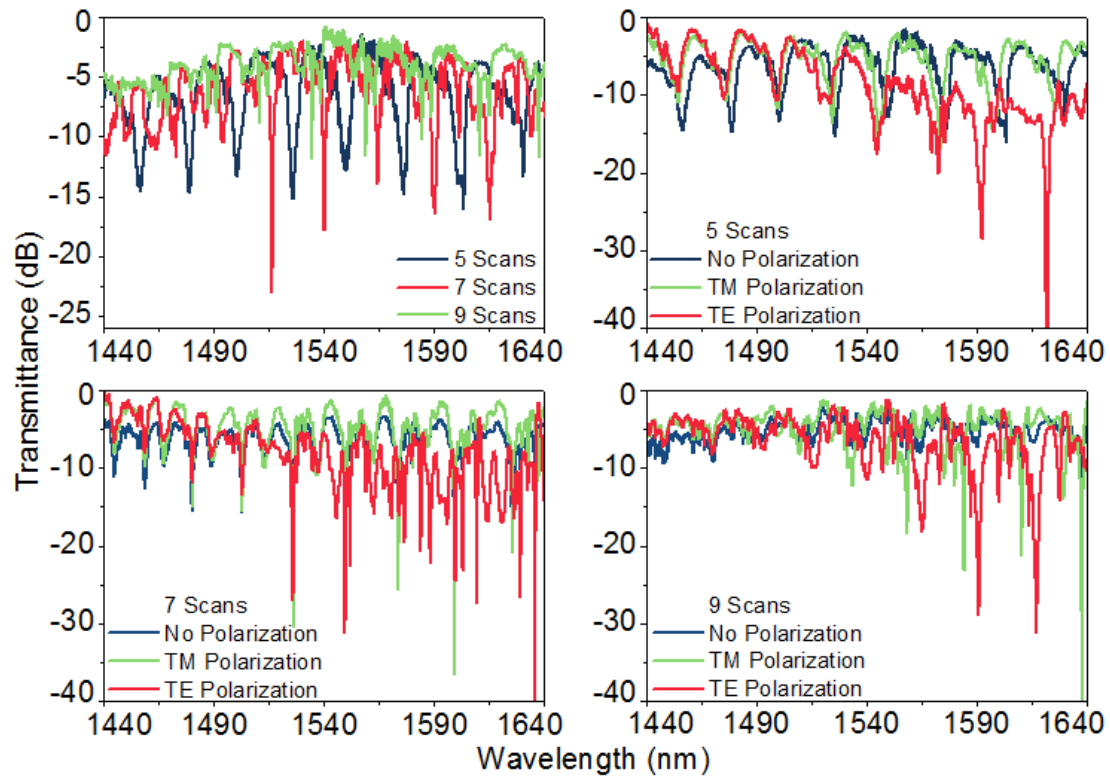


Fig. 6.10. Resonance dependence to the thickness of the rings (top left) is presented in top left diagram, where 5 scans, 7 scans and 9 scans microrings corresponds to blue curve, red curve and green curve respectively. Top right, bottom left and bottom right diagrams present the transmission spectra (blue curve), as well as the TM (green curve) and TE (red curve) polarization spectra of 5 scans, 7 scans and 9 scans rings respectively.

The fact that some rings reveals an increased sensitivity while operating in TE polarization, while some others when operating in TM polarization, could be attributed to the orientation of the fabricated microrings onto the tapered fibers. It has to be noted here that in order to find the correct position where the microring should be fabricated, a CCD camera was used. Even though, it is difficult one to succeed exactly the same position for each sample. Few hundreds of nm discrepancy either at the height or on the horizontal displacement from the center of the tapered fiber could affect the spectral response of the fabricated microresonators. Moreover, even if the fibers were tapered using the same parameters at the thermal processing apparatus, it is possible slight differences at the dimensions of the obtained tapered optical fibers to be observed.

According to the experimental results presented above, we came to the conclusion that the microrings with $20 \mu\text{m}$ diameter exhibited well defined resonant spectra, in comparison with the microrings of $30 \mu\text{m}$ and $40 \mu\text{m}$ diameter that were more complicated. Moreover, the 7 scans fabricated microrings reveals higher fringe

visibilities and Q factors instead of 5 scans and 9 scans microrings. To this end, for the following experiments 20 μm diameter rings of 7 scans will be fabricated.

6.3 Coupled and defected ring resonators structures

During the last years, there is an increased interest for the fabrication of coupled resonating systems due to their properties. In coupled systems there is interaction between the resonators, that increases significantly the sensitivity of the devices. Moreover, the interference between the coupled resonators can be observed in the recording spectra. These properties can be useful for the fabrication of highly sensitive sensors. The sensing mechanism can be relied in the changes of the interference spectrum due to the changes of the distance or position of the resonators between the coupled cavities [27-30]. Furthermore, multi-sensing systems could be fabricated, by functionalizing the surfaces of the microresonators with different materials in order to be able to sense different substances at the same time, which will affect the resonance spectrum in different ways [31, 32].

Parallel coupled double WGM ring microresonators, as well as defected WGM ring microresonators were also fabricated and characterized, in order to test further the functionality of the proposed fabrication technique. Moreover, the spectral response of these coupled microresonators will be compared with the response of the single WGM microresonators, in terms of sensitivity.

6.3.1 Parallel coupled microring resonators

SEM images of the fabricated parallel coupled double WGM ring microresonators are presented in Figure 6.10. The diameter of the rings was 20 μm , while the center to center distance was varied at 27 μm , 25 μm and 22 μm , as presented in Fig. 6.11(a) from the left to the right. During the fabrication process all the coupled microrings were observed to be separated by the specified distance through the CCD camera of the fabrication system. After the wet development of the samples, the double rings that were separated by 25 μm and 22 μm distance (see Fig. 6.11(a)), were attracted to each other by electrostatic forces, while attached to each other and being deformed. On the contrary, the parallel coupled WGM microresonators, separated by 27 μm distance, were not affected by the development process.

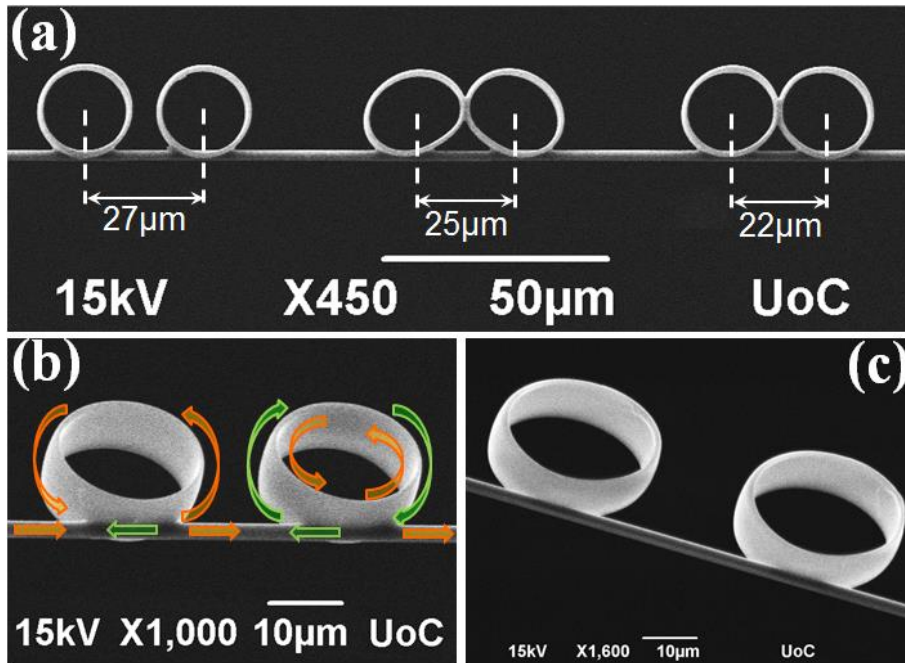


Fig. 6.11. SEM images of 20 μm diameter coupled ring resonators onto 2.2 μm diameter tapered fiber. (a) Top view, (b) tilted view of coupled ring resonators and the light propagation (orange arrows) and interaction (green arrows) between them (d) tilted view.

These distances were chosen, according to the evanescence field of the single ring calculating from FDTD simulations. To simplify the simulation process, the design consisting of a slice of the ring with height of 7 μm and thickness of 900 nm, while the thickness of the slide was 1 μm (see inset design of Figure 6.12). The refractive index of the ring slide was $n_{\text{ring}} = 1.52$.

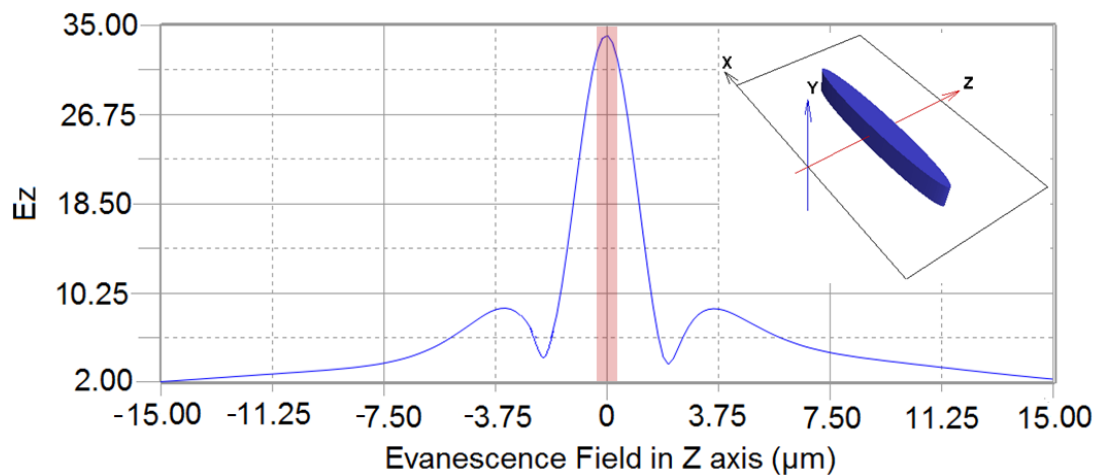


Figure 6.12. Evanescence field of a single ring resonator, simulated by FDTD software. The pink area symmetrically to the zero point of evanescence field axis denote the thickness of the walls of the fabricated ring. The inset Figure presents the simplified design that was used for the simulation.

According to the simulation, the evanescence field of the fundamental mode of the single ring layout for 5 μm symmetrically to its walls (see Figure 6.12, the pink area symmetrically to the zero point of evanescence field axis denote the thickness of the walls of the fabricated ring). If one takes into account the higher order modes that

are supporting from the ring resonator, then the evanescence field could spread out for at least of 7.5 μm . The modal indices supporting by the ring are presented in Table I.

Mode Number	TE Modes	TM Modes
	Modal Index	Modal Index
0	1.18077289	1.29350691
1	1.11942222	1.24564803
2	1.08914671	1.21534573
3	1.04541825	1.16921240
4	-	1.11347266
5	-	1.05650441

Table I. Modal indices of the TE and TM modes that are supported by a single ring resonator, emerged from FDTD simulations.

Figure 6.13 presents the characteristic spectrum of a single ring with blue curve and of a parallel coupled ring resonating device with the red curve. It can be observed that the splitting due to the coupled microresonators is introduced in the recorded spectrum [29, 33].

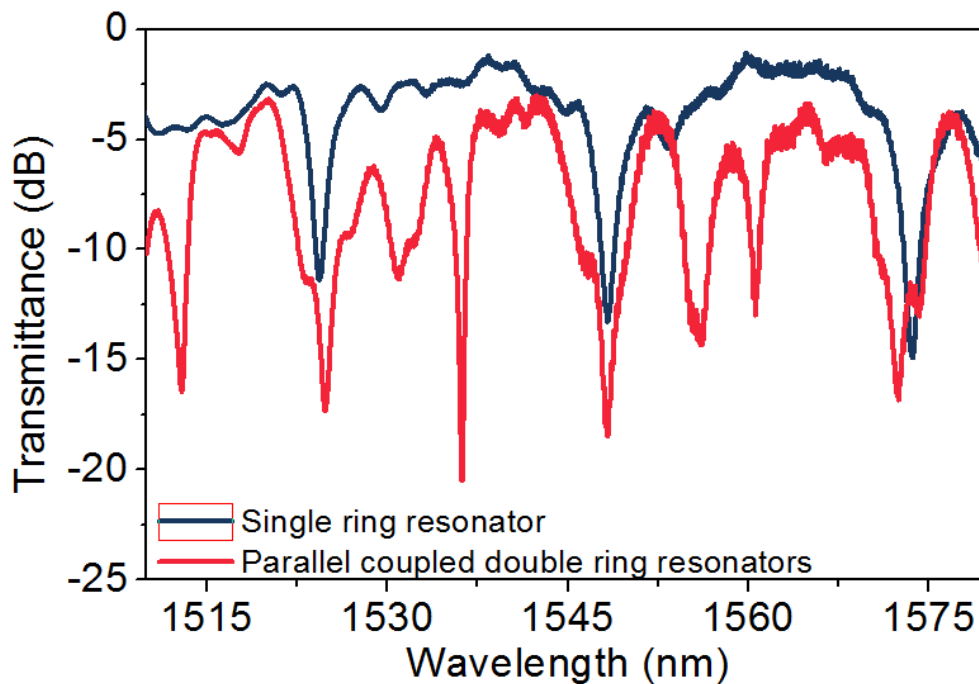


Fig. 6.13. Interference transmission spectrum of a single ring resonator (blue curve) and parallel coupled double ring resonators (red curve).

For the spectral characterization of the coupled ring microresonators, the experimental configurations that were used for the transmission and reflection measurements are presented in section 6.1 (see Fig. 6.2). In case of the couple

microring resonators we were able to record also the spectra in reflection mode, since the part of the light that was coupled in the second ring from its interaction with the first ring was reflected backwards (see green arrows in Fig. 6.11b). Therefore, the second ring reacts as a reflector. This is the reason why no reflection measurements were presented in the section of single ring resonators.

As it was mentioned, the coupled microresonators were characterized by exciting the WGM of the “molecule” from both sides, in order to test the coupling conditions and record the differences in the spectral response. For this reason, each ring of the coupled microresonators was characterized by a capital letter (namely “A” and “B”). These letters will be used to denote the configuration that was used during the measurements (see section 6.1).

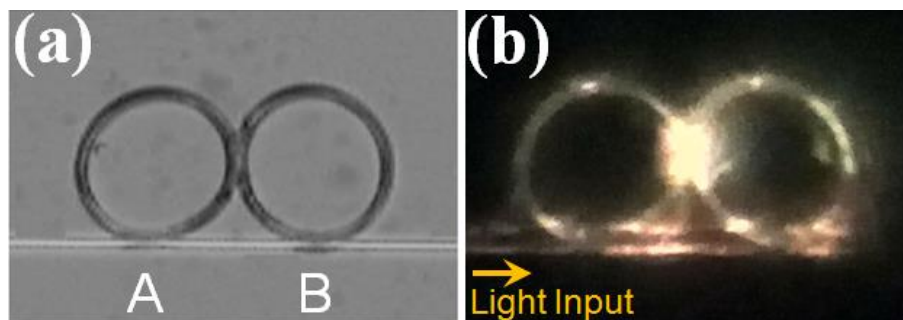


Fig. 6.14. Optical microscope images of the parallel coupled microresonators with a center to center distance of $22\ \mu\text{m}$. (a) Configuration (“A” and “B” rings) that will be used for the spectral characterization. (b) Experimental demonstration of WGM excited by a supercontinuum laser source (SCLS).

The configuration of “A” and “B” rings, for the parallel coupled microresonators with a center to center distance of $22\ \mu\text{m}$ is noted on an optical microscope image, presented in figure 6.14(a). Additionally, figure 6.14(b) presents an optical microscope image of the coupled microresonators, when they are excited by a supercontinuum laser source (SCLS), (spectral range of 400–2000 nm, NKT SuperK Compact). In this image, the interference between the two rings can be observed.

As it is observed from the transmission spectra in figure 6.15 (top left and bottom left spectra, blue curves) the visibility of the fringes is almost the same in both cases (A-B and B-A configurations) and equal to 5dB, while the Q factors calculated to 0.33×10^3 . In contrast, the fringes of the reflection spectrum of “B” ring (Fig. 6. 15, top left, red curve) presents almost the double strength visibility than those of ring “A” (Fig. 6. 15, bottom left, red curve), namely 17dB and 8 dB, respectively. Moreover, in case of reflectance of ring “B” the fringes that appear, due to the excited resonance modes, are well defined and the splitting due to the coupled microresonators is introduced in the recorded spectrum. Using the reflection spectrum of ring “B” (Fig. 6.15, top left, red curve), the free spectral range for the single ring (FSR_{SR}) was calculated to be 25.93 nm, corresponding to an effective diameter (D_{eff}) of $20.44\ \mu\text{m}$, while the free spectral range for the coupled microresonators (FSR_{CR}) was calculated to be 21.02 nm, corresponding to an effective diameter of the coupled cavity of $42.04\ \mu\text{m}$. Both the calculated effective diameters are in good agreement with the design,

since the diameter of each ring was expected to be 20 μm , while the coupled cavity was expected to be 42 μm .

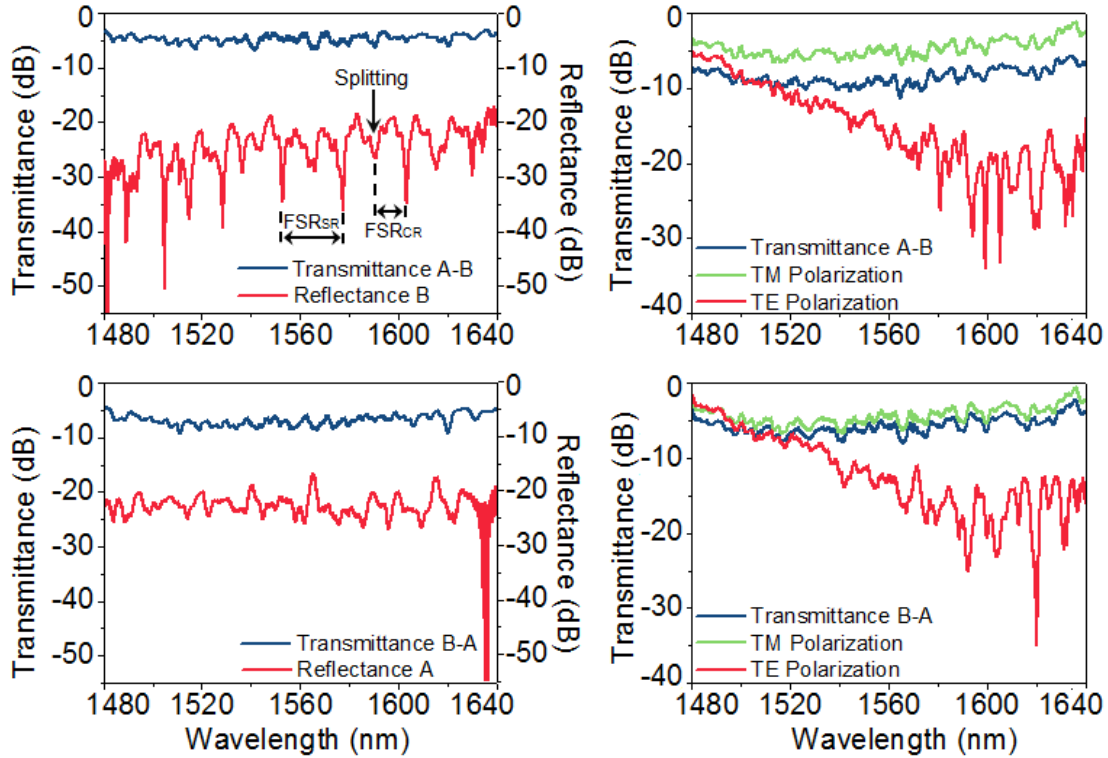


Fig. 6.15. Resonance spectra of the parallel coupled microresonators with a center to center distance of 22 μm . (Top left) Transmittance (blue curve) and reflectance (red curve) spectra of A-B and B respectively. The free spectral ranges for the single ring (FSR_{SR}) and for the coupled microresonators (FSR_{CR}) are noted on the figure. (Top right) Transmittance (blue curve), TM polarization (green curve) and TE polarization (red curve) spectra of A-B. (Bottom left) Transmittance (blue curve) and reflectance (red curve) spectra of B-A and A respectively. (Bottom right) Transmittance (blue curve), TM polarization (green curve) and TE polarization (red curve) spectra of B-A.

The Q factor in case of the reflection spectrum “B” (Fig. 6. 15, top left, red curve), was calculated to 1.14×10^3 . Considering now the polarization spectra (Fig. 6. 15, top right and bottom right), the fabricated device shows increased sensitivity, while operating in TE polarization (red curves) for both configurations (A-B and B-A), while in case of TM polarization (green curves), the recorded spectra do not reveal significant changes from those operating in transmission mode (blue curves). More specifically, in case of transmission and TM polarization spectra, the fringe visibility was 5 dB with Q factors of the order of 0.33×10^3 , while in case of TE polarization for A-B configuration the fringe visibility was 15 dB with Q factor equals to 1.61×10^3 . Correspondingly for B-A configuration, the highest fringe visibility recorded to be approximately 23dB with Q factor of the order of 0.71×10^3 .

The next parallel coupled microresonators which were examined, was that with a center to center distance of 25 μm . In figure 6.16 are presented the optical microscope images with the configuration of the rings (6.16(a)) and the experimental demonstration of the excited WGM coupled microresonators (6.16(b)). In this case, the interference between the two rings seems to be lower. This might occurs due to the bigger distance that separates the rings, as well as to the greater extent of deformation,

that allows fewer modes to be excited and circulated inside the coupled microresonators.

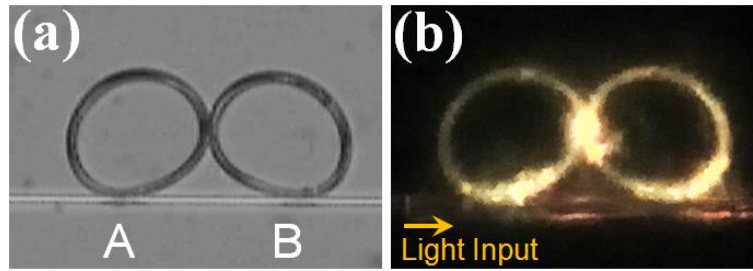


Fig. 6.16. Optical microscope images of the parallel coupled microresonators with a center to center distance of $25\ \mu\text{m}$. (a) Configuration of “A” and “B” rings. (b) Experimental demonstration of WGM excited by a supercontinuum laser source (SCLS).

According to the spectral characterization, the transmission spectra presented in figure 6.17 (top left and bottom left spectra, blue curves), reveal a fringe visibility of 7dB in both cases (A-B and B-A configurations).

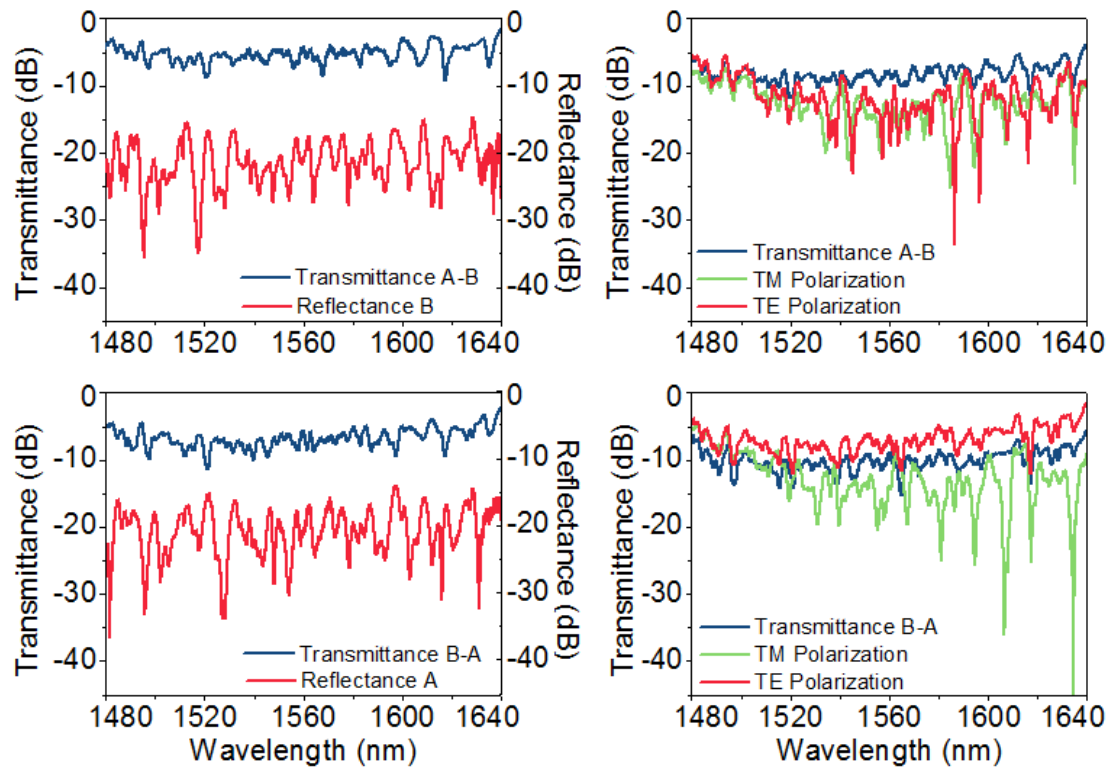


Fig. 6.17. Resonance spectra of the parallel coupled microresonators with a center to center distance of $25\ \mu\text{m}$. (Top left) Transmittance (blue curve) and reflectance (red curve) spectra of A-B and B respectively. (Top right) Transmittance (blue curve), TM polarization (green curve) and TE polarization (red curve) spectra of A-B. (Bottom left) Transmittance (blue curve) and reflectance (red curve) spectra of B-A and A respectively. (Bottom right) Transmittance (blue curve), TM polarization (green curve) and TE polarization (red curve) spectra of B-A.

The Q factor in case of A-B configuration is slightly higher than this of B-A, namely 0.83×10^3 and 0.67×10^3 respectively. The same behavior seems to have also the reflection spectra (Fig 6.17, top left and bottom left spectra, red curves), with a fringe visibility of 18 dB. In this case, the difference between the Q factors is higher.

For the reflection spectrum of “B” ring (Fig. 6.17, top left, red curve) the Q factor calculated to be 1.13×10^3 , while this of ring “A” (Fig. 6.17, bottom left, red curve), equals to 2.02×10^3 . Herein, the spectra are more complicated – noisy, probably due to the fact that the deformation of both rings is more significant. However, the splitting of the fringes due to the coupled microresonators exists. The free spectral range for the single ring (FSR_{SR}) calculated to be 22.68 nm, corresponding to an effective diameter (D_{eff}) of 23.8 μm , while the free spectral range for the coupled microresonators (FSR_{CR}) was calculated to be 12.14 nm, corresponding to an effective diameter of the coupled cavity of 44.2 μm . According to the microscope images, the calculated effective diameters are in good agreement with the fabricated design in this case, since the diameter of each ring was expected to be 20 μm , but due to the deformation both rings seems to have larger dimensions of those that expected to have. Additionally, the coupled cavity was expected to be 45 μm , but from the microscope images, it appears that the deformation of the rings towards the connection point between them reduced the cavity length.

Moreover, the existing coupled microresonators revealed different sensitivities during the polarization measurements (Fig. 6. 17, top right and bottom right). The A-B configuration exhibited higher sensitivity in TE polarization (Fig. 6.17 top right, red curve) with fringe visibility of 25 dB and a Q factor of 2.26×10^3 , whereas the fringe visibility was 16 dB with a Q factor of the order of 0.96×10^3 for the TM polarization (Fig. 6.17 top right, green curve). On the contrary, B-A configuration shows increased sensitivity, while operating in TM polarization (Fig. 6.17 bottom right, green curve), with fringe visibility of 25 dB and Q factor of 1.16×10^3 . At this configurations (B-A) the recorded TE polarization (Fig. 6.17 bottom right, red curve) had a Q factor of 0.83×10^3 , while the highest fringe visibility was 11 dB.

The coupled microresonator with 27 μm distance is presented in figure 6.18. These coupled microresonators have not been deformed and as it is observed through the microscope image, the excited modes that circulate through the rings seem to interact. The interference light can be observed within the gap that separates the rings.

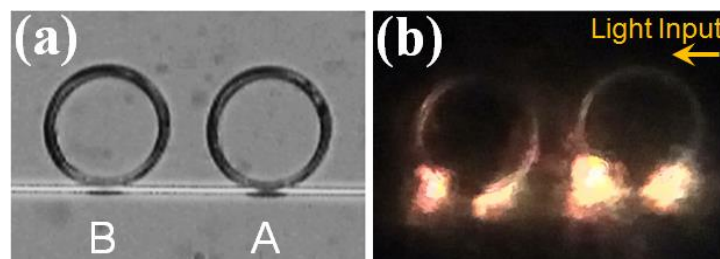


Fig. 6.18. Optical microscope images of the parallel coupled microresonators with a center to center distance of 27 μm . (a) Configuration (“A” and “B” rings) that will be used for the spectral characterization. (b) Experimental demonstration of WGM excited by a supercontinuum laser source (SCLS).

The selected transmission and reflection spectra for both configurations of these coupled microresonators are presented in figure 6.19 (top left and bottom left). Herein, the recorded transmission spectra through B-A configuration (Fig. 6.19 bottom left, blue curve) results stronger fringes, namely 18 dB with Q factor of $1.56 \times$

10^3 , in comparison with A-B configuration (Fig. 6.19 top left, blue curve) that presents almost the half fringe visibility, namely 9.5 dB with calculated Q factor of the order of 1.30×10^3 . The free spectral range for the single ring (FSR_{SR}) calculated to be 25.4 nm, corresponding to an effective diameter (D_{eff}) of 20.66 μm , while the free spectral range for the coupled microresonators (FSR_{CR}) was calculated to be 23.91 nm, corresponding to an effective diameter of the coupled cavity of 47.83 μm . These calculated values are not differ much from the expected dimensions, since each single ring were expected to have a diameter of 20 μm , while the diameter of the coupled cavity was expected to be 47 μm .

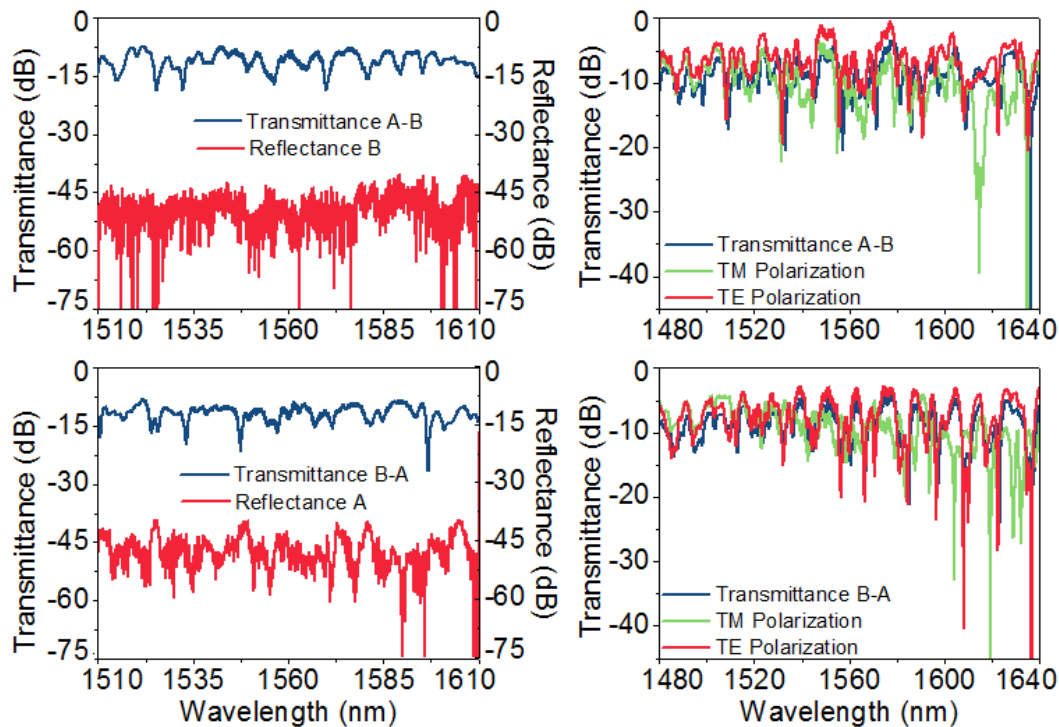


Fig. 6.19. Resonance spectra of the parallel coupled microresonators with a center to center distance of 7 μm . (Top left) Transmittance (blue curve) and reflectance (red curve) spectra of A-B and B respectively. (Top right) Transmittance (blue curve), TM polarization (green curve) and TE polarization (red curve) spectra of A-B. (Bottom left) Transmittance (blue curve) and reflectance (red curve) spectra of B-A and A respectively. (Bottom right) Transmittance (blue curve), TM polarization (green curve) and TE polarization (red curve) spectra of B-A.

According to the polarization spectra (Fig. 6.19, top right and bottom right), the A-B configuration reveals higher sensitivities at TM polarization (Fig. 6.19, top right, green curve) resulting maximum fringe visibility of 25 dB with a calculated Q factor of 1.56×10^3 , in comparison with the TE polarization (Fig. 6.19, top right, red curve) that shows a fringe visibility of 17 dB with Q factor of the order of 1.33×10^3 . On the contrary, for B-A configuration, TE polarization appears to result stronger fringes, with visibilities up to 38.5 dB and Q factor of 3.82×10^3 . The TM polarization in this case results fringe visibility of 24.5 dB, while the Q factor calculated at 2.95×10^3 .

In this coupled ring system, the reflection spectra in both cases are quite noisy (Fig. 6.19, top left and bottom left, red curves). This is due to the fact that this time the rings are separated with a bigger distance and they do not touch each other.

Eventhough there is an interaction between them and can be observed in the transmission spectra, the reflected field is not strong enough in order to give strong fringes.

Up to now, the coupled microresonators that performed the best recorded results, with the higher Q factors and fringe visibilities, were these of a center to center distance of 27 μm . We would like to mention here that these were the also the microresonators that have not been deformed.

6.3.2 Defected microring resonator

The next step, was to fabricate a sinlge ring with a small defect fabricated onto the tapered fiber and in a small distance from the ring. Figure 6.20 presents the fabricated defected microresonator. The ring was designed again with 20 μm diameter, while the defect was fabricated at a distance of 8 μm from the conection point of the ring to the fiber. As it is observed from figure 6.20(b), many modes are excited or trapped to the defect.

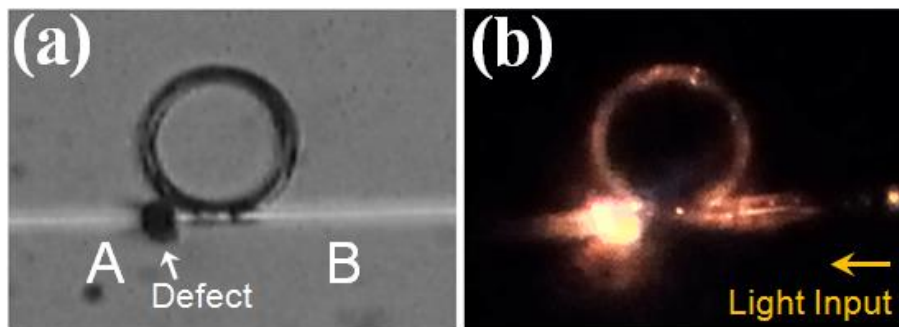


Fig. 6.20. Optical microscope images of defected microresonator with distance between the connection point of the ring onto the tapered fiber and the defect of 8 μm .. (a) Configuration (“A” defect and “B” ring) that will be used for the spectral characterization. (b) Experimental demonstration of WGM excited by a supercontinuum laser source (SCLS).

The operation of this defected sample was also examined by the use of the set-up in figure 6.2. For the A-B configuration, the fringe visibility of the transmission spectrum was 17 dB, with a Q factor of 2.13×10^3 (Fig. 6.21, top left, blue curve), while for the B-A configuration, the fringe visibility was 12 dB with a Q factor of the order of 1.81×10^3 (Fig. 6.21, bottom left, blue curve). Moreover, in both cases, the splitting effect of fringes, due to the coupled defected microresonator, is observed.

According to the calculations, the free spectral range for the single ring calculated to be 25.09 nm, corresponding to an effective diameter (D_{eff}) of 20.57 μm , while the free spectral range for the coupled defected microresonator was calculated to be 28.19 nm, corresponding to an effective diameter of the coupled defected cavity of 18.35 μm . These calculated values are in good agreement with the design, since as was already mentioned the diameter of the microring was designed at 20 μm , while the defect cavity was designed at 18 μm . The reflection spectra that were recorded in both configurations (A-B and B-A), were quite noisy in this case (Fig. 6.21, top left and bottom left, red curves). As regards the recorded polarization spectra, the A-B

configuration is more sensitive to TE polarization with fringe visibility up to 32.5 dB and Q factor of 4.70×10^3 (Fig. 6.21, top right, red curve) in contrary to TM polarization which has 26 dB fringe visibility and Q factor of 0.9×10^3 (Fig. 6.21, top right, green curve). For the B-A configuration, the TM polarization reveals higher values of fringe visibility and Q factor, namely 31 dB and 2.99×10^3 respectively, while these values were calculated to 21.5 dB and 2.23×10^3 in case of TE polarization fringes.

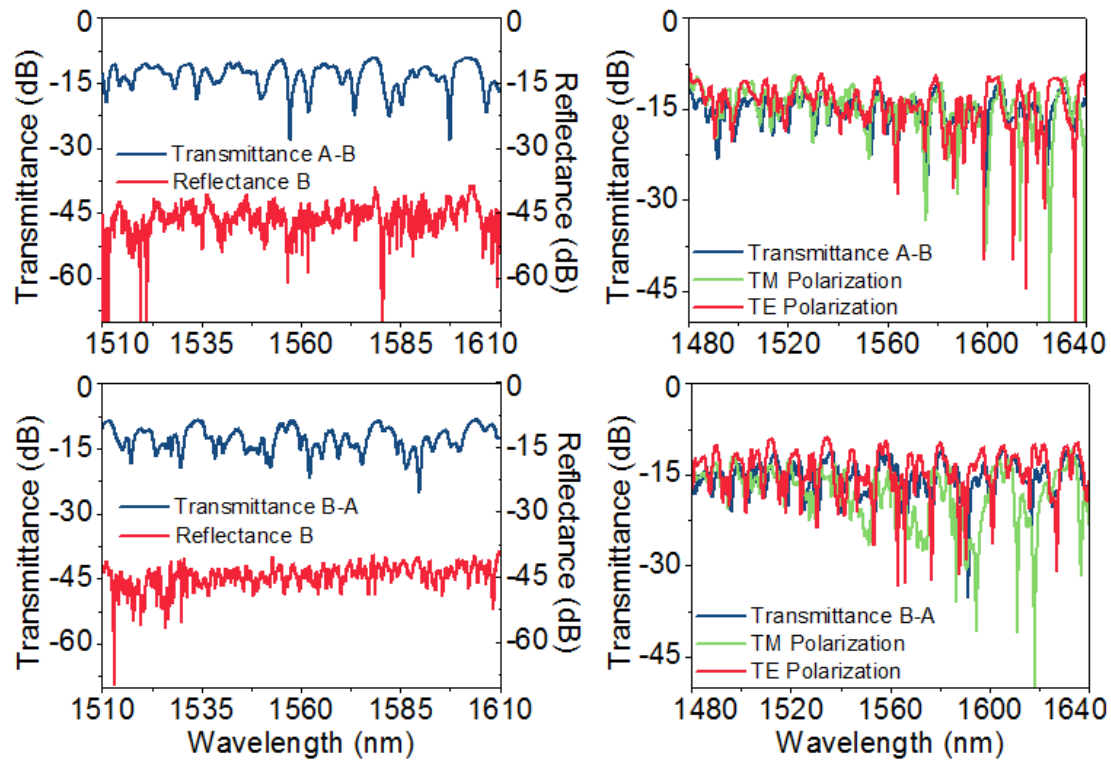


Fig. 6.21. Resonance spectra of the defected microresonator, with distance between the connection point of the ring onto the tapered fiber and the defect of $8 \mu\text{m}$. (Top left) Transmittance (blue curve) and reflectance (red curve) spectra of A-B and B respectively. (Top right) Transmittance (blue curve), TM polarization (green curve) and TE polarization (red curve) spectra of A-B. (Bottom left) Transmittance (blue curve) and reflectance (red curve) spectra of B-A and A respectively. (Bottom right) Transmittance (blue curve), TM polarization (green curve) and TE polarization (red curve) spectra of B-A.

To conclude, it was observed that the defected coupled microresonator exhibits good spectral resonance, with the splitting effect of the fringes introduced in the recorded spectra. Moreover, the sensitivity of this defected coupled microresonator could be comparable with the sensitivity of the parallel coupled microresonators with a center to center distance of $27 \mu\text{m}$.

6.4 Summary and Conclusions

To summarize, single ring, parallel coupled and defected microresonators were presented in this chapter. Initially the spectral characterization of a single ring microresonator was presented. Additionally, simulations for the modal order location of the resonance pattern were carried out using Airy approximation and FDTD

simulations show that the experimental results are in good agreement with the simulated resonance spectra. Then the resonance dependence to the diameter and the thickness of the microrings was tested. The experimental results show that the 20 μm diameter microrings exhibited well defined resonant spectra, while the spectra of the 30 μm and 40 μm diameter microrings were more complicated. Moreover, the 7 scans fabricated microring, corresponding to ~ 900 nm thickness of the fabricated ring, revealed fringe visibility of 20 dB and Q factor of 3.55×10^3 for the polarization spectra. These values were higher in comparison with the 5 scans (~ 800 nm) and 9 scans (~ 1000 nm) microrings, which fringe visibilities were equal to 12 dB and 10 dB respectively, with Q factors of the order of 0.92×10^3 and 1.19×10^3 respectively for the polarization spectra.

Afterwards, were presented the results of three parallel coupled microresonators with different center to center distance. In all cases, the resonance spectra show the expected splitting effect. The fringe visibility and Q factor of the coupled microresonator with a 27 μm center to center distance were 38.5 dB and 3.82×10^3 respectively for the polarization spectra. This coupled microresonator revealed the higher sensitivities in comparison with the other two coupled microresonators which microrings were separated with smaller distances.

Finally, it was observed that defected coupled microresonator exhibits good spectral resonance, with the splitting effect of the fringes introduced in the recorded spectra. Moreover, the fringe visibility and Q factor in this case were 32.5 dB and 4.70×10^3 respectively.

To conclude, the successful fabrication of single and coupled ring WGM microresonating devices directly onto tapered fibers by DLW was presented. The fabrication of different diameter and thickness of the single ring WGM cavities as well as the different configurations for the coupled and defected WGM microresonating cavities vouches the early indications of the functionality and robustness for the fabricated devices.

References

- [1] Y. Ding, H. Fan, X. Zhang, X. Jiang, and M. Xiao, "Ultralow-threshold neodymium-doped microsphere lasers on a silicon chip," *Optics Communications*, vol. 395, pp. 51-54, Jul 15 2017.
- [2] J. Lin, Y. Xu, Z. Fang, M. Wang, J. Song, N. Wang, *et al.*, "Fabrication of high-Q lithium niobate microresonators using femtosecond laser micromachining," *Scientific Reports*, vol. 5, Jan 28 2015.
- [3] H. Xu and H. Sun, "Femtosecond laser 3D fabrication of whispering-gallery-mode microcavities," *Science China Physics, Mechanics & Astronomy*, vol. 58, p. 114202, 2015.
- [4] B. Ozel, R. Nett, T. Weigel, G. Schweiger, and A. Ostendorf, "Temperature sensing by using whispering gallery modes with hollow core fibers," *Measurement Science and Technology*, vol. 21, p. 5, Sep 2010.

- [5] G. A. Rodriguez, S. Hu, and S. M. Weiss, "Porous silicon ring resonator for compact, high sensitivity biosensing applications," *Optics Express*, vol. 23, pp. 7111-7119, Mar 23 2015.
- [6] M. W. Puckett, R. Sharma, F. Vallini, S. Shahin, F. Monifi, P. N. Barrina, *et al.*, "Silicon nanoridge array waveguides for nonlinear and sensing applications," *Optics Express*, vol. 23, pp. 28224-28233, Nov 2 2015.
- [7] J. M. Ward, Y. Yang, and S. N. Chormaic, "Glass-on-Glass Fabrication of Bottle-Shaped Tunable Microlasers and their Applications," *Scientific Reports*, vol. 6, p. 8, Apr 2016.
- [8] A. W. Schell, J. Kaschke, J. Fischer, R. Henze, J. Wolters, M. Wegener, *et al.*, "Three-dimensional quantum photonic elements based on single nitrogen vacancy-centres in laser-written microstructures," *Scientific Reports*, vol. 3, Apr 2 2013.
- [9] G. M. Parsanasab, M. Moshkani, and A. Gharavi, "Femtosecond laser direct writing of single mode polymer micro ring laser with high stability and low pumping threshold," *Optics Express*, vol. 23, pp. 8310-8316, Apr 2015.
- [10] T. Grossmann, S. Schleede, M. Hauser, T. Beck, M. Thiel, G. von Freymann, *et al.*, "Direct laser writing for active and passive high-Q polymer microdisks on silicon," *Optics Express*, vol. 19, pp. 11451-11456, Jun 2011.
- [11] J. T. Lin, S. J. Yu, Y. G. Ma, W. Fang, F. He, L. L. Qiao, *et al.*, "On-chip three-dimensional high-Q microcavities fabricated by femtosecond laser direct writing," *Optics Express*, vol. 20, p. 6, Apr 2012.
- [12] K. Kosma, G. Zito, K. Schuster, and S. Pissadakis, "Whispering gallery mode microsphere resonator integrated inside a microstructured optical fiber," *Optics Letters*, vol. 38, pp. 1301-1303, 2013/04/15 2013.
- [13] K. Milenko, I. Konidakis, and S. Pissadakis, "Silver iodide phosphate glass microsphere resonator integrated on an optical fiber taper," *Optics Letters*, vol. 41, pp. 2185-2188, 2016/05/15 2016.
- [14] G. S. Murugan, J. S. Wilkinson, and M. N. Zervas, "Optical excitation and probing of whispering gallery modes in bottle microresonators: potential for all-fiber add-drop filters," *Optics Letters*, vol. 35, pp. 1893-1895, 2010/06/01 2010.
- [15] F. Monifi, Ş. K. Özdemir, and L. Yang, "Tunable add-drop filter using an active whispering gallery mode microcavity," *Applied Physics Letters*, vol. 103, p. 181103, 2013.
- [16] H. Wei and S. Krishnaswamy, "Direct Laser Writing Polymer Micro-Resonators for Refractive Index Sensors," *Ieee Photonics Technology Letters*, vol. 28, pp. 2819-2822, Dec 15 2016.
- [17] J. Song, J. Lin, J. Tang, Y. Liao, F. He, Z. Wang, *et al.*, "Fabrication of an integrated high-quality-factor (high-Q) optofluidic sensor by femtosecond laser micromachining," *Optics Express*, vol. 22, pp. 14792-14802, 2014/06/16 2014.
- [18] Y. Dong, K. Wang, and X. Jin, "Package of a dual-tapered-fiber coupled microsphere resonator with high Q factor," *Optics Communications*, vol. 350, pp. 230-234, 9/1/ 2015.

- [19] FiberCore,
["https://www.newport.com/medias/sys_master/images/images/h88/hab/8797309042718/Zing-Polarizing-Fiber.pdf."](https://www.newport.com/medias/sys_master/images/images/h88/hab/8797309042718/Zing-Polarizing-Fiber.pdf)
- [20] K. Okamoto, "Wave Theory of Optical Waveguides," in *Fundamentals of Optical Waveguides (Second Edition)*, ed Burlington: Academic Press, 2006.
- [21] K. Thyagarajan, A. K. Ghatak, and A. Sharma, "Vector modes of an optical fiber in the weakly guiding approximation," *Journal of Lightwave Technology*, vol. 7, pp. 51-54, 1989.
- [22] X. Jin, "Optical Fiber Index Taper–Theoretical Analysis and Experiment Demonstration," *International Journal of Infrared and Millimeter Waves*, vol. 19, pp. 875-886, 1998/06/01 1998.
- [23] A. Francois and M. Himmelhaus, "Optical Sensors Based on Whispering Gallery Modes in Fluorescent Microbeads: Size Dependence and Influence of Substrate," *Sensors*, vol. 9, pp. 6836-6852, Sep 2009.
- [24] N. M. Hanumegowda, C. J. Stica, B. C. Patel, I. White, and X. D. Fan, "Refractometric sensors based on microsphere resonators," *Applied Physics Letters*, vol. 87, Nov 2005.
- [25] "Information about OptiFDTD software: URL: <https://optiwave.com/category/products/component-design/optifdtd/>."
- [26] J. D. Love, W. M. Henry, W. J. Stewart, R. J. Black, S. Lacroix, and F. Gonthier, "Tapered single-mode fibres and devices. I. Adiabaticity criteria," *IEE Proceedings J - Optoelectronics*, vol. 138, pp. 343-354, 1991.
- [27] Y. Xiong, P. Pignalosa, T. He, and Y. S. Yi, "Coupled Photonic Systems Between Core-Shell Nanoparticle and Integrated Microresonator," *IEEE Journal of Quantum Electronics*, vol. 50, pp. 677-682, 2014.
- [28] W. Li-Ting, G. Rui-Peng, C. Tie-Jun, and C. Jing, "A photonic analog of Möbius strips using coupled optical ring resonators," *Journal of Optics*, vol. 19, p. 025101, 2017.
- [29] Y. C. Li, F. Abolmaali, K. W. Allen, N. I. Limberopoulos, A. Urbas, Y. Rakovich, *et al.*, "Whispering gallery mode hybridization in photonic molecules," *Laser & Photonics Reviews*, vol. 11, Mar 2017.
- [30] K. Kosma, K. Schuster, J. Kobelke, and S. Pissadakis, "An "in-fiber" Whispering-Gallery-Mode bi-sphere resonator, sensitive to nanometric displacements," *Applied Physics B*, vol. 124, p. 1, November 29 2017.
- [31] S. Carrasco, E. Benito-Pena, D. R. Walt, and M. C. Moreno-Bondi, "Fiber-optic array using molecularly imprinted microspheres for antibiotic analysis," *Chemical Science*, vol. 6, pp. 3139-3147, 2015.
- [32] M. Bahadoran, A. Noorden, K. Chaudhary, F. Mohajer, M. Aziz, S. Hashim, *et al.*, "Modeling and Analysis of a Microresonating Biosensor for Detection of Salmonella Bacteria in Human Blood," *Sensors*, vol. 14, p. 12885, 2014.
- [33] S. Darmawan and M. K. Chin, "Critical coupling, oscillation, reflection, and transmission in optical waveguide-ring resonator systems," *Journal of the Optical Society of America B*, vol. 23, pp. 834-841, 2006/05/01 2006.

Chapter 7

Ring resonators on tapered fibers; devices and processing

Fiber optic sensors utilising whispering gallery modes (WGMs) resonance have attracted increasing academic interest due to their wide range of potential applications. Several examples have been investigated including lasing [1-3], nonlinear optics [4], optomechanics [5], optofluidics [6], filters [7, 8], refractometric sensors [9], force sensors [10], pressure sensors [11], biosensors [12, 13], gas sensors [14], temperature sensors [15, 16], biosensors [12, 17] etc.

Recently, gas and chemical vapor sensors based on microring resonators have been proposed and investigated [18-22]. Although the ring resonators are only a few tens to few hundreds of micrometers in size, the effective detection length can significantly be enhanced due to the high Q-factors of the WGMs. In the presence of vapor molecules, depending upon the fabrication material the microring resonating structure undergoes optical loss, refractive index (RI) and/or thickness changes, manifested in an alteration of the spectral properties of the WGM spectrum. Hence, ring resonator technology enables portable devices with multiplexed detection capabilities.

In this chapter three organic vapor and gas sensing optical fiber taper devices with photopolymerized microring resonators onto them will be presented and analyzed. Initially, the experimental apparatus used for spectro-gaseous characterization of these devices will be described. Then, a single ring microsensor will be used for the detection of ethanol vapors at room temperature, depicting the basic sensing capabilities of the system. Following a pair of coupled microresonators will be used for ethanol vapour sensing; the same photonic molecule will be used as a pressure sensor for Krypton and Nitrogen gasses. Primary results depicting the potential capabilities of the devices which could constitute basic platforms for other sensing and switching devices.

7.1 Experimental apparatus for the characterization of the ring resonating optical fiber structures

Since the performance of the ethanol sensor was going to be tested with concentrations down to ppm quantities and the photopolymerized structures were extremely sensitive to humidity adsorption and contamination from air particles, a chamber was required for these experiments. Moreover, for the gas measurements a clean atmosphere of controlled pressure conditions was required. Thus, a specially designed Teflon chamber of 1400 ml volume was used (Figure 7.1).

The optical fiber taper device was sitting at the bottom of the chamber. Fit-through connectors were adapted to the chamber allowed the ends of the optical fiber device to be coupled to a Superluminescence light source (SLD) (Q Photonics) and

out-coupled to an optical spectrum analyzer (OSA) ANDO AQ6317B. The device has been optimized for operation in the spectral region lying between 1440 nm and 1660 nm, while being interrogated in transmission mode. A Zing™ Polarizing Optical Fiber obtained from Fibercore was used, allowing the recording of TE and TM polarized spectra [23]. Suitable inlets and outlets were fitted on the chamber for the injection/pumping of gaseous or liquid species. A precision manometer was also fitted into the chamber allowing the measurement of changes in pressure due to the evaporation of the organic solvent, or measuring the pressure of the Kr or N gases used. Finally, a plexiglas window fitted on the top of the chamber allowed the inspection of the sample during the experiments.

For avoiding the devices to be adsorbed by humidity, the chamber was under Nitrogen over-pressure (50mbar), when no experiment was carried out. For maintaining in the measurements, before the injection of the solvent or the gas, the chamber was cleaned using nitrogen flow, eliminating residual humidity.

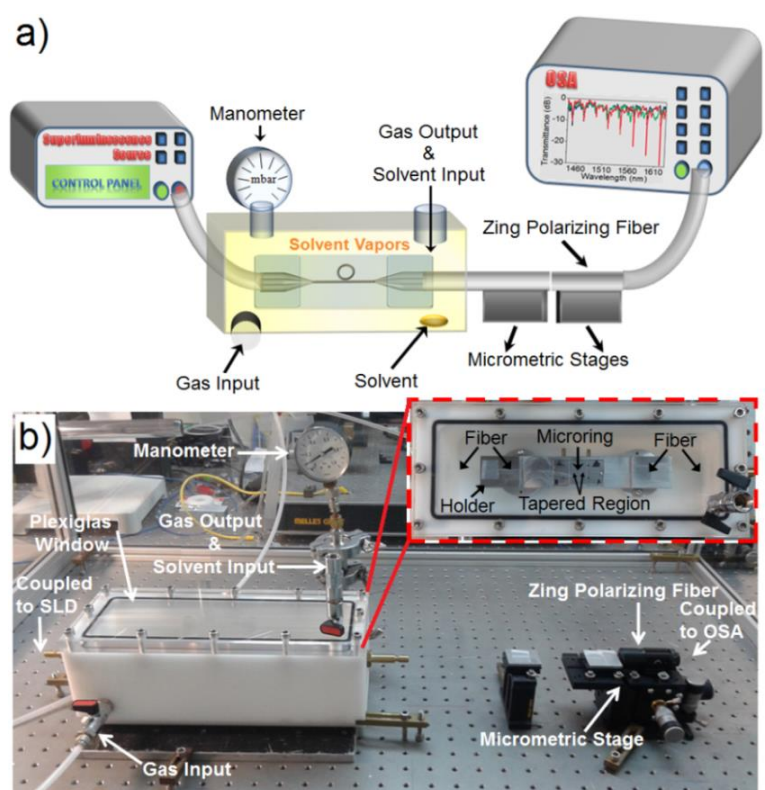


Fig. 7.1. Experimental apparatus that was used for testing the optical fiber taper WGM devices as organic vapor and inert gas sensors. (a) Schematic representation of the experimental setup, (b) photograph of the chamber and the micrometric stages that were used for the signal out-coupling with the Zing polarizing fiber. The inset image in the red dashed line shows the top view of the chamber and the WGM device inside the chamber.

When the devices were tested as sensors for ethanol vapors the liquid solvent (purchased from Sigma Aldrich, purity 99.9%), was inserted directly into the chamber at various volumes from 0.0007 ml to 0.056 ml, corresponding to 0.5 ppm to 40 ppm for the specific chamber volume; then, left evaporating for vapour generation. Following the injection of the desirable solvent volume into the chamber, whispering

gallery mode (WGM) polarized resonance spectra were recorded in real time, until saturation level of the recorded spectra was reached. All the measurements were performed at ambient conditions ($T = 23^{\circ}\text{C}$). The experiments were repeated under the same ethanol pressure conditions for obtaining TE and TM polarization spectra (TE and TM) to be recorded.

In case that the WGM device was tested as gas pressure sensor, diatomic Nitrogen (N_2) and Krypton (Kr) were used as buffer gases. Both gases were chosen to be tested due to their use in several research and industrial applications [24, 25]. Moreover both gases are chemically inert at room temperature, property which facilitated the experimental process. As it was already mentioned, before the injection of the gas at different pressures, the chamber was cleaned using gas flow in order to eliminate residual humidity and achieve accuracy in the measurements. In this case, before N_2 or Kr injection in the chamber for testing the sensing device, the chamber was cleaned with gas flow of the corresponding gas that was going to be tested. Afterwards, the gas was injected in the chamber until the desirable pressure was achieved, by using the control valve that had been adjusted at the input gas channel of the chamber. Following the injection of the desirable gas into the chamber, WGM polarized resonance spectra were recorded. All the measurements were performed at ambient conditions ($T = 23^{\circ}\text{C}$) and for gas pressures up to 600 mbars. The experiments were repeated under the same pressure conditions; in order both polarization spectra (TE and TM) to be recorded.

7.2 First device: Single ring WGM microsensor for ethanol vapors detection

Initially, a single ring microresonator fabricated directly onto a $2.2\ \mu\text{m}$ diameter tapered optical fiber was tested as sensing device for the detection of ethanol vapors. For the fabrication of the $20\ \mu\text{m}$ diameter microring, the laser power was adjusted at 59 mW, while the scanning speed was set at $2000\ \mu\text{m}/\text{sec}$, for 7 scans.

7.2.1 Characterization of the sensing probe

Before the sensing device be exposed to the ethanol vapors, the transmission spectrum of the fabricated microresonator was recorded and it presents in Figure 7.2. The free spectral range (FSR) of the microresonator equals to 23.3 nm corresponding to an effective ring diameter of $20.67\ \mu\text{m}$. The fringe visibility is approximately 10 dB, while the maximum Q factor was calculated at 1.86×10^3 .

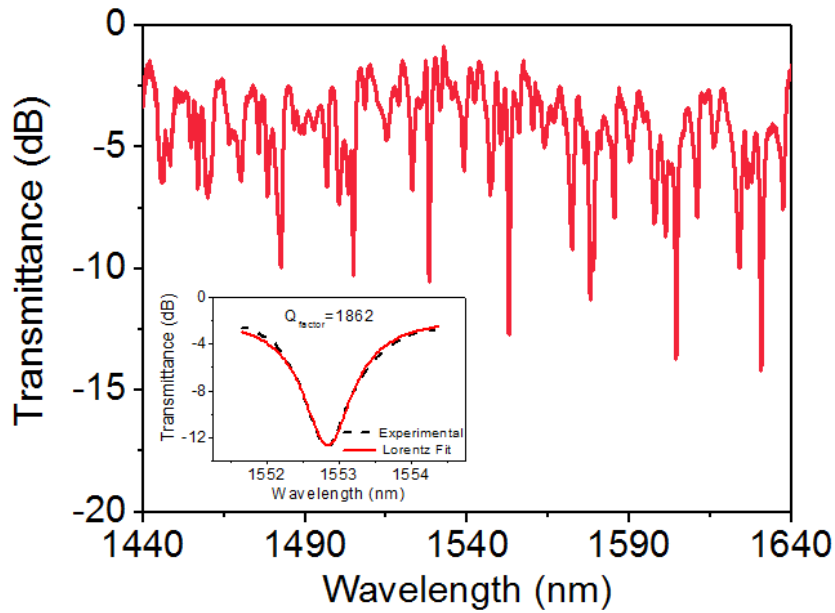


Fig. 7.2. Characteristic transmission spectrum of the fabricated $20\ \mu\text{m}$ diameter WGM microresonator. The inset diagram presents the Lorentz fit and the calculated Q -factor of a selected fringe.

Afterwards, the device was placed in the chamber, as it was described above (see section 7.1) and the TE and TM polarization spectra were recorded. According to Figure 7.3, the TM polarization spectrum (green solid line) presents higher fringe visibility in comparison with the TE polarization spectrum (red solid line), namely 37 dB and 25 dB respectively. In order these experimental resonance patterns to be characterized and identified with the theoretical modal order locations, Airy approximation [9, 26] was used. The green dashed line corresponds to the TM theoretical modal order locations, while the red dashed line to the TE modal order locations (see Fig. 7.3). As it is observed from Figure 7.3, the experimental resonance spectra are in good agreement with the calculated theoretical modal order locations.

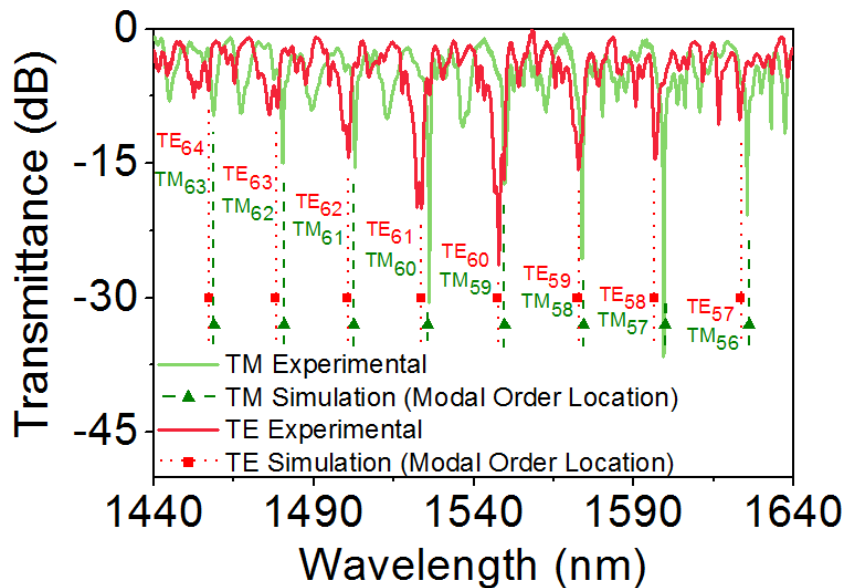


Fig. 7.3. Simulated modal order location of the TE and TM polarization spectra. Green and red solid lines correspond to the experimental spectra, while red and green dashed lines to the simulated modal order locations of the TM and TE polarization spectra respectively.

7.2.2 Sensing of ethanol vapors using single ring WGM microresonator device

In order the fabricated device to be tested as an ethanol vapor sensor, it was exposed to different ethanol concentrations (0.5 ppm to 40 ppm) following the procedure described in paragraph 7.1.

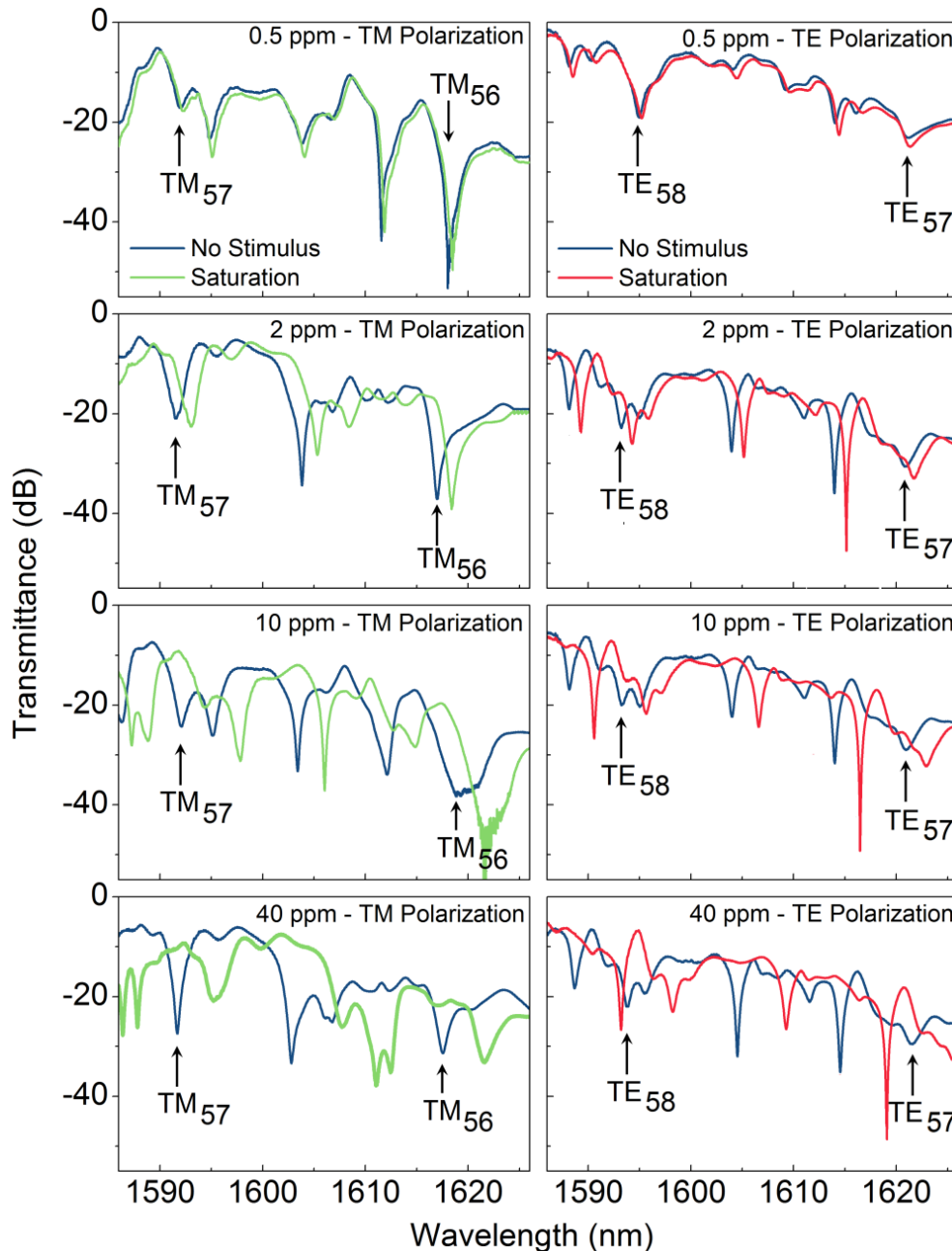


Fig. 7.4. Resonance spectra of measurements before stimulus (blue curves) and at saturation for ethanol vapor concentrations of 0.5 ppm, 2 ppm, 10 ppm and 40 ppm. The left-side presented spectra correspond to TM polarization measurements while the right-side to TE polarization. Green curves right-side to TE polarization correspond to TM polarization measurements at saturation, while red curves to TE polarization measurements at saturation.

For the thorough testing of the probe, both TE and TM polarization spectra were recorded for all the examined ethanol concentrations. It should be noted that the TE and TM polarization spectra were recorded alternating for each ethanol concentration

under investigation. This procedure was followed because we wanted to ensure that the device will not be affected by higher concentrations of vapors for the measurements with one polarization and then could not be reused in order to measure the lower concentrations for the other polarization. Following this procedure, we had to re-align the output of the tapered fiber to the input of the Zing™ Polarizing Optical for every measurement alternating. Even though we tried to ensure the best coupling conditions before stimulus for each ethanol concentration, some differences at the fringe visibility of the excited modes can be observed in the recorded spectra (see Fig. 7.4). Moreover, in some cases a slight spectral shift in wavelength was also observed due to the differences of alignment (see Fig. 7.4). It had been observed that a slight difference in the alignment of the tapered optical fiber to the Zing™ polarizing optical fiber, or a small misalignment between the high precision bare fiber rotator that the Zing polarizing fiber was mounted on and the SMF-28 optical fiber which hosting the ring resonator, affected the recording spectrum.

The recorded resonance spectra for different ethanol concentrations are presented in Figure 7.4. The left-side presented spectra correspond to TM polarization measurements while the right-side to TE polarization, for a spectra region lying between 1586 nm and 1626 nm. In both cases, measurements before stimulus are presented with blue curves, while green and red curves corresponds respectively to TM and TE polarization measurements recorded at saturated atmosphere due to the vapors of ethanol for concentrations of 0.5 ppm, 2 ppm, 10 ppm and 40 ppm presented from top to the bottom diagrams respectively. Moreover, the TM and TE modes that appeared in the examined spectral region (1586 nm – 1626 nm) are noted on the diagrams.

The results presented in Figure 7.4 reveal that upon exposure to ethanol vapors, a spectral shift is observed, related with the absorption of ethanol onto the surface of the ring resonator. The spectral shift for the lowest vapor concentration that had been used, namely 0.5 ppm, a 0.31 nm red shift was measured in case of TM polarization spectra (see Fig, 7.4, top left), while for TE polarization the shift was 0.14 nm (see Fig, 7.4, top right). The shift was increased up to 3.99 nm and 4.11 nm for TM and TE polarization spectra respectively in the case of 40 ppm vapor concentration (see Fig. 7.4 bottom left and right respectively). It has to be noted that in both cases TE₅₇ and TM₅₇ polarization modes were examined. Moreover, it was observed that for the higher vapor concentrations, the resonance spectra presented changes in terms of fringe visibility and quality factor (Q factor) of the notches. For example, the TM₅₇ notch in case of 40 ppm of ethanol vapors had a strength visibility of 19.5 dB with a Q factor equal to 1.67×10^3 before stimulus (see Fig. 7.4, blue curve, bottom left), while at saturation the strength visibility was reduced to 11.4 dB resulting a Q factor of 0.45×10^3 (see Fig. 7.4, green curve, bottom left). On the contrary, the TE₅₇ notch for the same vapor concentration the amplitude strength was 4.6 dB with a Q factor of 1.59×10^3 before stimulus (see Fig. 7.4, blue curve, bottom right), while at saturation the strength visibility was increased to 7.3 dB resulting a slightly increased Q factor of 1.62×10^3 (see Fig. 7.4, red curve, bottom right). By increasing the vapors concentration, the refractive index of the environment within chamber increases. This

increment at the refractive index around the tapered fiber, increases the penetration depth of the evanescent field (see Eq. 2.96 in Chapter 2, section 2.3.3) [27-29], and increases the coupling conditions within the ring resonator. This is the reason why the Q factor and the fringe visibility were increased for the TE polarization for the higher vapor concentration.

To obtain a more detailed picture of the sensing process, both TM and TE polarization spectra were recorded every minute (1 min). The results are presented in top left and right diagrams of Figure 7.5 for four different vapor concentrations. As it is observed, in case of TM polarization spectra the device revealed higher sensitivity, since the spectral shift was stabilized after 7 minutes for lower vapor concentrations (0.5 ppm - 10 ppm) and after 12 minutes for the highest vapor concentration (40 ppm) (see Fig. 7.5, top left). On the contrary, the spectral shifts of TE polarization measurements required more time in order to be stabilized. More specifically, the spectral shift was saturated after 10 minutes for vapor concentrations up to 2 ppm, while for 10 ppm and 40 ppm the time that was required for spectral saturation was 28 minutes and 37 minutes respectively. Considering the barrel shape of the fabricated WGM microresonator, which characterized by a smaller surface on the horizontal axis, approximately of 900 nm thicknesses, in comparison with the vertical axis, where the ring had a height of $\sim 7 \mu\text{m}$, the fact that the TM polarization spectra needed less time to be saturated, can be explained.

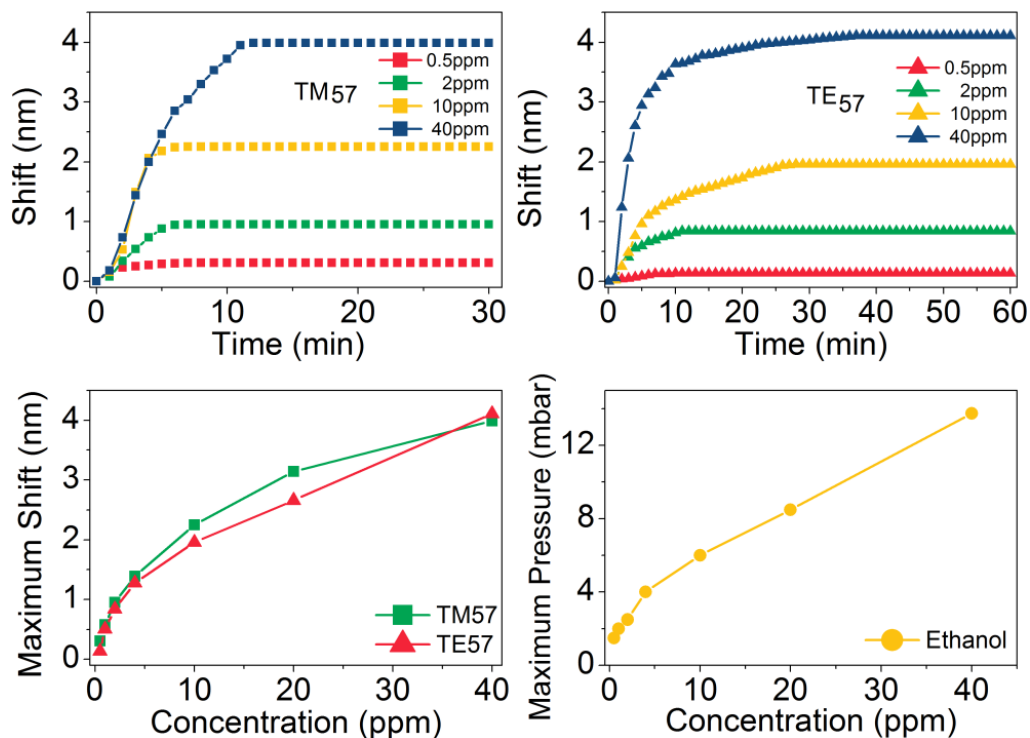


Fig. 7.5. Spectral shift to time for the TM polarization spectra (top-left) and TE polarization spectra (top-right) (TM₅₇ and TE₅₇ notches respectively) for four different vapor concentrations. Maximum shift to ethanol vapor concentrations, for TM (green curve) and TE (red curve) polarization measurements (bottom-left). Maximum pressure reached in chamber due to ethanol vapors for different concentrations (bottom-right).

Furthermore, in this case the spectra presented immediately a monotonic red shift in wavelength versus time for both TM and TE polarization measurements, in comparison with the endface FP optical fiber devices. In that case, the fabricated resonating devices had presented initially a blue shift in wavelength and then a direct red shift. Only after annealing treatment at 250oC, the device presented a direct red shift in wavelength. That blue shift had been related to the porous photopolymerized reflection surface (see sections 5.2.1 and 5.2.2). Thus, herein the absence of this blue shift indicates the absence of a porous effect in the sensing process, result of a smooth surface of the photopolymerized ring. This could be expected, since the material that had been used for the photopolymerization of the ring resonators presented a lower polymerization threshold resulting smoother surfaces in comparison with that one that had been used in case of the endface FP sensing heads (see section 3.1.1b).

The maximum shifts of the notches for TM and TE polarization spectra for all the examined ethanol vapor concentrations are presented in bottom-left diagram of Figure 7.5. Additionally, the maximum pressure that was reached in the chamber due to the evaporation of the ethanol in different concentrations is presented in bottom-right diagram in Figure 7.5. As it is observed, for the same vapor concentrations the maximum shift for both TM and TE polarization spectra follows the same pattern with small differences. For 0.5 ppm of ethanol vapors the saturated pressure in the chamber was recorded to be 1.5 mbar (see Fig. 7.5 bottom right). For this concentration, TM polarization spectrum shifted more than the TE spectrum, namely 0.31 nm and 0.14 nm respectively. For the maximum examined concentration, that of 40 ppm, the saturated pressure in the chamber was 13.75 mbar. The corresponding shifts in this case were 3.99 nm and 4.11 nm for TM and TE polarization spectra respectively. It seems that for concentrations up to 20 ppm the TM mode presents a higher sensitivity in comparison with that of TE modes, since not only the values of spectral shift is slightly higher, but also because the spectral shift stabilizes faster in time, as it was already discussed earlier.

Moreover, this single ring sensing device presented detectivity figure of $\Delta\lambda_{TM}/c_{eth} \sim 0.6$ nm/ppm and $\Delta\lambda_{TE}/c_{eth} \sim 0.3$ nm/ppm (c_{eth} ethanol concentration) for TM and TE polarization spectra respectively, for ethanol vapour concentrations of 0.5 ppm.

After its set of measurements, the chamber was pumped with pure Nitrogen, in order to remove the ethanol vapors. At it is observed from Figure 7.6, the sensing probe was full recovered to its initial spectral response. This indicated that in this case also, the sensing mechanism relies on physisorption phenomena, since upon flashing with Nitrogen the ethanol molecules desorbed from surface of the ring resulting no hysteresis phenomena. Even though the sensing time defers during the exposure of the device to ethanol vapors, the recovery figure is almost similar for both configurations.

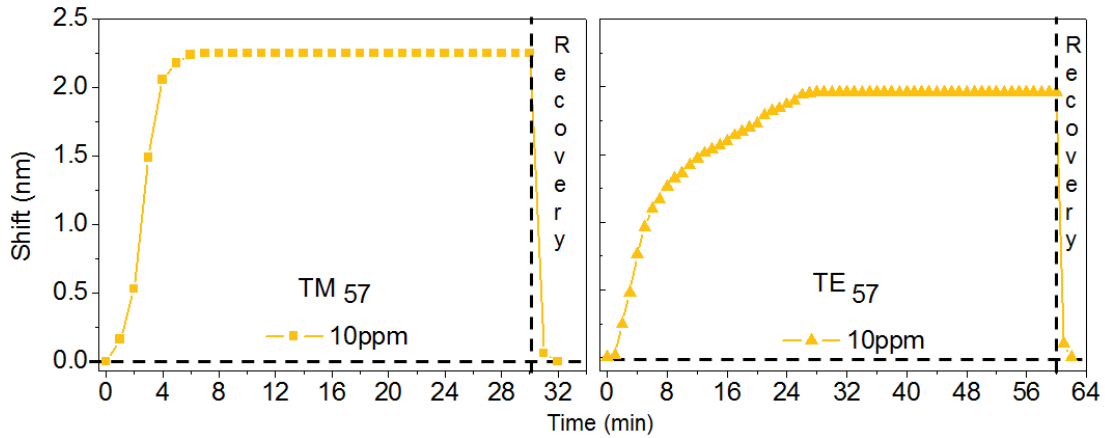


Fig. 7.6. Shift in wavelength versus time and recovery of the sensing device which is constitute from a 20 μm diameter microring resonator directly fabricated onto tapered optical fiber upon flushing the chamber with nitrogen.

These primarily sensing results presented and analyzed above can constitute a first basis for potential applications of the developed WGM probe.

7.3 Second device: WGM Coupled microresonators device for gas sensing

Herein, the fabricated parallel coupled double WGM ring microresonators were tested as gas-pressure sensing device. The response of the WGM coupled device was investigated, while the device was exposed to different gas pressures. Diatomic nitrogen (N_2) and Krypton (Kr) were used in order to excite the sensing device. As it was already mentioned, these gases were chosen to be used because both of them are chemically inert gases in room temperature, while they are widely used in laboratory and industrial processes [30, 31]. The coupled WGM microresonators that were tested here as sensing device, were that presented in paragraph 6.2 (see Fig. 6.18 and 6.19). A 27 μm center to center distance between the microrings was used. Moreover, the experimental process for the gas detection was described in details in paragraph 7.1.

7.3.1 Characterization of sensing probe using diatomic Nitrogen and Krypton

As it was already mentioned in section 7.1, before N_2 or Kr injection in the chamber for testing the sensing device, the chamber was cleaned with flow of the corresponding gas in order to eliminate residual humidity and achieve accuracy in the measurements. Then the inlets and outlets of the chamber were closed and transmission spectra without polarization, as well as spectra of TE and TM polarization were recorded. Afterwards, using the gas inlet valve, the gas was injected in the chamber until the desirable pressure was reached and the TE and TM polarization spectra were recorded.

Figure 7.7 presents the transmission spectrum without polarization (blue curve) and TM (green curve) and TE (red curve) polarization spectra, while the chamber was closed, after the flow of N_2 throughout the chamber. The fringe visibility of the spectrum without polarization was 12 dB and it was increased to 17 dB in case of TE polarization and up to 22 dB for TM polarization spectrum. Additionally, the Q factor

was 0.52×10^3 for the spectrum without polarization, while it was increased to 1.55×10^3 and 2.15×10^3 in case of TE and TM polarization spectra respectively.

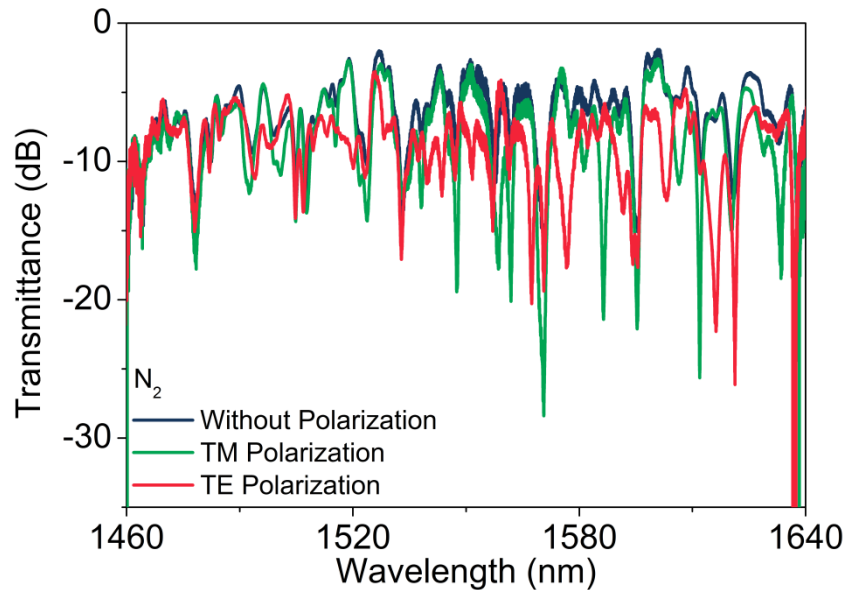


Fig. 7.7. Spectra in transmission mode of the coupled WGM while the chamber was closed after N_2 flow. Blue curve corresponds to the transmission spectrum without polarization, while green and red curves correspond to the TM and TE polarization spectra respectively.

Subsequently, the TM polarization spectra were recorded while the pressure due to the N_2 injection in the chamber was varying from 0 mbar to 600 mbar with a step of 50 mbar. Afterwards, the TE polarization spectra were recorded for the same gas pressures. The results for different modes recorded at different wavelength regions are presented in Figure 7.8. In more details Figure 7.8(Ia) presents a fringe of TE polarization spectrum in the wavelength region lying between 1624 nm - 1634 nm. The blue curve corresponds to the measurement before the Nitrogen injection in the chamber, while red curve to the measurement at 600 mbar nitrogen pressure. Figures 7.8(IIa) and 7.8(IIIa) present fringes of TM polarization spectra in wavelength regions lying between 1624 nm - 1634 nm for the first case and 1600 nm – 1610 nm in the second case. Again the blue curves correspond to the measurements before the Nitrogen injection in the chamber, while green curves to the measurement at 600 mbar nitrogen pressure. Figures 7.8(Ib), 7.8(IIb) and 7.8(IIIb) presented the shift of both minimums of the recorded fringes (1st and 2nd minimum noted on the diagrams) that were recorded for the different gas pressures. Blue curves correspond to the shift of the 1st minimum, while shift of the 2nd minimum of the fringes corresponds to the red curve in case of TE polarization and green curves for the TM polarization. Finally, Figures 7.8(Ic), 7.8(IIc) and 7.8(IIIc) present the splitting of the two minimums of the recorded fringe.

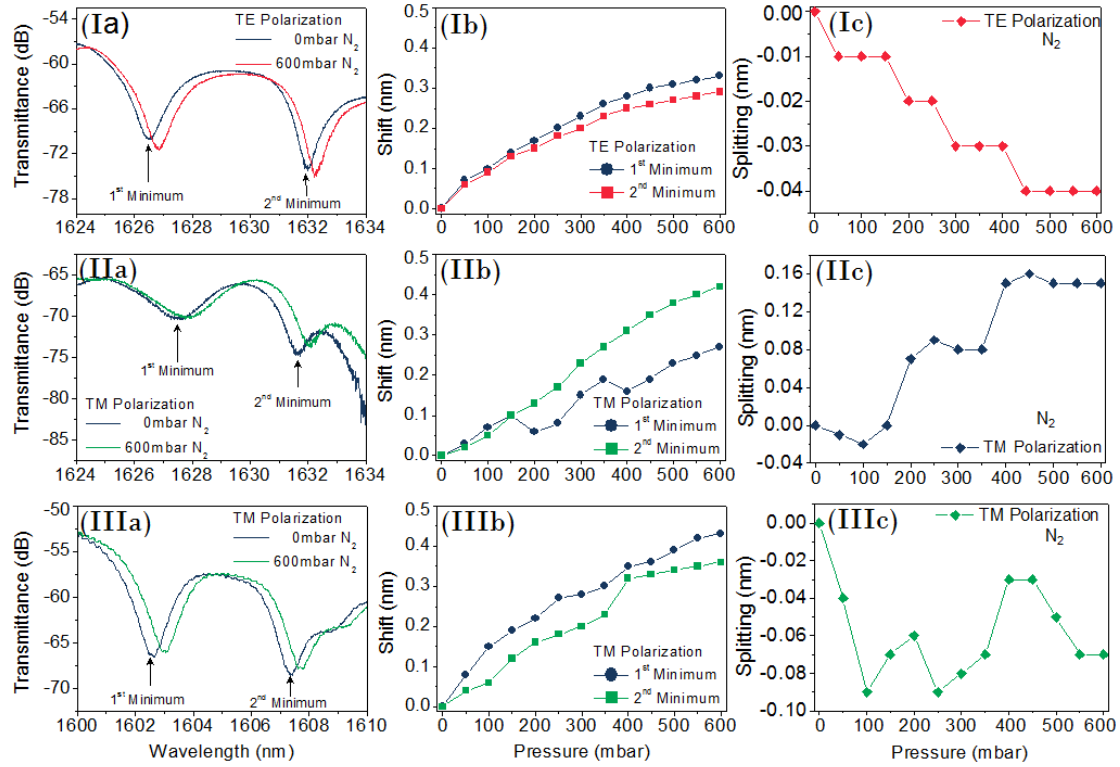


Fig. 7.8. Transmission spectra of the coupled WGM device for TE polarization (Ia) and TM polarization (IIa and IIIa) measurements, where blue curves corresponds to spectra before N_2 injection in the chamber (0 mbar), while red and green curves correspond to TE and TM polarization spectra respectively, at 600 mbar. (Ib, IIb and IIIb) present the shift of the 1st and 2nd minimum of the fringes versus the pressure reached in the chamber due to N_2 , for TE polarization spectra (Ib) and TM polarization spectra (IIb and IIIb) respectively, where blue curves corresponds to the shift of the 1st minimum and red and green curves corresponds to the shift of the 2nd minimum for TE and TM polarization spectra respectively. Finally, (IIIa, IIIb and IIIc) present the splitting of the two minimums during the exposure at N_2 .

The initial evidences show that for both polarizations the sensing device was sensitive to the changes of the pressure in the chamber due to the gas presence. It has to be noted here that when the single ring resonating device was exposed to this Nitrogen pressures, the maximum shift that had been recorded for 600 mbar pressure was 0.06 nm, value that considered insignificant (the resolution of the optical spectrum analyzer was set at 0.05 during the experiment).

The TE polarization measurements, presented in Figures 7.8(Ia), 7.8(Ib) and 7.8(Ic). In Figure 7.8(Ia) blue curve corresponds to the measurement at 0 mbar of N_2 , while red curve corresponds to 600 mbar of N_2 in the chamber. By studying the spectral shift of the minimum of the fringe versus the exposure pressure a monotonic behavior was observed (see Fig. 7.8(Ib)). The maximum shift of the 1st minimum (see Fig. 7.8 (Ib), blue curve) was 0.33 nm and that of the 2nd minimum was 0.29 nm. The splitting effect recorded at this fringe is presented in Figure 7.8(Ic), revealing a decreasing distance between the minimums of the fringe down to 0.4 nm for pressure of 600 mbar.

Regarding to the fringes studied in TM polarization, laying in the spectral region of 1624 nm to 1634 nm (Fig. 7.8(IIa)), the maximum shift of the 1st minimum was 0.27 nm, while for the 2nd minimum the maximum shift was 0.42 nm at 600 mbar (see

Fig. 7.8(IIb)). The corresponding maximum shifts for the other TM fringe at 600 mbar (see Fig. 7.8(IIIa), were 0.43 nm and 0.36 nm for the 1st and 2nd minimums respectively (see Fig. 7.8(IIIb). As it is observed, for the first recorded mode (Fig. 7.8(IIa) and (IIb)) the 2nd minimum of the fringe was shifted more than the 1st minimum, while in the case of the other recorded mode (Fig. 7.8(IIIa) and (IIIb)) the opposite happened. In these cases the splitting effect versus pressure revealed a non-monotonic behavior as it is observed in Figure 7.8(IIc) and 7.8(IIIc) respectively. For the TM fringe presented in Figure 7.8(IIc) the deeps of the fringe were separated with a splitting of 0.15 nm, while for the other TM fringe (see Fig. 7.8(IIIc)) the deeps of the fringe got closer by a value of 0.07nm for pressure of 600 mbar.

These phenomena could be explained if one considers that upon the increment of the pressure in the chamber, the shape of the microrings could be slightly affected and moreover the distance between the rings could change. By this way the interaction that existing between the coupled rings through their evanescent field will change, due to the change of the intermediate distance, resulting chances in the distance between the deeps of the recorded fringes [32]. These phenomena had been already studied before using microspheres [32-34].

Afterwards, the chamber was cleaned using Kr gas flow, in order N₂ species to be washout. Then, the inlet and outlet of the chamber was closed and the transmission spectrum without polarization (blue curve) as well as TM (green curve) and TE (red curve) polarization spectra were recorded and are presented in Figure 7.9 presents. The fringe visibility of the transmission spectrum without polarization was 10.5 dB, while the Q factor was calculated to 0.98×10^3 . During the polarization measurements the fringe visibility increased up to 13.5 dB and 16 dB for the TE and TM polarization spectrum respectively. The Q factors were increased up to 1.21×10^3 in case of TE polarization spectrum and 2.12×10^3 for TM polarization spectrum.

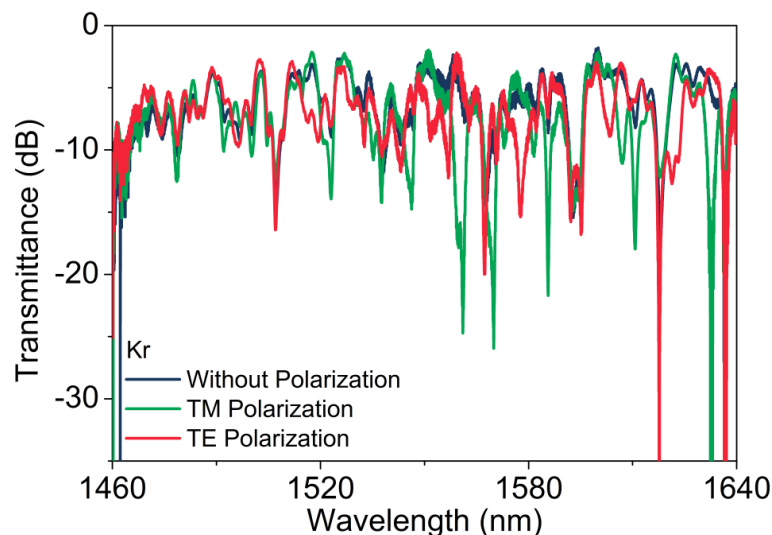


Fig. 7.9. Spectra in transmission mode of the coupled WGM while the chamber was closed after Kr flow. Blue curve corresponds to the transmission spectrum without polarization, while green and red curves correspond to the TM and TE polarization spectra respectively.

The TM and TE polarization spectra were recorded for Kr pressures varying from 0 mbar to 600 mbar and for modes recorded at different wavelength regions. The results are presented in Figure 7.10. Figures 7.10(Ia) and 7.10(IIa) present the TE polarization spectra of the coupled WGM resonating for two different modes. The blue curve corresponds to the measurement at 0 mbar of Kr while red curve corresponds to the measurement at 600 mbar pressure of Kr in the chamber. The first TE polarization mode was laying in the spectral region of 1576 nm to 1586 nm (Fig. 7.10(Ia), were 0.14 nm and 0.48 nm maximum spectral shifts were recorded for the 1st and 2nd minimums (see Fig. 7.10(Ib) blue curve and red curve respectively). The other recorded TE polarization mode was laying in the spectral region of 1582nm to 1592 nm (see Fig 7.10(IIa)) with the maximum shifts being 0.41 nm and 0.11 nm for the 1st and 2nd minimums respectively (see Fig. 7.10(IIb) blue curve and red curve respectively). Moreover, Figures 7.10(Ic) and 7.10(IIc) present the splitting effect versus exposure pressure, were the minimums of the fringe in the first case were separated by a distance of 0.35 nm, while in the second case they got closer by 0.3 nm for pressure of 600 mbar.

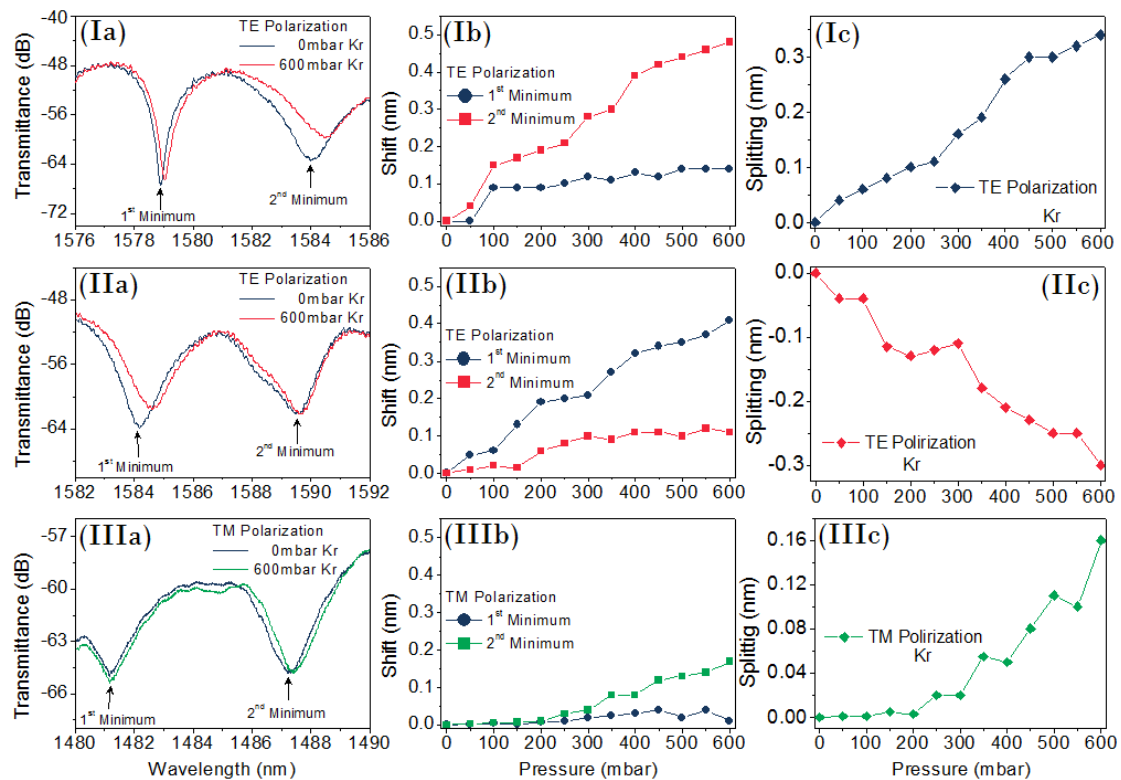


Fig. 7.10. Transmission spectra of the coupled WGM device for TE polarization (Ia and IIa) and TM polarization (IIIa) measurements, where blue curves corresponds to spectra before Kr injection in the chamber (0 mbar), while red and green curves correspond to TE and TM polarization spectra respectively, at 600 mbar. (Ib, IIb and IIIb) present the shift of the 1st and 2nd minimum of the fringes versus the pressure reached in the chamber due to Kr, for TE polarization spectra (Ib and IIb) and TM polarization spectra (IIIb) respectively, where blue curves corresponds to the shift of the 1st minimum and red and green curves corresponds to the shift of the 2nd minimum for TE and TM polarization spectra respectively. Finally, (IIa, IIIa and IIIc) present the splitting of the two minimums during the exposure at Kr.

In addition, Figure 7.10(IIIa) presents the TM polarization fringe that was

recorded in the spectral region laying between 1480 nm and 1490nm. The blue curve corresponds to the measurement before the injection of Kr (0 mbar) while green curve corresponds to the measurement at 600 mbar of Kr pressure in the chamber. In this case, the maximum shift that was recorded for the 1st minimum of the fringe was 0.04 nm, presented with the blue in Figure 7.10(IIIb), while green curve corresponds to the shift of the 2nd minimum of the fringe revealing a maximum shift of 0.17 nm. The splitting of the fringe in this case was 0.16 nm (see Fig. 7.10(IIIc)) for pressure of 600 mbar.

7.3.2 Comparison between Nitrogen and Krypton sensing

Initially, before the increase of the gas flow in the chamber, the sensing device show increased sensitivity while operating in TM polarization. Namely, after the wash of the chamber with N₂ flow the fringe visibility for TM polarization spectrum was 22 dB with a Q factor of 2.15×10^3 , while after Kr flow the fringe visibility was 16 dB and the Q factor was of the order of 2.12×10^3 .

Then, during the N₂ measurements the device was more sensitive while was operating in TM polarization mode. On the contrary, TE polarization mode reveals higher sensitivities in case of Kr measurements. More specifically the detectivity figures in case of N₂ were $\Delta\lambda_{1TM}/\Delta P_{N_2} = 4.5 \times 10^{-4}$ nm/mbar and $\Delta\lambda_{2TM}/\Delta P_{N_2} = 7.0 \times 10^{-4}$ nm/mbar respectively for the 1st and 2nd minimum of the fringe in case of TM polarization spectrum, while for Kr the corresponding values were $\Delta\lambda_{1TM}/\Delta P_{Kr} = 0.6 \times 10^{-4}$ nm/mbar and $\Delta\lambda_{2TM}/\Delta P_{Kr} = 2.8 \times 10^{-4}$ nm/mbar ($\Delta P_{N_2} = \Delta P_{Kr} = 600$ mbar). In case of TE polarization spectra the detectivity figures for the N₂ were $\Delta\lambda_{1TE}/\Delta P_{N_2} = 5.5 \times 10^{-4}$ nm/mbar and $\Delta\lambda_{2TE}/\Delta P_{N_2} = 4.8 \times 10^{-4}$ nm/mbar, while for Kr these values were $\Delta\lambda_{1TE}/\Delta P_{Kr} = 6.4 \times 10^{-4}$ nm/mbar and $\Delta\lambda_{2TE}/\Delta P_{Kr} = 1.8 \times 10^{-4}$ nm/mbar (see Table 7.1).

Detectivity		$\Delta\lambda/\Delta P_{N_2}$ (nm/mbar) for Diatomic Nitrogen (N ₂)	$\Delta\lambda/\Delta P_{Kr}$ (nm/mbar) for Krypton (Kr)
TM	1 st Minimum	4.5×10^{-4}	0.6×10^{-4}
	2 nd Minimum	7.0×10^{-4}	2.8×10^{-4}
TE	1 st Minimum	5.5×10^{-4}	6.4×10^{-4}
	2 nd Minimum	4.8×10^{-4}	1.8×10^{-4}

Table 7.1. Detectivities of the coupled WGM gas sensor for the diatomic Nitrogen (N₂) and Krypton (Kr). The detectivities were calculated as $\Delta\lambda/\Delta P$ (nm/mbar) where $\Delta\lambda$ was the maximum shift for the 1st or 2nd minimum of the recorder WGM fringe for TM and TE polarization spectra and $\Delta P=600$ mbar.

To conclude, the initial results show that the fabricated coupled WGM microresonator could be used as a gas-pressure sensor with the higher recorded detectivity down to 0.6×10^{-4} nm/mbar in case of Kr sensing. More experiments have to be done for the characterization of this sensing device in order to fully understand the sensing mechanism.

7.4 Third device: WGM Coupled microsensor for ethanol vapors detection

The coupled WGM microresonator, fabricated with a distance of 27 μm from center to center of the rings, presented in paragraph 6.2 (see Fig. 6.18 and 6.19) was also tested as sensing device for the detection of ethanol vapors. The experimental process that was used was described in details in paragraph 7.1.

7.4.1 Sensing of ethanol vapors using a coupled WGM microresonator device

In order the coupled WGM microresonator to be evaluated as a vapor sensing device, it was exposed to different ethanol vapor concentrations. Both TE and TM polarization spectra were recorded, as in the aforementioned single WGM microresonator device (see paragraph 7.2.2).

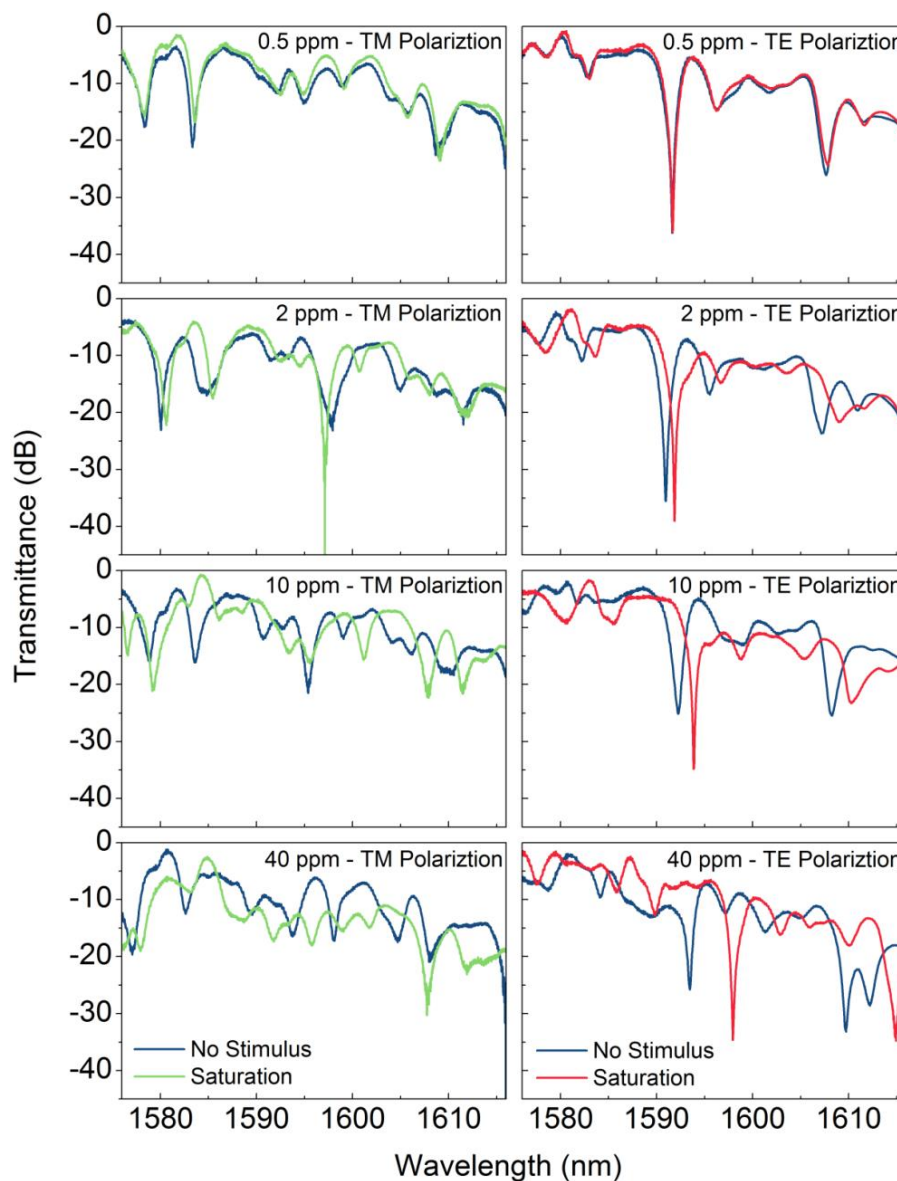


Fig. 7.11. The left-side presented spectra correspond to TM polarization measurements while the right-side to TE polarization. Resonance spectra of measurements before stimulus (blue curves) and at saturation (green curves corresponds to TM polarization measurements, while red curves to TE polarization measurements) for ethanol vapor concentrations of 0.5 ppm, 2 ppm, 10 ppm and 40 ppm presented from top to the bottom diagrams respectively.

Figure 7.11 presents the resonance TM and TE polarization spectra, recorded for a spectral region lying between 1576 nm and 1616 nm. The results are presented from top to bottom by increasing the ethanol vapor concentration, namely 0.5 ppm, 2 ppm, 10 ppm and 40 ppm. The TM polarization measurements are presented in the left-side diagrams and TE polarization measurements on right-side diagrams. Blue curves correspond to measurements before stimulus, while green and red curves corresponds to TM and TE polarization measurements respectively at saturated atmosphere due to the vapors of ethanol.

In this case, the modal order location is difficult to be calculated since in the coupled WGM microresonators a splitting of the fringes is introduced in the interference spectra (see Fig. 6.13, in section 6.3.1), due to the interaction between the two rings through their evanescence field [35-37]. For this reason the stronger modes presenting the higher strength visibility will be studding bellow. The interference spectra of the measurements show that the spectra were shifted to longer wavelengths at the presence of ethanol vapors in the chamber, even for 0.5 ppm ethanol vapors which was the lower concentration that was used (see Fig. 7.11). As the vapor concentration increases, the spectral shift is more significant. More specifically, the TM polarization spectrum shifts 0.27 nm for 0.5 ppm of ethanol vapors (Fig. 7.11, top-left), while for 40 ppm the shift increased to 3.01 nm (Fig. 7.11, bottom-left). The equivalent shifts for the TE polarization spectra were 0.06 nm and 4.49 nm for concentrations of 0.5 ppm and 40 ppm of ethanol vapors respectively (Fig. 7.11 top-right and bottom-right spectra). Moreover, it is observed that as the concentration of the ethanol vapors increases, more significant changes at the spectral response are recorded. Even the higher order modes that were excited, and were presented as noise in the characteristic WGM resonance spectra, were noticed to have changes in their fringe visibility at the presence of higher vapor concentrations. As it was already discussed in Section 7.2.2, when the ethanol is injected in the chamber in high concentrations, the refractive index of the environment within chamber increases. This increment at the refractive index around the tapered fiber, increases the penetration depth of the evanescence field (see Eq. 2.96 in Chapter 2, section 2.3.3) [27-29], and increases the coupling conditions within the ring resonator. Moreover, herein, we have also the interaction between the two rings through their evanescence field. These reasons can affect the interference spectrum in higher concentration.

For a more detailed picture of the operation of the coupled WGM sensing device, the shifts of the notches to time are presented in figure 7.12. Top-left diagram presents the shifts of the TM resonance spectra for different vapor concentrations, while the top-right diagram presents the shifts of the TE resonance spectra. In case of TM resonance spectra the time that is required for the saturation of the spectra is shorter than this needed for the TE polarization spectra. As it was already mentioned before (see paragraph 7.2.2) this was something that could be predicted due to the barrel shape of the fabricated WGM microresonators. The fabricated microresonators have bigger surfaces area in the vertical axis. Due to this fact, this surface area of the WGM microresonators required more time in order the ethanol vapors to be deposited on it.

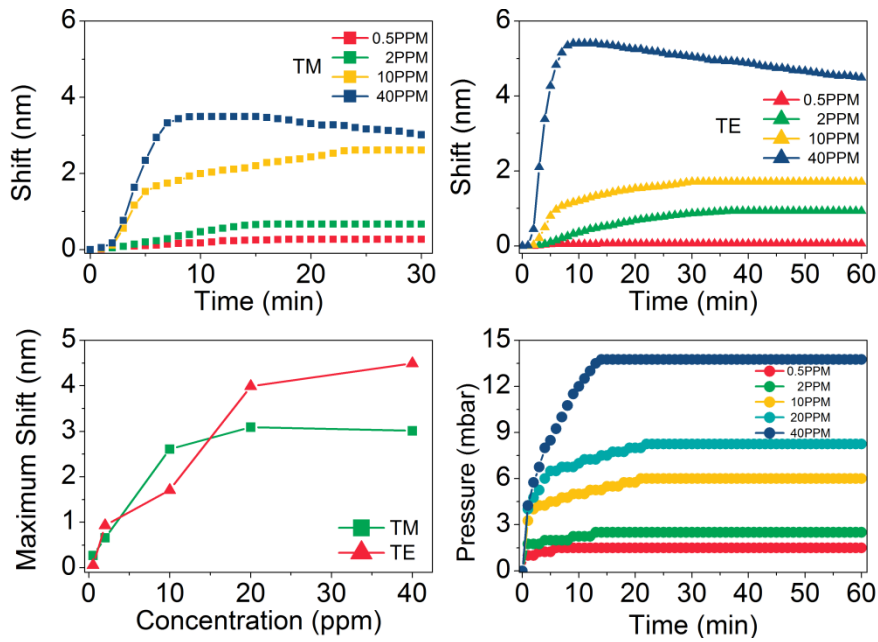


Fig. 7.12. Spectral shift to time for the TM polarization spectra (top-left) and TE polarization spectra (top-right) (TM and TE notches respectively) for four different vapor concentrations. Maximum shift to ethanol vapor concentrations, for TM (green curve) and TE (red curve) polarization measurements (bottom-left). Pressure reached in chamber due to ethanol evaporation during time, for different concentrations (bottom-right).

In the TM polarization measurements of the coupled WGM sensing device, the time that was required for saturation was 16 minutes for concentrations up to 2 ppm, while for 10 ppm the corresponding time was 24 minutes. In all these cases the time required for saturation was increased in comparison with those needed in case of the single WGM sensing device, which was 7 minutes (see paragraph 7.2.2). Moreover, herein a non-monotonic spectral shift is observed in case of 40 ppm of ethanol vapors. Initially, for the first 10 minutes a red shift of the order of 3.49 nm was observed. From the 10th minute to 14th minute the shift seemed to be saturated. After the 15th minute a blue shift was observed reducing the shift to 3.01 nm. As it is observed from the bottom-right diagram which presents the pressure reached in the chamber due to the evaporation of the ethanol as time passes, the pressure was saturated at the 14th minute for the 40 ppm of ethanol, reached the 13.75 mbars. Probably, within the first 10 minutes the vapors occupy the surface of the microresonators resulting the red shift. This amount of vapors is enough to saturate the sensing device, and as a result to introduce the plateau presented in the spectral shift curve between the 10th and 14th minute. After the 14th minute that the pressure was saturated in the chamber, an amount of ethanol vapors were probably condensed between the gap of the two fabricated microresonators, and on the junctions of the microresonators to the tapered fiber occurring the blue shift observed in the spectral shift diagram.

Likewise, for the TE polarization measurements, the time needed the spectral shift to be saturated was 14 minutes for the 0.5 ppm ethanol vapor concentration and 37 minutes for 2 ppm and 10 ppm concentrations. For the higher vapor concentration that was examined, that of 40 ppm, the non-monotonic spectral shift was observed too. A 5.4 nm spectral red shift was recorded until the 9th minute and then a saturated plateau

was observed till the 14th minute. Finally, when the pressure was saturated in the chamber due to the ethanol evaporation, a blue shift of down to 4.49 nm was recorded. As it was mentioned before, in case of the TE polarization spectra, the bigger surface area of the barrel shape WGM microresonators demand more time in order to be covered with the ethanol vapors.

7.4.2 Comparison of single and coupled WGM microring ethanol sensing devices

Both the single and coupled WGM microring resonating probes were tested as ethanol vapor sensing devices under the same experimental conditions. The experimental results show that both the devices were able to detect ethanol vapors down to 0.5 ppm concentration. Specifically the maximum shifts recorded for the TM polarization spectra were 0.31 nm and 0.27 nm for the single ring and coupled device respectively. In case of TE polarization measurements the recorded maximum shifts were 0.14 nm for the single ring device and 0.06 nm for the coupled device. These spectral shifts correspond to detectivity figures of $\Delta\lambda_{SR-TM} / c_{eth} = 0.62$ nm/ppm, $\Delta\lambda_{SR-TE} / c_{eth} = 0.28$ nm/ppm for the single ring sensing device and $\Delta\lambda_{CR-TM} / c_{eth} = 0.54$ nm/ppm, $\Delta\lambda_{CR-TE} / c_{eth} = 0.12$ nm/ppm for the coupled WGM microring sensing device (SR=single ring, CR=coupled microrings, c_{eth} = ethanol concentration).

The main difference between the single ring and the coupled microresonating sensing devices was estimated at the spectral response for the higher ethanol vapor concentration that was examined, namely 40 ppm. While for the single ring the spectral response had a monotonic behavior and was shifted to longer wavelength values (red shift), in case of the coupled sensing device the spectral response was non-monotonic. More specifically, the maximum shifts in case of the single ring were increased up to 3.99 nm (stabilized at 12 min) and 4.11 nm (stabilized at 37 min) for TM and TE polarization spectra respectively. On the contrary, for the coupled device, a red shift was initially observed until the 9th minute. Then a plateau was presented in the spectral shift curve until the 14th minute when the pressure was saturated in the chamber and afterwards the spectra were shifted to shorter wavelengths (blue shift). The maximum shifts at the plateaus were 3.49 nm (TM polarization) and 5.4 nm (TE polarization) and they were reduced down to 3.01 nm and 4.49 nm respectively.

To conclude, the experimental results show that both fabricated WGM devices were able to detect ethanol vapors down to 0.5 ppm concentration. The single ring device responded and stabilized faster when exposed to ethanol vapors in comparison with the coupled ring device which needed more time to be stabilized. This was expected due to the more complicated design of the coupled WGM sensing device.

7.5 Summary and Conclusions

Summarizing, three different devices based on WGM sensing cavities were presented in this chapter. The first device was a single ring sensing probe for the detection of ethanol vapors presented sensitivities down to 0.5 ppm with a detectivity figure of $\Delta\lambda_{TM}/c_{eth} \sim 0.6$ nm/ppm and $\Delta\lambda_{TE}/c_{eth} \sim 0.3$ nm/ppm. The second device was

a coupled WGM microresonating sensor tested as a gas sensor for the detection of inert gases widely used in laboratory and industrial processes, those of diatomic Nitrogen (N₂) and Krypton (Kr). The maximum pressure that the sensing device was exposed to was up to 600 mbar with the higher recorded detectivity down to 0.6×10^{-4} nm/mbar in case of Kr sensing and 4.5×10^{-4} nm/mbar for N₂. The last sensing device that was examined again for ethanol vapor detection was a coupled WGM microresonating probe. The experimental process was similar to that one used for the single ring sensing device. The sensor presented sensitivities down to 0.5 ppm with detectivities of $\Delta\lambda_{TM} / c_{eth} \sim 0.5$ nm/ppm, $\Delta\lambda_{TE} / c_{eth} \sim 0.1$ nm/ppm.

The difference between the single ring and the coupled microresonating sensors were the response time and the upper level of the ethanol vapor concentration that could be detected properly. The single ring device presented faster response and spectral stabilization in comparison with the coupled ring device which needed more time to be stabilized. Moreover, while single ring device presented a monotonic spectral response to 40 ppm ethanol vapor concentration, the couple ring device presented a non-monotonic spectral response for this vapor concentration.

To conclude, the aforementioned sensing devices presented good spectral response. Both single ring and coupled ring WGM cavities would be primarily used for the detection of organic vapours targeting breath analysis applications, related to the early diagnosis of lung cancer [38] and metabolic diseases [39], potentially being implemented in a standard spirometric diagnostic process. Moreover, the coupled ring WGM device could be farther tested and characterized using more gasses in order to be used as gas sensor with potential applications to indoor air quality measurements for personal health and safety.

References

- [1] S. M. Spillane, T. J. Kippenberg, and K. J. Vahala, "Ultralow-threshold Raman laser using a spherical dielectric microcavity," *Nature*, vol. 415, pp. 621-623, 02/07/print 2002.
- [2] D. Ristić, S. Berneschi, M. Camerini, D. Farnesi, S. Pelli, C. Trono, *et al.*, "Photoluminescence and lasing in whispering gallery mode glass microspherical resonators," *Journal of Luminescence*, vol. 170, pp. 755-760, 2016/02/01/ 2016.
- [3] M. Kuwata-Gonokami, S. Ozawa, R. H. Jordan, A. Dodabalapur, H. E. Katz, M. L. Schilling, *et al.*, "Polymer microdisk and microring lasers," *Optics Letters*, vol. 20, pp. 2093-2095, 1995/10/15 1995.
- [4] G. Kozyreff, J. Luis Dominguez-Juarez, and J. Martorell, "Nonlinear optics in spheres: from second harmonic scattering to quasi-phase matched generation in whispering gallery modes," *Laser & Photonics Reviews*, vol. 5, pp. 737-749, Nov 2011.
- [5] T. J. Kippenberg and K. J. Vahala, "Cavity Opto-Mechanics," *Optics Express*, vol. 15, pp. 17172-17205, 2007/12/10 2007.

- [6] J. D. Suter, Y. Sun, D. J. Howard, J. A. Viator, and X. Fan, "PDMS embedded opto-fluidic microring resonator lasers," *Optics Express*, vol. 16, pp. 10248-10253, 2008/07/07 2008.
- [7] P. Rabiei and W. H. Steier, "Tunable polymer double micro-ring filters," *Ieee Photonics Technology Letters*, vol. 15, pp. 1255-1257, Sep 2003.
- [8] P. Rabiei, W. H. Steier, C. Zhang, and L. R. Dalton, "Polymer micro-ring filters and modulators," *Journal of Lightwave Technology*, vol. 20, pp. 1968-1975, Nov 2002.
- [9] N. M. Hanumegowda, C. J. Stica, B. C. Patel, I. White, and X. D. Fan, "Refractometric sensors based on microsphere resonators," *Applied Physics Letters*, vol. 87, Nov 2005.
- [10] T. Ioppolo, M. Kozhevnikov, V. Stepaniuk, M. V. Ötügen, and V. Sheverev, "Micro-optical force sensor concept based on whispering gallery mode resonators," *Applied Optics*, vol. 47, pp. 3009-3014, 2008/06/01 2008.
- [11] T. Ioppolo and M. V. Ötügen, "Pressure tuning of whispering gallery mode resonators," *Journal of the Optical Society of America B*, vol. 24, pp. 2721-2726, 2007/10/01 2007.
- [12] F. Vollmer, D. Braun, A. Libchaber, M. Khoshshima, I. Teraoka, and S. Arnold, "Protein detection by optical shift of a resonant microcavity," *Applied Physics Letters*, vol. 80, pp. 4057-4059, 2002.
- [13] H.-C. Ren, F. Vollmer, S. Arnold, and A. Libchaber, "High-Q microsphere biosensor - analysis for adsorption of rodlike bacteria," *Optics Express*, vol. 15, pp. 17410-17423, Dec 10 2007.
- [14] Q. Ma, L. Huang, Z. Guo, and T. Rossmann, *Whispering-Gallery Mode Silica Micro-Sensors for Temperature and Gas-Phase Concentration Measurements*, 2010.
- [15] G. Guan, S. Arnold, and V. Otugen, "Temperature Measurements Using a Microoptical Sensor Based on Whispering Gallery Modes," *AIAA Journal*, vol. 44, pp. 2385-2389, 2006/10/01 2006.
- [16] B. Ozel, R. Nett, T. Weigel, G. Schweiger, and A. Ostendorf, "Temperature sensing by using whispering gallery modes with hollow core fibers," *Measurement Science and Technology*, vol. 21, p. 5, Sep 2010.
- [17] F. Vollmer and S. Arnold, "Whispering-gallery-mode biosensing: label-free detection down to single molecules," *Nature Methods*, vol. 5, p. 591, 06/27/online 2008.
- [18] G. Zhang, X. L. Feng, B. Liedberg, and A. Q. Liu, "Gas Sensor for Volatile Organic Compounds Detection Using Silicon Photonic Ring Resonator," *Procedia Engineering*, vol. 168, pp. 1771-1774, 2016/01/01/ 2016.
- [19] Y. Sun and X. Fan, "Analysis of ring resonators for chemical vapor sensor development," *Optics Express*, vol. 16, pp. 10254-10268, 2008/07/07 2008.
- [20] Y. Sun, S. I. Shopova, G. Frye-Mason, and X. Fan, "Rapid chemical-vapor sensing using optofluidic ring resonators," *Optics Letters*, vol. 33, pp. 788-790, 2008/04/15 2008.

- [21] F. Pang, X. Han, F. Chu, J. Geng, H. Cai, R. Qu, *et al.*, "Sensitivity to alcohols of a planar waveguide ring resonator fabricated by a sol-gel method," *Sensors and Actuators B: Chemical*, vol. 120, pp. 610-614, 2007/01/10/ 2007.
- [22] A. Ksendzov, M. L. Homer, and A. M. Manfreda, "Integrated optics ring-resonator chemical sensor with polymer transduction layer," *Electronics Letters*, vol. 40, pp. 63-65, Jan 2004.
- [23] FiberCore,
["https://www.newport.com/medias/sys_master/images/images/h88/hab/8797309042718/Zing-Polarizing-Fiber.pdf."](https://www.newport.com/medias/sys_master/images/images/h88/hab/8797309042718/Zing-Polarizing-Fiber.pdf)
- [24] <https://www.lenntech.com/periodic/elements/kr.htm>.
- [25] ["https://www.lenntech.com/periodic/elements/n.htm."](https://www.lenntech.com/periodic/elements/n.htm)
- [26] A. Francois and M. Himmelhaus, "Optical Sensors Based on Whispering Gallery Modes in Fluorescent Microbeads: Size Dependence and Influence of Substrate," *Sensors*, vol. 9, pp. 6836-6852, Sep 2009.
- [27] J. D. Love, W. M. Henry, W. J. Stewart, R. J. Black, S. Lacroix, and F. Gonthier, "Tapered single-mode fibres and devices. I. Adiabaticity criteria," *IEE Proceedings J - Optoelectronics*, vol. 138, pp. 343-354, 1991.
- [28] S. E. Skelton, M. Sergides, R. Patel, E. Karczewska, O. M. Maragó, and P. H. Jones, "Evanescent wave optical trapping and transport of micro- and nanoparticles on tapered optical fibers," *Journal of Quantitative Spectroscopy and Radiative Transfer*, vol. 113, pp. 2512-2520, 2012/12/01/ 2012.
- [29] J. Bures and R. Ghosh, "Power density of the evanescent field in the vicinity of a tapered fiber," *Journal of the Optical Society of America A*, vol. 16, pp. 1992-1996, 1999/08/01 1999.
- [30] R. I. I. (Krypton),
["https://refractiveindex.info/?shelf=main&book=Kr&page=Bideau-Mehu."](https://refractiveindex.info/?shelf=main&book=Kr&page=Bideau-Mehu)
- [31] R. I. I. (Nitrogen),
["https://refractiveindex.info/?shelf=main&book=N2&page=Peck-0C."](https://refractiveindex.info/?shelf=main&book=N2&page=Peck-0C)
- [32] V. S. Ilchenko, M. L. Gorodetsky, and S. P. Vyatchanin, "Coupling and tunability of optical whispering-gallery modes: a basis for coordinate meter," *Optics Communications*, vol. 107, pp. 41-48, 1994/04/01/ 1994.
- [33] D. Thompson, D. Keating, E. Guler, K. Ichimura, M. E Williams, and K. Fuller, *Separation-sensitive measurements of morphology dependent resonances in coupled fluorescent microspheres* vol. 18, 2010.
- [34] S. P. Ashili, V. N. Astratov, and E. C. H. Sykes, "The effects of inter-cavity separation on optical coupling in dielectric bispheres," *Optics Express*, vol. 14, pp. 9460-9466, 2006/10/02 2006.
- [35] D. G. Rabus, *Integrated Ring Resonators The Compendium*. New York: Springer, 2007.
- [36] Y. C. Li, F. Abolmaali, K. W. Allen, N. I. Limberopoulos, A. Urbas, Y. Rakovich, *et al.*, "Whispering gallery mode hybridization in photonic molecules," *Laser & Photonics Reviews*, vol. 11, Mar 2017.

- [37] S. Darmawan and M. K. Chin, "Critical coupling, oscillation, reflection, and transmission in optical waveguide-ring resonator systems," *Journal of the Optical Society of America B*, vol. 23, pp. 834-841, 2006/05/01 2006.
- [38] R. F. Machado, D. Laskowski, O. Deffenderfer, T. Burch, S. Zheng, P. J. Mazzone, *et al.*, "Detection of lung cancer by sensor array analyses of exhaled breath," *American Journal of Respiratory and Critical Care Medicine*, vol. 171, pp. 1286-1291, Jun 1 2005.
- [39] F. Baldini and A. G. Mignani, "Optical-fiber medical sensors," *Mrs Bulletin*, vol. 27, pp. 383-387, May 2002.

Chapter 8

Conclusions

The aim of this thesis was to combine standard single mode optical fibers and multi-photon lithography in order to produce two different kinds of light resonating structures directly onto the optical fibers that would be further exploited as fiber-optic gas or liquid sensors in the time being.

8.1 Summary and conclusions for the endface FP optical fiber devices

In the first part fiber-optic devices based on Fabry-Perot interferometers were fabricated on the endface of optical fibers, in three different designs. The first FP resonator, named microdrum resonator, was consisting of a thin flat membrane suspended of four pillars, which were attached on the endface of the optical fiber. By this way a multiple FP resonator was developed. In order to avoid this multiple FP cavity, two different designs were fabricated, namely the microfunnel resonator and the microprism resonator. At the first one, an inclination of approximately 20° at a funnel-shape was introduced homocentrically with the membrane, while at the second one the inclination was given all across the outer surface, resulting a prism-like shape. By this way single endface FP resonators were developed giving similar interference spectrum. The difference between these two single FP resonators is that the microfunnel endface resonator has to be precisely aligned to the core of the optical fiber otherwise it gives a multiple FP interference spectrum. The spectral performance of these devices was tested in the wavelength region of 1550 nm.

Moreover, two different simulation methods were used to predict the interference spectrum of the endface FP cavities. The first simulation method that was developed was based on two-beam optical interference approximation resulting special simulating models for each design of endface FP microresonator. The second simulation method was based on Finite-Difference Time-Domain (FDTD) method. A commercially available software, (OptiFDTD, Optiwave Systems Inc.) was used and simulated the behavior of the modes during the light propagation throughout the FP devices, as well as the reflected interference spectrum. The simulated results in both cases were in good agreement with the experimental data.

At our knowledge, even if multiphoton polymerization technique had already been used in order optical microstructures to be fabricated on the endface of optical fibers, it is the first time that this technique was used to fabricate FP resonators. With the present experiments, it was proved that multiphoton polymerization technique can be used to fabricate robust structures that are functional and the FP cavities can be transformed easily and fast, by changing either the design or the dimensions of the FP cavity according to the requirements of the experiments.

Then, the microprism endface FP devices were tested as vapor and liquid sensors. More specifically, the fabricated device was initially tested as vapor sensor for the

detection of species of two different organic solvents, those of ethanol and chloroform. Its sensitivity with respect to the surface porosity of the fabricated micro-prism sensing head was studied by reducing the pores size of the photopolymerized reflection surface using annealing treatment processes. Results show the dependence of the sensitivity and selectivity/specificity upon the porosity of the fabricated FP cavity. Moreover, the studies of the two different organic solvents revealed that the operation mechanism of the fabricated sensing device did not depend only on the optical and vapor pressure characteristics of the solvents but also on their molecular structure and affinity to the sensing surfaces. To the end, the fabricated endface FP optical fiber device was able to detect concentrations of vapor traces down to 4 ppm, revealing sensitivities of $\sim 1.5 \times 10^3$ nm/RIU after the annealing treatment at 250°C.

Afterwards, the porous (as-fabricated) FP optical fiber device was further tested as vapors sensor for the detection of traces of three different Cl-VOCs. As it was expected, the physisorption mechanism relied not only on the differences of the refractive indices and the vapor pressures of the chlorinated solvents, but also on the chlorine coordination/number of the three different chlorinated molecules which resulting different polarizabilities. Thus, the experimental results show distinct spectra response versus sensing time, for each chlorinated solvent that was examined herein, even for vapor concentrations down to 4 ppm, without any further chemical analysis needed.

After the successful use of the fabricated endface FP optical fiber device as a vapor sensor, we considered to test it as a liquid sensor. Thus the device was used for the probing of substances of oily media. Their diffusion behavior in the porous fabricated reflection surface was tested and results revealed that each of the oily liquids exhibited a distinct spectral response versus sensing time, depending on the diffusion process of the oily liquid into the photopolymerized porous reflection surface.

Additionally, theoretical models, based on two-beam optical interference approximation, were used for all the sensing devices, in order to confirm the experimental results and the sensing mechanism of the fabricated devices.

The material that was used for these experiments is a hybrid organic-inorganic photosensitive material that does not require any further fixation process in order to be used for the sensing experiments. In all the previous cases, results show that the sensing mechanism of the devices was based on physisorption phenomena, allowing the full recover of the sensing probes to their initial spectral response (after pumping with nitrogen) and their reuse for several times. This is one more advantage of the fabricated devices since other optical fiber devices based on chemisorption phenomena has limited margins of use, since in most cases, the principal sensing operation relies on chemisorption processes on the surface of the actuating material enabling damages and/or surface corrosion that reduce the sensing device performance.

8.2 Summary and conclusions for the WGM microring resonating devices fabricated directly onto tapered fibers

Regarding to the second part of this thesis, we proposed and realized for the first time the fabrication of micro-ring resonators directly onto tapered single mode telecommunication fibers by employing the multi-photon polymerization technique. Such an approach allowed the demonstration of integrated and robust tapered optical fiber WGM resonators of straightforward packaging capabilities, while preserving high quality light localization and spectral characteristics.

A hybrid organic-inorganic photosensitive material was used for the fabrication of the light resonating components. For the fabrication of these fiber-optic interferometric devices new processes for the sample preparation were explored and developed. The designs of the interferometric components and their fabrication parameters were studied in order to produce functional structures.

Initially the spectral characterization of a single ring microresonator was presented. The spectral performance of the WGM resonators was tested in the wavelength region of 1550 nm. Simulations for the modal order location of the resonance pattern were carried out using Airy approximation and FDTD simulations show that the experimental results were in good agreement with the simulated resonance spectra. Then the resonance dependence to the diameter and the thickness of the microrings was tested. The experimental results show that the 20 μm diameter microrings exhibited well defined resonant spectra. In contrast, the spectra of the 30 μm and 40 μm diameter microrings were more complicated due to the higher order modes that were excited within the resonance path, derive from the extended contact of the polymerized ring onto the tapered fiber. Moreover, the 7 scans fabricated microring, corresponding to ~ 900 nm thickness of the fabricated ring, revealed fringe visibility of 20 dB and Q factor of 3.55×10^3 for the TM polarization spectra that gave the best waveguiding conditions. These values were higher in comparison with the 5 scans (~ 800 nm) and 9 scans (~ 1000 nm) microrings, which fringe visibilities were equal to 12 dB and 10 dB respectively, with Q factors of the order of 0.92×10^3 and 1.19×10^3 respectively for the TE polarization spectra that gave the best waveguiding conditions. These results revealed the fabrication parameters that had to be used during the photopolymerization, since the 5 scans resulted rings of thin walls that deformed after the wet development resulting weak waveguiding, while in contrary 9 scans resulting thick walls that could support higher order modes affecting the waveguiding conditions. Moreover, TE polarization expected to give spectra with higher Q-factors, since the light would propagate in the thinner part of the ring, which would support less modes resulting better waveguiding conditions. Even though, there were few fabricated devices which presented better Q factors and higher fringe visibility, while were excited in TM polarization. This reveals that the position and the angle that the microring is fabricated and attached onto the tapered fiber, is very significant for the performance of the device.

Furthermore, parallel coupled microresonators with different center to center distance were fabricated. In all cases, the resonance spectra show the expected

splitting effect due to the interference between the two rings. The fringe visibility and Q factor of the coupled microresonator with a 27 μm center to center distance were 38.5 dB and 3.82×10^3 respectively for the TE polarization spectra. This coupled microresonator revealed the higher sensitivities in comparison with the other two coupled microresonators which microrings were separated with smaller distances. This could be explained, since the coupled microring that were separated with smaller distances, got deformed after the wet development. This deformation affected the waveguiding conditions. In addition, in case of the coupled microring resonators we were able to record reflection spectra, since the second ring acts as reflector.

Finally, it was observed that defected coupled microresonator exhibits good spectral resonance, with the splitting effect of the fringes introduced in the recorded spectra. Moreover, the fringe visibility and Q factor in this case were 32.5 dB and 4.70×10^3 respectively.

The fabricated single ring resonating devices as well as the parallel coupled ring resonators, were tested as sensors for ethanol vapors detection. Moreover, the photonic molecule (parallel coupled ring resonators) was further tested as an ultrasensitive detector for pressure variations in inert gasses.

For the first device a single ring sensing probe was used for the detection of ethanol vapors. In this case, the spectra presented immediately a monotonic red shift in wavelength, a fact which indicates that the surface of the photopolymerized microrings does not present porosity effects, in contrast with the endface FP optical fiber resonating devices. The sensing device presented sensitivities down to 0.5 ppm with a detectivity figure of $\Delta\lambda_{\text{TM}}/c_{\text{eth}} \sim 0.6 \text{ nm/ppm}$ and $\Delta\lambda_{\text{TE}}/c_{\text{eth}} \sim 0.3 \text{ nm/ppm}$. It was observed that the sensing device corresponding faster while operating in TM polarization, presented stabilization spectra within the first 7 min for concentrations up to 10 ppm of ethanol vapors, while for the higher concentration 12 min required for the spectral stabilization. The corresponding time for TE polarization spectra was 10 minutes for concentrations up to 2 ppm, while for higher concentrations it was more than 37 min. In this case also, the sensing mechanism was relied on physisorption effects, since the sensing probe was full recovered to its initial spectral response and reused for several times.

The second device was a parallel coupled ring sensor tested as a pressure sensor for the detection of inert gases, those of diatomic Nitrogen (N_2) and Krypton (Kr). The maximum pressure that the sensing device was exposed to was up to 600 mbar with the higher recorded detectivity down to $0.6 \times 10^{-4} \text{ nm/mbar}$ in case of Kr sensing and $4.5 \times 10^{-4} \text{ nm/mbar}$ for N_2 .

The last sensing device that was examined was again for ethanol vapor detection using a coupled WGM microresonating probe. The experimental process was similar to that one used for the single ring sensing device. The sensor presented sensitivities down to 0.5 ppm with detectivities of $\Delta\lambda_{\text{TM}} / c_{\text{eth}} \sim 0.5 \text{ nm/ppm}$ and $\Delta\lambda_{\text{TE}} / c_{\text{eth}} \sim 0.1 \text{ nm/ppm}$. It was observed that the single ring device presented faster response and spectral stabilization for the lower vapor concentrations in comparison with the coupled ring device which needed more time to be stabilized for the volumes up to 2 ppm, namely 15 min and 35 min in TM and TE polarization respectively. Moreover,

while single ring device presented a monotonic spectral response to 40 ppm ethanol vapor concentration, the couple ring device presented a non-monotonic spectral response for this vapor concentration, which might could be explanted if we assume that there was liquefaction of the vapors within the spacing of the rings.

To conclude, the successful fabrication of endface FP optical fiber devices, as well as of WGM ring resonators directly fabricated onto tapered fibers devices by multiphoton lithography was presented. The fabrication of different designs and cavity lengths, as well as the different configurations in case of coupled and defected WGM microresonating cavities vouches the early indications of the functionality and robustness for the fabricated devices. In case of the WGM ring resonators, the Q factors could be further increased by improving the positioning of the microring onto the tapered fiber during the polymerization process. To the end, the results of the sensing devices depicting the potential capabilities of the devices and processes demonstrated herein.

8.3 Applications of the devices presented in this thesis

The fabricated endface Fabry-Perot fiber-optic devices had been tested as gas sensors for the detection of ethanol [1] and chlorinated volatile organic compounds [2] and also as liquid sensors for oily samples [3]. On the other hand, the WGM micro-ring resonators had been tested as gas sensors for the detection of ethanol vapors, as well as for the measurement of pressure variation of inert Nitrogen and Krypton gases.

Ethanol vapor sensing can be found in beverage and food industry related with fermentation processes, as well as in the automotive fuel sector, wherein ethanol can be mixed with gasoline for tuning octane performance and fuel price. Moreover, the detection of ethanol in ppm concentrations can be quite advantageous for specific breath analysis applications, related to the early diagnosis of lung cancer [4-6] and metabolic diseases [7, 8], while being implemented in a standard spirometric diagnostic process in off-line mode [9].

The detection of chlorinated volatile organic compounds (Cl-VOCs) can also have significant impact applications in environmental and industrial safety monitoring, since they are widely used substances for a large variety of everyday household and industrial products such as pharmaceuticals, pesticides, freon refrigerants liquids, paper, rubber and dyes [10, 11].

On the other hand, the endface Fabry-Perot fiber-optic device tested with oily samples can be further tested in order to develop fiber-optic sensing probes for the identification of adulterants [12, 13] and plasticizers [14] in oily media targeting the olive oil markets.

Finally, Nitrogen and Krypton are gases that are widely used in laboratory and industrial processes thus it is important to monitor their concentration levels in high accuracy [15] using the WGM devices onto optical fiber tapers.

Moreover, the endface FP fiber-optic sensors and the WGM microring resonators could constitute basic platforms for other sensing and switching devices. For example,

the endface FP fiber-optic device could be tested for its performance as magnetic sensor [16, 17] or even as DNA sensor after the proper functionalization of the photopolymerized sensing head [18, 19]. The single ring resonator device could be used as lasing cavity [20, 21], while the fabricated photonic molecules fabricated in this thesis can find direct applications in optomechanical resonators [22-24], slow light devices and add-drop multiplexers and switches [25-28].

References

- [1] V. Melissinaki, M. Farsari, and S. Pissadakis, "A Fiber-Endface, Fabry-Perot Vapor Microsensor Fabricated by Multiphoton Polymerization," *Ieee Journal of Selected Topics in Quantum Electronics*, vol. 21, p. 10, Jul-Aug 2015.
- [2] V. Melissinaki, I. Konidakis, M. Farsari, and S. Pissadakis, "Fiber endface Fabry-Perot microsensor with distinct response to vapors of different chlorinated organic solvents," *IEEE Sensors Journal*, vol. PP, pp. 1-1, 2016.
- [3] V. Melissinaki, M. Farsari, and S. Pissadakis, "A Fiber Optic Fabry-Perot Cavity Sensor for the Probing of Oily Samples," *Fibers*, vol. 5, p. 1, 2017.
- [4] K. Mitsubayashi, K. Yokoyama, T. Takeuchi, and I. Karube, "Gas-Phase Biosensor For Ethanol," *Analytical Chemistry*, vol. 66, pp. 3297-3302, Oct 15 1994.
- [5] R. F. Machado, D. Laskowski, O. Deffenderfer, T. Burch, S. Zheng, P. J. Mazzone, *et al.*, "Detection of lung cancer by sensor array analyses of exhaled breath," *American Journal of Respiratory and Critical Care Medicine*, vol. 171, pp. 1286-1291, Jun 1 2005.
- [6] J. Rudnicka, M. Walczak, T. Kowalkowski, T. Jezierski, and B. Buszewski, "Determination of volatile organic compounds as potential markers of lung cancer by gas chromatography-mass spectrometry versus trained dogs," *Sensors and Actuators B-Chemical*, vol. 202, pp. 615-621, Oct 2014.
- [7] F. Baldini and A. G. Mignani, "Optical-fiber medical sensors," *Mrs Bulletin*, vol. 27, pp. 383-387, May 2002.
- [8] S. Nair, K. Cope, R. H. Terence, and A. M. Diehl, "Obesity and female gender increase breath ethanol concentration: Potential implications for the pathogenesis of nonalcoholic steatohepatitis," *American Journal of Gastroenterology*, vol. 96, pp. 1200-1204, Apr 2001.
- [9] N. Queralto, A. N. Berliner, B. Goldsmith, R. Martino, P. Rhodes, and S. H. Lim, "Detecting cancer by breath volatile organic compound analysis: a review of array-based sensors," *Journal of Breath Research*, vol. 8, Jun 2014.
- [10] A. McCulloch, "Chloroform in the environment: occurrence, sources, sinks and effects," *Chemosphere*, vol. 50, pp. 1291-1308, 3// 2003.
- [11] B. Huang, C. Lei, C. Wei, and G. Zeng, "Chlorinated volatile organic compounds (Cl-VOCs) in environment - sources, potential human health impacts, and current remediation technologies," *Environment International*, vol. 71, pp. 118-138, Oct 2014.

- [12] G. Fragaki, A. Spyros, G. Siragakis, E. Salivaras, and P. Dais, "Detection of Extra Virgin Olive Oil Adulteration with Lampante Olive Oil and Refined Olive Oil Using Nuclear Magnetic Resonance Spectroscopy and Multivariate Statistical Analysis," *Journal of Agricultural and Food Chemistry*, vol. 53, pp. 2810-2816, 2005/04/01 2005.
- [13] V. G. Dourtoglou, T. Dourtoglou, A. Antonopoulos, E. Stefanou, S. Lalas, and C. Poulos, "Detection of olive oil adulteration using principal component analysis applied on total and regio FA content," *Journal of the American Oil Chemists' Society*, vol. 80, pp. 203-208, 2003.
- [14] X. Bi, X. Pan, S. Yuan, and Q. Wang, "Plasticizer Contamination in Edible Vegetable Oil in a U.S. Retail Market," *Journal of Agricultural and Food Chemistry*, vol. 61, pp. 9502-9509, 2013/10/02 2013.
- [15] <https://www.lenntech.com/periodic/elements/kr.htm>.
- [16] Y. Chen, Q. Han, T. Liu, X. Lan, and H. Xiao, "Optical fiber magnetic field sensor based on single-mode–multimode–single-mode structure and magnetic fluid," *Optics Letters*, vol. 38, pp. 3999-4001, 2013/10/15 2013.
- [17] F. Chen, Y. Jiang, H. Gao, and L. Jiang, "A high-finesse fiber optic Fabry–Perot interferometer based magnetic-field sensor," *Optics and Lasers in Engineering*, vol. 71, pp. 62-65, 2015/08/01/ 2015.
- [18] M. Barozzi, A. Manicardi, A. Vannucci, A. Candiani, M. Sozzi, M. Konstantaki, *et al.*, "Optical Fiber Sensors for Label-Free DNA Detection," *Journal of Lightwave Technology*, vol. 35, pp. 3461-3472, 2017.
- [19] A. Candiani, M. Sozzi, A. Cucinotta, S. Selleri, R. Veneziano, R. Corradini, *et al.*, "Optical Fiber Ring Cavity Sensor for Label-Free DNA Detection," *Ieee Journal of Selected Topics in Quantum Electronics*, vol. 18, pp. 1176-1183, May-Jun 2012.
- [20] A. Francois, N. Riesen, H. Ji, S. Afshar, and T. M. Monro, "Polymer based whispering gallery mode laser for biosensing applications," *Applied Physics Letters*, vol. 106, p. 4, Jan 2015.
- [21] M. Sumetsky, "Lasing microbottles," *Light: Science & Applications*, vol. 6, p. e17102, 10/06/online 2017.
- [22] M. Tomes and T. Carmon, "Photonic Micro-Electromechanical Systems Vibrating at X-band (11-GHz) Rates," *Physical Review Letters*, vol. 102, Mar 2009.
- [23] G. Bahl, J. Zehnpfennig, M. Tomes, and T. Carmon, "Stimulated optomechanical excitation of surface acoustic waves in a microdevice," *Nature Communications*, vol. 2, p. 403, 07/26/online 2011.
- [24] T. Carmon, H. Rokhsari, L. Yang, T. J. Kippenberg, and K. J. Vahala, "Temporal behavior of radiation-pressure-induced vibrations of an optical microcavity phonon mode," *Physical Review Letters*, vol. 94, p. 4, Jun 2005.
- [25] A. K. Dunn, A. Devor, H. Bolay, M. L. Andermann, M. A. Moskowitz, A. M. Dale, *et al.*, "Simultaneous imaging of total cerebral hemoglobin concentration,

- oxygenation, and blood flow during functional activation," *Optics Letters*, vol. 28, pp. 28-30, 2003/01/01 2003.
- [26] H. Du, F. Chau, and G. Zhou, "Mechanically-Tunable Photonic Devices with On-Chip Integrated MEMS/NEMS Actuators," *Micromachines*, vol. 7, p. 69, 2016.
- [27] B. A. Dorin and W. N. Ye, "Two-mode division multiplexing in a silicon-on-insulator ring resonator," *Optics Express*, vol. 22, pp. 4547-4558, 2014/02/24 2014.
- [28] F. Monifi, S. K. Ozdemir, and L. Yang, "Tunable add-drop filter using an active whispering gallery mode microcavity," *Applied Physics Letters*, vol. 103, p. 4, Oct 2013.

Publications

Results of this thesis were published in Academic Journals

1. “Hybrid sensors based on Ring Resonators Fabricated onto Optical Fiber Tapers”, **V. Melissinaki**, M. Farsari and S. Pissadakis, In preparation
2. “A fiber optic Fabry-Perot cavity sensor for the probing of oily samples”, **V. Melissinaki**, M. Farsari and S. Pissadakis, *Fibers*, Vol: 5, Pages: 1 - 10, (January, 2017), doi:10.3390/fib5010001.
3. “Fiber Endface Fabry–Perot Microsensor with Distinct Response to Vapors of Different Chlorinated Organic Solvents”, **V. Melissinaki**, I. Konidakis, M. Farsari and S. Pissadakis, *IEEE Sensors Journal*, Vol: 16, Issue: 19, Pages: 7094 – 7100, (October 1, 2016), doi: 10.1109/JSEN.2016.2596139.
4. “A fiber-endface, Fabry-Perot vapor microsensor fabricated by multiphoton polymerization”, **V. Melissinaki**, M. Farsari and S. Pissadakis, *IEEE Journal of Selected Topics in Quantum Electronics*, Vol. 21, No. 04, 5600110, (2015); DOI: 10.1109/JSTQE.2014.2381463.

Publications in Academic Journals from collaborating projects

1. “3D laser nano-printing on fiber paves the way for super-focusing of multimode laser radiation”, G. S. Sokolovskii, **V. Melissinaki**, K. A. Fedorova, V. V. Dudelev, S. N. Losev, W. Sibbett, M. Farsari, E. U. Rafailov, Submitted.
2. “Design, Fabrication and Computational Characterization of a 3D Micro-Valve Built by Multi-Photon Polymerization”, S. Galanopoulos, N. Chatzidai, **V. Melissinaki**, A. Selimis, C. Schizas, M. Farsari and D. Karalekas, *Micromachines*, Volume 5, Pages 505-514, (2014).
3. “Improvement of the Fabrication Accuracy of Fiber Tip Microoptical Components via Mode Field Expansion”, A. Žukauskas, **V. Melissinaki**, D. Kaskelyte, M. Farsari and M. Malinauskas, *Journal of Laser Micro/Nanoengineering*, Volume 9, No. 1, Pages 68-72, (2014).

Conference papers

1. “Fiber endface Fabry-Perot vapor microsensors fabricated by multiphoton polymerization technique”, **V. Melissinaki**, I. Konidakis, M. Farsari and S. Pissadakis, *Proc. SPIE 9374*, Advanced Fabrication Technologies for Micro/Nano Optics and Photonics VIII, 93740D (March 13, 2015); doi:10.1117/12.2079439.
2. “Optical trapping with superfocused high-M² laser diode beam”, G. S. Sokolovskii, V. V. Dudelev, **V. Melissinaki**, S. N. Losev, K. K. Soboleva, A. G. Deryagin, V. I. Kuchinskii, M. Farsari, W. Sibbett, E. U. Rafailov, *Proc. SPIE 9343*, Laser Resonators, Microresonators, and Beam Control XVII, 93430Q (March 3, 2015); doi:10.1117/12.2078957.
3. “Superfocusing of high-M² semiconductor laser beams: experimental demonstration”, G.S.Sokolovskii, **V. Melissinaki**, V.V.Dudelev, S.N.Losev, K.K.Soboleva, E.D.Kolykhalova, A.G.Deryagin, V.I.Kuchinskii, E.A.Viktorov, M.Farsari, W.Sibbett and E.U.Rafailov, *Proc. SPIE 9134*, Semiconductor Lasers and Laser Dynamics VI, 91341N (May 2, 2014); doi:10.1117/12.2052483.

Conferences

1. Oral Presentation: “Whispering Gallery Mode microbarrel resonators fabricated by multiphoton polymerization technique onto tapered standard telecom fibers“, DPG-Frühjahrstagung (DPG Spring Meeting), Mainz, Germany, (6 - 10 March 2017).
2. Poster Presentation: “Fiber endface Fabry-Perot microsensors for gaseous and liquid species fabricated by multiphoton polymerization technique“, Merging Micro- and Nano-Optics: 3D Printing for Advanced and Functional Optics, Bad Honnef, Bonn/Germany, (9 – 11 January 2017).
3. Oral Presentation: “Fiber endface Fabry-Perot vapour microsensors fabricated by multiphoton polymerization technique”, at "Advanced Fabrication Technologies for Micro/Nano Optics and Photonics VIII", Photonics West, SPIE, San Francisco, California, USA, (07-12 February 2015).
4. Oral Presentation: “Fabry-Perot Vapor Microsensor onto Fibre Endface Fabricated by Multiphoton Polymerization Technique”, 30th Panhellenic Conference on Solid-State Physics and Materials Science, Heraklion, Crete, Greece, (21-24 September 2014).
5. Oral Presentation: “Fabry-Perot Vapor Microsensor onto Fibre Endface Fabricated by Multiphoton Polymerization Technique”, COST Action TD1003: Bio-inspired nanotechnologies: from concepts to applications, Thematic Workshop: Integrated approaches for biomolecular detection: nanostructures, biosensors and lab-on-chip devices, Catania, Sicily, Italy, (28-30 April 2014).
6. Oral Presentation: “Fabry-Perot Vapor Microsensor onto Fibre Endface Fabricated by Multiphoton Polymerization Technique”, Photonics Meets Biology Workshop, Hersonissos, Crete, Greece, (3 - 4 October 2013).
7. Poster Presentation: “Fabry-Perot Vapor Microsensor onto Fibre Endface Fabricated by Multiphoton Polymerization Technique”, Photonics Meets Biology Summer School, Hersonissos, Crete, Greece, (30 September – 3 October 2013).
8. Oral Presentation: “Fabry-Perot Vapor Microsensor onto Fibre Endface Fabricated by Multiphoton Polymerization Technique”, CLEO/EUROPE - IQEC 2013, Munich, Germany, (12-16 May 2013).
9. Oral Presentation: “Fabry-Perot Vapour Microsensors Fabricated onto Fibre Endface by Multiphoton Polymerization Technique”, PULMM Workshop, Cargese, Corsica, France, (14-19 April 2013).
10. Poster Presentation: “Direct Laser Writing of Fabry-Perot microsensor for Vapor Pressure measurements”, 5th International Conference on Micro - Nanoelectronics, Nanotechnologies and MEMS, Kokkini Hani, Heraklion, Crete, Greece, (7-10 October 2012).

Funding

1. GSRT grant Thales (MIS 380278)



2. GSRT funded project, «ΑΝΑΠΤΥΞΙΑΚΕΣ ΠΡΟΤΑΣΕΙΣ ΕΡΕΥΝΗΤΙΚΩΝ ΦΟΡΕΩΝ- ΚΡΗΠΙΣ»
3. FP7 Information and Communication Technologies Access Center for Photonics Innovation Solutions and Technology Support ACTPHAST



4. FP7 Coordination and support action, Action to Support Photonic Innovation Clusters in Europe ASPICE

